Living Reviews in Solar Physics (2022) 19:1
https://doi.org/10.1007/s41116-022-00032-9

REVIEW ARTICLE

Magnetic reconnection: MHD theory and modelling

David I. Pontin[1] · Eric R. Priest[2]

Received: 28 May 2021 / Accepted: 10 January 2022 / Published online: 10 May 2022
© The Author(s) 2022

Abstract

In this review we focus on the fundamental theory of magnetohydrodynamic reconnection, together with applications to understanding a wide range of dynamic processes in the solar corona, such as flares, jets, coronal mass ejections, the solar wind and coronal heating. We summarise only briefly the related topics of collisionless reconnection, non-thermal particle acceleration, and reconnection in systems other than the corona. We introduce several preliminary topics that are necessary before the subtleties of reconnection can be fully described: these include null points (Sects. 2.1–2.2), other topological and geometrical features such as separatrices, separators and quasi-separatrix layers (Sects. 2.3, 2.6), the conservation of magnetic flux and field lines (Sect. 3), and magnetic helicity (Sect. 4.6). Formation of current sheets in two- and three-dimensional fields is reviewed in Sect. 5. These set the scene for a discussion of the definition and properties of reconnection in three dimensions that covers the conditions for reconnection, the failure of the concept of a flux velocity, the nature of diffusion, and the differences between two-dimensional and three-dimensional reconnection (Sect. 4). Classical 2D models are briefly presented, including magnetic annihilation (Sect. 6), slow and fast regimes of steady reconnection (Sect. 7), and non-steady reconnection such as the tearing mode (Sect. 8). Then three routes to fast reconnection in a collisional or collisionless medium are described (Sect. 9). The remainder of the review is dedicated to our current understanding of how magnetic reconnection operates in three dimensions and in complex magnetic fields such as that of the Sun's corona. In Sects. 10–12, 14.1 the different regimes of reconnection that are possible in three dimensions are summarised, including at a null point, separator, quasi-separator or a braid. The role of 3D reconnection in solar flares (Sect. 13) is reviewed, as well as in coronal heating (Sect. 14), and the release of the solar wind (Sect. 15.2). Extensions including the role of reconnection in the magnetosphere (Sect. 15.3), the link between reconnection and turbulence (Sect. 16), and the role of reconnection in particle acceleration (Sect. 17) are briefly mentioned.

Extended author information available on the last page of the article

Keywords Sun: corona · Sun: magnetic fields · Magnetic reconnection · Magnetohydrodynamics

Contents

1 Introduction

Magnetic reconnection is a fundamental process responsible for many dynamic phenomena in solar physics. It occurs in any plasma that is almost-ideal, in the sense that the global Lundquist number (i.e., the magnetic Reynolds number based on the Alfvén speed)

$$R_{me} \equiv S \equiv \frac{L_e v_{Ae}}{\eta} \tag{1}$$

is much greater than unity, where L_e is the global length scale, B_e is the corresponding magnetic field, η is the magnetic diffusivity, and $v_{Ae} = B_e/\sqrt{\mu\rho}$ is the global Alfvén speed. In this article we give a review of the MHD aspects of reconnection theory and refer the reader for further details to Priest and Forbes (2000), Birn and Priest (2007), Yamada et al. (2010) and Priest (2014), including collisionless theory and observational effects of reconnection. Many aspects that have been fully developed in Priest (2014) are treated more briefly here, but newer aspects are added including the magnetic topology of global coronal magnetic fields (Sects. 2.5, 2.7), current sheet formation in 3D magnetic fields (Sects. 5.3–5.6), the plasmoid instability (Sect. 8.3), fast reconnection in a collisional or collisionless medium (Sect. 9), new aspects and models of 3D reconnection and its implications for coronal dynamics (Sects. 10–14), reconnection during flux emergence (Sect. 15.1.2), interchange reconnection (Sect. 15.2), and brief overviews of our understanding of 3D reconnection in the Earth's magnetosphere (Sect. 15.3), in

turbulence (Sect. 16) and non-thermal particle acceleration during reconnection (Sect. 17).

When the plasma is ideal ($R_{me} \rightarrow \infty$), the magnetic connections between plasma elements are preserved. However, when non-ideal effects in the induction equation come into play in a *localised region* of size L ($\ll L_e$), say, magnetic reconnection can occur—i.e., there can be a *change of connectivity of plasma elements* (as indicated in Fig. 1). Often the following physical effects are produced by magnetic reconnection:

(a) the generation of strong electric currents, electric fields and shock waves, which in the solar atmosphere may accelerate fast particles;
(b) ohmic dissipation of the currents, which transforms some of the magnetic energy into heat;
(c) the appearance of strong Lorenz forces, which accelerate plasma to high speeds;
(d) changes in the global connections of magnetic field lines, which alter the paths of fast particles and heat flow.

Resistive MHD provides a good model when the plasma is highly collisional, such as in the Sun's interior and low atmosphere. Even in the collisionless outer corona, it still gives a reasonable model under certain caveats (see Birn and Priest 2007; Priest 2014), but Hall MHD with a two-fluid approach or a kinetic model provide fuller treatments, especially in the interiors of the tiny diffusion region and shock waves (Sect. 9).

In this review, we first develop the background and fundamental concepts that are necessary for understanding the nature of reconnection (Sects. 1–5). We discuss the structure of null points, where the magnetic field vanishes, both in two dimensions (2D) (Sect. 2.1) and three dimensions (3D) (Sect. 2.2), as well as the ways in which such nulls collapse. Then we describe other geometrical features such as separatrices and quasi-separatrices, which map out the skeleton and quasi-skeleton of a complex magnetic configuration (Sects. 2.5,2.6). Other useful and subtle concepts are magnetic helicity (Sect. 4.6), the conservation of magnetic flux and field lines (Sect. 3.2), magnetic diffusion and field-line motion (Sect. 3.3). These

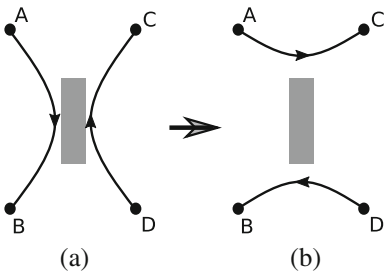

Fig. 1 A change of magnetic connectivity is produced by reconnection in a localised diffusion region (shaded), such that a plasma element A is initially connected to a plasma element B but after reconnection it has become connected to C. For a related movie (courtesy of K. Galsgaard) see Supplementary Information

enable us to go on to describe the different models for 2D and 3D reconnection in Sects. 6–12, as well as some applications and extensions in Sects. 13–17.

1.1 Historical overview

Reconnection theory originated with: Giovanelli (1947)'s idea that electric fields near a magnetic neutral point may accelerate particles and generate heat in solar flares; Cowling (1953)'s realisation that a current sheet only a few metres thick and created by the collapse of an X-type neutral point could do so; and Dungey (1961)'s proposal of reconnection at the Earth's Magnetosphere.

There have been four phases in the development of the theory, as follows.

(i) The *Sweet–Parker model* (Sweet 1958a; Parker 1957) for steady-state reconnection in a thin current sheet of length L, in which magnetic field B_i is carried into the sheet at a speed

$$v_i = \frac{v_{Ai}}{R_{mi}^{1/2}}, \qquad \text{where} \qquad v_{Ai} = \frac{B_i}{\sqrt{\mu\rho}} \quad \text{and} \quad R_{mi} = \frac{L v_{Ai}}{\eta} \tag{2}$$

are the *inflow Alfvén speed* and *magnetic Reynolds number*, respectively, based on B_i, L and v_{Ai}. When $R_{mi} \gg 1$, the reconnection rate (v_i) is much smaller than v_{Ai}, and so this model describes *slow reconnection*.
Then Furth et al. (1963) discovered several resistive reconnection instabilities of a current sheet, including the *tearing mode* (Sect. 8). Also, Petschek (1964) proposed the first regime of *fast reconnection*, whose maximum reconnection rate is typically a hundredth or a tenth of the global Alfvén speed ($0.1 v_{Ae}$), and so it is indeed rapid enough for a solar flare. Most of the energy conversion takes place at four slow-mode shock waves that stand in the flow and extend outwards from a tiny central Sweet–Parker current sheet.

(ii) Numerical experiments (Biskamp 1986) revealed solutions quite different from Petschek's. These at first cast doubt on the validity of the Petschek mechanism, until Priest and Forbes (1986) discovered a whole family of *Almost-Uniform* models for *fast reconnection*, which include the solutions of both Petschek and Biskamp as special cases. The stability of these models has been clarified by Baty et al. (2009a, b), who found them to be stable when the magnetic diffusivity in the diffusion region is enhanced, which may well be produced by current-induced micro-turbulence. Such fast reconnection is thus one way to produce fast reconnection in the solar atmosphere.

(iii) The realisation that fast reconnection at a similar rate to Petschek's mechanism also occurs in two other situations, namely, *collisionless reconnection* and *impulsive bursty reconnection*. When reconnection is collisionless, the Hall effect creates an ion diffusion region of width equal to an ion inertial length together with a smaller electron diffusion region, and these replace the resistive diffusion region (Shay et al. 1998; Huba 2003). Here, the *GEM Challenge* has revealed that the same fast rate of

reconnection is produced by full-particle, hybrid and Hall MHD codes (Birn et al. 2001). In impulsive bursty reconnection, the diffusion region becomes unstable to secondary tearing (Bulanov et al. 1979; Biskamp 1986; Priest 1986; Forbes and Priest 1987; Loureiro et al. 2007; Bhattacharjee et al. 2009).

(iv) Most of the attention is now focused on 3D reconnection, which is revealing many new features that are completely different from 2D reconnection (Priest et al. 2003). A key realisation (Schindler et al. 1988) is that the condition for reconnection in 3D is the presence of an electric field ($E_\parallel$) parallel to the magnetic field, namely,

$$\int E_\parallel \, ds \neq 0,$$

where the integral is taken along a magnetic field line through a diffusion region where the plasma is not ideal. If it is evaluated over all field lines, its maximum value determines the reconnection rate. Unlike the situation in 2D, this can occur in the absence of null points.

Various types of 3D reconnection have been discovered whenever strong localised currents form, depending on whether the current is concentrated along the spine or fan of a null point or along a separator (joining two null points) or a quasi-separator field line (i.e., a hyperbolic flux tube) or in a braid, namely:

- *torsional spine or torsional fan reconnection* (Sect. 10.2) with rotational motions near a null;
- *spine-fan reconnection* with shearing motions near a null (Sect. 10.2);
- *separator reconnection* (Sect. 11) at the intersection of two separatrix surfaces;
- *quasi-separator or HFT reconnection* (Sect. 12) at the intersection of two quasi-separatrix layers (QSLs);
- and *braid reconnection* (Sect. 14.1).

Across a separatrix surface the mapping of magnetic field lines changes discontinuously, whereas across a QSL it changes extremely rapidly but continuously. Quasi-separator reconnection has also been referred to as *slip-running reconnection* (Aulanier et al. 2006), which refers to the *magnetic flipping* process (Priest and Forbes 1992) that is a common feature of much reconnection in three dimensions.

1.2 Summary of reconnection concepts

The behaviour of magnetic fields in 3D is much more subtle and complex than in 2D and exhibits many new features [see Sect. 4 and Priest (2014) for details]. If the plasma behaves in a nonideal way in a finite localised region, then 2D reconnection is only one of several classes of behaviour that obey Faraday's law and $\nabla \cdot \mathbf{B} = 0$. The largest subclass is the one that conserves electromagnetic flux ($\int_{S(t)} \mathbf{B} \cdot d\mathbf{S} + \int_{S(t)} \mathbf{E} \cdot d\mathbf{l} \; dt = \text{const}$). Within that, there lie two large classes of

solution, namely, those that conserve magnetic flux ($\int_{S(t)} \mathbf{B} \cdot d\mathbf{S} = \text{const}$) and those that represent 3D reconnection Hornig, 2001. These in turn intersect in the subclass of 2D reconnection.

Magnetic flux is conserved when the magnetic flux through any surface moving with the plasma is constant, whereas *magnetic field lines are conserved* when any pair of plasma elements lying initially on a magnetic field line remain connected by a field line. For an ideal plasma, $\mathbf{E} + \mathbf{v} \times \mathbf{B} = \mathbf{0}$ and both of these conservation laws hold. A consequence of this is that the magnetic topology is also conserved, where *magnetic topology* refers to any property that is preserved during a smooth deformation, such as the linkage or knottedness of magnetic field lines.

However, when the plasma is non-ideal, so that $\mathbf{E} + \mathbf{v} \times \mathbf{B} = \mathbf{N}$, say, where $\mathbf{N} \neq 0$ represents any nonideal process, the physical effects depend on the form of $\mathbf{N}$. Thus, when $\mathbf{B} \times (\nabla \times \mathbf{N}) = \mathbf{0}$ magnetic field lines are conserved, but when $\nabla \times \mathbf{N} = \mathbf{0}$ magnetic flux is conserved. The forms of these conditions imply that flux conservation and field-line conservation are no longer equivalent, in the sense that flux conservation implies field-line conservation, but the opposite is not true (Sect. 3.2).

There is an important distinction between *magnetic diffusion* and *magnetic reconnection* (Sect. 4.1). Reconnection is a global process which includes diffusion in a localised region, but there are examples of diffusion with no reconnection; for example, the magnetic field may diffuse though the plasma with plasma elements not changing their magnetic connectivity.

The form of $\mathbf{N}$ determines whether diffusion or reconnection occurs and also the type of reconnection. If it cannot be written in the general form $\mathbf{N} = \mathbf{u} \times \mathbf{B} + \nabla \Phi$, then 2.5D or 3D reconnection takes place. However, if it can be written in this form, then:

(a) if $\mathbf{u}$ is smooth, the magnetic field diffuses or slips through the plasma without reconnection;

(b) but if $\mathbf{u}$ is singular, then 2D reconnection occurs.

In 2D, therefore, one can either have slippage of the magnetic field, or reconnection (at an X-type null point), or destruction or generation of magnetic flux (at an O-type null point).

3D reconnection, however, has a completely different nature to 2D reconnection (Sect. 4.4). For example, in 2D, reconnection takes place at an X-point, with the field lines slipping through the plasma in the diffusion region in a manner described by the flux velocity and changing their connections only at the X-point. However, none of these properties hold in 3D, where reconnection may take place at a null or at a separator or quasi-separator (or hyperbolic flux tube), and in the diffusion region field lines continually change their connections. Also, the concept of a flux velocity has to be rethought, since a single flux velocity no longer exists (Sect. 3.3.3, Sect. 4.4).

All of the above concepts are developed in detail in Priest (2014) and briefly in the following sections. However, we begin in the next two sections by discussing important aspects of magnetic field structure in two and three dimensions.

2 Topological and geometrical features of magnetic fields

In two dimensions reconnection occurs only at null points (described in Sect. 2.1). These nulls may be pre-existing in the field and undergo local collapse to form a current sheet (Sect. 2.1), or a one-dimensional current sheet may form, within which a 2D null is created when reconnection is initiated. By contrast, in three dimensions, reconnection is not constrained to occur only at null points: several other magnetic field structures may be sites of reconnection, since they are natural locations where current concentrations tend to form and dissipate. These include separatrix surfaces and their intersections in separator curves (Sect. 2.3), which form a *topological skeleton* or web-like structure in a complex magnetic configuration (Sect. 2.5). Separatrices contribute to the topological structure of a configuration, which may undergo sudden changes in structure, called bifurcations (Sect. 2.4). In addition, non-topological (i.e., geometrical) features, called quasi-separatrix layers (QSLs), can be an important part of the geometry of a magnetic field and form a *quasi-skeleton*. They intersect in *quasi-separators* or *hyperbolic flux tubes* (HFTs), where strong currents may also accumulate (Sect. 2.6). The term *structural skeleton* has been suggested by Titov to refer to the sum of the topological and quasi-skeleton (i.e., both the separatrices and QSLs) and it may be best identified by Titov's Q-factor (Sect. 2.6) (Titov 2007; Titov et al. 2009). For an in-depth account of magnetic topology which complements this review, see Longcope (2005).

2.1 Null points in two dimensions

Special locations in a magnetic configuration where the field vanishes are called *neutral points* or *null points*. In 2D, they come in two types, *X-points* or *O-points*, near which the field lines are hyperbolic or elliptic, respectively (Fig. 2). X-points have a tendency to collapse and form intense sheets of current where reconnection takes place, whereas O-points can be locations of creation or destruction of magnetic flux.

Sufficiently close to a generic magnetic null, the field is dominated by linear terms and has the form

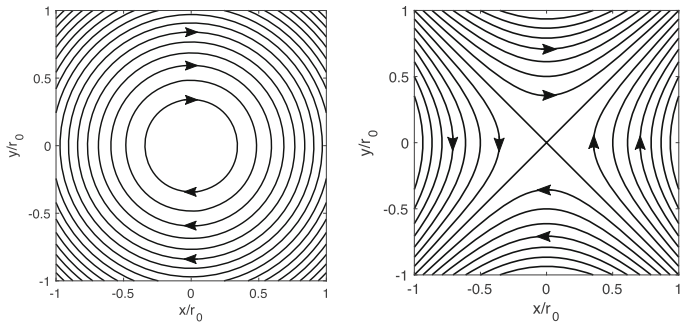

Fig. 2 Examples of 2D null points of (left) O-type and (right) X-type

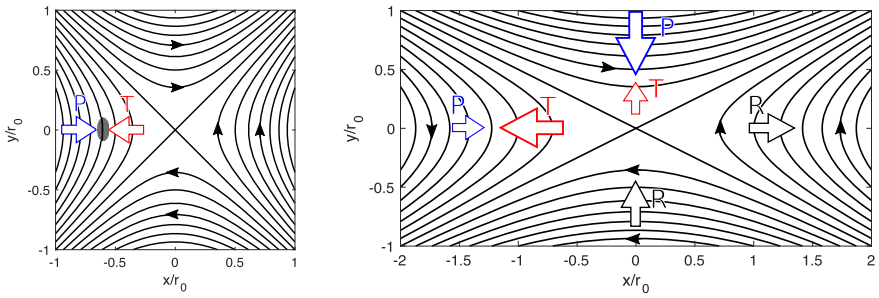

Fig. 3 (left) The field lines of an X-point in equilibrium, with perpendicular separatrices, such that the magnetic pressure (P) and tension (T) forces acting on a plasma element (shaded) balance one another. (right) A perturbation with uniform current produces a resultant force $R = T + P$ that acts to make the separatrices close up. Here we show P and T in just the top and left quadrants and R in just the bottom and right quadrants

$$\mathbf{B} = [B_x, B_y] = \frac{B_0}{r_0}[y, \bar{\alpha}^2 x], \tag{3}$$

where B_0, r_0 and $\bar{\alpha}$ are constants.

From $\mathbf{j} = \nabla \times \mathbf{B}/\mu$, the value of the current density (in the z-direction) is

$$j_z = \frac{B_0}{\mu r_0}(\bar{\alpha}^2 - 1). \tag{4}$$

O-points arise when $\bar{\alpha}^2 < 0$, with the particular case $\bar{\alpha}^2 = -1$ giving circular field lines (Fig. 2a). X-points arise when $\bar{\alpha}^2 > 0$, for which the limiting field lines $y = \pm\bar{\alpha}x$, known as *separatrices*, are inclined at $\pm\tan^{-1}\bar{\alpha}$ to the x-axis. The particular case $\bar{\alpha} = 1$, gives a separatrix angle of $\frac{1}{2}\pi$ (Fig. 2b) and makes the current density vanish (Eq. 4).

An *X-type neutral point* tends to be locally unstable if the sources of the magnetic field are free to move (Dungey 1953). This may be demonstrated by a qualitative physical analysis, a linear analysis or a nonlinear self-similar solution, as detailed in Priest (2014).

An equilibrium X-point (Eq. 3) with $\bar{\alpha} = 1$ has field lines given by $y^2 - x^2 =$ const (Fig. 3a), and is acted on by a Lorentz force ($\mathbf{j} \times \mathbf{B}$), which may be split into a magnetic tension force ($\mathbf{T} \equiv \mathbf{B} \cdot \nabla)\mathbf{B}/\mu$) acting outwards and a magnetic pressure force ($\mathbf{P} \equiv -\nabla(B^2)/(2\mu)$) acting inwards. Initially, these two balance one another, but, if the field is distorted by keeping the form of Eq. (3) and letting $\bar{\alpha}^2 < 1$, it is no longer in equilibrium (Fig. 3b). The equation for the magnetic field lines becomes $y^2 - \bar{\alpha}^2 x^2 = \text{const}$, with the separatrix field lines ($y = \pm\bar{\alpha}x$) no longer being inclined at $\frac{1}{2}\pi$. Along the x-axis, the outwards magnetic tension force now dominates the magnetic pressure due to the increase in field-line curvature, while along the y-axis the inwards magnetic pressure dominates. The equilibrium (3) is unstable, because the Lorentz force tends to make the separatrices close up even more. The resulting increase in $\bar{\alpha}$ implies that the current density also increases.

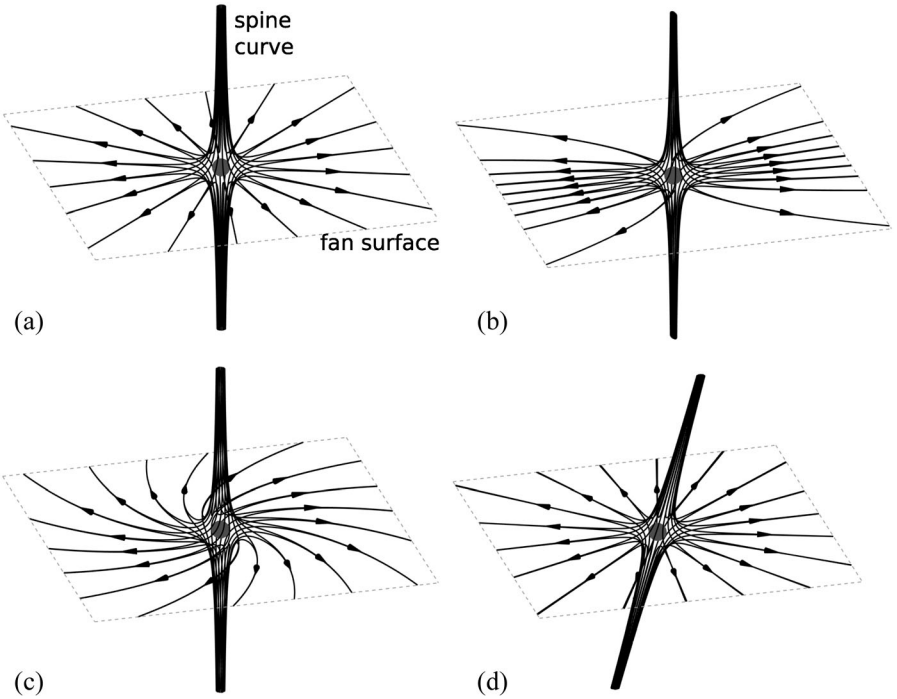

Fig. 4 The two main features of a 3D null point are the spine field line [using Priest and Titov (1996)'s notation] (or γ-line, using Lau and Finn (1990)'s notation) and the fan surface (or Σ-surface). For **a** a proper radial null, the field lines of the fan spread out radially in all directions, while for **b** an improper radial null, most of them touch one of the directions. **c** A spiral null point occurs when $j_{\parallel}$ exceeds a critical value, while **d** an oblique null point results when $j_{\perp} \neq 0$ (see Eq. 6)

Note that the instability occurs only if conditions at distant boundaries allow. It cannot take place in, for example, a potential magnetic configuration whose field lines are tied to the boundaries, since such a minimum-energy state would be stable. However, for a more complex non-potential configuration containing extra energy, collapse may be a means of forming strong currents and so dissipating the excess energy. A series of thorough linear analyses of X-type collapse have been undertaken (e.g., Bulanov et al. 1990; Craig and McClymont 1991, 1993; Titov and Priest 1993). They demonstrate that collapse occurs for a wide variety of initial and boundary conditions, provided the perturbation rate is fast enough that dynamic effects are important, and they show surprisingly that magnetic reconnection during the linear regime is fast and scales as $1/(\ln \eta)$.

2.2 Null points in three dimensions

At a *linear 3D null point* the magnetic field vanishes, and nearby the field increases linearly with distance from it. The simplest example has magnetic components

$$(B_x, B_y, B_z) = (x, y, -2z), \tag{5}$$

and obeys $\nabla \cdot \mathbf{B} = 0$ identically. The magnetic field lines satisfy $dx/B_x = dy/B_y = dz/B_z$, and so their equations are given by $y = Cx$ and $z = K/x^2$, where C and K are constant. They give rise to quite a different structure from 2D (see Fig. 4).

Two special families of field lines pass through a 3D null point (Fig. 4a), as first discussed in a far-sighted paper by Lau and Finn (1990). The terms *spine* and *fan* were later coined for them by Priest and Titov (1996). In the linear null point field of Equation (5), the spine curve is the single field line that approaches or recedes from the origin along the z-axis, with nearby field lines making up two bundles that spread apart as they approach the xy-plane (i.e., the fan surface). When the fan field lines radiate from the null we refer to it as a *positive null point*, whereas when they converge on the null we call it a *negative null point*. A positive null has topological degree -1 while a negative null has topological degree $+1$: they were referred to as "B-type" and "A-type", respectively, by Lau and Finn (1990).

The above null point (Equation 5) is referred to as a *proper radial null*, since it has fan field lines that are straight. A broader class of null points has field components

$$(B_x, B_y, B_z) = (x, ay, -(a+1)z).$$

When $a \neq 1$, we have an *improper radial null*, whose fan field lines are curved, touching the y-axis when $0 < a < 1$ and the x-axis when $a > 1$ (Fig. 4b).

A general linear null possesses a magnetic field with nine arbitrary constants. However, these may be reduced to only four independent constants $(a, b, j_\parallel, j_\perp)$ by using $\nabla \cdot \mathbf{B} = 0$, normalising and rotating the coordinate axes (Parnell et al. 1996), so that

$$\begin{pmatrix} B_x \\ B_y \\ B_z \end{pmatrix} = \begin{pmatrix} 1 & \frac{1}{2}(b - j_\parallel) & 0 \\ \frac{1}{2}(b + j_\parallel) & a & 0 \\ 0 & j_\perp & -a-1 \end{pmatrix} \begin{pmatrix} x \\ y \\ z \end{pmatrix}. \tag{6}$$

When the component $(j_\perp)$ of the current perpendicular to the spine vanishes, the fan surface is normal to the spine: otherwise it is referred to as an *oblique null* (Fig. 4d). When the component $(j_\parallel)$ of current parallel to the spine is sufficiently large, the eigenvalues of the matrix in Eq. (6) become complex and it transforms into a *spiral null*, whose fan field lines spiral into or out of the null (Fig. 4c). The collapse of a linear 3D null point in different ways has been studied, for example, by Bulanov and Olshanetsky (1984), Parnell et al. (1997), and Mellor et al. (2003).

The existence of null points in the solar corona has been discussed by several authors. Twelve hexagonal supergranule cells with sources at their boundaries and centres were modelled by Inverarity and Priest (1999). The distribution of coronal null points due to a random distribution of photospheric sources possesses typically one coronal null for every ten photospheric sources (Schrijver and Title 2002;

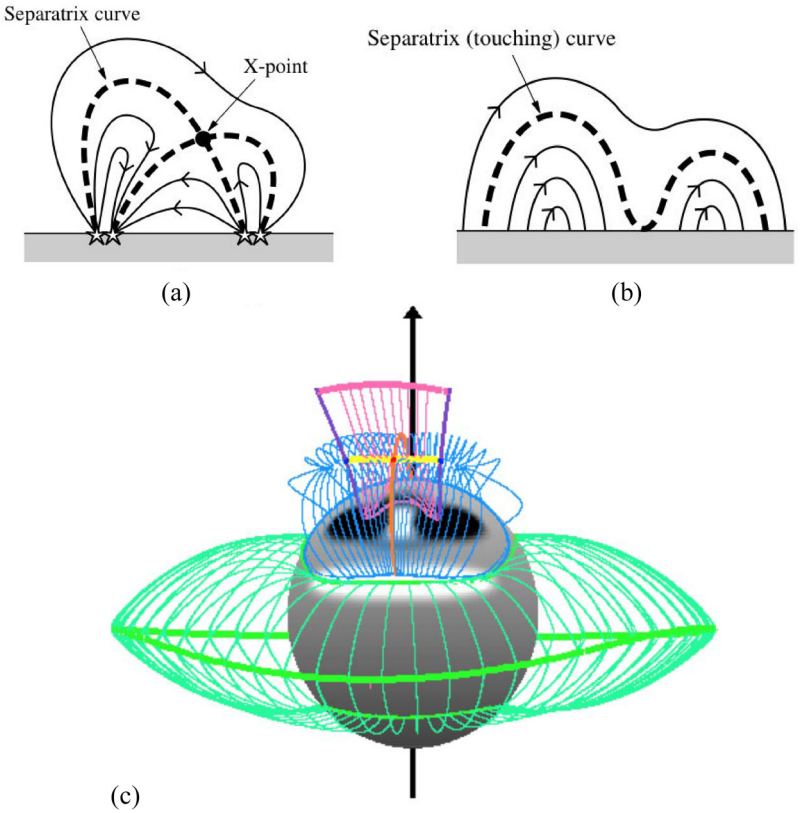

Fig. 5 In two dimensions, separatrix curves **a** may arise from an X-point or **b** they may touch a boundary. **c** In three dimensions, an example of the topology of a global potential field extrapolation. Null points are dark blue and red, while separatrix surfaces are pale blue and pink, intersecting in separators (yellow). Images (**a**) and (**b**) are reproduced with permission from Priest (2014), copyright by CUP, and (**c**) from Platten et al. (2014), copyright by ESO

Longcope et al. 2003). For a field extrapolated from an observed MDI magnetogram, Longcope and Parnell (2009) found one null above a height of 1.5 Mm per 322 Mm^2 patch of the quiet Sun, but this has not yet been repeated for higher-resolution SDO/HMI or SUNRISE magnetograms. Freed et al. (2015) searched for magnetic nulls in potential field source-surface (PFSS) extrapolations based on synoptic magnetograms from the Wilcox Solar Observatory, and compared them with observations of coronal emissions from SDO/AIA. Using only 29 harmonics in the expansion they found 582 null points in the extrapolated field between $1.05\,R_\odot$ and $2.5\,R_\odot$. They also discussed whether the presence of nulls can be inferred from coronal observations of hyperbolic X-type shapes in the emission.

2.3 Separatrices and separators

The coronal magnetic field may be modelled as being produced by continuous or discrete photospheric flux sources and sinks. A two-dimensional field in general contains special field lines, called *separatrix curves*, which divide the plane up into topologically distinct regions, each containing the field lines that start from a particular source and end at a particular sink. Figure 5a,b illustrates the two types of separatrix curve that are possible in 2D, namely, those that originate at X-points and those that touch the boundary in a so-called *bald patch* (Titov et al. 1993). During 2D reconnection, the field lines are broken and rejoined at an X-point as magnetic flux moves from one topological region to another across the separatrices.

These ideas naturally extend into three dimensions, where surfaces of field lines called *separatrix surfaces* or *separatrices* divide the volume into regions of distinct field-line connectivity. When these surfaces intersect one another, they do so in a special field line called a *separator*, which begins and ends at null points or on the boundary (Figs. 5c, 6). Separators were first considered in a ground-breaking paper by Sweet (1958b) and later analysed by many others (Lau and Finn 1990; Priest and Titov 1996; Longcope and Cowley 1996; Longcope 2005; Parnell et al. 2010). The separatrix surfaces are of two types, namely *separatrix fan surfaces*, which are the fan surfaces of null points described in the previous section, and *separatrix touching surfaces*, which touch a boundary in a curve referred to as a *bald patch* (Fig. 5) (Seehafer 1986; Titov et al. 1993; Bungey et al. 1996; Titov and Démoulin 1999). The concept of a touch curve for the Earth's magnetic field was proposed by Hide (1979), and the role of bald patches has been considered for solar prominences and flares (Delannée and Aulanier 1999; Aulanier et al. 2000; Aulanier and Schmieder 2002; Schmieder et al. 2001; Pariat et al. 2004). The global topology or so-called *skeleton* of complex fields due to many sources then comprises a network of separatrix surfaces and their associated null points and separators. Many different configurations are possible, as discussed in Sect. 2.5.

Two types of separatrix may be seen in Fig. 7, namely, *open separatrices* and *closed separatrices* (Priest 2014). Open separatrix surfaces are bounded by spines and meet the boundary in non-closed curves, so that, even though the field-line mapping has a discontinuity as the separatrix is crossed, all the field lines occupy one region, since any two points in the volume can be joined by a curve that does not cross any separatrices. On the other hand, closed separatrices meet the boundary in closed curves, and so form closed flux surfaces that split the volume into topologically different regions.

2.4 Changes in topology and creation of null pairs by a bifurcation

A *local bifurcation* takes place when the number or nature of null points changes, whereas a *global bifurcation* in 2D makes the separatrices change their connectivity. In general, a *local separator bifurcation* may create or destroy isolated null points in pairs (N_1 and N_2, say). The topological structure of the magnetic field during this process is shown in Fig. 7a, where the spines of each null lie in the fans of the other null. The fans (F_1 and F_2) are bounded by the spines (S_2 and S_1) of the opposite

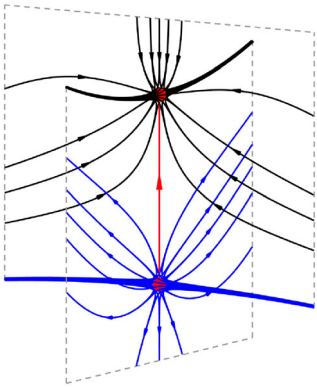

Fig. 6 Magnetic field line structure formed when the fan surfaces of two null points intersect to form a separator line (red) joining the two nulls. For a related movie see Supplementary Information. The movie shows a rotating 3D perspective (courtesy of K. Galsgaard)

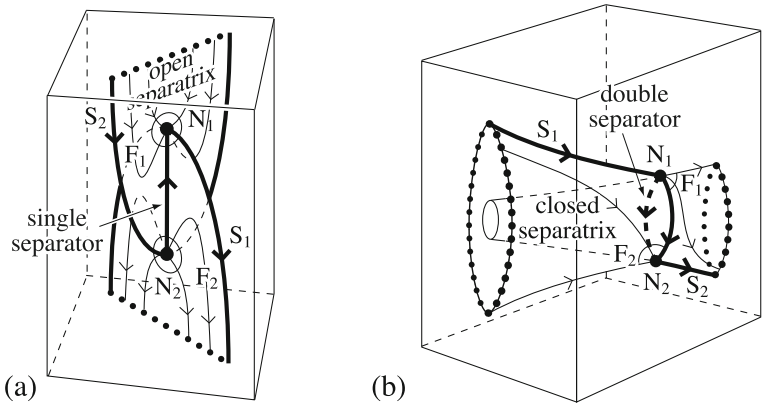

Fig. 7 The topological structure of the field near a pair of nulls (N_1 and N_2), with spines S_1 and S_2 and fans F_1 and F_2. In **a** the fans of the two nulls are *open separatrices* that intersect the boundary in non-closed curves (indicated by dotted lines) and intersect each other in a *single separator* line. This is the generic case for the creation or destruction of a separator by a local bifurcation. In **b** the fans are *closed separatrices* that intersect the boundary in closed curves and each other in a *double separator* forming a closed curve; the spines of the other nulls lie on them but do not bound them: they represent the only field lines that connect to the other nulls. Image reproduced with permission from Priest (2014), copyright by CUP

nulls and form two sheets which intersect in a *single separator* that links one null to the other (see also Fig. 6). During the creation of a linear null pair, a second-order null appears and then splits into two nulls joined by a separator, as shown. Additional separators joining a pair of nulls can be created by a global bifurcation. For instance, Fig. 7b shows a *double separator* consisting of a pair of separators, both of which join the two nulls.

Albright (1999) described the way that null points can form in *clusters*, due to fluctuations in the weak-field region surrounding a null of a "large-scale" field. Thus, another way in which a pair of null points can be created is near a pre-existing null, as shown in Fig. 8. Separators link the new lateral nulls to the central null, and

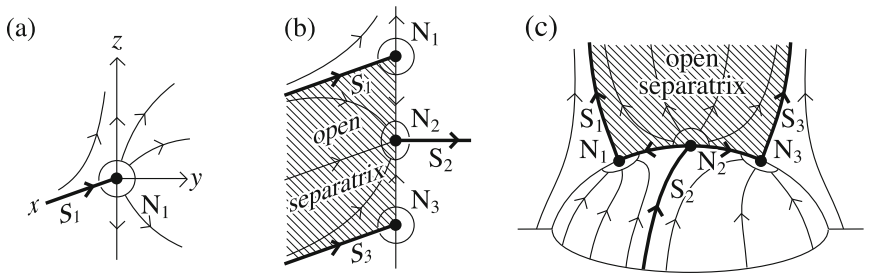

Fig. 8 **a** An initial null point (N_1), which **b** spawns two new nulls (N_2 and N_3) by means of a local double separator bifurcation. The resulting topology possesses an open separatrix coming from the fan F_2 of (N_2) and bounded by spines S_1 and S_3 of the other two nulls (Brown and Priest 2001). **c** A common situation in the corona where a dome that arches down to the solar surface consists of the fans F_1 and F_3 of two nulls, while an open separatrix expands outwards from a third null and is bounded by the spines S_1 and S_3. Image reproduced with permission from Priest (2014), copyright by CUP

the fan of the central null is an open separatrix (Fig. 8b). A common situation in the corona (Fig. 8c) is to have a separatrix dome possessing three nulls and an open separatrix, which can make up a *pseudo-streamer* (Titov et al. 2011; Scott et al. 2021).

The reason why null points are invariably created in pairs is that the topological degree of the volume must be preserved at all times (unless nulls cross the boundary): nulls contribute either $+1$ (negative null) or -1 to this topological degree, and so must be created in pairs of opposite sign. Many numerical experiments, such as those on coronal heating or flux emergence, possess a large number of null points that form like beads on a string or chain, joined in multiple ways by short separators (Parnell et al. 2010; Haynes and Parnell 2010). These separators tend to appear as either tiny *intracluster separators* connecting nulls inside a cluster or as long *intercluster separators* that join distant nulls or other clusters.

Topological or structural stability refers to a situation where the topological features of a magnetic configuration (comprising its skeleton) are not changed by a small change in the field (Hornig and Schindler 1996). *Topological instability*, on the other hand, implies that an arbitrary change of the magnetic field causes a topological change. Linear null points are structurally stable in 2D or 3D (Hornig and Schindler 1996), but *null lines* or *null sheets* (which comprise curves or surfaces where the field vanishes) are structurally unstable, since they will usually break up into a set of null points when perturbed. In general, null points are structurally unstable when they are *degenerate*, so that the Jacobian matrix ($D\mathbf{B}$) given by Eq. (6) is singular.

2.5 Skeletons of complex magnetic configurations

To understand the dynamics of complex magnetic fields such as the field of the solar corona, a key question is how to characterise the magnetic field's structure. The photospheric magnetic field is concentrated by convection into many intense flux

tubes, and each corresponding photospheric flux concentration is itself linked in the corona to many other sources by magnetic field lines (e.g., Schrijver and Title 2002). Magnetic nulls, separatrices and separators are potentially important locations for rapid energy conversion, and so together they can reveal important clues to understanding the dynamics of the solar atmosphere. Thus, a powerful way to understand the behaviour of plasmas threaded by such complicated magnetic fields is to construct the *skeleton* of the field, namely, the set of separatrix surfaces that originate both in the fans of null points and in bald patches and which intersect in separators (see Sect. 2.3).

Early analyses of the different topological magnetic field structures that might be found in the corona made use of the *magnetic charge topology* approach (see Longcope 2005, for an extensive review). In this model, the photospheric flux concentrations are approximated by magnetic point sources (monopoles). Priest et al. (1997), Brown and Priest (1999) catalogued the different configurations that are possible when three photospheric sources are present, and the bifurcations that occur during transitions between those states. This was extended to four flux sources by Beveridge et al. (2002, 2003). These magnetic charge topology models contain a number of photospheric and coronal null points (and separators joining them). However, when the field is modelled alternatively with continuous flux sources, some of the photospheric nulls are no longer present (Lee and Brown 2020), while some of the separators become quasi-separators (or hyperbolic flux tubes) (Sect. 2.6).

Later, the magnetic skeleton in fields with continuous photospheric flux distributions was analysed in detail, with different characteristic structures identified. Platten et al. (2014) showed that the separatrices associated with coronal magnetic nulls (and the spines of those nulls that typically bound one or more fans as in Figs. 7, 8) can intersect with one another in various different configurations involving both closed and open separatrix structures. They identified new topological features, such as *separatrix caves* and *separatrix tunnels* (Fig. 10).

In the solar corona, the skeleton thus possesses several building blocks:

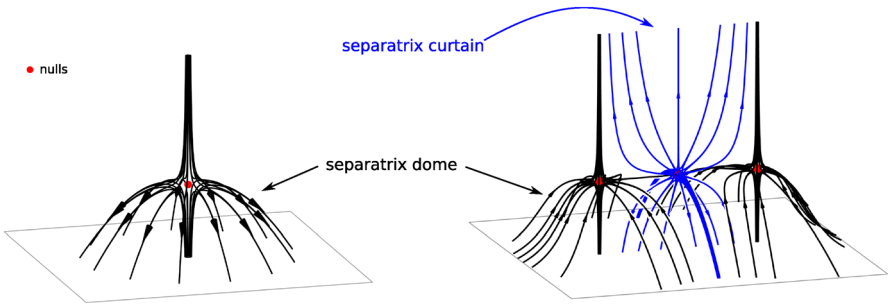

Fig. 9 Building blocks for coronal magnetic field topology arising from coronal nulls. Separatrix domes are formed by the spreading of the fan of the null point down to the solar surface, while separatrix curtains form when a null-point fan is open into the high corona

- *separatrix domes*, whose photospheric field encloses a region of parasitic polarity, above which lies a coronal null (N) with a fan that closes down to the photosphere (Fig. 9a);
- *separatrix curtains*, which spread out from the fans of coronal nulls as open flux sheets that project out into the solar wind, either as closed separatrices or open separatrices (Fig. 9b);
- *bald-patch separatrices*, which touch the solar surface at bald patches;
- *separatrix caves*, having open separatrix domes with one opening, formed from a dome that does not intersect the photosphere on all sides but is bounded by the spine of an opposite polarity null (Fig. 10);
- *separatrix tunnels*, having open separatrix domes with two openings, formed from a dome that does not intersect the photosphere on all sides but is bounded by two spines from opposite polarity nulls (Fig. 10).

2.6 Quasi-skeletons

2.6.1 Quasi-separatrix layers (QSLs) and the squashing factor

As described above, magnetic nulls and separators are potential sites of reconnection in three dimensions. This is in part because they produce discontinuities of the field-line mapping, and so stress tends to accumulate at these structures and drive growth of the electric current (see Sect. 5). However, intense electric currents can also accumulate at locations where the field-line mapping (or connectivity) is continuous, but exhibits steep gradients. Such locations are called *quasi-separatrix layers* (QSLs), a concept first proposed by Priest and Démoulin (1995), built on an earlier idea of singular field lines (Priest and Forbes 1989) and later improved (Titov et al. 2002) and soon applied extensively to active regions and flares (Démoulin et al. 1996a, 1997b, a; Démoulin 2006; Aulanier et al. 2006). A collection of QSLs of a field is known as a *quasi-skeleton*.

Consider the mapping of a 2D X-point field ($B_x = x,\ B_y = -y$) from one point (x_0, y_0) on the boundary to another point (x_1, y_1). When (x_0, y_0) crosses a separatrix, there is a discontinuity in the mapping as the point (x_1, y_1) suddenly jumps in location (Fig. 11a).

In 3D, discontinuities in the mapping are also present at separatrix surfaces that spread out from the fans of null points or from bald patches. In the absence of nulls and bald patches, there are no separatrices, and so the mapping from one footpoint to another is continuous (Schindler et al. 1988). Priest and Démoulin (1995), however, discovered that, even when the mapping is continuous, there often exists a remnant structure known as a *quasi-separatrix layer*, where the gradient of the mapping is much larger than normal. For example, suppose we add a uniform field $l\hat{\boldsymbol{z}}$ to the 2D X-point field to give

$$(B_x, B_y, B_z) = (x, -y, l)$$

inside a cube of side 1 ($-\frac{1}{2} \leqslant x \leqslant \frac{1}{2},\ -\frac{1}{2} \leqslant y \leqslant \frac{1}{2},\ 0 \leqslant z \leqslant 1$). Suppose $l \ll 1$, so that $e^{-1/l} = \epsilon \ll 1$. Then the planes $x = 0$ and $y = 0$ are QSLs, which can be seen as

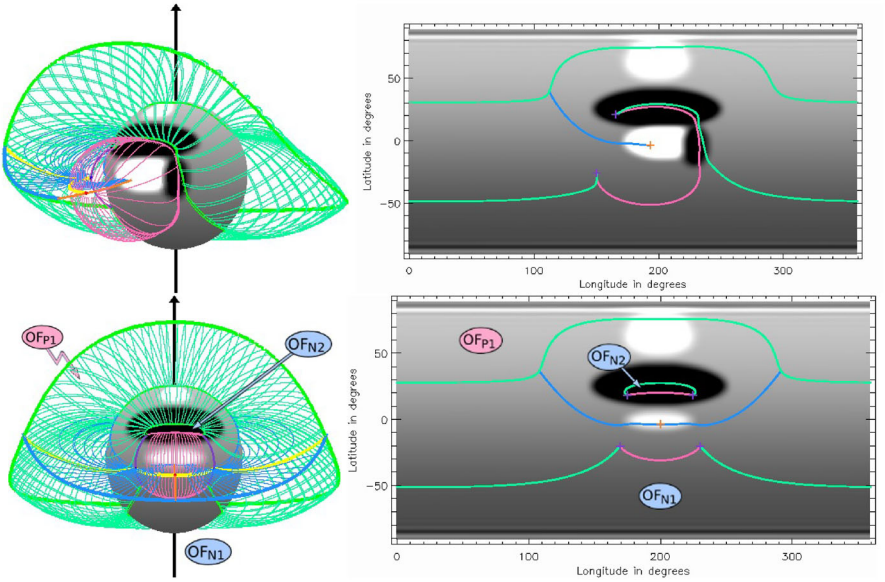

Fig. 10 The structure in pink of a separatrix cave (above) and a separatrix tunnel (below). 3D images of the topology are shown (left) together with maps of the locations where the skeleton meets the photosphere (right). Blue represents a separatrix curtain and green a heliospheric current sheet curtain. Images reproduced with permission from Platten et al. (2014), copyright by ESO

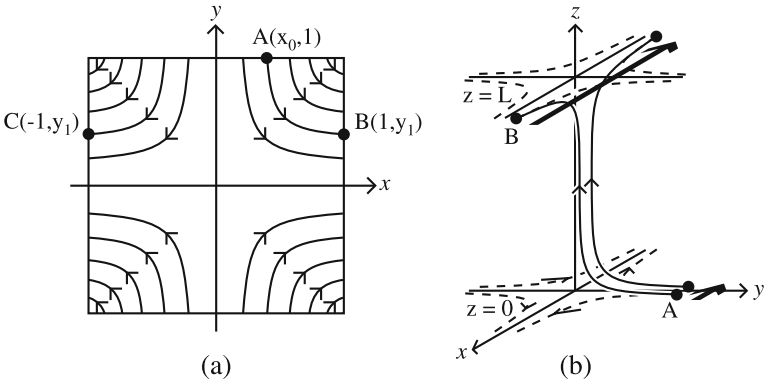

Fig. 11 **a** A 2D X-field has a discontinuity in the mapping of footpoints from the top boundary of a square to the side boundary, **b** but a 3D sheared X-field has a mapping that is continuous from one plane $z = 0$ to another plane $z = L$. Image reproduced with permission from Priest and Démoulin (1995), copyright by AGU

follows. The mapping from the base $z = 0$ to the top $z = 1$ and side $x = \frac{1}{2}$ is given by

$$x_1 = x_0\, e^{z_1/l}, \qquad y_1 = y_0\, e^{-z_1/l}.$$

Thus, as the point A moves a small distance across $x = 0$ from $x_0 = -e^{-1/l}$ to $x_0 = e^{-1/l}$, while y_0 remains constant, so x_1 moves rapidly over a large distance on the top from $-1/2$ to $+1/2$, as indicated in Fig. 11b (y_1 remains constant and very much smaller than y_0).

In order to investigate more generally the quasi-topology of a 3D configuration, the technique is to calculate the mapping of field-line footpoints from one part of a boundary to the other and to determine where the mapping gradient is large (Priest and Démoulin 1995). For example, follow Titov et al. (2002) in considering a typical solar active region with field lines joining photospheric domains of positive and negative polarity (Fig. 12). Set up Cartesian coordinates with $z = 0$ representing the photosphere and suppose the two photospheric footpoints of a given field line have coordinates (x_+, y_+) and (x_-, y_-). The mappings are represented by vector functions $X_-(x_+, y_+)$ and $Y_-(x_+, y_+)$ for the mapping in one direction, as well as $X_+(x_-, y_-)$ and $Y_+(x_-, y_-)$ for the mapping in the opposite direction. Priest and Démoulin (1995) had suggested that the location of QSLs can be found from the condition $N_\pm \gg 1$, where $N_\pm$ are the norms of the footpoint mapping matrices, defined by

$$N_\pm \equiv N(x_\pm, y_\pm) = \left[\left(\frac{\partial X_\mp}{\partial x_\pm}\right)^2 + \left(\frac{\partial X_\mp}{\partial y_\pm}\right)^2 + \left(\frac{\partial Y_\mp}{\partial x_\pm}\right)^2 + \left(\frac{\partial Y_\mp}{\partial y_\pm}\right)^2\right]^{1/2}.$$

Applying this condition for the location of a QSL to magnetic fields in active regions worked well (e.g., Démoulin et al. 1997a), but Titov et al. (2002) and Titov (2007) realised that it could be improved. They suggested instead that N be normalised to give the so-called *squashing factor* (Q) and imposed the condition $Q \gg 2$ to identify QSLs, where Q is defined to be either

$$Q_+ = \frac{-N_+^2}{B_{z+}/B_{z-}} \qquad \text{or} \qquad Q_- = \frac{-N_-^2}{B_{z-}/B_{z+}}. \tag{7}$$

When a circle of footpoints is mapped along field lines to give an ellipse, its aspect ratio is given by $Q/2 + \sqrt{Q^2/4 - 1}$, which tends to Q when $Q \gg 2$. Thus, Q

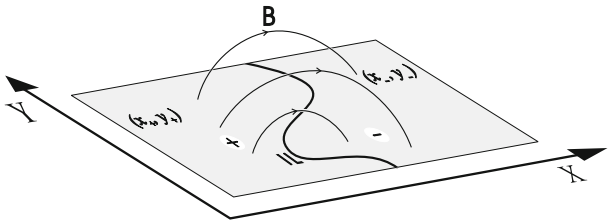

Fig. 12 The photospheric plane and magnetic field lines connecting positive and negative polarities from (x_+, y_+) to (x_-, y_-), which are separated by the polarity inversion line (IL). Image reproduced with permission from Titov et al. (2002), copyright by AGU

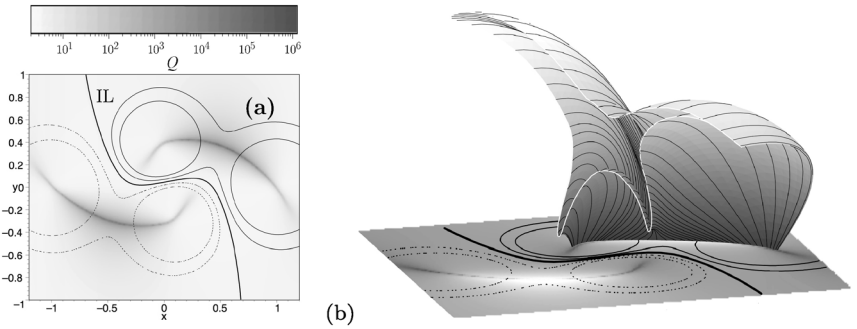

Fig. 13 A potential quadrupole configuration, showing the photospheric distributions of **a** the squashing degree Q superimposed on a few iso-contours of the corresponding magnetogram and **b** half of the magnetic flux surface $Q = 100$ demonstrating the shape of the mid cross-section of the HFT. Image reproduced with permission from Titov et al. (2002), copyright by AGU

represents the degree of squashing of an infinitesimal flux tube, which becomes a thin layer-like flux tube when $Q \gg 2$. The basic properties of Q are as follows:

(i) Q is independent of the direction of the mapping so $Q_+ = Q_-$;
(ii) $Q \to \infty$ at a separatrix surface;
(iii) $Q \gg 2$ at a quasi-separatrix layer;
(iv) Maps of Q identify the locations (i.e., both separatrices and QSLs) where large current densities may accumulate, provided appropriate velocities are present, and therefore where reconnection has the potential to occur.

Titov stresses that a QSL is a geometric rather than a topological feature and also emphasizes its importance for current sheet formation by stagnation-point flows (Cowley et al. 1997; van Ballegooijen 1985; Mikić et al. 1989; Longcope and Strauss 1994; Galsgaard and Nordlund 1996).

Later, Titov (2007) derived a covariant form for the squashing factor (Q) which enabled him to diagnose the presence of QSLs in closed and open configurations with arbitrary boundary shapes. He also showed that the perpendicular squashing factor ($Q_\perp$) is superior to Q, since it eliminates the projection effect that is present in field lines that nearly touch a boundary. Furthermore, Titov et al. (2009) introduced the concept of slip-forth (Q_{sf}) and slip-back squashing factors (Q_{sb}), which enable the identification of flux tubes that have either just reconnected or are about to be reconnected (Sect. 12.1).

2.6.2 Examples of QSLs

Titov (2007) described two examples of simple configurations for modeling solar flares. The first is a potential quadrupole configuration (Sweet 1969; Baum and Bratenahl 1980; Gorbachev and Somov 1988), which possesses a separator joining two nulls when the photospheric magnetic flux is concentrated in discrete patches. However, when the photospheric flux is distributed smoothly, the nulls and

separator disappear, but a *quasi-separator* (or hyperbolic flux tube) remains, as shown in Fig. 13.

The quasi-separator represents the intersection of two quasi-separatrix layers (QSLs), and the region around the quasi-separator is known as a *Hyperbolic Flux Tube* (HFT) (Titov et al. 2002). The Hyperbolic Flux Tube is bounded by the magnetic flux surface $Q = \text{const} \gg 2$ and has a shape that continuously transforms along the tube from a narrow flattened tube to a cross and then to a second orthogonal narrow flattened tube at the other end, as follows (Titov et al. 2002):

The second example is a model for a twisted flux tube, which also contains a pair of QSLs and a quasi-separator (or hyperbolic flux tube) (Démoulin et al. 1996b). Titov and Démoulin (1999) suggested an approximate, cylindrically symmetric equilibrium for a thin force-free toroidal flux rope with a net current I, major radius R and minor radius a (Fig. 14). The symmetry axis of the flux rope lies below the photospheric plane $z = 0$ at a depth d. There is a balance between the outward radial $\mathbf{j} \times \mathbf{B}$ self-force of the flux rope and the field of two magnetic charges of opposite sign located on that symmetry axis below the photosphere at distances $\pm L$ from the torus plane. The field outside the torus is current-free and contains a magnetic X-line.

A line current I_0 is added along the symmetry axis and creates a toroidal field component, which turns the environment of the X-line into an HFT, as can be seen in the photospheric distribution of Q in Fig. 15a (Titov 2007).

The most intense squashing occurs in very thin QSLs whose footprints have the shape of narrow fishhook-like strips. Fig. 15b shows the flux surface $Q = 100$ of the

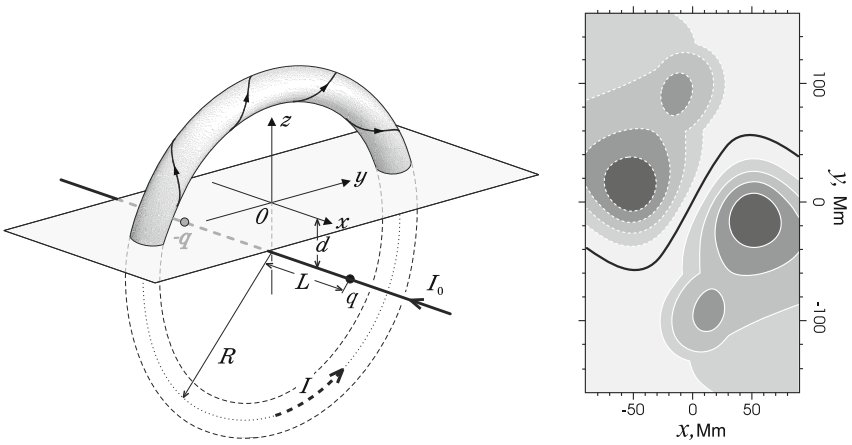

Fig. 14 The Titov–Démoulin model of a circular force-free flux rope (left) with a net current I, embedded in a potential background field produced by two subphotospheric magnetic charges $(-q, q)$ and a line current (I_0). The resulting coronal field has a photospheric magnetogram (right) that resembles that of a typical solar active region. The solid and dashed curves represent positive and negative iso-contours of B_z, respectively. Image reproduced with permission from Titov and Démoulin (1999), copyright by ESO

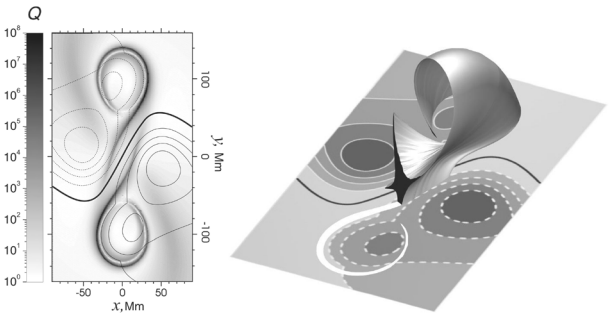

Fig. 15 For the twisted flux tube configuration of Fig. 14 **a** the photospheric distribution of the squashing degree Q together with magnetogram iso-contours, and **b** a cut through the HFT by a midplane with its cross-section and footprint shown in black and white, respectively. Image reproduced with permission from Titov (2007), copyright by AAS

HFT. The variation of its cross-section is similar to that of the first example, except that the whole structure is also twisted.

2.7 Global topology of coronal magnetic fields and methods of analysis

Several complementary tools have been developed in order to find the skeleton or quasi-skeleton of a magnetic configuration. For the magnetic skeleton, the first step is to locate the magnetic nulls, for which a common, robust way is the *trilinear method* described by Haynes and Parnell (2007). Other techniques for finding magnetic nulls exist, depending on the type of data, and these are compared by Olshevsky et al. (2020). From the nulls, the spine and fan field lines can be followed. Finding separator lines is challenging since the field lines tend to diverge away from them, but subtle techniques have been developed by Haynes and Parnell (2010).

Platten et al. (2014) used these methods to find the magnetic skeleton of the global corona; they noted incredible complexity, especially as the resolution of the magnetogram used for coronal field extrapolation is increased. In general, as the magnetogram resolution is increased, many more nulls appear, usually at low altitudes. Generally speaking, at solar minimum the apex of the helmet streamer separatrix remains relatively close to the equator, and open and closed separatrix fans are found in abundance at low latitudes (Fig. 16a). On the other hand, at solar maximum the complexity tends to be greater, with separatrices of different types extending up to the source surface at all latitudes (Fig. 16b). Platten et al. (2014) made a statistical analysis of the topological complexity during the cycle. They found that the number of nulls is anti-correlated with the sunspot number (and as a result so too is the number of separators), which can be understood from the fact more of the photosphere is covered by mixed polarity at solar minimum. On the other hand the nulls and associated separators are located higher in the corona at solar maximum. Again there is an intuitive explanation, namely, that null points tend to form at heights on the order of the separation of the photospheric flux patches responsible for their presence, and these flux patches are large at solar

maximum. While this and many previous studies (see Sect. 2.5) focussed on potential fields, Edwards et al. (2015) analysed the topological skeleton of a force-free model for the coronal field. They showed that there are substantial differences with the topology of the equivalent potential field models: for example, open field domains (coronal holes) that are present in one model can be absent in the other. It is also worth noting that, while the existence of nulls is relatively robust to the extrapolation method, the details of the null spine-fan structure can be dependent on the force-free extrapolation method (Metcalf et al. 2008). It is clear that extension beyond potential field models is an important future avenue of research.

One disadvantage of calculating the magnetic skeleton is that QSLs and HFTs are not included, leaving an incomplete picture of potential sites for reconnection. By contrast, the *squashing factor* (Q) reveals the locations of both separatrices and QSLs. However, it does not distinguish between them, except for the fact that separatrices appear generally as thinner structures in practice (e.g., Titov 2007; Titov et al. 2012; Masson et al. 2012). This is because separatrices correspond to surfaces at which $Q \to \infty$, whereas the finite resolution of such calculations means that they deal only with large, finite Q values. A recent advance which allows fast, accurate calculation of Q is the `qslsquasher` code developed by Tassev and Savcheva (2017). It allows for accurate calculations of Q that are not susceptible to noise, even for large integration steps along the field line, so that Q can be calculated much more quickly than before (for a given spatial resolution).

Thus, in order to obtain a full and accurate picture of the important magnetic field structures for reconnection, both the skeleton and the squashing factor should be

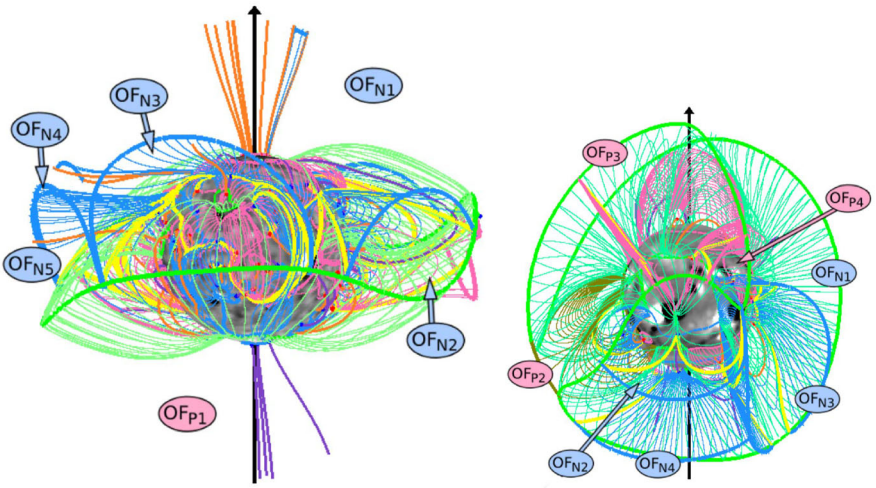

Fig. 16 Magnetic skeleton with positive (green) and negative (blue) field lines, as calculated by Platten et al. (2014) at **a** solar minimum and **b** solar maximum. Positive and negative polarity open-field regions are labelled OF$_{P1}$, OF$_{P2}$, ...and OF$_{N1}$, OF$_{N1}$, ...respectively. Topological structures include separators (thick yellow), and separatrix surfaces (green and blue) traced from nulls and from the null lines (thick green and blue) on the outer boundary at the base of the heliospheric current sheet (HCS). Image reproduced with permission from Platten et al. (2014), copyright by ESO

obtained. Recently, Scott et al. (2018, 2019) have used global calculations of Q to *segment* the coronal volume into magnetic flux domains bounded by surfaces of high Q, and have additionally calculated the magnetic nulls. Their motivation was to explore the nature of structures bounding open and closed magnetic flux in the corona: it is proposed that "interchange" reconnection—i.e., reconnection between closed and open magnetic field lines—may be important for structuring the solar wind (Fisk et al. 1998; Crooker et al. 2002; Antiochos et al. 2011)—see Sect. 15.2. They discovered that, in a survey of potential fields, approximately half of these "S-web" structures contain magnetic nulls, while the other half do not (Scott et al. 2019). This highlights the importance of determining the locations of both the QSLs and the nulls and separatrices.

3 Conservation of magnetic flux or field lines

Central to understanding magnetic reconnection in three dimensions are the concepts of flux and field-line conservation, which are much more subtle than normally appreciated. For an ideal MHD plasma, the situation is straightforward, since both flux and field lines are conserved, and the plasma velocity is identical with the flux velocity and the field-line velocity (Sect. 3.1). In nonideal MHD, however, flux and field-line conservation are no longer equivalent (Hornig and Schindler 1996), and neither flux velocity nor field-line velocity is unique (Sect. 3.2). Hornig (1997) has developed a more general concept of *Electromagnetic Flux Conservation*, of which magnetic flux conservation is just a subclass [see Priest (2014)], but here we focus just on the concepts of flux and field-line conservation, following Hornig (1997, 2001).

3.1 Conservation in an ideal plasma

When the magnetic Reynolds number is very large ($R_m \gg 1$), the plasma behaves in an ideal manner. The induction equation for magnetic field evolution and Ohm's law reduce to

$$\frac{\partial \mathbf{B}}{\partial t} = \nabla \times (\mathbf{v} \times \mathbf{B}) \quad \text{and} \quad \mathbf{E} + \mathbf{v} \times \mathbf{B} = 0. \tag{8}$$

It may then be shown that magnetic flux, magnetic field lines and magnetic topology are all conserved, and that the components perpendicular to the magnetic field of plasma velocity ($\mathbf{v}_\perp$), flux velocity ($\mathbf{w}_\perp$) and field-line velocity ($\mathbf{w}_{L\perp}$) are the same, namely,

$$\mathbf{v}_\perp = \mathbf{w}_\perp = \mathbf{w}_{L\perp} = \frac{\mathbf{E} \times \mathbf{B}}{B^2}.$$

For *Magnetic Flux Conservation*, the magnetic flux ($\int_S \mathbf{B} \cdot \mathbf{dS}$) through any surface composed of plasma elements is fixed (Fig. 17). *Magnetic Field Line Conservation*, on the other hand, implies that two plasma elements that are initially linked by a magnetic field line, will continue to be so at later times (Fig. 18).

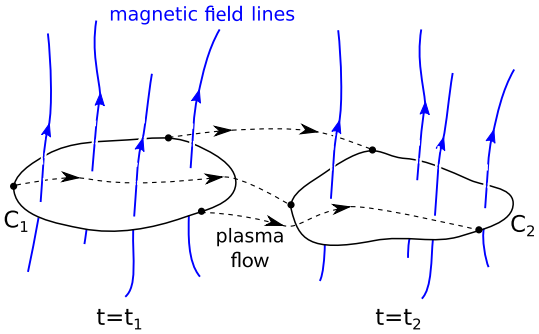

Fig. 17 Magnetic flux conservation: the flux through a curve C_1 at time t_1 remains constant when it is distorted into a curve C_2 at time t_2 by a plasma motion

3.2 Conservation in a non-ideal plasma

When the plasma is not ideal, we assume that Ohm's law takes the form

$$\mathbf{E} + \mathbf{v} \times \mathbf{B} = \mathbf{N}, \tag{9}$$

where the term $\mathbf{N}$ on the right is any general non-ideal term due to for instance collisions, fluctuations, particle inertia or classical resistivity; in the case of classical resistivity, it is written $\mathbf{N} = \eta \nabla \times \mathbf{B}$. We shall find that flux and field-line conservation depend on the form of $\mathbf{N}$.

3.2.1 Magnetic flux conservation in a non-ideal plasma

The concept of flux transport can be extended to include non-ideal plasmas, although the velocity of this transport is not unique. If a magnetic flux velocity ($\mathbf{w}$) exists with the same flux-preserving property as in ideal MHD, namely, one for which

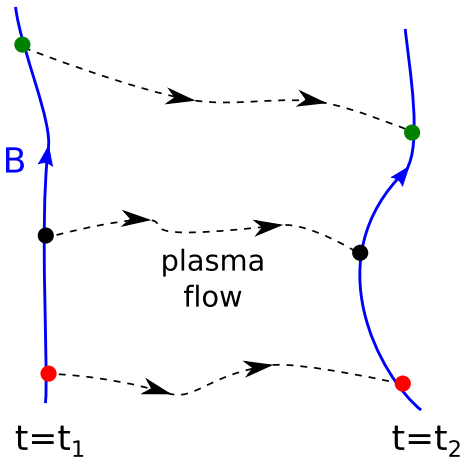

Fig. 18 Magnetic field-line conservation: plasma elements (red, black, green circles) that lie on the same field line at an initial time (t_1) will continue to lie on a single field line at later times (t_2)

$$\frac{\partial \mathbf{B}}{\partial t} = \nabla \times (\mathbf{w} \times \mathbf{B}), \tag{10}$$

then we say that magnetic field evolution satisfying Eq. (10) is *flux-preserving*. For an Ohm's Law of the form (9), Faraday's equation ($\partial \mathbf{B}/\partial t = -\nabla \times \mathbf{E}$) implies that

$$\frac{\partial \mathbf{B}}{\partial t} = \nabla \times (\mathbf{v} \times \mathbf{B} - \mathbf{N}). \tag{11}$$

Comparing Eq. (10) with Eq. (11), we see that a flux velocity ($\mathbf{w}$) exists—and so *Magnetic Flux is Conserved*—provided the nonideal term in Eq. (9) can be written in the form

$$\mathbf{N} = \mathbf{u} \times \mathbf{B} + \nabla \Phi, \tag{12}$$

where Φ is a potential and the difference ($\mathbf{u} \equiv \mathbf{v} - \mathbf{w}$) between the plasma and flux velocities is the slippage velocity. Since $\mathbf{u} \times \mathbf{B}$ is perpendicular to $\mathbf{B}$, it can be seen from Eq. (9) that it is the $\nabla \Phi$ term that can produce a component ($E_{\|}$) of $\mathbf{E}$ along the magnetic field, which is essential for 3D reconnection (Sect. 4.5). Furthermore, Ohm's law can then be written in terms of the flux velocity as

$$\mathbf{E} + \mathbf{w} \times \mathbf{B} = \nabla \Phi. \tag{13}$$

In addition, magnetic flux is conserved provided $\mathbf{N}$ satisfies

$$\nabla \times \mathbf{N} = 0. \tag{14}$$

3.2.2 Magnetic flux velocity

Since displacements along the magnetic field are arbitrary when considering transport of flux, we may set them to zero, so that $(\mathbf{w} - \mathbf{v}) \cdot \mathbf{B} = 0$. Then, useful information about the nature of $\mathbf{w}$ can be found by taking the vector and scalar products of Eq. (13) with $\mathbf{B}$. First of all, taking vector products of the two forms (9) and (13) of Ohm's law with $\mathbf{B}$ and subtracting them implies that the flux velocity may be written

$$\mathbf{w} = \mathbf{v} + \frac{(\mathbf{N} - \nabla \Phi) \times \mathbf{B}}{B^2}, \tag{15}$$

which implies that ($\mathbf{w}$) may become singular at a null point (where $B = 0$).

Next, take the scalar product of Eq. (13) with $\mathbf{B}$ to give

$$\mathbf{B} \cdot \nabla \Phi = \mathbf{E} \cdot \mathbf{B},$$

which, provided nulls or boundary conditions do not lead to difficulty, may be integrated along a field line $\mathbf{B}$ from an arbitrary value $\Phi_0(\mathbf{r}_0, t)$ at some reference surface ($\mathbf{r}_0$), say, to give

$$\Phi(\mathbf{r},t) = \int_{\mathbf{r}_0}^{\mathbf{r}} \mathbf{E}\cdot\mathbf{ds} + \Phi_0(\mathbf{r}_0,t). \tag{16}$$

Since Φ_0 is arbitrary, both $\Phi(\mathbf{r},t)$ and $(\mathbf{w})$ in Eq. (15) are not unique.

When $E_\parallel = 0$ there is no 3D reconnection, but there is magnetic diffusion with a slippage velocity given for a resistive Ohm's law by Eq. (15) as

$$\mathbf{u} \equiv \mathbf{v} - \mathbf{w} = -\frac{\mathbf{j}\times\mathbf{B}}{\sigma B^2}.$$

In order to avoid Φ becoming multiple-valued as one integrates around a closed field line, a necessary condition for (16) to be valid is that

$$\Phi = -\oint \mathbf{E}\cdot\mathbf{dl} = 0$$

around such a field line. When the magnetic field is steady (so that $\nabla\times\mathbf{E} = 0$), this is always satisfied, but, when it is unsteady, it may fail (Hornig 2001).

3.2.3 Magnetic field line conservation in a non-ideal plasma

Whenever magnetic flux is conserved, it turns out that magnetic field lines are also conserved. By contrast, there are many evolutions in a non-ideal plasma that conserve field lines but do not conserve flux. In a non-ideal plasma, magnetic flux is conserved if Eq. (10) holds, whereas magnetic field lines are conserved if

$$\frac{\partial\mathbf{B}}{\partial t} = \nabla\times(\mathbf{w}_L\times\mathbf{B}) + \lambda_L\mathbf{B}, \tag{17}$$

so that, by comparing with Eq. (11), $\mathbf{N}$ must have the property that $\nabla\times\mathbf{N}$ is parallel to $\mathbf{B}$, i.e., field lines are conserved if

$$\mathbf{B}\times(\nabla\times\mathbf{N}) = 0. \tag{18}$$

In Eq. (17), $\mathbf{w}_L$ is a magnetic field-line velocity and λ is a scalar function of position, and so, by choosing $\lambda = \lambda_L + \nabla\cdot\mathbf{w}_L$ and using $\nabla\cdot\mathbf{B} = 0$, Eq. (17) may be rewritten

$$\frac{\partial\mathbf{B}}{\partial t} + (\mathbf{w}_L\cdot\nabla)\mathbf{B} - (\mathbf{B}\cdot\nabla)\mathbf{w}_L = \lambda\mathbf{B}.$$

Thus, if we choose $\lambda_L = 0$ and $\mathbf{w}_L = \mathbf{w}$, Eq. (17) for field-line conservation reduces to Eq. (10) for flux conservation. In other words, when flux is conserved, field lines are conserved too. On the other hand, when $\lambda_L \neq 0$, field lines are conserved but flux is not.

3.2.4 Magnetic field line velocity

When the plasma is not ideal, the field-line velocity component $(\mathbf{w}_{L\perp})$ can be defined uniquely if and only if Ohm's Law may be written as

$$\mathbf{E} + \mathbf{w}_L \times \mathbf{B} = \mathbf{a}, \tag{19}$$

with $\nabla \times \mathbf{a} = -\lambda_L \mathbf{B}$, in which case Eq. (19) and Eq. (8) imply Eq. (17). This definition is field-line preserving but is only flux preserving when $\nabla \times \mathbf{a} = \mathbf{0}$, so that $\mathbf{a} = \nabla \Phi$ and $\lambda_L = 0$.

When the plasma is ideal, it is always possible to write Eq. (19), and so the perpendicular component of the field-line velocity is

$$\mathbf{w}_{L\perp} = \frac{\mathbf{E} \times \mathbf{B}}{B^2},$$

but it is also possible when $\mathbf{E} \cdot \mathbf{B} = 0$. More generally, when Eq. (19) holds, the field-line velocity is

$$\mathbf{w}_{L\perp} = \frac{(\mathbf{E} - \mathbf{a}) \times \mathbf{B}}{B^2}.$$

However, this form is not unique, since the magnetic field is unchanged if we replace $\mathbf{a}$ by $\mathbf{a}' = \mathbf{a} + \nabla \Psi^*$, with $(\mathbf{B} \cdot \nabla)\Psi^* = 0$, such that $\mathbf{B}\cdot$(19) does not change, but the field-line velocity becomes instead

$$\mathbf{w}'_{L\perp} = \frac{(\mathbf{E} - \mathbf{a}') \times \mathbf{B}}{B^2}.$$

The concepts of flux and field line velocity, and their uniqueness or otherwise, are invaluable when considering the properties of 3D reconnection (Sect. 4).

3.3 Magnetic diffusion and field-line motion

To complete our discussion of field line motion we consider the case of pure diffusion (with plasma velocity $\mathbf{v} = 0$). Wilmot-Smith et al. (2005) presented examples of magnetic diffusion in 1D (Sect. 3.3.1), 2D (Sect. 3.3.2) and 3D (Sect. 3.3.3). Often, diffusion can be described with the help of a magnetic flux velocity, but such a velocity is usually non-unique, so that the field lines may be said to move in several different ways. For straight magnetic field lines with diffusion in a current sheet, the magnetic field behaves as if the flux disappears either at a current sheet and/or at infinity. In a similar manner, circular field lines diffuse as if the magnetic field moves either towards the O-type neutral line and/or towards infinity. In 3D, although magnetic field lines can always be defined at any time, the decay of a field cannot necessarily be described in terms of the motion of magnetic field lines, since it is not always possible to define a flux velocity. Instead, it may be possible to describe the field behaviour in terms of a *dual flux velocity* (Sect. 3.3.3, Sect. 4.4). For more details on these ideas, see Wilmot-Smith et al. (2005).

Consider resistive diffusion of a magnetic field with uniform magnetic diffusivity (η), for which $\mathbf{E} = \eta \nabla \times \mathbf{B}$ and the induction equation becomes

$$\frac{\partial \mathbf{B}}{\partial t} = \nabla \times (\eta \nabla \times \mathbf{B}) = \eta \nabla^2 \mathbf{B}, \tag{20}$$

while the existence of a magnetic flux velocity (or flux transporting velocity) ($\mathbf{w}$) requires Eq. (10). 1D, 2D, and 3D scenarios are considered in turn below.

3.3.1 Diffusion of a magnetic field with straight field lines

When a 1D magnetic field ($\mathbf{B} = B(x,t)\hat{\mathbf{y}}$) diffuses, magnetic field lines can disappear either at a neutral sheet or at the boundary, and the diffusion equation (20) reduces to

$$\frac{\partial B}{\partial t} = \eta \frac{\partial^2 B}{\partial x^2}.$$

Consider, for example, a magnetic field whose value is held fixed at two points ($\pm\ell$) with $B(\ell,t) = -B(-\ell,t) = B_0$, and that initially has a step profile with $B(x,0) = B_0$ for $x > 0$, and $B(x,0) = -B_0$ for $x < 0$, representing an infinitesimally thin current sheet. The solution to the diffusion equation is

$$B(x,t) = B_0 \frac{x}{\ell} + \frac{2B_0}{\pi} \sum_{n=1}^{\infty} \frac{1}{n} \exp\left(-n^2\pi^2\eta t/\ell^2\right) \sin\left(\frac{n\pi x}{\ell}\right),$$

and the resulting magnetic field diffuses away very rapidly towards the steady-state solution, $B(x) = B_0 x/\ell$. In terms of energy, a decrease in magnetic energy is accounted for by Ohmic heating (j^2/σ) and an outwards Poynting flux $\mathbf{E} \times \mathbf{B}/\mu = -(\eta/\mu)\partial B/\partial x\, \hat{\mathbf{x}}$ into the boundaries $x = \pm\ell$. In the final steady state, the ohmic heating ($j^2/\sigma = (\eta/\mu)(B_0/\ell)^2$ per unit length) is provided by a continual inflow of energy through the boundaries.

In this case, a flux velocity ($\mathbf{w} = w\hat{\mathbf{x}}$) exists and Eq. (13) becomes

$$\eta \frac{\partial B}{\partial x} + wB = E_0(t),$$

with solution

$$w = -\frac{\eta}{B}\frac{\partial B}{\partial x} + \frac{E_0}{B},$$

where $E_0(t)$ is an arbitrary function representing a nonuniqueness in the form of the flux velocity.

There are several physically reasonable ways of choosing E_0, one of which is $E_0 = 0$, so that $\mathbf{w} = \mathbf{E} \times \mathbf{B}/B^2$ and $\mathbf{w}$ is then a flux velocity associated with the energy flow. In this case, the field lines are initially stationary (except at the origin) and later move towards the origin with a singular velocity at $x = 0$. The field is, therefore, evolving as if the field lines are moving towards the origin and disappearing (or "annihilating") there at a neutral sheet. As time increases, the flux velocity increases everywhere in magnitude towards its steady-state value.

3.3.2 Diffusion of a magnetic field with circular field lines

Consider next diffusion of a field $B(r,t)\hat{\boldsymbol{\theta}}$ where $B = -\partial A/\partial r$, for which the diffusive limit of the induction equation with uniform diffusivity in terms of the flux function ($A(r, t)$) becomes

$$\frac{\partial A}{\partial t} = \eta\left(\frac{\partial^2 A}{\partial r^2} + \frac{1}{r}\frac{\partial A}{\partial r}\right).$$

For diffusion of an isolated circular flux tube of flux F_0 at radius a with an initial field $B(r,0) = F_0\delta(r-a)$ and flux $A(r,0) = 0$ for $r<a$, and $A(r,0) = -F_0$ for $r > a$, the solution is, in terms of the Bessel function I_0,

$$A(r,t) = -\frac{F_0}{2\eta t}\int_a^\infty s e^{-(s^2+r^2/(4\eta t)}\mathrm{I}_0\left(\frac{rs}{2\eta t}\right)\mathrm{d}s,$$

for which the maximum field strength decreases in time, while the flux spreads outwards.

The resulting total flux is

$$A(0,t) - A(\infty,t) = F_0(1 - e^{-a^2/(4\eta t)}),$$

which decays away from an initial value of F_0 to zero with a time-scale of $a^2/(4\eta)$. The corresponding radial flux velocity is

$$w = \frac{1}{B}\left(E_0 - \eta\frac{\partial B}{\partial r}\right),$$

where $E_0(t)$ is an arbitrary function of time, which can again be chosen in a variety of ways. For example, if $E_0(t)$ is chosen to make w vanish at infinity, the field lines would be disappearing at the O-point. This surprising fact that field lines can disappear at O-points in 2D makes one wonder whether they can disappear in 3D.

3.3.3 Magnetic field diffusion in three dimensions

If a closed magnetic field line C exists enclosing a surface S, then the rate of change of magnetic flux through S is

$$\frac{d}{dt}\int_S \mathbf{B}\cdot\mathrm{d}\mathbf{S} = -\int_S \mathbf{V}\times\mathbf{E}\cdot\mathrm{d}\mathbf{S} = -\int_C \mathbf{E}\cdot\mathrm{d}\mathbf{l}.$$

If, further, a flux velocity ($\mathbf{w}$) exists, then there is a function Φ such that Eq. (13) holds, where $\mathbf{E} = \eta\mathbf{V}\times\mathbf{B}$, which implies, since $\mathbf{w}\times\mathbf{B}$ is perpendicular to $d\mathbf{l}$ on C, that

$$\int_C \mathbf{E}\cdot \mathrm{d}\mathbf{l} = \int_C \nabla\Phi \cdot \mathrm{d}\mathbf{l} = 0,$$

so that the flux through C does not change in time. Thus, if the flux through a closed field line does indeed change in time, Eq. (13) cannot hold and no flux velocity ($\mathbf{w}$) exists.

As an example, consider the diffusion of a linear force-free field satisfying $\nabla \times \mathbf{B} = \alpha_0 \mathbf{B}$, where α_0 is constant. The diffusive induction Eq. (20) reduces to

$$\frac{\partial \mathbf{B}}{\partial t} = -\eta \alpha_0^2 \mathbf{B} \qquad \text{with solution} \qquad \mathbf{B}(x,y,z,t) = \mathbf{B}_0(r,\theta,\phi) e^{-\eta\alpha_0^2 t},$$

where $\mathbf{B}_0(r,\theta,\phi)$ is the initial state. As a particular case, consider the lowest-order axisymmetric, linear-force-free field in a sphere of radius a, as sketched in Fig. 19, which has flux function $A = r^{1/2} \mathrm{J}_{3/2}(\alpha_0 r) \sin^2\theta$ with $\alpha_0 a \approx 4.49$ as the first zero of the Bessel function $\mathrm{J}_{3/2}$.

This field possesses a closed field line (C) in the equatorial plane ($\theta = \frac{1}{2}\pi$) at the location $\alpha_0 r = 2.46$ of the first maximum of $\partial A/\partial r$. Within C the poloidal flux decreases in time, and so no single flux velocity exists. However, a pair of flux velocities ($\mathbf{w}_p$ and $\mathbf{w}_t$) may be introduced as follows.

Denoting poloidal and toroidal components by subscripts p and t, $\mathbf{B}_p$ and $\mathbf{B}_t$ change in time according to

$$\frac{\partial \mathbf{B}_p}{\partial t} = -\nabla \times \mathbf{E}_t \qquad \text{and} \qquad \frac{\partial \mathbf{B}_t}{\partial t} = -\nabla \times \mathbf{E}_p.$$

Thus, two separate *dual flux velocities* velocities $\mathbf{w}_p$ and $\mathbf{w}_t$ may be defined by

$$\mathbf{E}_t + \mathbf{w}_p \times \mathbf{B}_p = \mathbf{0} \qquad \text{and} \qquad \mathbf{E}_p + \mathbf{w}_t \times \mathbf{B}_t = \mathbf{0},$$

which are perpendicular to $\mathbf{B}_p$ and $\mathbf{B}_t$, respectively. As it decays in time, the field in Fig. 19 behaves as if the poloidal field is shrinking at $\mathbf{w}_p$ towards the closed toroidal field line (C) and disappearing into the O-points of the poloidal field. At the same

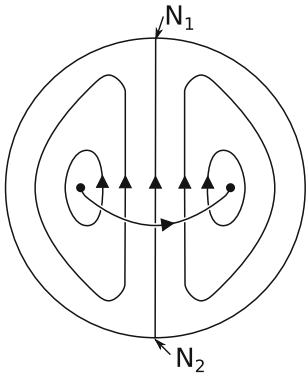

Fig. 19 A diffusing magnetic field inside a sphere whose poloidal field lines are shrinking towards the toroidal line, while the toroidal field is diffusing towards the separator

time the toroidal field can be regarded as shrinking and disappearing at the separator joining the null points N_1 and N_2.

4 The nature of reconnection in three dimensions

Before describing the different regimes for reconnection in 3D, we need to lay the groundwork by describing various fundamental concepts and the technique for classification. In addition, we enumerate the many ways in which reconnection in 3D is very different from reconnection in 2D.

Ohm's law may be written in a non-ideal plasma as

$$\mathbf{E} + \mathbf{v} \times \mathbf{B} = \mathbf{N}, \tag{21}$$

and it is the form of the nonideal term ($\mathbf{N}$) that determines whether there is simple diffusion of magnetic field lines or 2D reconnection or 3D reconnection. In 2D the notion of a *flux velocity* is helpful in describing what happens, but in 3D it fails, although it is possible to replace it by a *dual flux velocity* (Sect. 3.3.3, Sect. 4.4).

4.1 Form of the non-ideal term for reconnection: diffusion and reconnection

First, suppose that the nonideal term $\mathbf{N}$ in Eq. (21) can be written as

$$\mathbf{N} = \mathbf{u} \times \mathbf{B} + \nabla \Phi.$$

Then the curl of Eq. (21) implies

$$\frac{\partial \mathbf{B}}{\partial t} = \nabla \times (\mathbf{w} \times \mathbf{B}), \tag{22}$$

in terms of the flux velocity ($\mathbf{w} = \mathbf{v} - \mathbf{u}$) and slippage velocity ($\mathbf{u}$). In this case, the magnetic field may be said to move with the velocity $\mathbf{w}$. Thus we see that the nature of the evolution depends on the form of $\mathbf{N}$, as follows:

(a) if $\mathbf{N} = \mathbf{u} \times \mathbf{B} + \nabla \Phi$ and $\mathbf{u}$ is smooth, the magnetic field slips or diffuses through the plasma, but there is no reconnection;
(b) if $\mathbf{N} = \mathbf{u} \times \mathbf{B} + \nabla \Phi$ and $\mathbf{u}$ is singular at a point, then 2D reconnection takes place there;
(c) if $\mathbf{N} \neq \mathbf{u} \times \mathbf{B} + \nabla \Phi$, then reconnection occurs in 2.5D or 3D.

The relation between diffusion and reconnection is that reconnection implies diffusion (in an isolated region), but diffusion can take place without any reconnection.

4.2 Two-dimensional reconnection ($\mathbf{E} \cdot \mathbf{B} = 0$)

Suppose that $\mathbf{E}$ is perpendicular to $\mathbf{B}$. Then from Eq. (21) $\mathbf{N}$ is also perpendicular to $\mathbf{B}$, and we have a two-dimensional situation. For instance, if $\mathbf{v}$ and $\mathbf{B}$ lie in the xy-

plane and depend only on x and y, then $\mathbf{E}$ and $\mathbf{N}$ are in the z-direction. In this case we may write $\nabla\Phi \equiv \mathbf{0}$, so that the slippage velocity is

$$\mathbf{u} = \frac{(\mathbf{B} \times \mathbf{N})}{B^2}.$$

Also, Eq. (21) reduces to

$$\mathbf{E} + \mathbf{w} \times \mathbf{B} = \mathbf{0},$$

and so there exists a flux velocity $\mathbf{w}_\perp = \mathbf{E} \times \mathbf{B}/B^2$ that conserves the flux and is smooth except possibly where the magnetic field vanishes. Three possibilities arise:

(a) If $\mathbf{B} \neq \mathbf{0}$, then *flux-conserving* slippage of the magnetic field takes place, since $\mathbf{w}$ is smooth everywhere;
(b) If there is an O-type null point at which $\mathbf{E} \neq 0$, then $\mathbf{w}$ possesses a divergent singularity at the O-point, where magnetic flux is destroyed or generated;
(c) If there is an X-type null point at which $\mathbf{E} \neq 0$, then $\mathbf{w}$ possesses a hyperbolic singularity, where magnetic flux is reconnected and flux is weakly conserved with $\mathbf{w}$ regular except at the X-point.

4.3 Non-existence of a flux velocity in 3D

The notion of a flux velocity has been central to the theory of 2D reconnection, but it fails in 3D (when $\mathbf{E} \cdot \mathbf{B} \neq 0$), since, for an isolated 3D nonideal region, a flux-conserving velocity ($\mathbf{w}$) does not in general exist (Priest et al. 2003). The proof is straightforward. If a flux velocity does exist, then Eq. (22) holds and a function Φ exists such that

$$\mathbf{E} + \mathbf{w} \times \mathbf{B} = \nabla\Phi.$$

From this equation we may deduce that $\mathbf{E} \cdot \mathbf{B} = \nabla\Phi \cdot \mathbf{B}$, which may be integrated along a magnetic field line from one point ($\mathbf{r}_1$) to another ($\mathbf{r}_2$) on opposite sides of the diffusion region, to give

$$\int_{\mathbf{r}_1}^{\mathbf{r}_2} E_\parallel ds = \Phi(\mathbf{r}_2) - \Phi(\mathbf{r}_1).$$

We may next assume that $E_\parallel$ is, say, positive in the diffusion region, and so $\Phi(\mathbf{r}_2) > \Phi(\mathbf{r}_1)$. However, everywhere outside the isolated diffusion region, $\mathbf{w} = \mathbf{v}$ and $\nabla\Phi = \mathbf{0}$, so that Φ is uniform outside the diffusion region and therefore $\Phi(\mathbf{r}_2) = \Phi(\mathbf{r}_1)$. Thus, we have a contradiction, which leads to the conclusion that a flux velocity does not exist, as required.

4.4 Fundamental differences between 2D and 3D reconnection

Magnetic reconnection in 3D is profoundly different from 2D with many new features. Among the aspects of reconnection in 2D that do not survive in 3D are the following:

(2D:i) Reconnection occurs only at neutral points of X-type; these nulls may be pre-existing in the field and undergo local collapse to form a current sheet, or a one-dimensional current sheet may form, within which a 2D null is created when reconnection is initiated;

(2D:ii) A flux velocity ($\mathbf{w}$) exists and describes the speed at which magnetic flux moves, slipping relative to the plasma at a velocity $\mathbf{w} - \mathbf{v}$, but preserving the magnetic field line connections between points on the boundary; the exception is at an X-point, where $\mathbf{w}$ becomes singular and the connections change as the field lines break;

(2D:iii) Before two flux tubes reconnect, they approach the diffusion region with velocity $\mathbf{w} = \mathbf{v}$, and then they break and re-connect perfectly to create two new flux tubes, such that, once they have left the diffusion region, they move out at $\mathbf{w} = \mathbf{v}$ (Fig. 20a);

(2D:iv) When a magnetic flux tube has part of its length inside a diffusion region and part outside, the central section slips through the plasma with $\mathbf{w} \neq \mathbf{v}$, while the two wings of the flux tube are frozen to the plasma and move with $\mathbf{w} = \mathbf{v}$ (Figs. 20b).

In contrast, 3D reconnection has the following properties:

(3D:i) Magnetic reconnection may occur wherever sufficiently intense electric current concentrations form, for example at a null point, a separator or a quasi-separator (i.e., a hyperbolic flux tube) (Sects. 2.6, 5);

(3D:ii) In general a single flux tube velocity ($\mathbf{w}$) does not exist (Sect. 4.3), but it can be replaced by a pair ($\mathbf{w}_{\rm in}, \mathbf{w}_{\rm out}$) of flux velocities (called a *dual flux velocity*), which describe behaviour from two points of view, namely, a field line that enters a diffusion region or one that leaves it (Sect. 4.7.2);

(3D:iii) In the absence of a null point or bald patch, the field-line mapping from one section of a boundary to another is continuous;

(3D:iv) Magnetic field lines continually change their connections as part of them pass through a diffusion region; another way to view this is the following;

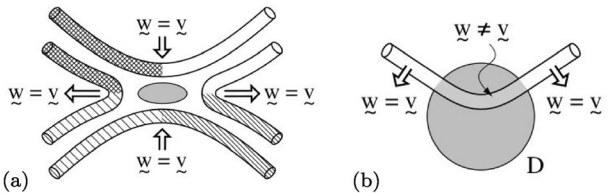

Fig. 20 The nature of 2D reconnection. **a** Two flux tubes come in, break in the diffusion region (shaded) and re-connect perfectly. **b** While in the diffusion region, a flux tube slips through the plasma but preserves its connections, except at the X-point. For a related movie see Supplementary Information. Image reproduced with permission from Priest et al. (2003), copyright by AGU

(3D:v) In the process of reconnecting, two flux tubes split into four parts, each of which flips in a different manner (Fig. 21b); field lines that are projected through to the other side of a diffusion region flip, i.e., they move with a virtual velocity that differs from the plasma velocity (Sect. 4.3);

(3D:vi) In general magnetic field lines do not break and reform pairwise, and neither do pairs of flux tubes (Figs. 21).

An illustrative example of this behaviour is presented in Sect. 4.7.2.

4.5 Classification and nature of 3D reconnection: general reconnection or singular reconnection

To reiterate the above, in 2D the basic features of magnetic reconnection are:

(i) Two pairs of field lines approach an X-point, and are then broken and rejoined;

(ii) There is an electric field ($\mathbf{E}$) perpendicular to the 2D plane;

(iii) During reconnection, the magnetic connectivity of plasma elements is changed at the X-point surrounded by a localised non-ideal diffusion region.

In 3D, since reconnection can occur without null points or separatrices (contrary to (i)), Schindler et al. (1988) proposed a concept of *"General Magnetic Reconnection"* that is based on (iii) above and includes any process of local nonidealness that gives rise to an electric field component ($E_{\parallel}$) parallel to the magnetic field. Thus, the generalisation of (ii) above is that the integral

$$\int E_{\parallel}\, ds \neq 0, \tag{23}$$

where the integral is performed along a magnetic field line. The maximum value of this integral over all field lines that thread the non-ideal region represents the rate of reconnection. Equivalently, 3D reconnection occurs if and only if the magnetic helicity (Sect. 4.6) changes in time. As shown by Schindler et al. (1988) and Hesse and Schindler (1988) when the condition (23) is met, plasma elements experience a change in magnetic field line connectivity.

With 3D reconnection requiring that the condition (23) be met, it is the formation of a localised current concentration that is the precondition for such reconnection. The reason why reconnection occurs at nulls, separators, quasi-separators (or hyperbolic flux tubes) and braids is that they are the natural locations where strong currents focus (see Sect. 5). It should be noted, however, that the nulls, separators and quasi-separators themselves are not the (only) locations for reconnection, since it occurs throughout the finite diffusion regions that surround them.

The theory of general reconnection has been exemplified, developed and applied in several directions. An analytical example of general magnetic reconnection has been presented by Schindler et al. (1988) that demonstrates how a plasmoid can be

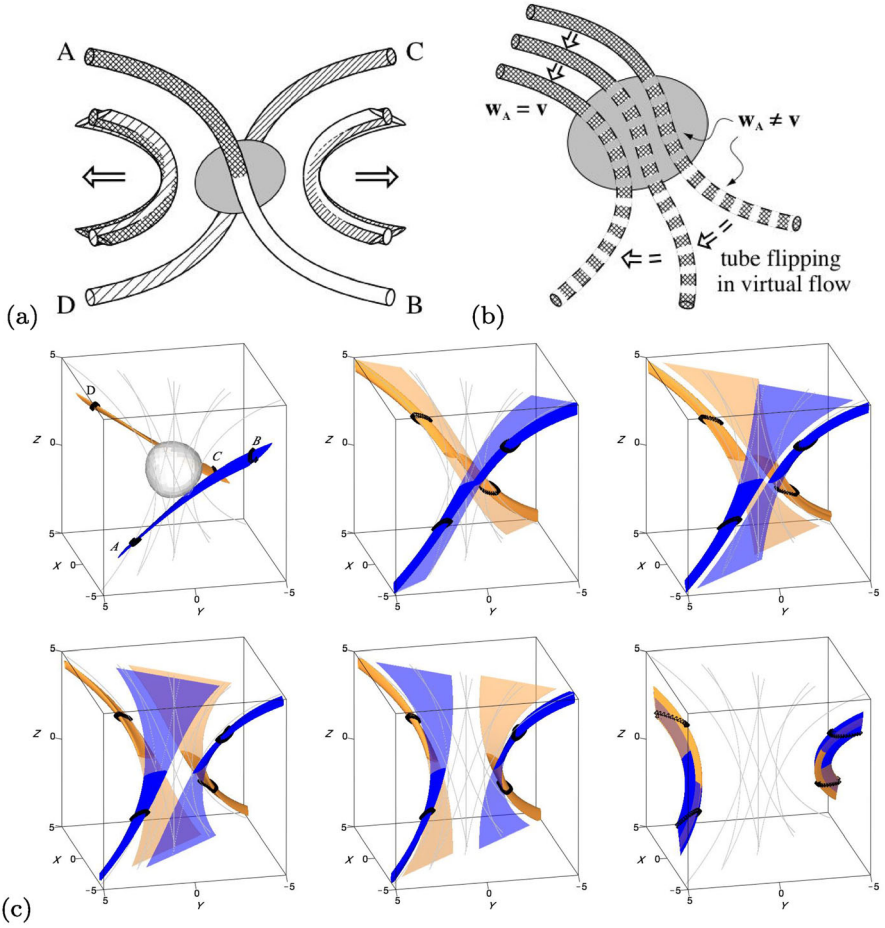

Fig. 21 The nature of reconnection in 3D: **a** two magnetic flux tubes approach one another, break and partly rejoin, but **b** the projection of a flux tube beyond a diffusion region flips through the plasma in a virtual flow. Image reproduced with permission from Priest et al. (2003), copyright by AGU. **c** Illustration of the principles in (**a**) and (**b**), wherein the evolution of two representative flux tubes from the solution of Hornig and Priest (2003) (see Sect. 4.7.2) are traced from ideal comoving footpoints (marked black); the dark sections of the tubes move at the local plasma velocity (outside D), while the light sections correspond to field lines that pass through the diffusion region. A localised diffusion region (shaded surface in the first frame) is present around the origin. From Pontin (2011). For a related movie see Supplementary Information

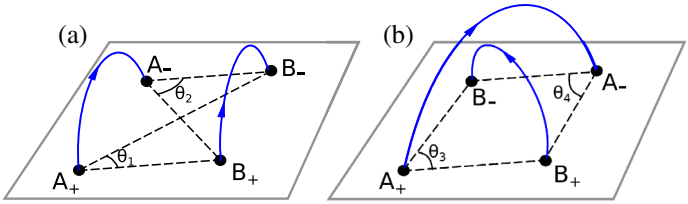

Fig. 22 Nearby flux tubes have a mutual helicity of **a** $(\theta_1 - \theta_2)F_A F_B/\pi$, whereas crossing flux tubes have **b** $(\theta_3 + \theta_4)F_A F_B/\pi$ (after Berger 1999)

formed in 3D in the absence of a null point or separatrix. Furthermore, a mathematical formalism for General Magnetic Reconnection has been developed by Hesse and Schindler (1988), in which they express the magnetic field in terms of Euler potentials (α, β) and find equations for the time-behaviour of α and β.

Sub-classes of general magnetic reconnection may be defined in different ways, for example as driven and spontaneous reconnection, depending on whether motions of flux at large distances or local effects (such as enhanced resistivity or instability) dominate. Another way of categorising reconnection is in terms of the form of the nonideal term in Ohm's law, which distinguishes slippage from 2D reconnection and 3D reconnection (See Sect. 4.1). While 2D reconnection occurs only at X-points, the properties of generic 3D reconnection (with a localised diffusion region within which $\mathbf{E} \cdot \mathbf{B} \neq 0$) depend on whether a null-point is present (3D null reconnection) or not (3D non-null reconnection)—as discussed in more detail in Sects. 10-12.

General Reconnection includes examples of diffusion and slippage (such as in double layers or shock waves) that are not usually included in the concept of reconnection, and so it may be regarded as too general a concept. An alternative is therefore to restrict the definition of reconnection to *Singular field-line Reconnection*, in which the presence of $E_{\|}$ along a field line is supplemented by the condition that the nearby field has a certain topology in a plane perpendicular to the field line (Priest and Forbes 1989; Hornig and Rastätter 1998). If the transverse topology is X-type, then we would refer to it as *X-type Singular Reconnection*, which is close in spirit to traditional 2D reconnection and includes most cases of separator and quasi-separator (or hyperbolic flux tube) reconnection. If the transverse topology is O-type, then we would refer to it as *O-type Singular Reconnection*, which includes *Flux Tube Disconnection* (Wilmot-Smith and Priest 2007) and some examples of separator reconnection discovered in numerical experiments (Parnell et al. 2010). For further details, see Priest and Forbes (2000).

4.6 Magnetic helicity and its changes during 3D reconnection

Magnetic helicity measures the twisting and kinking of a flux tube (called *self-helicity*), together with the linkage between different flux tubes (called *mutual helicity*). In an ideal medium, as a global topological invariant it does not change, whereas, in a resistive medium, it decays very slowly over the global magnetic diffusion time (τ_d). During reconnection, magnetic helicity is approximately conserved, although it can be converted from one form to another: for example, mutual may be converted to self during the initial stages of a coronal mass ejection or eruptive solar flare, which may explain much of the twist that is observed (e.g., Priest and Longcope 2017). However, during 3D reconnection the tiny change in magnetic helicity that does take place is intimately related to its very occurrence, as demonstrated below.

Magnetic helicity is thought to be critical in the Sun's cycle: continual photospheric motions energise the coronal magnetic field and increase the (modulus of the) helicity; and the coronal magnetic field evolves through states that are nearly

force-free, building up magnetic helicity until it is ejected by coronal mass ejections (Heyvaerts and Priest 1984; Rust and Kumar 1994; Low 2001). An important step in this understanding was the development of a theory for relative helicity by Berger and Field (1984). Here we give definitions of magnetic helicity (Sect. 4.6.1, 4.6.2) and discuss its evolution (Sect. 4.6.3, 4.6.4).

4.6.1 Definition of magnetic helicity

For a closed volume (V) that is bounded by a surface S, with normal vector $\mathbf{n}$, the *magnetic helicity* is defined as

$$H_0 = \int_V \mathbf{A} \cdot \mathbf{B}\, dV, \tag{24}$$

where the magnetic field may be written $\mathbf{B} = \nabla \times \mathbf{A}$ in terms of the vector potential ($\mathbf{A}$). Note that an arbitrary gauge $\nabla \Phi_A$ may be added to $\mathbf{A}$ without changing $\mathbf{B}$, but it can be shown that the magnetic helicity is independent of this gauge, i.e., it is gauge invariant, provided that all magnetic field lines close within the volume (i.e., $\mathbf{B} \cdot \mathbf{n} = 0$ on S).

However, if the boundary is open in the sense that magnetic fields enter or leave it, Berger and Field (1984) made an important breakthrough in realising that a *relative magnetic helicity*, defined as

$$H = \int_{V_\infty} \mathbf{A} \cdot \mathbf{B} - \mathbf{A}_0 \cdot \mathbf{B}_0\, dV, \tag{25}$$

is also gauge invariant, where $\mathbf{B}_0 = \nabla \times \mathbf{A}_0$ is a reference field with respect to which H_0 is being measured, and V_∞ is the whole of space, including the volume both inside and outside V. $\mathbf{B}_0$ is usually taken to be potential inside V, to be identical with $\mathbf{B}$ outside V and to have $\mathbf{A} \times \mathbf{n} = \mathbf{A}_0 \times \mathbf{n}$ on S.

4.6.2 Magnetic helicity of flux tubes

The magnetic helicity of a collection of flux tubes of magnetic flux F_i and twist Φ_{T_i} may be written as a sum

$$H = \sum_{i=1}^{N} H_{si} + \sum_{\substack{i,j=1 \\ i<j}}^{N} H_{mij},$$

of *self-helicities*

$$H_{si} = \frac{\Phi_{T_i} F_i^2}{2\pi},$$

for each flux tube due to their own internal twist, and *mutual helicities*

$$H_{mij} = 2L_{ij}\, F_i F_j, \tag{26}$$

due to the linking of one tube with another, where L_{ij} is the *linking number* (Berger 1984).

For example, consider two coronal flux tubes having fluxes F_A and F_B, with positive polarity footpoints A_+, B_+ and negative footpoints A_-, B_- (Fig. 22). The mutual helicity may be written in terms of angles $\angle B_+A_-B_-$ at footpoint A_+ and $\angle B_+A_+B_-$ at footpoint A_+ as

$$H = (-\angle B_+A_-B_- + \angle B_+A_+B_-)\frac{F_A F_B}{2\pi}.$$

The structures in Fig. 22 then have helicities $(\theta_1 - \theta_2)F_A F_B/\pi$ and $(\theta_3 + \theta_4)F_A F_B/\pi$ in terms of the angles shown.

4.6.3 Rate of change of magnetic helicity

If the gauge of the vector potential is chosen such that $\nabla \cdot \mathbf{A}_p = 0$ and $\mathbf{A}_p \cdot \mathbf{n} = 0$ on the boundary S, the rate at which magnetic helicity changes may be written

$$\frac{dH}{dt} = -2\int_V \mathbf{E}\cdot\mathbf{B}\, dV + 2\int_S \mathbf{A}_p \times \mathbf{E}\cdot\mathbf{n}\, dS. \tag{27}$$

Furthermore, when there is no diffusion on S and $\mathbf{E}$ is given by Ohm's Law ($\mathbf{E} = -\mathbf{v}\times\mathbf{B} + \mathbf{j}/\sigma$), this reduces to

$$\frac{dH}{dt} = -2\int_V \mathbf{j}\cdot\mathbf{B}/\sigma\, dV + 2\int_S (\mathbf{B}\cdot\mathbf{A}_p)(\mathbf{v}\cdot\hat{\mathbf{n}}) - (\mathbf{v}\cdot\mathbf{A}_p)(\mathbf{B}\cdot\hat{\mathbf{n}})\, dS, \tag{28}$$

where $\hat{\mathbf{n}}$ is the outwards normal to the volume.

The first term on the right of Eq. (28) represents resistive dissipation of magnetic helicity on a time-scale equal to the global diffusion time ($\tau_d = L^2/\eta$), where L is the global length-scale over which the magnetic field varies. Thus, on times much smaller than this, if the boundary is closed so that the normal components of $\mathbf{B}$ and $\mathbf{v}$ vanish, the magnetic helicity is conserved. Furthermore, the second term represents the rate at which magnetic helicity is carried across the boundary by plasma motions normal to the boundary, whereas the third term shows that the magnetic helicity may be injected into the volume or extracted from it by lateral motions.

4.6.4 Magnetic helicity changes during 3D reconnection

Since reconnection involves magnetic diffusion only in a diffusion region (D_R), which is a small part of the volume, the total magnetic helicity is approximately conserved during reconnection. However, the very occurrence of three-dimensional reconnection is directly related to the small change in magnetic helicity that takes place. Consider Eq. (27). Since the electric field is perpendicular to the magnetic field ($\mathbf{E}\cdot\mathbf{B} = 0$) everywhere except in the diffusion region D_R, the first term on the

right reduces to an integral over D_R alone. If also the electric field vanishes ($\mathbf{E} = 0$) on the surface S, the second term vanishes, and so the equation becomes

$$\frac{dH}{dt} = -2\int_{D_R} \mathbf{E}\cdot\mathbf{B}\, dV = -2\int_{D_R} E_\parallel B\, dV. \tag{29}$$

Recall that, by definition, 3D reconnection takes place when the parallel electric field is non-zero ($E_\parallel \neq 0$) in D_R, and so from Eq. (29) the occurrence of such reconnection is equivalent to there being a change of magnetic helicity H with time. Furthermore, if V_R is the diffusion region volume and δH is the change of magnetic helicity in a time δt, the parallel electric field is

$$E_\parallel \simeq \frac{1}{2V_R B_0}\frac{\delta H}{\delta t}.$$

The helicity is then approximately conserved even in an evolution involving 3D reconnection because at high R_m the current layers are very thin, so that V_R is very small compared to the domain volume.

Although the total helicity in a volume is approximately conserved during reconnection, it may be redistributed within a configuration. When the field is modelled as being composed of discrete flux tubes this can be interpreted as a change from mutual helicity to self helicity or vice versa. Alternatively, for continuous fields the notion of a *field line helicity* (Antiochos 1987; Berger 1988) can be useful in interpreting how the linkage of flux is changed during reconnection. The field line helicity is defined as

$$\mathcal{A} = \int_{F(\mathbf{x})} \mathbf{A}\cdot d\mathbf{l}, \tag{30}$$

where $d\mathbf{l}$ is tangent to the field line $F(\mathbf{x})$. For a suitable choice of gauge, it measures the net linkage of all field lines in the domain with the field line of interest, while a flux-weighted integral of $\mathcal{A}$ over all field lines yields the helicity of the volume, justifying the name (Berger 1988; Russell et al. 2015). Moreover, its distribution uniquely describes the magnetic topology of the field (Yeates and Hornig 2013). It has been used, for example, to characterise the structure and evolution of active regions (Moraitis et al. 2019, 2021). Russell et al. (2015) investigated the way in which the distribution of field line helicity can be changed by reconnection within the volume, although this remains to be fully explored.

4.7 Techniques for modelling 3D reconnection

In three dimensions, reconnection may take place in a variety of different regimes and a variety of different geometries, namely, at a null point (Sect. 10), at a separator (Sect. 11) or at non-null regions such as a quasi-separator (Sect. 12) or a braided field (Sect. 14.1). Which of these regimes occurs depends both on the geometry (i.e., whether the magnetic configuration contains a null point, a separator, a quasi-separator or a braid) and on the nature of the plasma flow. The properties of these different regimes are being discovered by a combination of several

complementary techniques that we describe here, namely, kinematic models that are either ideal (Sect. 4.7.1) or resistive (Sect. 4.7.2) and numerical computations (Sect. 4.7.3).

4.7.1 Kinematic ideal models

The full MHD equations for determining the plasma velocity (**v**) and magnetic field (**B**) include the induction equation and the equation of motion, but in a kinematic approach one neglects the equation of motion and considers the implications of just the induction equation by either imposing **v** and determining **B** or imposing **B** and solving for **v**. Lau and Finn (1990) and Priest and Titov (1996) began by exploring the nature of the flow in the ideal region around a diffusion region during steady 3D reconnection. They prescribed the form of the magnetic field (**B**) and solved the kinematic equations for the plasma velocity (**v**) and electric field (**E**), namely,

$$\mathbf{E} + \mathbf{v} \times \mathbf{B} = \mathbf{0} \quad \text{(a)} \quad \text{and} \quad \nabla \times \mathbf{E} = \mathbf{0}. \quad \text{(b)} \tag{31}$$

First of all, Eq. (31b) implies that $\mathbf{E} = \nabla \Phi$ and so the component of Eq. (31a) perpendicular to **B** yields

$$\mathbf{B} \cdot \nabla \Phi = 0, \tag{32}$$

which implies that Φ is constant along magnetic field lines. If the values of Φ are imposed on a surface (S) surrounding the ideal region, then Eq. (32) may be integrated along field lines (characteristics) to determine the value of Φ (and therefore **E**) throughout the volume. A variety of different boundary conditions may be imposed on the surface S, and so give rise to different solutions. Next, the component of Eq. (31a) perpendicular to **B** determines the plasma velocity normal to **B** everywhere as

$$\mathbf{v}_\perp = \frac{\nabla \Phi \times \mathbf{B}}{B^2}. \tag{33}$$

This approach was used to show that current is likely to become focused along either the spine or the fan of a null point or along a separator and so to lead to different null-point reconnection regimes, as described in Sects. 10.1.1, 11.

4.7.2 Kinematic resistive modelling

However, the next step is to model what goes on inside a diffusion region. Hornig and Priest (2003) developed a formalism for modelling kinematically an isolated 3D diffusion region in which flux freezing breaks down, and they applied their formalism to a case without null points, although it was later applied to null points (Sect. 10.1.2) and separators. They solved

$$\mathbf{E} + \mathbf{v} \times \mathbf{B} = \eta \mathbf{j}, \tag{34}$$

where $\nabla \times \mathbf{E} = \mathbf{0}$, $\mathbf{j} = \nabla \times \mathbf{B}/\mu$ and $\nabla \cdot \mathbf{B} = 0$. Their idea was to impose a sufficiently simple magnetic field that both the mapping and the inverse mapping of the

magnetic field can be found analytically. Then, after writing $\mathbf{E} = \nabla\Phi$, the integral of the component of Eq. (34) parallel to $\mathbf{B}$ determines Φ everywhere as

$$\Phi = \int \frac{\eta\ \mathbf{j}\cdot\mathbf{B}}{B}\ ds + \Phi_e = \int \eta\ \mathbf{j}\cdot\mathbf{B}\ ds^* + \Phi_e, \tag{35}$$

where Φ_e is the imposed value of Φ at one end of the field lines, s is the distance along field lines, and s^* is a stretched distance such that $ds^* = ds/B$. Then the flow normal to the field lines is determined by the component of Eq. (34) perpendicular to $\mathbf{B}$ as

$$\mathbf{v}_\perp = \frac{(\nabla\Phi - \eta\ \mathbf{j})\times\mathbf{B}}{B^2}. \tag{36}$$

Here we illustrate this approach by describing the solution of Hornig and Priest (2003), who considered the simple QSL field

$$\mathbf{B} = \frac{B_0}{L}\left(y\ \hat{\mathbf{x}} + k^2 x\ \hat{\mathbf{y}} + \hat{\mathbf{z}}\right), \tag{37}$$

namely, a 2D X-point field in the xy-plane with a uniform field in the z-direction, and a uniform current $\mathbf{j} = (k^2-1)B_0/L\ \hat{\mathbf{z}}$. The equations ($\mathbf{X}(\mathbf{x}_0, s^*)$) of field lines whose initial point is $\mathbf{x}_0$ follow from integrating $d\mathbf{X}/ds^* = \mathbf{B}$ as

$$\begin{aligned} X &= x_0\cosh(B_0 k s^*/L) + (y_0/k)\sinh(B_0 k s^*/L),\\ Y &= y_0\cosh(B_0 k s^*/L) + x_0 k\sinh(B_0 k s^*/L),\\ Z &= z_0 + B_0 s^*, \end{aligned} \tag{38}$$

while the inverse mapping is given by

$$\begin{aligned} X_0 &= x\cosh(B_0 k s^*/L) - (y/k)\sinh(B_0 k s^*/L),\\ Y_0 &= y\cosh(B_0 k s^*/L) - xk\sinh(B_0 k s^*/L),\\ Z_0 &= z - B_0 s^*. \end{aligned} \tag{39}$$

In order to obtain a localised non-ideal term ($\eta\mathbf{j}$), since $\mathbf{j}$ is constant, it is necessary to localise the resistivity, and in order to obtain an analytical solution for Φ, they chose the following form

$$\eta(x_0, y_0, s^*) = \eta_0 \exp\left(-\frac{B_0^2 s^{*2} + x_0^2 + y_0^2}{l^2}\right), \tag{40}$$

where $z_0 = 0$, so that x_0, y_0 are coordinates of field lines in the plane $z = 0$. Thus, η is positive with a maximum value of η_0 at the origin, and it decreases exponentially with distance from the origin. The diffusion region D has the shape of a sphere distorted towards a tetrahedron (Fig. 23a).

Then Eq. (35) may be integrated to give

$$\Phi(x_0, y_0, s^*) = \frac{\sqrt{\pi} B_0\ \eta_0\ l\ (k^2 - 1)\ \mathrm{erf}(B_0 s^*/l)}{2L \exp((x_0^2 + y_0^2)/l^2)} + \Phi_e(x_0, y_0), \tag{41}$$

where (x_0, y_0, s^*) is given in terms of (x, y, z) by Eq. (39) and $\mathbf{v}_\perp$ follows from Eq. (36). Furthermore, a component of velocity parallel to $\mathbf{B}$ can be added to make $v_z = 0$, say. The freedom of being able to choose $\Phi_e(x_0, y_0)$ is linked with the following splitting of Ohm's law into non-ideal and ideal parts:

$$\nabla\Phi_{\mathrm{nid}} + \mathbf{v}_{\mathrm{nid}} \times \mathbf{B} = \eta\mathbf{j}, \tag{42}$$

$$\nabla\Phi_{\mathrm{id}} + \mathbf{v}_{\mathrm{id}} \times \mathbf{B} = \mathbf{0}. \tag{43}$$

Depending on the choice of $\Phi_e(x_0, y_0)$, we can consider *pure solutions* or *composite solutions*.

For a *pure solution*, set $\Phi_e(x_0, y_0) \equiv 0$, so that $\mathbf{v}$ vanishes when $z = 0$. In this case, counter-rotating flows are produced in the ideal regions above and below the plane $z = 0$ (Fig. 23b). Such flows are confined to a region, a hyperbolic flux tube (HFT) (Sect. 2.6.2), that contains only the field lines that thread the diffusion region D, as indicated in Fig. 23a. The flows are circular close to $z = 0$, but become highly elongated at large distances from D. They are associated with flipping and with the small change in magnetic helicity essential to 3D reconnection (Sect. 4.6.3).

The rate of reconnection of flux is calculated by evaluating the integral

$$\frac{d\Phi_{\mathrm{mag}}}{dt} = \int E_\parallel ds \tag{44}$$

along a field line through the diffusion region (Schindler et al. 1991; Hesse et al. 2005). For this example this turns out to be $2\Phi(0, 0, \infty)$, which has quite a different interpretation from the normal 2D picture, where flux is cut and reconnected at one

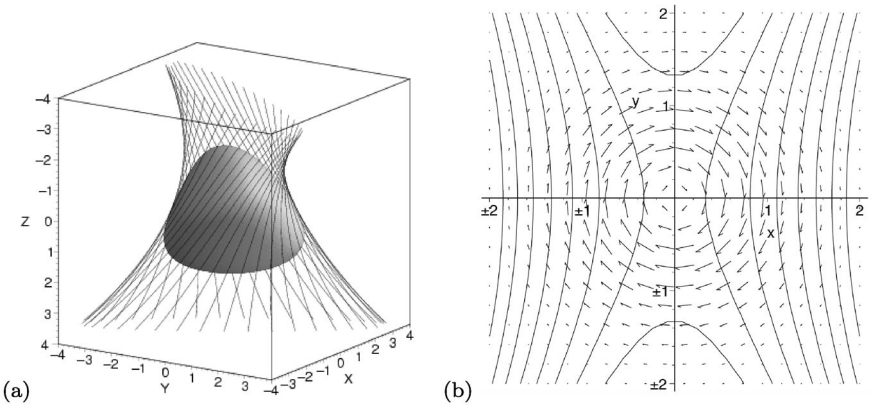

Fig. 23 **a** The diffusion region D (shaded) at 2% of the maximum diffusivity, and the hyperbolic flux tube that encloses it when $k = 2$, $L = 10$, $l = 1$. **b** In the $z = 0$-plane, the field lines and the difference $(\mathbf{w}^{\mathrm{in}} - \mathbf{w}^{\mathrm{out}})$ between the flux velocities of field lines anchored above and below D. Image reproduced with permission from Hornig and Priest (2003), copyright by AIP

location in the diffusion region (D), namely, an X-point, and there is a unique flux velocity. Instead, in 3D, every field line in the HFT continually changes its connection in D, and two flux-conserving velocities ($\mathbf{w}^{\rm in}$ and $\mathbf{w}^{\rm out}$) are needed, one of which describes the motion of field lines attached to plasma elements above D, while the other represents the velocity of field lines attached to plasma below it (Sect. 4.4). Thus, for a given $\mathbf{B}$, $\mathbf{w}^{\rm in}$ satisfies

$$\mathbf{E}^{\rm in} + \mathbf{w}^{\rm in} \times \mathbf{B} = \mathbf{0}, \quad \text{where} \quad \mathbf{E}^{\rm in} = \nabla \Phi^{\rm in}, \quad \text{so that} \quad \mathbf{w}^{\rm in}_{\perp} = \frac{\nabla \Phi^{\rm in} \times \mathbf{B}}{B^2},$$

while $\mathbf{w}^{\rm out}$ satisfies

$$\mathbf{E}^{\rm out} + \mathbf{w}^{\rm out} \times \mathbf{B} = \mathbf{0}, \quad \text{where} \quad \mathbf{E}^{\rm out} = \nabla \Phi^{\rm out}, \quad \text{so that} \quad \mathbf{w}^{\rm out}_{\perp} = \frac{\nabla \Phi^{\rm out} \times \mathbf{B}}{B^2}.$$

Outside D, $\mathbf{w}^{\rm in}$ is just the same as $\mathbf{v}$ on one side of D, while $\mathbf{w}^{\rm out}$ is the same on the other side, so for $\Phi^{\rm in}$ we can just choose the asymptotic value of Φ from Eq. (41) on one side, say, $\Phi(x_0, y_0, -\infty)$, and for $\Phi^{\rm out}$ we choose the asymptotic value on the other side, namely, $\Phi(x_0, y_0, \infty)$ or

$$\Phi^{\rm in} = -\frac{\sqrt{\pi} B_0 \eta_0 l (k^2 - 1)}{2L \exp((x_0^2 + y_0^2)/l^2)}, \qquad \Phi^{\rm out} = \frac{\sqrt{\pi} B_0 \eta_0 l (k^2 - 1)}{2L \exp((x_0^2 + y_0^2)/l^2)}.$$

The rate of mismatching of flux in, say, the $z = 0$ plane is then the difference between $\mathbf{w}^{\rm in}$ and $\mathbf{w}^{\rm out}$ there, namely,

$$\Delta \mathbf{w}_{\perp} = \mathbf{w}^{\rm out}_{\perp} - \mathbf{w}^{\rm in}_{\perp} = \frac{(\nabla \Phi^{\rm out} - \nabla \Phi^{\rm in}) \times \mathbf{B}}{B^2} = 2 \frac{\nabla \Phi^{\rm out} \times \mathbf{B}}{B^2}.$$

The corresponding vector field is shown in Fig. 23b. The resulting rate at which magnetic flux crosses a radial line between the origin and the boundary of D is just the potential difference across the line, namely,

$$\Delta \Phi_{\Delta w} = 2 \Phi^{\rm out} = 2 \Phi(0, 0, \infty),$$

which is identical to the reconnection rate and so provides us with a physical interpretation.

For a *composite solution*, any ideal flow may be added to the pure flow, and particularly useful is a stagnation flow,

$$\Phi_{\rm id} = -\Phi_0 \frac{x_0 \; y_0}{l^2},$$

since it carries magnetic flux into the diffusion region (D), lets it reconnect, and then removes it from D. The field line behaviour is then governed by a combination of the external stagnation flow and the inherent counter-rotational flow associated with the "pure" reconnection solution. As described by Hornig and Priest (2003), different field line behaviours are possible in different regimes. Field lines transported into the non-ideal region tend to split in two (when followed from two plasma

elements above and below the diffusion region), before exiting the diffusion region connected to different partners, as illustrated in Figure 21(b,c).

These solutions may be regarded as either kinematic (i.e., satisfying just the induction equation) or as fully dynamic in the limit of uniform density and slow flow (since they also satisfy the equations $\nabla \cdot \mathbf{v} = 0$ and $\nabla p = \mathbf{j} \times \mathbf{B}$). This resistive kinematic approach has also been used to discover different reconnection regimes near null points, as described in Sect. 10.1.2.

4.7.3 Computational modelling

Although the analytical approach of kinematic modelling has been invaluable in pointing the way and suggesting what kinds of 3D reconnection are likely, computational experiments have been crucial in going beyond the limitations of the kinematic approach by solving the full set of MHD equations and revealing many new features. These experiments build on previous examples of 2D and 2.5D modelling.

The phrase "2D reconnection" refers to a strictly two-dimensional field $[B_x(x,y), B_y(x,y)]$ that varies in two dimensions, whereas 2.5D has a field of the form $[B_x(x,y), B_y(x,y), B_z(x,y)]$ with a guide field $[B_z(x,y)]$, and "3D reconnection" refers to a fully 3D field $[B_x(x,y,z), B_y(x,y,z), B_z(x,y,z)]$. Thus, a 2D field should not be confused with a 2.5D field, which is topologically unstable in the sense that a small general 3D perturbation will destroy its topological structure. Many useful theories and simulations in 2D and 2.5D have helped clarify our understanding of reconnection, but most examples in nature are three-dimensional, and so the 2D and 2.5D understanding is likely to be only partial. For example, when a 2.5D simulation models so-called "anti-parallel" reconnection, it is likely to represent in reality a local snapshot of what in 3D would be null-point reconnection, whereas so-called "component" reconnection should more properly be referred to as a local snapshot of separator or quasi-separator reconnection. Numerical experiments have shown that the current $\mathbf{j}$ naturally builds up at null points, separators, quasi-separators and in braids—see Sect. 5—and so naturally leads to reconnection at these locations. What's more, dedicated simulations at each of these structures has helped to reveal the rich behaviour of these different 3D reconnection regimes. These simulations and reconnection regimes—as well as applications to understanding observations from the Sun and beyond—are discussed in detail in Sects. 10–15.

5 Formation of current sheets

Magnetic reconnection may occur in 3D fields wherever sufficiently intense current concentrations form (property (3D:i) in Sect. 4.4). Thus, to understand where reconnection takes place we must first determine where and how currents accumulate. Typically, the current accumulates in narrow layers called *current sheets*, across which there is a change in the tangential component of the magnetic field. In this section, we treat such sheets as discontinuities. In practice, however,

they are resolved by diffusion processes and so possess a small finite width, which is modelled in the sections that follow on magnetic annihilation and reconnection. It should also be noted that in this section we focus on slow formation of current sheets through quasi-static states, but they may also form by a dynamic local "collapse" process as described by Forbes et al. (1982) (Sect. 6.3).

When a perturbed magnetic configuration evolves towards an equilibrium with partial or no reconnection (due to time constraints or microscopic limitations), the new equilibrium will often contain current sheets. Such sheets may later dissipate as reconnection transfers magnetic flux from one topological region to another (Sect. 7) or they may go unstable to tearing mode instability (Sect. 8). Here we suppose for simplicity that no reconnection takes place and describe techniques to model current sheet appearance. First of all, we focus on 2D current sheets, where an elegant and powerful technique was discovered by Green (1965), in which the sheets are treated as cuts in a complex plane when the surrounding field is potential. Then we discuss what happens in 2.5D and 3D configurations.

5.1 Current sheets in 2D potential fields

Here we describe static current sheets in 2D potential fields. The results can be applied to quasi-static formation or the evolution of such sheets through a series of equilibria. They can also be modified to allow for reconnection of a given amount of flux.

In 2D, a current-free (i.e., potential) magnetic field obeys

$$\frac{\partial B_y}{\partial x} - \frac{\partial B_x}{\partial y} = 0 \qquad \text{and} \qquad \frac{\partial B_x}{\partial x} + \frac{\partial B_y}{\partial y} = 0, \tag{45}$$

which are satisfied by the following combination of its components $(B_x(x, y), B_y(x, y))$

$$B_y + iB_x = f(z),$$

where $z = x + iy$ is the complex variable and $f(z)$ is any analytic function of z. Thus, for example, a linear X-point field $B_x = y, B_y = x$ (Fig. 24a) may be written as

$$B_y + iB_x = x + iy \equiv z. \tag{46}$$

Then the question arises: if a motion of the sources of the magnetic field leads to the formation of a series of equilibria with a current sheet growing from the X-point and containing Y-points at its ends ($z = \pm iL$), as in Fig. 24b, what is the best way to describe the equilibria? Green (1965) came up with an elegant answer, namely, to write the field as

$$B_y + iB_x = (z^2 + L^2)^{1/2}, \tag{47}$$

with a cut in the complex plane from one end of the current sheet to the other. This behaves like z at large distances, and the separatrix field lines through the Y-points are inclined at an angle $2\pi/3$.

A more general solution with singularities at the ends of the sheet when $a \neq L$ was discovered by Somov and Syrovatsky (1976), namely,

$$B_y + iB_x = \frac{z^2 + a^2}{(z^2 + L^2)^{1/2}}, \tag{48}$$

where $a^2 < L^2$ (Fig. 24c), and was later generalised further by Bungey and Priest (1995).

Other extensions have generalised the above 2D models in a variety of ways. Some of these are summarised briefly in the following, and in much more detail by, e.g., Priest and Forbes (2000). First, a two-dipole field geometry external to the sheet has been considered as a model for two bipolar regions on the Sun with either a planar or curved current sheet (e.g., Sweet 1958a; Priest and Raadu 1975). Such current sheets have been invoked in models of coronal loops (Low 1981, 1986) and solar prominences (e.g., Kippenhahn and Schluter 1957; Malherbe and Priest 1983). Priest et al. (1995) included time dependence in the model describing the nonlinear evolution for the dynamic time-dependent formation of a current sheet by solving the low-beta equation of motion and the ideal induction equation. Titov (1992) developed a clever technique for computing 2D potential fields with multiple current sheets by placing image sheets below the photosphere.

Furthermore, Priest and Syntelis (2021) have described a technique for dealing with 2D sheets without resorting to complex variable theory, which is invaluable because it may then be generalised to 3D. The approach involves constructing a current sheet from an infinite set of line currents. This method is illustrated in the following section for modelling an axisymmetric field at a separator ring. Finally, models for 2D current sheets may be extended to the case of finite plasma pressure. In this case the field will relax towards a force-free state in which the total pressure $(p + B^2/(2\mu))$ balances across the separatrices, leading to different geometries such as cusp-shaped and curved separatrices (e.g., Bajer 1990; Bungey and Priest 1995).

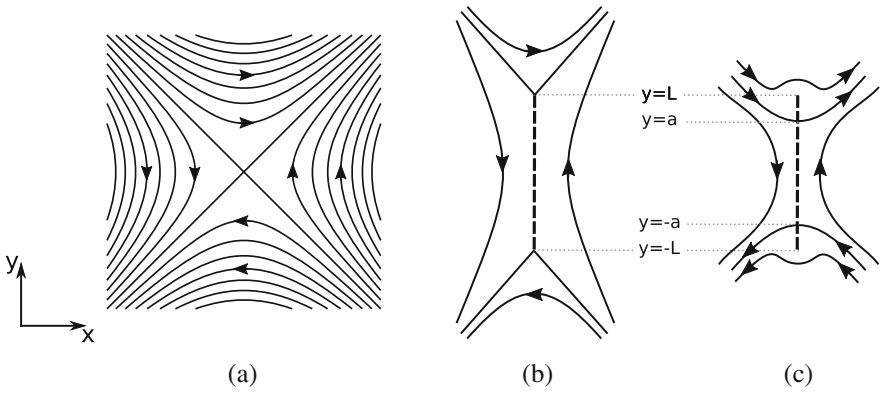

Fig. 24 The magnetic field **a** near an X-type null point which evolves to a field with a current sheet having at its ends either **b** Y-points or **c** reversed currents and singularities

5.2 Lateral or shearing motion of 2.5D fields to form sheets at separators and separatrices

When going beyond 2D potential fields to model magnetic fields that are 3D potential or force-free or magnetohydrostatic, current sheets can no longer be treated with complex variable theory and so other approaches are needed. By a "2.5D" field we mean a field such as $(B_x(x,y), B_y(x,y), B_z(x,y))$ with all three magnetic components that vary with only two variables (x, y).

5.2.1 Three-dimensional axisymmetry near a separator

The magnetic field of a 3D axisymmetric annular current sheet created between two approaching dipoles was first analysed by Tur (1977) and Longcope and Cowley (1996). Indeed, Longcope and Cowley (1996) considered the topological admissibility of sequences of equilibria (as done for 2D X-points by Syrovatsky 1971), and argued that equilibria containing tangential discontinuities at the separator should result from certain perturbations. Building on their ideas, Priest and Syntelis (2021) developed a model in which the magnetic field is written in terms of cylindrical polar coordinates (R, ϕ, z), as

$$(B_R, B_z) = (z, r) + (b_{SR}(R,z), b_{Sz}(R,z)),$$

due to a ring of X-points near $R = R_0$ and the field (b_{SR}, b_{Sz}) of the current sheet itself. The current $J\hat{\boldsymbol{\phi}}$ in the sheet is related to the R-component (B_S) of the field at the edge of the sheet by

$$\mu J(R) = 2B_S(R).$$

The profile of B_S and therefore of current J that makes the normal component $(B_z(R_0'))$ of magnetic field vanish at the current sheet is then given by

$$R = -\lim_{z\to 0} b_{Sz}(R,z) \tag{49}$$

at the sheet, which is found by first calculating the field due to a current ring and then summing over an infinite set of infinitesimal current rings to find the field of the current sheet.

To lowest order in $(r^2+z^2)^{1/2}/R_0'$, the z-component of the magnetic field close to a current ring is

$$B_z \approx -\frac{\mu I_0}{4\pi}\left\{\frac{2r}{r^2+z^2} + \frac{1}{R_0'}\log_e \frac{(z^2+r^2)^{1/2}}{8R_0'}\right\},$$

where $r = R - R_0'$. The first term is the field due to a straight current, while the second term gives the effect of the curvature of the current ring, which decreases the field on the outside of the ring and increases it on the inside of the ring, as shown in Fig. 25(a). After summing over a series of infinitesimal current rings to give a

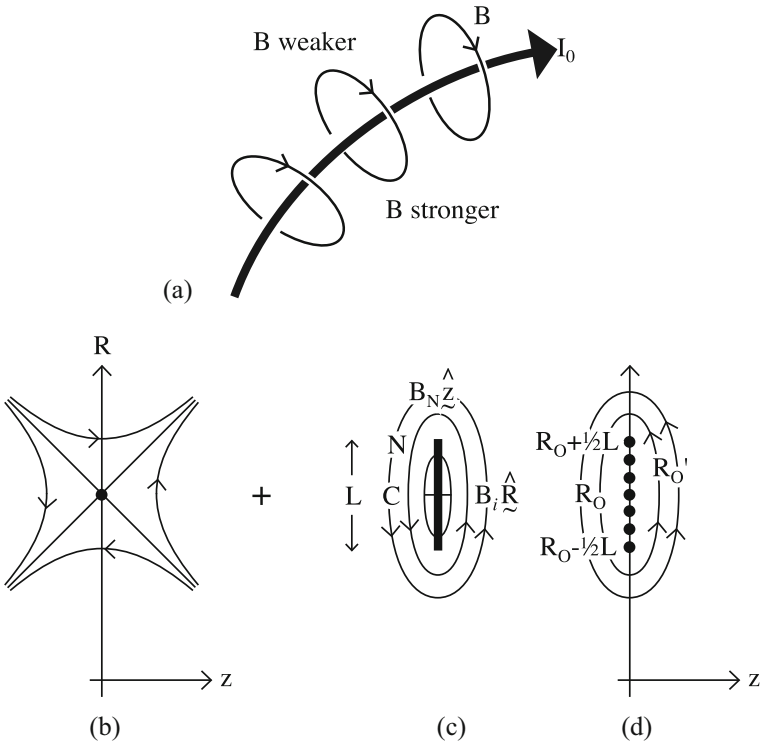

Fig. 25 **a** The magnetic field near part of a circular current loop of current I_0. **b–d** The magnetic field near an axisymmetric current sheet due to the sum of (**b**) a ring of nulls at radius R_0 and **c** a current sheet of length L or equivalently **d** a set of current rings. Image reproduced with permission from Priest and Syntelis (2021), copyright by ESO

current sheet, the condition (Eq. 49) for the tangential field to vanish at the sheet becomes

$$R = \frac{1}{\pi}\lim_{z\to 0}\int_{-L/2}^{L/2}\tfrac{1}{2}B_S(r_0')\left\{\frac{2(r-r_0')}{z^2+(r_0'-r)^2}+\frac{1}{R_0}\log_e\frac{[z^2+(r_0'-r)^2)]^{1/2}}{8R_0}\right\}dr_0'.$$

This integral equation has been solved by Priest and Syntelis (2021) to give the profile of $B_S(R)$ and applied to the problem of chromospheric and coronal heating by photospheric flux cancellation. Longcope (1996) used the formation of current sheets along separators as the basis for a model for reconnection, flaring and heating in the corona.

5.2.2 Shearing of separatrices of a 2.5D field

Current sheets may also be created when a separatrix touches a boundary at a *bald patch* (Fig. 26a) (Titov et al. 1993). Converging motions will give rise to a current sheet extending upwards, as in Fig. 26b, but shearing motions produce a long

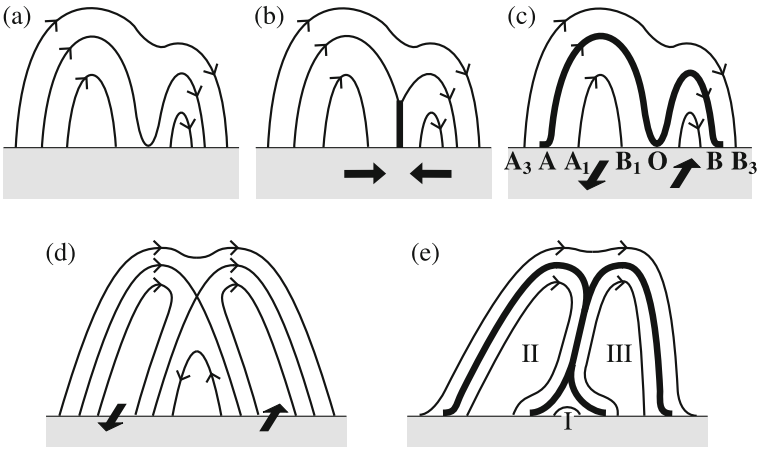

Fig. 26 A simple current sheet (thick curve) is produced in (**b**) by the effect of converging motions on (**a**) a quadrupolar field with no X-point, but the effect of (**c**) shearing motions is to create a current sheet all along the separatrix. Similarly, if there is an X-point present, shearing motions also create (**e**) a separatrix current sheet. Image reproduced with permission from Priest (2014), copyright by CUP

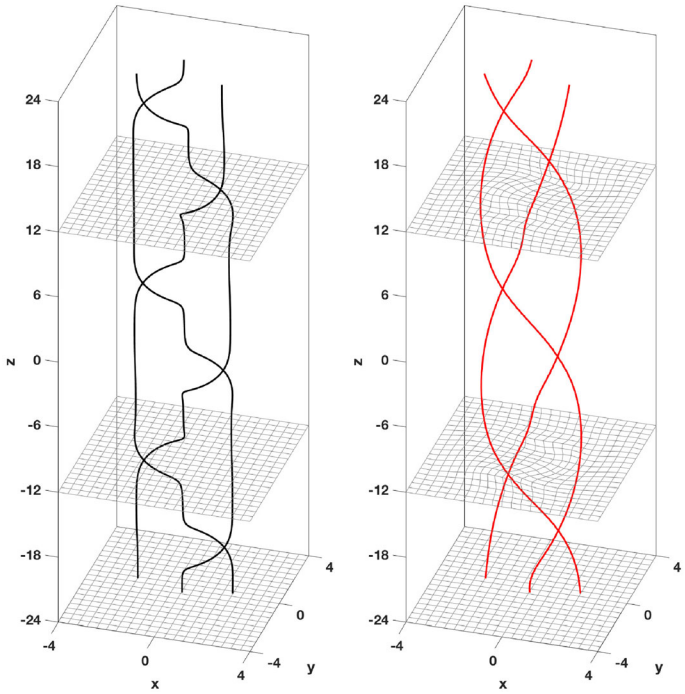

Fig. 27 Illustration of the Lagrangian relaxation computational approach, showing some representative grid lines (grey) and magnetic field lines both prior to relaxation (left) and in the numerically obtained equilibrium (right). The grid deforms to allow field lines to equilibrate the twist or stress along their length. Image reproduced with permission from Pontin and Hornig (2020), copyright by the authors, based on the simulations of Wilmot-Smith et al. (2009b)

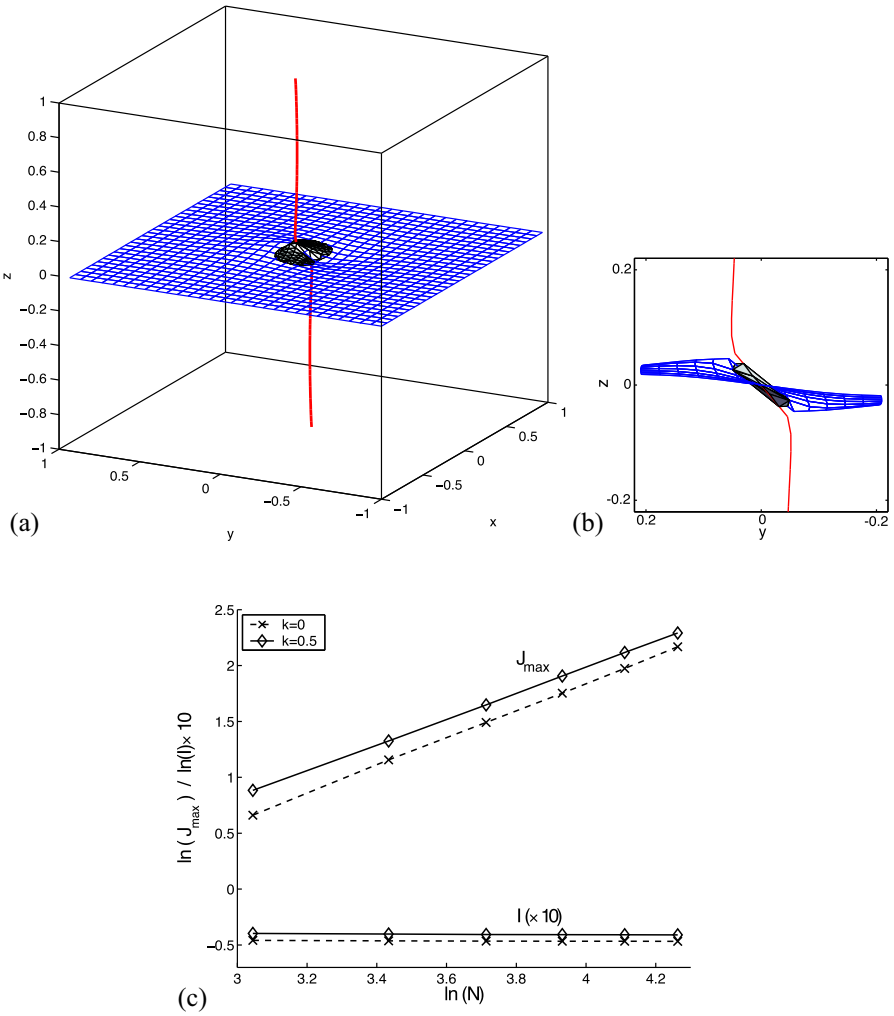

Fig. 28 (a, b) Spine (red) and fan (blue) structure in the final equilibrium obtained through an ideal relaxation simulation in which the spine footpoints are displaced, together with an isosurface (3D contour) of the current density (grey). The two different images show two different angles and illustrate the local collapse of the spine and fan. (c) Scaling of the peak current density $J_{\max}$ and total current flux I with the numerical resolution for the 3D null (marked "$k = 0.5$") and for an equivalent simulation for a 2D null (marked "$k = 0$"). Modified from Pontin and Craig (2005) with permission, copyright by AIP

curved sheet stretching all along the separatrix (Fig. 26c) (Low and Wolfson 1988; Vekstein et al. 1991; Amari and Aly 1990). This may be analysed by considering a 2.5D equilibrium field of the form $(B_x, B_y, B_z) = (\partial A/\partial y, -\partial A/\partial x, B_z(A))$, where the force-free condition $\mathbf{j} \times \mathbf{B} = \mathbf{0}$ gives rise to the *Grad–Shafranov equation* for the flux function (A), namely,

$$\nabla^2 A + B_z \frac{dB_z}{dA} = 0. \tag{50}$$

If a smooth footpoint displacement of a potential field of the form $\mathbf{B}_p = (\partial A/\partial y, -\partial A/\partial x)$ is imposed, the integral of the field-line equation becomes $B_z(A) = d(A)/V(A)$, in terms of the difference $d(A)$ in footpoint displacement out of the plane and the *differential flux volume* $V(A) = \int ds/B_p$. Although $B_z(A)$ is constant along a given field line, its values on field lines above and below the separatrix AOB may be quite different, which turns the whole separatrix into a current sheet (Fig. 26c). Similarly, a 2D field with an X-point (Fig. 26d) is transformed by shearing motions into two cusp points at the ends of a current sheet extending all along the separatrices (Vekstein and Priest 1992, 1993) (Fig. 26e).

5.3 Magnetic relaxation

The preceding sections describe analytical models for current sheets in magnetic fields with certain symmetries. A useful technique for producing magnetic equilibria in more general geometries—often containing current sheets—is "magnetic relaxation" (e.g., Sturrock and Woodbury 1967; Arnol'd 1974; Klimchuk et al. 1988). Conceptually, the idea is to begin with a magnetic configuration that is not in equilibrium (and does not contain current sheets) and then to lower the total energy and so move towards an equilibrium while maintaining the magnetic field line topology (i.e., prohibiting reconnection). For example, Moffatt (1985) described the formation of current sheets in a three-dimensional configuration consisting of two linked flux tubes.

Computational implementations of ideal magnetic relaxation take advantage of the fact that the magnetic field evolves like a line element in a flow and use a Lagrangian computational mesh. In this way, the magnetic topology can be exactly maintained, since the expression for $\mathbf{B}$ is derived directly from the numerical mesh deformation (Craig and Sneyd 1986). Various different evolution equations can be used (Candelaresi et al. 2015), but, since it is the final state that is of interest rather than the evolution towards it, evolutions that minimise the magnetic energy in the most efficient way are chosen in practice. A common choice is

$$\rho \frac{\partial \mathbf{v}}{\partial t} = -\nabla p + \mathbf{j} \times \mathbf{B} - K\mathbf{v}, \tag{51}$$

where K is a friction coefficient, with the relaxation being described as magnetofrictional (Chodura and Schlueter 1981; Craig and Sneyd 1986). This choice of evolution equation has the great advantage that the total magnetic energy decreases monotonically in time. Alternatively, the energy may be damped by a viscous term, in which case the sum of the magnetic and kinetic energies decays monotonically (Moffatt 1985). In either case, the magnetic energy tends to a finite limit, which is non-zero if the initial topology is nontrivial in the sense that not all of the field lines can shrink to a point without cutting other field lines (see, e.g., Fig. 27).

The final state of such a relaxation (with the lowest limit for the magnetic energy) is determined by the magnetic field topology. Depending on the evolution equation

used, the final state may be force-free ($\mathbf{j} \times \mathbf{B} = \mathbf{0}$) or magnetostatic ($\mathbf{j} \times \mathbf{B} = \nabla p$) and may possess current sheets, across which $\mathbf{n} \cdot \mathbf{B} = 0$ and the total pressure $(p + B^2/(2\mu))$ is continuous. This technique has been used to explore the properties of current sheets at both 2D and 3D magnetic null points (Craig and Litvinenko 2005; Pontin and Craig 2005), in response to the kink instability (Craig and Sneyd 1990), and in various configurations conforming to the geometry of Parker's braiding model—see the following section for details. It is worth noting that the method can fail if the computational grid becomes too distorted (Pontin et al. 2009), which has been somewhat mitigated in a new implementation by Candelaresi et al. (2014).

5.4 Current sheets at 3D magnetic nulls

Much like 2D magnetic nulls, 3D nulls are potential sites for current sheet formation. As in 2D (see Sect. 2.1), the Lorentz force at a 3D null tends to reinforce any perturbation to an equilibrium field, and, when the linear field about the null is considered in isolation, the current is shown to blow up in a finite time (Klapper et al. 1996; Bulanov and Sakai 1997). As in 2D, the energy that drives the collapse comes from the surrounding volume outside the modelled domain, so that the effect of the external conditions is being neglected in such models.

Antiochos (1996) was the first to sketch the form of the magnetic field when a discontinuity forms at a 3D null. The formation of such current sheets was first demonstrated explicitly by Pontin and Craig (2005) using ideal relaxation simulations (as in Sect. 5.3). They showed that any perturbation that disturbs the locations on the boundary of the footpoints of the spine or fan from their equilibrium positions leads to the formation of a current layer at the null in which the peak current shows a power-law divergence with the numerical resolution (Fig. 28c)—the expected signature of an underlying, unresolved current sheet. The divergence identically mirrors the behaviour for a 2D null (dashed curve in the figure) while the net flux of current in the sheet remains fixed with resolution in both cases.

The field line geometry takes the form of a local collapse of the spine towards the fan, directly analogous to the closing up of the separatrices when current sheets form at 2D nulls (Fig. 28a,b; see also Fuentes-Fernández and Parnell 2013). Fuentes-Fernández and Parnell (2012) considered ideal relaxation of non-equilibrium fields containing spiral nulls. In all but the exactly axisymmetric case they reported an infinite-time singularity of the current in a sheet that extends along the spine and weak-field fan direction (the spine and fan remain perpendicular to one another). More complex field geometries containing nulls have also been examined in ideal relaxation experiments, with signatures of singular current structures present at the nulls for a broad range of fields and perturbations (e.g., Pontin and Huang 2012; Craig and Pontin 2014; Candelaresi et al. 2015).

For current singularities at both 2D and 3D nulls, increasing the plasma pressure is found to weaken the divergence of the current with numerical resolution, but not to mitigate that divergence (Craig and Litvinenko 2005; Pontin and Craig 2005). This is consistent with the fact that locally around the null—where the field is

linear—it can be shown that the $\mathbf{j} \times \mathbf{B}$ force never takes the form of a gradient, and therefore cannot be balanced locally by a pressure gradient (Parnell et al. 1997).

5.5 Line-tied magnetic fields without null points

5.5.1 Topological dissipation

As described in Sect. 5.1–5.3, when a magnetic field contains topologically distinct flux systems, partitioned by separatrices, an ideal evolution from one smooth equilibrium to another is not always possible and instead—in the absence of reconnection—current sheets form at null points and along separatrices. However, Parker (1972, 1979, 1989, 1994) went a step further by arguing that current sheets might also form during the evolution of magnetic fields without any separatrices, but with a complex winding of their magnetic field lines—and may therefore possibly contribute to coronal heating (Fig. 29).

He suggested that such a configuration cannot, in general, adjust to a new smooth force-free equilibrium in response to finite-amplitude footpoint motions, but should instead evolve towards a configuration containing tangential discontinuities of $\mathbf{B}$, or current sheets. The formation of these current sheets and subsequent rapid reconnection he called *topological dissipation*, since it is the field line topology (winding or "braiding") that is responsible for the formation of the current sheets. Relentless motions of the photospheric footpoints of coronal field lines implies that the field is continually responding by reconnecting and converting magnetic energy into heat, which offers a way to heat the solar corona, especially active regions. Since it was proposed, this idea has stimulated substantial debate, with many different approaches used to attempt to prove or disprove the hypothesis. This became known as the "Parker problem". Here we briefly summarise relevant results, and direct the reader to the review by Pontin and Hornig (2020) for more details.

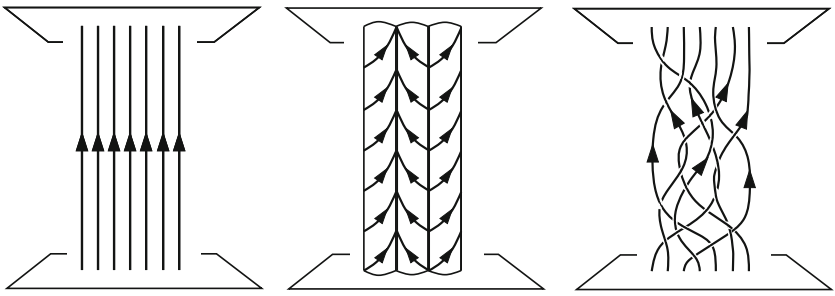

Fig. 29 The effect on **a** an initial field of **b** twisting and **c** braiding motions

5.5.2 Arrays of flux tubes

If a set of flux tubes is closely packed together and each is twisted in the same direction, then Parker (1979) realised that current sheets will form at the boundaries of the tubes. He considered a magnetic field ($B_x = \partial A/\partial y, B_y = -\partial A/\partial x$, $B_z =$ constant) in equilibrium such that

$$A = K \sin k_x x \, \sin k_y y.$$

This rectangular array of twisted flux tubes has adjacent cells with opposite twist. If instead all the cells have the same sense of twist, they are not in equilibrium and form current sheets at their boundaries. A similar configuration was considered by

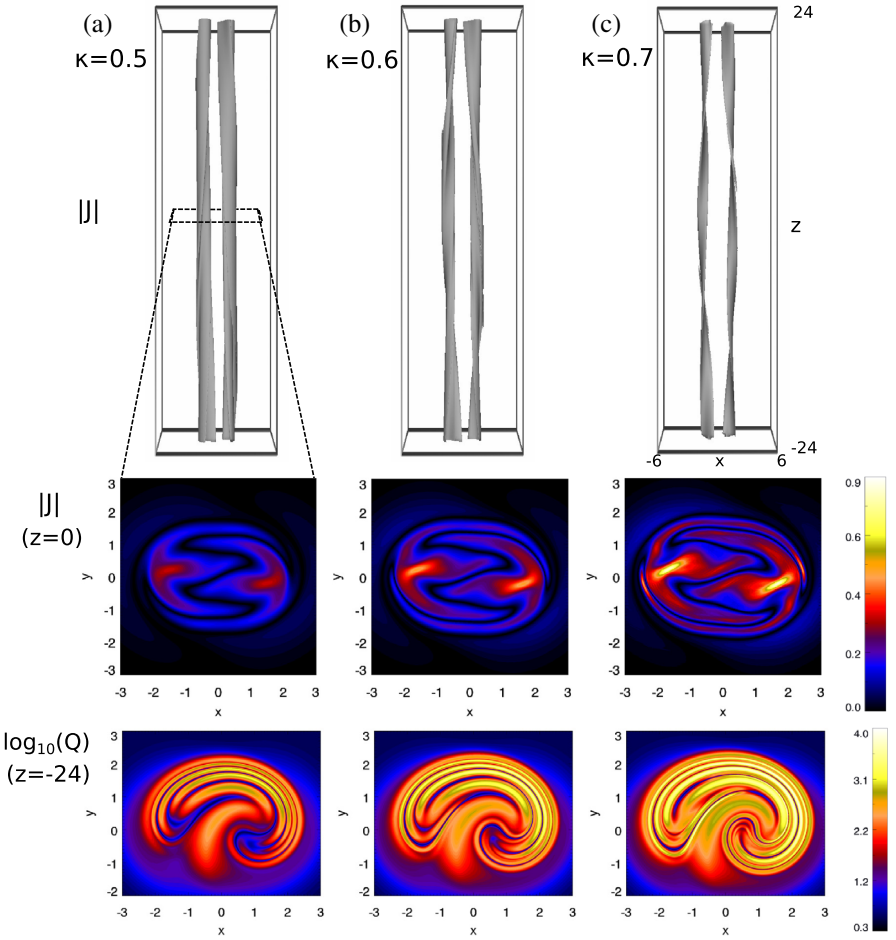

Fig. 30 The ideal relaxation of a braided field. Top: isosurface of the modulus $|\mathbf{j}|$ of the current density at 60% of maximum. Middle: $|\mathbf{j}|$ in the plane $z = 0$. Bottom: $\log_{10}(Q)$ in the plane $z = -24$. For twist parameter given by **a** $k = 0.5$, **b** $k = 0.6$, **c** $k = 0.7$. Image modified with permission from Pontin and Hornig (2015), copyright by AAS

Longcope and Strauss (1994), who studied the coalescence instability (Finn and Kaw 1977) between pairs of flux tubes with the same sense of twist. In the absence of line-tying of these flux tubes, the current sheet that forms between the tubes is singular. However, the line-tying provides an additional magnetic tension force that halts the collapse when the current layer thickness is still finite.

Another candidate mechanism that has been proposed to explain current sheet formation in the context of coronal heating and solar flares is the ideal kink instability (Kruskal et al. 1958; Hood and Priest 1979). Again, in the absence of line-tying, singular current sheets form, on resonant surfaces. In the line-tied case a current layer still forms at the radius that corresponds to the resonant surface. The thickness of this current layer scales inversely with the distance between the line-tied boundaries, and the growth-rate of the instability is reduced as described by Huang et al. (2010). However, the issue of current sheet formation in the nonlinear phase of the instability is not yet fully resolved.

5.5.3 Magnetic braids

In the original paper, Parker (1972) considered infinitesimal departures from a uniform field between parallel, perfectly conducting plates. He argued that, if the pattern of small-scale variations is not uniform along the large-scale field, then the field cannot be in magnetostatic equilibrium. In other words, equilibrium exists only if the field variations consist of a simple twist extending from one footpoint to another. However, van Ballegooijen (1985) pointed out an error in the calculation, and indeed argued that a smooth equilibrium should *always* be accessible following an infinitesimal perturbation to a uniform field (see also Sakurai and Levine 1981; Zweibel and Li 1987). This is consistent with the paper by Bineau (1972) who proved that smooth force-free fields (where $\mathbf{j} \times \mathbf{B} = 0$) exist in the vicinity of the potential field (i.e., for small α, where $\nabla \times \mathbf{B} = \alpha \mathbf{B}$).

In spite of the above results, there have been numerous arguments put forward for the formation of tangential discontinuities of $\mathbf{B}$ in response to finite-amplitude perturbations. These include persuasive intuitive arguments based on the optical analogy (e.g., Parker 1994), as well as studies of "topologically untwisted" fields by Low (2006), Low and Flyer (2007), Janse and Low (2009). Nevertheless, none of these studies explicitly demonstrates formation of tangential discontinuities, and indeed counter-arguments have been made demonstrating that simple tangential discontinuities (in the form of single smooth surfaces) cannot form in response to smooth boundary motions (van Ballegooijen 1985; Longcope and Strauss 1994; Cowley et al. 1997).

Computational approaches to the Parker problem typically involve ideal relaxation simulations using the approach described in Sect. 5.3. In short, such approaches have not found any conclusive evidence for the formation of current sheets (e.g., Craig and Sneyd 2005; Wilmot-Smith et al. 2009b). What is, however, clear is that, as the boundary perturbations are progressively increased, the corresponding equilibrium in the domain contains current layers that are progressively thinner and more intense (van Ballegooijen 1988a, b; Mikić et al. 1989; Rappazzo and Parker 2013). To understand why this must generally be the case,

consider the following intuitive argument (Pontin and Hornig 2015). In a force-free field (with $\nabla \times \mathbf{B} = \alpha \mathbf{B}$), α is constant along magnetic field lines (since $\mathbf{B} \cdot \nabla \alpha = 0$). Thus, if the field line mapping between the two line-tied boundaries contains small perpendicular length scales then so must α (assuming that it is not constant but rather varies between field lines). Now, $\alpha = \mathbf{j} \cdot \mathbf{B}/\mathbf{B} \cdot \mathbf{B} = j_{\parallel}/|\mathbf{B}|$, or $j_{\parallel} = \alpha |\mathbf{B}|$, so that $j_{\parallel}$ must have the same perpendicular length scales as α and the field line mapping. (The modifying factor of the field strength is approximately constant in the Parker problem geometry.) The same conclusion is reached for magnetic fields *close to* force-free equilibrium by considering the correlation length of α along field lines—see Pontin et al. (2016). This was demonstrated explicitly by Pontin and Hornig (2015) who simulated the ideal relaxation of a set of braided fields (following the earlier approach of Wilmot-Smith et al. 2009b). In their model, the "twist parameter" k (see Fig. 30) determines the field complexity, with larger k corresponding to "more braided" fields. This can be quantified using the squashing factor Q (see Sect. 2.6), which exhibits progressively larger numbers of thinner layers with higher values of Q as the field becomes more braided (see also Wilmot-Smith et al. 2009a). As shown in Fig. 30, the equilibria for these magnetic braids contain both QSLs and current layers whose thickness scales exponentially—with the same exponent—with the twist parameter. The conclusion from these studies is that continual braiding of the coronal field lines may not lead to tangential discontinuities of $\mathbf{B}$ (singular current sheets), but nevertheless onset of reconnection is inevitable as the current layers become exponentially thinner and more intense as the field lines become more tangled.

5.6 Current sheet formation at hyperbolic flux tubes or quasi-separators

What kinds of motion encourage current sheets to form at a quasi-separator and the region that surrounds it, namely, a hyperbolic flux tube (HFT)? Démoulin et al. (1996a) conjectured that any footpoint motion would tend to do so, and this was followed by a series of numerical experiments that confirmed formation of concentrated currents for specific geometries (Inverarity and Titov 1997; Galsgaard et al. 2003b; Aulanier et al. 2005; De Moortel and Galsgaard 2006a). Later, Titov (2007) clarified the problem by showing how pinching motions are much more effective at concentrating currents than rotating motions.

Like separators, HFTs (or quasi-separators) are favourable magnetic structures for current sheet formation, because their field lines in a quadrupolar configuration connect regions of strong and weak photospheric magnetic field, which provides a favourable condition for pinching by a stagnation flow.

Consider a straightened-out HFT formed between four sunspots lying in two planes. Shearing displacements will either turn the flux tube or twist it and will produce at the midplane either a rotation or a stagnation flow. This will deform a Lagrangian grid in two different ways (Fig. 31) (Titov et al. 2003). For the case of "twist", most of the grid distortion is in a narrow central region, and so the middle of the HFT will pinch to a strong current layer.

The maximum current density (at the centre of the configuration) is

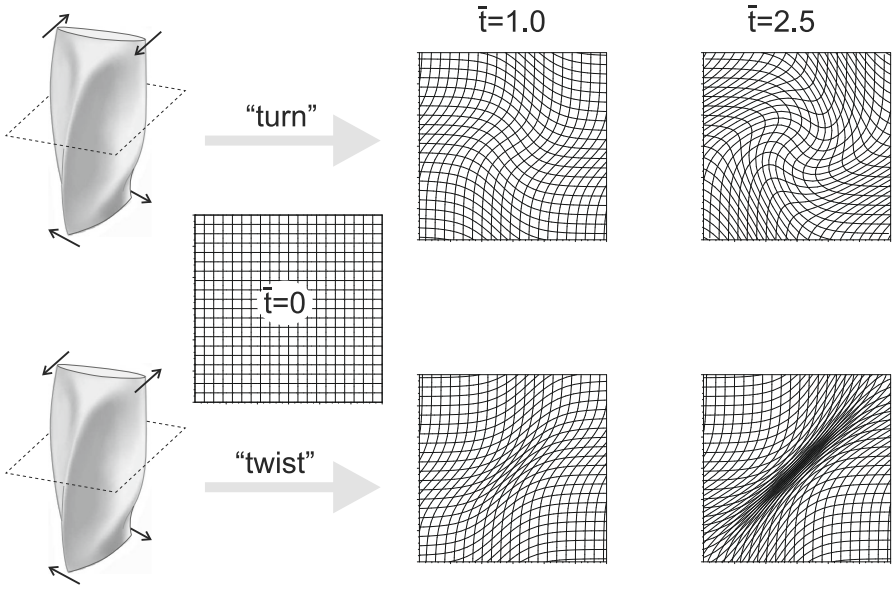

Fig. 31 Non-pinching (top) and pinching (bottom) deformations of an HFT in the midplane $z = 0$ (dashed) due to turning and twisting shearing motions, respectively, applied to the HFT footpoints. Image reproduced with permission from Titov (2007), copyright by CUP

$$j_z^* = \frac{2}{\mu}\left(h + \frac{B_\parallel}{2L}\right)\sinh\xi. \tag{52}$$

where $2L$ is the distance between the planes, h and $B_\parallel$ are the initial values of the transverse field gradient and longitudinal field at the centre, and $\xi = V_s t/l_{sh}$ is the dimensionless displacement of each sunspot moving with velocity V_s and creating a shear region of a half-width l_{sh}. Thus, when $\xi > 1$, a stagnation-point flow at the centre of the HFT causes it to pinch and the current density to grow exponentially with spot displacement.

At large ξ, the above kinematic estimate can be improved by relaxing the unbalanced stress in the current layer and allowing it to compress in the transverse direction to an approximately force-free state (Titov et al. 2003). The resulting central current density is

$$j_{z\,\mathrm{eq}}^* \simeq j_z^*\left[1 + e^{\xi}\left(0.91\frac{h l_{sh}}{B_\parallel} + 0.57\frac{l_{sh}}{L}\right)^2\right], \tag{53}$$

which is larger than the kinematic value j_z^* by a factor that grows exponentially with the displacement ξ and with decreasing $B_\parallel$. Effenberger et al. (2011) used an adaptive mesh code to study current accumulation in an HFT, observing extremely high current densities on the scale of the computational grid. In the limit $B_\parallel \to 0$ we find $j_{z\,\mathrm{eq}}^* \to \infty$, in agreement with the analysis of current accumulation at null points

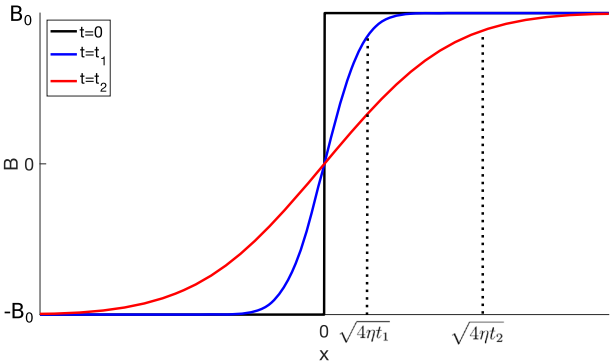

Fig. 32 The magnetic profile at three times ($t = 0$, t_1, t_2) during its diffusion from an initial 1D step function (see Eq. 58)

(Bulanov and Olshanetsky 1984; Priest and Titov 1996; Craig and Litvinenko 2005).

Interestingly, a strong current layer can form even in an initially uniform field, as can be seen by putting $h = 0$ in the above expressions (52) and (53). This is because the pair of twisting and shearing footpoint motions interlocks the coronal field lines and so forms an HFT even if none exists initially. Early numerical experiments on Parker braiding confirmed such an effect (see Mikić et al. 1989; Galsgaard and Nordlund 1996; Longbottom et al. 1998, and the preceding section).

6 Magnetic annihilation

6.1 A 1D current sheet with diffusion and advection

A closely related process to magnetic reconnection is *magnetic annihilation*, which refers to the inwards transport and cancellation of straight, oppositely-directed field

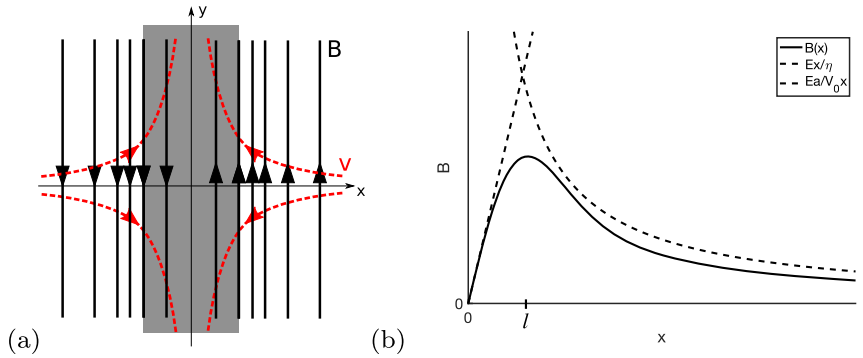

Fig. 33 **a** Steady-state model for magnetic annihilation in which straight magnetic field lines (solid lines) are carried in from both sides by a stagnation-point flow (red dashed). **b** The magnetic field B as a function of distance x (see Eq. 61), with the approximations when $x \ll l$ and $x \gg l$ shown dashed

lines in a current sheet (of infinite length). The variation of the magnetic field ($\mathbf{B}$) in time is described by the induction equation

$$\frac{\partial \mathbf{B}}{\partial t} = \nabla \times (\mathbf{v} \times \mathbf{B}) + \eta \nabla^2 \mathbf{B}, \tag{54}$$

due to the basic processes of advection of the magnetic field with the plasma and diffusion through the plasma. The ratio of advection to diffusion (i.e., of the two terms on the right-hand side of Eq. 54) for a length-scale l_0 is the magnetic Reynolds number $R_m = l_0 V_0/\eta$.

For a 2D steady state with flow $\mathbf{v} = v_x\hat{\mathbf{x}} + v_y\hat{\mathbf{y}}$ and magnetic field $\mathbf{B} = B_x\hat{\mathbf{x}} + B_y\hat{\mathbf{y}}$, Eq. (54) integrates to Ohm's Law

$$\mathbf{E} + \mathbf{v} \times \mathbf{B} = \eta \nabla \times B, \tag{55}$$

where Faraday's Law ($\nabla \times \mathbf{E} = \mathbf{0}$) implies that the electric field $\mathbf{E} = E\,\hat{\mathbf{z}}$ is uniform. In most parts of the interior and atmosphere of the Sun, the advection dominates, so that the right-hand side is negligible. This holds, for instance, in the ideal region around a diffusion region and outside shock waves.

For steady-state reconnection, the other main MHD equation is the equation of motion under the influence of a pressure gradient and a $\mathbf{j} \times \mathbf{B}$-force, namely,

$$\rho(\mathbf{v} \cdot \nabla)\mathbf{v} = -\nabla\left[p + \frac{B^2}{2\mu}\right] + \frac{(\mathbf{B} \cdot \nabla)\mathbf{B}}{\mu}. \tag{56}$$

When advection is negligible ($R_m \ll 1$) and the magnetic field ($B(x,t)\hat{\mathbf{y}}$) is one-dimensional, Eq. (54) reduces to a 1D diffusion equation

$$\frac{\partial B}{\partial t} = \eta\,\frac{\partial^2 B}{\partial x^2}, \tag{57}$$

and so field variations on a scale l_0 diffuse away in a time $\tau_d = l_0^2/\eta$ and with a speed $v_d = \eta/l_0$.

For an initial magnetic field $B(x, 0)$ the solution is

$$B(x,t) = \int G(x - x', t)\; B(x', 0)\; dx'$$

where $G(x - x', t) = (4\pi\eta t)^{-1/2} \exp[-(x - x')^2/(4\eta t)]$ is the Green's function.

For example, if initially there is an infinitesimally thin current sheet at the origin, so that the magnetic field is a step function ($B = B_0$ for $x > 0$ and $B = -B_0$ for $x < 0$), the solution becomes

$$B(x,t) = \frac{2B_0}{\sqrt{\pi}} \int_0^{x/\sqrt{(4\eta t)}} e^{-u^2} du, \tag{58}$$

and the steep magnetic gradient at $x = 0$ spreads out in time, as shown in Fig. 32. The width ($4\sqrt{\eta t}$) of the sheet increases in time, and the field is said to be annihilated, since the field strength at a fixed position decreases in time. During this

process, the field lines diffuse inwards through the plasma and cancel at $x = 0$, while the magnetic energy is converted into heat by ohmic dissipation.

In the opposite limit ($R_m \gg 1$) when advection dominates over diffusion, the magnetic field lines are frozen into the plasma. For example, the effect of a stagnation-point flow $v_x = -V_0 x/a$, $v_y = V_0 y/a$ on a 1D field ($B(x,t)\hat{\mathbf{y}}$) is to carry the field lines inwards from the sides and accumulate them near $x = 0$. Here the induction equation (54) becomes

$$\frac{\partial B}{\partial t} - \frac{V_0 x}{a}\frac{\partial B}{\partial x} = \frac{V_0 B}{a}, \tag{59}$$

which may be solved by the method of characteristics.

6.2 Stagnation-point flow model

As shown above, as the field lines in a current sheet diffuse inwards and cancel, the sheet naturally tends to diffusively broaden. However, a steady state can be maintained if this outwards diffusion is balanced by an inwards transport of the magnetic field ($B(x)\hat{\mathbf{y}}$) by a stagnation-point flow ($v_x = -V_0 x/a, v_y = V_0 y/a$), where V_0/a is constant (Fig. 33). When $R_m \gg 1$, an extremely thin current sheet is created with a small width (l) and thus a large magnetic gradient (∇B) and current ($j \sim B/(\mu l)$) (Parker 1973; Sonnerup and Priest 1975).

In this case Ohm's Law (55) with $E = \text{const}$ becomes

$$E - \frac{V_0 x}{a} B = \eta \frac{dB}{dx}, \tag{60}$$

whose solution is

$$B = \frac{2E_0 a}{V_0 l} \exp\left(-\frac{x^2}{l^2}\right) \int_0^{x/l} \exp(X^2)\, dX, \tag{61}$$

where $l^2 = V_0/(2\eta a)$, as shown in Fig. 33. When $x \gg l$, the right side of Eq. (60) is negligible, the field is frozen to the plasma and $B \approx (Ea)/(V_0 x)$. On the other hand, when $x \ll l$, the second term on the left is negligible, the field lines diffuse through the plasma and $B \approx Ex/\eta$. This represents one of the few exact nonlinear solutions of MHD, and it has been generalised to a 3D stagnation-point flow, with a field ($\mathbf{B}(x)$) that rotates as it is carried in (Sonnerup and Priest 1975).

6.3 Time-dependent current sheet

The purely one-dimensional behaviour of a current sheet involving a magnetic field $B(x,t)\hat{\mathbf{y}}$, plasma flow $v(x,t)\hat{\mathbf{x}}$, density ($\rho(x,t)$) and pressure ($p(x, t)$) has been described by Priest and Raadu (1975) using self-similar solutions for highly subsonic and sub-Alfvénic flows. Numerical computations have been carried out by Forbes et al. (1982) for the evolution of a current sheet when the magnetic diffusivity is suddenly enhanced.

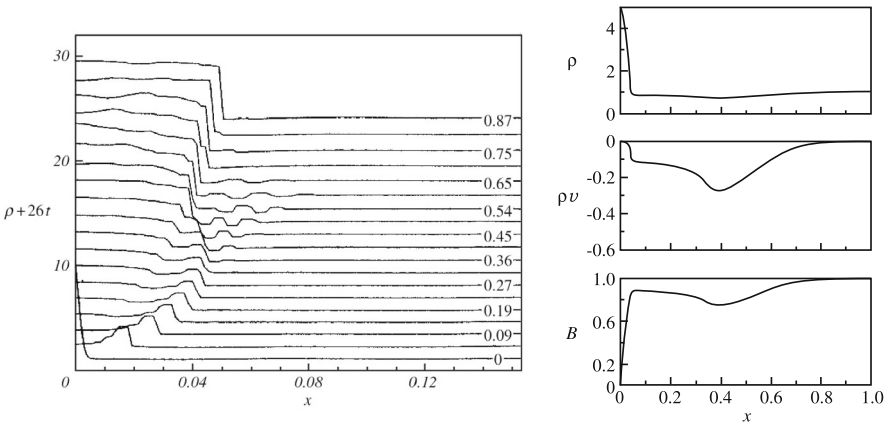

Fig. 34 Evolution of a current sheet in response to a sudden increase in diffusivity: (left) the density at small times when the shock is within the diffusion region and $\beta_\infty = 0.1$ is the plasma beta at large distances; (right) density (ρ), mass flux (ρv) and magnetic field (B) for $\beta_\infty = 0.2$ at large times when the waves are outside the diffusion region. Image reproduced with permission from Forbes et al. (1982), copyright by CUP

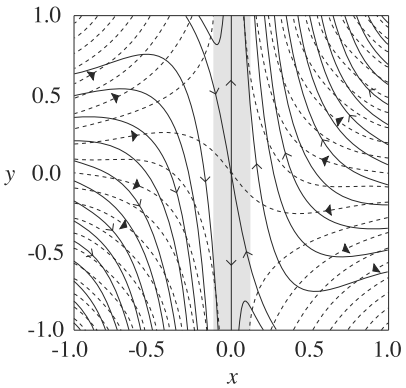

Fig. 35 The Craig–Henton reconnective annihilation model, showing streamlines (dashed) and magnetic field lines (solid) for $\lambda = 0.9$. The one-dimensional diffusion region (shaded) extends to infinity in the positive and negative y-directions. Image reproduced with permission from Priest (2014), copyright by CUP

At small times (Fig. 34(left)), within the diffusion region one sees the outwards propagation of a shock wave and an inflow of plasma, as well as a second shock that overtakes the first shock, coalescing with it. At large distances from the diffusion region (Fig. 34(right)), a magnetoacoustic wave pulse propagates outwards, consisting of a rarefaction followed by a compression (see also Takeshige et al. 2015). It turns out that this 1D model describes well the time-dependent formation of a current sheet by 2D null collapse, see Sect. 10.3.

6.4 Reconnective annihilation

The stagnation-point solution (Sect. 6.2), with inflow along the x-axis, namely,

$$v_x = -x, \qquad v_y = y, \qquad \mathbf{B} = B_y(x)\,\hat{\mathbf{y}},$$

has been generalised by Craig and Henton (1995) (Fig. 35) by superposing a 1D term $(G(x)\hat{\mathbf{y}})$ and a magnetic field $(\lambda\mathbf{v})$ that is parallel to a flow $v_x = -x, v_y = y - F(x)$, to give

$$\mathbf{B} = \lambda\mathbf{v} + G(x)\hat{\mathbf{y}}, \tag{62}$$

where λ is a constant and the functions $F(x)$ and $G(x)$ are determined by the equations of induction and motion. The parameter λ measures the departure of the solution from simple magnetic annihilation, while the plasma velocity in this exact solution of the incompressible MHD equations now consists of a stagnation-point flow plus a shear flow.

The process is known as *reconnective annihilation* (or *magnetic merging*) since it is closer in spirit to annihilation than to reconnection, with the 1D current sheet extending to infinity along the y-axis and both advection and diffusion being one-dimensional in nature. The width of the current sheet (like magnetic annihilation) scales with magnetic diffusivity like $\eta^{1/2}$.

Craig et al. (1995) and Craig and Fabling (1996) later extended the 2D solution to 3D, with a background 3D magnetic null point and stagnation-point flow. The authors present two solutions that involve current layers that are localised to either the spine or the fan. These are constructed by combining straight field lines (extending to infinity) with a background potential magnetic null point field using a construction as in Eq. (62). In each case the straight field lines are in oppositely-directed bundles localised to either the spine or fan, and form a tube of current around the spine ("spine reconnective annihilation") or a slab of current around the fan ("fan reconnective annihilation"). The solutions containing a planar current layer in the fan were demonstrated to be accessible through a dynamic evolution in an incompressible plasma by Craig and Fabling (1998). However, a pressure gradient is required within the current sheet, which is larger for thinner current sheets, i.e., for smaller η. This pressure gradient is a consequence of the restrictive but necessary choice of low-dimensionality disturbance fields: it is required to balance the Lorentz force within the current layer. It turns out that in a compressible plasma, such a pressure gradient cannot be maintained, and instead the magnetic field collapses, with the current layer becoming fully localised at the null rather than extending to infinity (Pontin et al. 2007a). By contrast, spine reconnective annihilation solutions appear not to be dynamically accessible (Titov et al. 2004; Pontin et al. 2007a).

7 Steady 2D reconnection models

In many applications reconnection is quasi-steady in the sense that it changes its behaviour slowly over many Alfvén travel times. Furthermore, steady reconnection is easier to study than time-dependent reconnection, so the emphasis in the early history of the subject was on understanding the nature of steady 2D reconnection. In particular, slow Sweet–Parker reconnection (Sect. 7.1) was followed by the fast

Petschek mechanism (Sect. 7.2) and by other types of fast reconnection (such as the Almost-Uniform family) that depend on the initial and boundary conditions (Sect. 7.3).

Fast reconnection is now the standard explanation for rapid energy release in the corona, but three possibilities arise, as mentioned in Sect. 1.1, namely, steady Petschek or Almost-Uniform reconnection, collisionless reconnection modified by the Hall effect, and impulsive bursty reconnection due to secondary tearing. However, in each of these three cases roughly the same maximum mean rate of reconnection is reached. See Sect. 9 for details of these three types of fast reconnection, both collisional and collisionless.

7.1 Sweet–Parker mechanism

The aim of early reconnection theory was to find the steady rate of reconnection, namely, the speed with which field lines may enter the reconnection site and have their connections to plasma elements changed. The first model by Sweet (1958a, b) and Parker (1957, 1963) modelled a diffusion layer of length ($2L$) stretching along the whole interface between opposing magnetic fields.

Equating the first and third terms in Ohm's law (54) gives the magnetic diffusion time

$$\tau_d = \frac{L_0^2}{\eta} = 10^{-9} L_0^2 T^{3/2},$$

with L_0 in metres and T in degrees K. This is huge in practice: for instance, a typical coronal length-scale ($L = 10^7$ m) and temperature ($T = 10^6$ K) yields a diffusion time of $\tau_d = 10^{14}$ sec. Releasing magnetic energy in a solar flare or coronal heating event therefore needs the creation of intense current sheets with enormous magnetic gradients and a tiny sheet thickness.

7.1.1 The basic Sweet–Parker model (1958)

Sweet and Parker gave an order-of-magnitude treatment for a current sheet or diffusion region of length $2L$ and width $2l$ (Fig. 36), for which oppositely directed magnetic fields $\pm B_i$ are carried in from both sides at a speed v_i. In a steady state, this

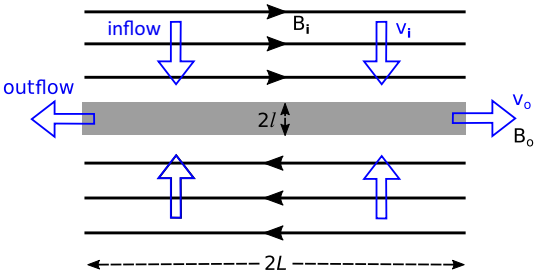

Fig. 36 The notation for Sweet–Parker reconnection, with magnetic field lines (black) transported into a diffusion region (shaded grey) by a plasma flow (blue arrows)

will be the same as the diffusion speed (τ_d/l) with which the sheet tends to diffuse outward, namely,

$$v_i = \frac{\eta}{l}. \tag{63}$$

Furthermore, conservation of mass implies that the rates at which plasma enters (at speed v_i) and leaves (at speed v_o) the sheet must be the same, so that, if the density is uniform,

$$L\, v_i = l\, v_o. \tag{64}$$

However, if the plasma is accelerated along the current sheet by the $\mathbf{j} \times \mathbf{B}$-force, the outflow speed is just the inflow Alfvén speed, namely,

$$v_o = v_{Ai} \equiv \frac{B_i}{\sqrt{\mu\rho}}. \tag{65}$$

After eliminating the width (l) between Eqns. (63) and (64), the reconnection rate becomes

$$v_i = \frac{v_{Ai}}{{R_{mi}}^{1/2}} \quad \text{or, in dimensionless terms,} \quad M_i = \frac{1}{R_{mi}^{1/2}}, \tag{66}$$

where

$$M_i \equiv \frac{v_i}{v_{Ai}} \qquad \text{and} \qquad R_{mi} \equiv \frac{L\, v_{Ai}}{\eta} \tag{67}$$

are the inflow Alfvén Mach number and magnetic Reynolds number, respectively.

According to the above equations, the plasma is ejected from a sheet of width $l = L/{R_{mi}}^{1/2}$ with a magnetic field strength $B_o = B_i l/L = B_i/{R_{mi}}^{1/2}$. Since $R_{mi} \gg 1$, we therefore find that, as well as $v_i \ll v_{Ai}$, the sheet width is much smaller than its length ($l \ll L$) and the outflow field is much smaller than the inflow field ($B_o \ll B_i$).

The Sweet–Parker mechanism has a sheet length (L) equal to the global external length-scale (L_e) and so R_{mi} becomes the *global magnetic Reynolds number* $R_{me} = L_e\, v_{Ae}/\eta$. In practice $R_{me} \gg 1$, and so the reconnection rate is very small. In the solar corona, for example, R_{me} is typically 10^8–10^{12}, giving a reconnection rate 10^{-4}–10^{-6} of the Alfvén speed, which is much too slow to account for, say, a solar flare.

Priest (2014) describes three interesting aspects of Sweet–Parker reconnection. The first is that a consideration of energetics implies that half the inflowing magnetic energy is converted into thermal energy and half into kinetic energy, so creating two hot fast jets of plasma with equipartition between thermal and kinetic energy. The second aspect concerns the assumption that the plasma pressures at the neutral point ($p_N = p_i + B_i^2/(2\mu)$) and outflow (p_o) are the same, so that the plasma is accelerated from rest at the neutral point to $v_o = v_{Ai}$ at the outflow, with pressure

gradients along the sheet playing no role. However, when pressure gradients are included, the reconnection rate (66) is modified to

$$M_i = \frac{2^{1/4}\left(1+\frac{1}{2}\beta_i(1-p_o/p_i)\right)^{1/4}}{\sqrt{R_{mi}}},$$

where $\beta_i = 2\mu p_i/B_i^2$. Thus, when the outflow pressure exceeds the neutral point pressure $(p_o > p_N)$, the outflow slows $(v_o < v_i)$ and the reconnection rate falls $(M_i < 1/\sqrt{R_{mi}})$. The third aspect concerns the effect of compressibility, which is to increase the reconnection rate (M_i) by a factor $(\rho_o/\rho_i)^{1/2}$ when $\rho_o > \rho_i$.

7.2 Petschek mechanism

Petschek (1964) realised that reconnection could be much faster (in terms of the rate at which magnetic flux is brought into the diffusion region) if the Sweet–Parker diffusion region were much smaller and occupied only a small part (of length $L \ll L_e$) of the boundary (of length L_e) between opposing fields. He also analysed the external flow outside the diffusion region (Fig. 37a) and suggested that most of the energy conversion takes place at four slow-mode MHD shock waves; indeed, $\frac{2}{5}$ of the inflowing magnetic energy is converted to heat and $\frac{3}{5}$ to kinetic energy. Petschek's maximum reconnection rate is typically a tenth or a hundredth of the Alfvén speed.

At the inflow to the diffusion region, values such as v_i and B_i are denoted by a subscript i and their relationship to external values (such as v_e and B_e) at large distances L_e can be determined. Reconnection models then depend on the *external* reconnection rate $(M_e = v_e/v_{Ae})$ and the *external* magnetic Reynolds number $(R_{me} = L_e v_{Ae}/\eta)$. *Fast reconnection* here refers to reconnection whose rate (M_e) is much larger than the Sweet–Parker value $(1/\sqrt{R_{me}})$.

The external region around the diffusion region is then analysed in order to determine how M_i depends on M_e. First of all, conservation of magnetic flux for a steady state $(v_i B_i = v_e B_e)$ may be written in dimensionless terms as

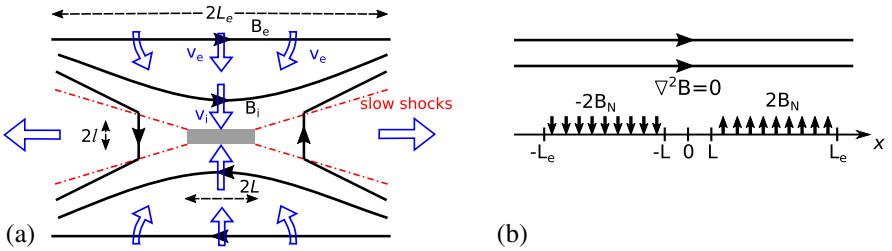

Fig. 37 **a** For any fast reconnection regime, including Petschek's mechanism: the magnetic field (B_e) at large distances L_e is brought in by a flow v_e towards a diffusion region (shaded) of dimensions $2l$ and $2L$, where the inflow field and flow are B_i and v_i, respectively. The plasma is heated and accelerated by four shock waves (red) and then expelled into two regions to left and right. **b** Notation for the analysis of the upper inflow region

$$\frac{M_i}{M_e} = \frac{B_e^2}{B_i^2}. \tag{68}$$

Also, the *Sweet–Parker relations* (63) and (64) determine the dimensions of the diffusion region in dimensionless terms as

$$\frac{L}{L_e} = \frac{1}{R_{me}} \frac{1}{{M_e}^{1/2}} \frac{1}{{M_i}^{3/2}}, \qquad \text{and} \qquad \frac{l}{L_e} = \frac{1}{R_{me}} \frac{1}{{M_e}^{1/2}} \frac{1}{{M_i}^{1/2}}. \tag{69}$$

Thus, after a model of the external region has determined B_i/B_e, Eq. (68) gives M_i/M_e while the diffusion region dimensions follow from Eq. (69) in terms of M_e and R_{me} alone. We first apply this approach to Petschek's model of the external region (Sect. 7.2.1), and then generalise it to a larger family of models known as *Almost-Uniform* reconnection (Sect. 7.3).

7.2.1 Petschek's model: almost-uniform, potential reconnection

In this context, the terms "potential", "nonpotential", "uniform" and "nonuniform" denote the magnetic field behaviour in the inflow region upstream of the diffusion region. Petschek's model is "almost-uniform" because the field in the inflow region is a weakly curved perturbation to a uniform field (B_e), and it is "potential" because there is no current in the inflow region. It possesses four slow-mode shock waves that stand in the flow and accelerate plasma to the Alfvén speed (v_A) parallel to the shock front (Fig. 37a). In the upper inflow region, the upstream plasma is moving downwards at the same speed (v_s) as the shock is trying to propagate upwards, namely, $v_s = B_N/\sqrt{(\mu\rho)}$, where B_N is the normal field component, and thus a steady state is maintained.

The magnetic field decreases from a uniform value (B_e) at large distances to B_i at the inflow to the diffusion region, while the flow speed increases from v_e to v_i. The shocks provide a normal field component (B_N) which causes a small distortion in the inflow field from the uniform value (B_e) at large distances. The field is therefore the sum of a uniform horizontal field $(B_e\hat{\mathbf{x}})$ and the field obtained by solving Laplace's equation in the upper half plane with a normal component (B_N) imposed along the shock waves and vanishing at the diffusion region. To lowest order, the shock inclination is neglected, apart from providing $B_y = 2B_N$ on the x-axis between L and L_e and $-2B_N$ between $-L_e$ and $-L$ (Fig. 37b). The resulting solution of Laplace's equation gives a field at the diffusion-region inflow of

$$B_i = B_e - \frac{4B_N}{\pi} \log \frac{L_e}{L}, \tag{70}$$

or, after writing $B_N/\sqrt{\mu\rho} = v_e$ from the shock relations,

$$B_i = B_e \left(1 - \frac{4M_e}{\pi} \log \frac{L_e}{L} \right). \tag{71}$$

Petschek found that the diffusion region size decreases and the shock angle increases as the reconnection rate (M_e) increases. He suggested that the mechanism

chokes itself off when M_e is too large, and, by putting $B_i = \frac{1}{2}B_e$, he estimated a *maximum* reconnection rate (M_e^*) of

$$M_e^* \approx \frac{\pi}{8 \log R_{me}}, \tag{72}$$

which in practice is much faster than Sweet–Parker and lies between 0.1 and 0.01.

7.2.2 Is fast Petschek reconnection possible with near-uniform resistivity?

When a spatially nonuniform resistivity is employed that is enhanced around the X-point, then numerical MHD simulations can produce Petschek and other fast regimes of reconnection. However, they do not produce a Petschek configuration when the resistivity is spatially uniform (Scholer 1989; Biskamp 1986; Yan et al. 1992). This produced some doubts as to the validity of Petschek reconnection (Biskamp 1993; Kulsrud 2001), but these have now been dispelled for three reasons:

(i) In analytical treatments of Petschek's mechanism, it is of course impossible to match the diffusion region and external region mathematically, since this is a highly complex fully two-dimensional nonlinear set of resistive MHD partial differential equations. But it is possible to match the resistive internal region and ideal external region using average properties of the diffusion region (Soward and Priest 1977; Priest and Forbes 1986).

(ii) In many examples of reconnection in the solar atmosphere, the physically relevant case is that in which the diffusion region may well have an enhanced resistivity due to for example current-induced microinstabilities, although this does need to be established by a full analysis (Sect. 9.3).

(iii) Recent carefully designed numerical experiments (Baty et al. 2006, 2009b, a) have shown that it is possible to set up and maintain a Petschek-like solution when a quasi-uniform resistivity is adopted, as summarised below. These suggest that a truly uniform resistivity is likely to be marginally stable and disrupted in practice by, for example, secondary tearing.

First of all, Baty et al. (2006) developed a helpful procedure for setting up a genuine Petschek solution with enhanced resistivity by overspecifying the boundary conditions, as follows. The initial state of their simulations is a one-dimensional current sheet with magnetic field

$$\mathbf{B} = B_0 \tanh(x/a)\ \hat{\mathbf{y}},$$

together with density and pressure profiles in static isothermal equilibrium. The usual time-dependent resistive MHD equations are solved in the first quadrant $0 \leqslant x \leqslant L_x$, $0 \leqslant y \leqslant L_y$, with symmetry conditions along $x = 0$ and $y = 0$. Each simulation has a resistivity profile

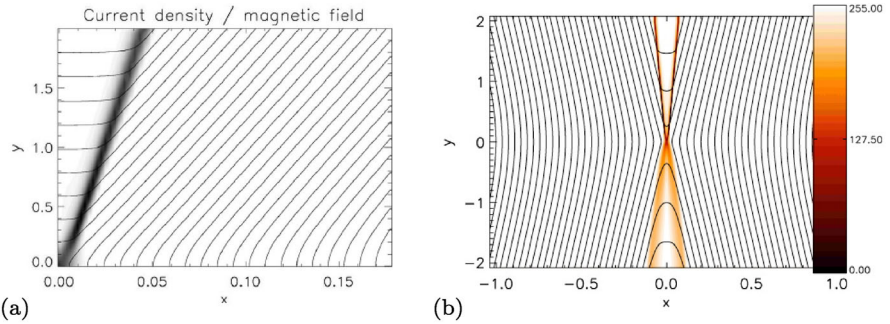

Fig. 38 **a** The magnetic field and current density structures for a numerical simulation of Petschek reconnection. Image reproduced with permission from Baty et al. (2006), copyright by AIP. **b** Magnetic field and current density structures for the final steady state with an asymmetric resistivity having a uniform resistivity of $\eta_0 = 10^{-3}$ in the lower half-plane. Image reproduced with permission from Baty et al. (2009b), copyright by AIP

$$\eta(x) = (\eta_0 - \eta_1)\exp[-(x/l_x)^2 - (y/l_y)^2] + \eta_1. \tag{73}$$

Petschek reconnection is a particular steady-state reconnection solution (Priest and Forbes 1986; Forbes and Priest 1987; Forbes 2001). It represents an undriven case in which the characteristics propagate information away from the X-point rather than towards it, and so it cannot easily be obtained by driving a flow with external forcing, since that is much more likely in practice to lead to one of the other reconnection regimes such as flux pileup (Priest and Forbes 1986). On the other hand, using a locally enhanced resistivity with free inflow and outflow conditions can produce a Petschek state (Scholer 1989).

What Baty et al. (2006) did was to use a much simpler procedure, namely, to overspecify the system by using fixed boundary conditions at the inflow boundary $x = L_x$ by imposing ρ, v_x, v_y, B_y and total energy. Free boundary conditions are adopted at the outflow boundary $y = L_y$. Then the system chooses its own inflow velocity (v_e) (and therefore reconnection rate M_e) that is different from the value $v_x = v_e^*$ being imposed. In a narrow boundary layer near $x = L_x$ the velocity changes from v_e^* to v_e. The resulting magnetic field (Fig. 38a) has all the features of a Petschek solution. Different solutions may be obtained by varying the value of l_y and they agree well with the analytical solutions of Priest and Forbes (1986) for $M_e(M_i)$.

Baty et al. (2006) considered the effect of varying the parameter η_1 (for fixed η_0). They concluded that a quasi-uniform resistivity profile with an extremely small negative gradient that dominates the inevitable numerical contribution near the X-point can produce a stable Petschek solution and that a truly uniform profile is probably marginally stable. Petschek's model and other fast reconnection regimes are therefore valid when the resistivity is enhanced or close to uniform. Indeed, one ripple of a resistivity fluctuation of small amplitude is sufficient to seed the Petschek mode.

Later, Baty et al. (2009b) carried out new numerical experiments using the same setup as before but over a domain centred at the origin without symmetry conditions on the axes. A uniform resistivity was adopted in the lower half-plane ($y \leqslant 0$) together with the resistivity profile from Eq. (73) in the upper half-plane ($y \geqslant 0$). The result is to produce a Petschek solution in the whole domain even though the resistivity is uniform in the lower half-plane and slightly nonuniform in the upper half-plane, as shown in Fig. 38(b) for $\eta_0 = 10^{-3}$ and $\eta_1 = 3 \times 10^{-5}$. Thus, Petschek reconnection with uniform resistivity in a half-plane is driven and maintained by Petschek reconnection with nonuniform resistivity in the other half-plane. Figure 38b presents the final steady state, in which the shocks in the lower half-plane are thicker due to the higher resistivity there. In this state, the inflow profiles lie between those associated with the large and small resistivities, as does the current density profile, which possesses a maximum amplitude that is shifted from the origin to a location in the upper half-plane. Furthermore, the X-point and stagnation point no longer coincide since the pressure gradient no longer vanishes at the X-point.

Subsequently, Baty et al. (2009a) were able to produce for the first time a fast Petschek solution with uniform resistivity in the whole domain. It was achieved by adopting a nonuniform viscosity profile and exhibited all the expected features of a classical Petschek solution, with two pairs of standing slow-mode shock waves attached to a central diffusion region and the inflowing plasma representing a weak fast-mode expansion. The diffusion region has a two-scale structure with an inner resistive region surrounded by a visco-resistive region.

7.2.3 Non-steady Petschek model

Semenov et al. (1983) and Heyn (1996) set up time-dependent solutions of Petschek type initiated by a localised resistivity increase in a pre-existing current sheet (Fig. 39a). Fast and slow magnetoacoustic waves are launched into the medium, and, in the incompressible case, the fast-mode waves propagate outwards instantaneously and set up an inflow towards the X-point. Unlike steady Petschek reconnection, the inflow is not uniform to lowest order but decreases with distance

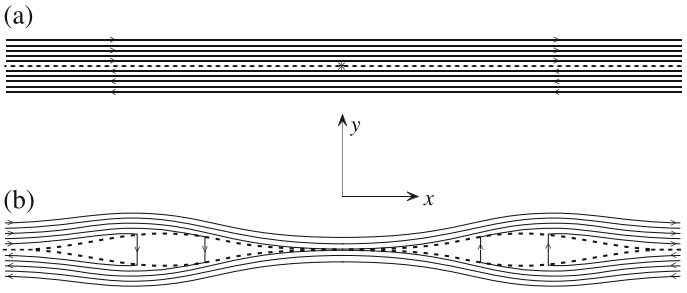

Fig. 39 Semenov's time-dependent model of Petschek-type reconnection with **a** initial oppositely directed magnetic field lines (solid) of a current sheet and **b** the evolution of the magnetic field and shocks (dashed). Image reproduced with permission from Priest and Forbes (2000), copyright by CUP

and vanishes at infinity. After reconnection stops, there is a switch-off phase with its effect propagating outwards, which is absent from steady-state solutions.

Near the X-line the inflow is super-slow-magnetosonic, and so curved slow-mode shock pairs form and enclose the rear of a tear-drop-shaped outflow (Fig. 39b). The front of this region propagates along the x-axis at the ambient Alfvén speed v_{Ae}, and so the external scale-length ($L_e = v_{Ae}t$) increases linearly with time, while near the origin a steady-state Petschek solution is set up.

The MHD equations in the inflow region are linearised about the initial state using a small parameter $\epsilon(t) = E^*(t)/(v_{Ae}B_e) \ll 1$, where $E^*(t)$ is the electric field at the X-line and B_e is the ambient field. The inflow is current-free to first order in $\epsilon(t)$, as in steady-state Petschek theory. The flux function $A(x, y, t)$ is to first order a solution of Laplace's equation ($\nabla^2 A = 0$), and so the general solution in the inflow region is $B_x = B_e + \partial A_1/\partial y, \quad B_y = -\partial A_1/\partial x$, where

$$A_1 = \frac{y}{2\pi}\int_{-\infty}^{\infty} \frac{A_1(x', 0, t)}{(x - x')^2 + y^2} dx'.$$

Here the function $A_1(x', 0, t')$ is determined by the slow-mode jump conditions to be

$$A_1(x', 0, t') = B_0|x'|g(|x'| - v_{Ae}t') - B_0 \int_0^{|x'|} g(\xi - v_{Ae}t')d\xi,$$

where $g(x - v_{Ae}t) = \epsilon(t - x/v_{Ae}) = -E^*(t - x/v_{Ae})/(B_0 v_{Ae})$ is the normalised reconnection rate (ϵ), which depends on the time-variation of the electric field at the X-line.

As in the steady Petschek analysis, the Sweet–Parker relations are invoked to find the maximum rate of reconnection, which, when η is held constant after an initial increase, becomes

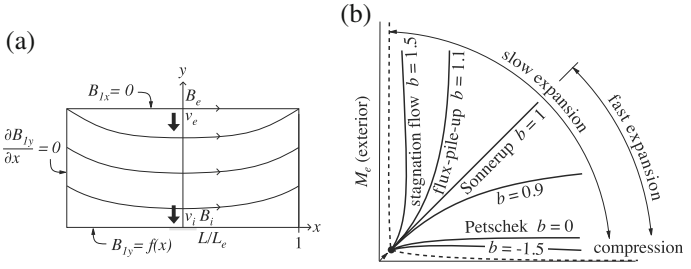

Fig. 40 Notation for **a** the ideal inflow region of Almost-Uniform Reconnection, where subscripts e and i refer to (external) values at $(0, L_e)$ and at the inflow to the diffusion region (shaded), respectively. **b** Reconnection rate ($M_e = v_e/v_{Ae}$) as a function of inflow Alfvén Mach number ($M_i = v_i/v_{Ai}$) for various values of the parameter b. Image reproduced with permission from Priest and Forbes (2000), copyright by CUP

$$\epsilon(t) = \frac{\pi}{4\ln[\epsilon^2(t) R_{me}(t)]} \approx \frac{\pi}{4\ln R_{me}(t)},$$

where $R_{me}(t) = v_{Ae} L_e(t)/\eta_{ave} = (v_{Ae}^2/\eta_{ave})t$ and η_{ave} is the average diffusivity in the diffusion region. Furthermore, the diffusion region dimensions

$$L = \frac{L_e(t)}{R_{me}(t)\,\epsilon^2(t)} = \frac{\eta_{ave}}{v_{Ae}} \left[\frac{4\,\ln(v_{Ae}^2 t/\eta)}{\pi}\right]^2$$

$$l = L_e(t)\epsilon(t) = \frac{\eta_{ave}}{v_{Ae}} \frac{4\,\ln(v_{Ae}^2 t/\eta)}{\pi}$$

grow logarithmically in time.

7.3 Other families of fast 2D reconnection

The form, value and number of the boundary conditions is of crucial importance when solving partial differential equations, since often much physics is incorporated in them. Petschek's mechanism, which is almost-uniform and potential, has been generalised in two distinct ways by adopting different boundary conditions to give regimes of *Almost-Uniform Reconnection*, which is almost-uniform but nonpotential, and *Nonuniform Reconnection*, as reviewed in Priest and Forbes (2000).

Spontaneous reconnection that is initiated by some localised instability (such as the tearing mode) and is not influenced by distant magnetic fields requires free boundary conditions and tends to produce *Potential Reconnection*, which can be either Almost-uniform or Non-uniform, depending on the initial state. However, in contrast, *Driven Reconnection* depends on the nature of the driving and tends to give rise to Non-potential Reconnection with waves of current stemming from the driven boundaries.

Numerical experiments have confirmed that fast reconnection can indeed be produced, provided a locally enhanced magnetic diffusivity is present in the diffusion region, due to current-induced micro-instabilities (Priest and Forbes 2000; Priest 2014). Thus, fast reconnection is a prime candidate for rapid release of magnetic energy in the solar atmosphere. Collisionless and impulsive bursty reconnection is summarised in Sect. 9.

The inflow region in Petschek's mechanism has the character of a fast-mode expansion, in which the pressure and field strength decrease and the flow converges as the magnetic field approaches the diffusion region. Priest and Forbes (1986) decided to explore different types of inflow, since, unlike Petschek's mechanism, some numerical reconnection experiments showed diverging flows and large pressure gradients. They solve the steady, two-dimensional, ideal, incompressible MHD equations to find the relation between the external and inflow Alfvén Mach numbers ($M_e = v_e/v_{Ae}$ and $M_i = v_i/v_{Ai}$) at the top and bottom of the box in Fig. 40a, i.e., the global and local reconnection rates. Solutions are sought in powers of the global reconnection rate ($M_e \ll 1$) that are a small perturbation to a uniform field ($\mathbf{B}_e = B_e\,\hat{\mathbf{x}}$), namely, $\mathbf{B} = \mathbf{B}_e + M_e\,\mathbf{B}_1 + \ldots$, $\mathbf{v} = M_e\,\mathbf{v}_1 + \ldots$, where $(B_{1x}, B_{1y}) = (\partial A_1/\partial y, -\partial A_1/\partial x)$.

After calculating B_i/B_e and substituting into Eq. (68) in place of Petschek's original expression (71), the graphs of M_e against M_i confirm that there is indeed a maximum reconnection rate (M_e^*), as Petschek had suggested (Fig. 40b).

To lowest order in M_e, the equation of motion becomes $\nabla^2 A_1 = -(\mu/B_e)\, dp_1/dy$, with a family of solutions having a rich diversity of properties

$$A_1 = -\sum_0^\infty \frac{a_n}{(n+\frac{1}{2})\pi}\left\{b - \cos\left[(n+\tfrac{1}{2})\pi\frac{x}{L}\right]\right\}\cosh\left[(n+\tfrac{1}{2})\pi\left(1-\frac{y}{L}\right)\right],$$

which depend on a parameter b.

The reconnection rate (M_e) as a function of M_i and b for a given R_{me} is plotted in Fig. 40b. The type and rate of reconnection depend on the parameter b and therefore the inflow boundary conditions, since the horizontal flow at $(x, y) = (L_e, L_e)$ is proportional to $(b - 2/\pi)$. When $b = 0$, Petschek's solution is recovered (Fig. 41a). Although it is one particular member of a much wider class, it is special in the sense that it tends to occur for spontaneous rather than driven reconnection, since it is the only regime for which the fast mode characteristics are propagating away from the diffusion region. After calculating B_i/B_e and substituting into Eq. (68) in place of Petschek's original expression (71), the graphs of M_e against M_i confirm that there is indeed a maximum reconnection rate (M_e^*), as Petschek had suggested.

Other values of b represent reconnection that is driven in various ways. When $b<0$, near the y-axis the flow converges and so compresses the plasma by a slow-mode compression. When $b > 1$, the flow diverges and so expands the plasma by a slow-mode expansion; this type is known as the *flux pile-up regime*, since the field strength increases as the diffusion region is approached (Fig. 41b). When $0<b<1$ a hybrid family of slow- and fast-mode expansions results. The central current sheet is much longer for the flux pile-up regime than the Petschek regime.

When the diffusion region becomes too long, it may become unstable to the secondary tearing or plasmoid instability (Sects. 8, 9.2) and a new regime of *impulsive bursty reconnection* results (Biskamp 1986; Priest 1986; Lee and Fu 1986b; Loureiro et al. 2007; Bhattacharjee et al. 2009). The almost-uniform theory has been compared with a variety of numerical experiments (Forbes and Priest

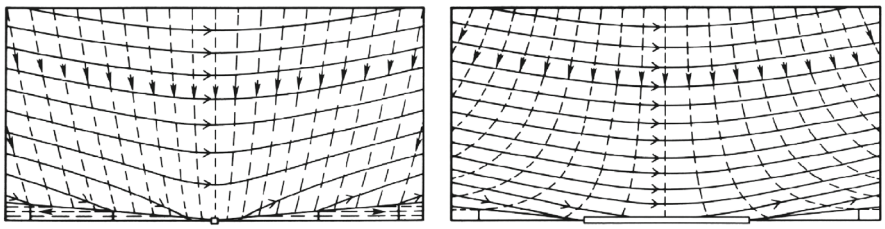

Fig. 41 *Almost-Uniform* reconnection, showing two cases of the magnetic field lines (solid) and streamlines (dashed) in the upper half-plane. Image reproduced with permission from Priest and Forbes (2000), copyright by CUP

1987). It has also been generalised to give nonuniform regimes whose field lines possess a large curvature in the inflow region (Priest and Lee 1990).

8 Unsteady reconnection by resistive instability

Furth et al. (1963) realised that an equilibrium current sheet or sheared magnetic field can go unstable to *resistive modes* by reconnecting in a time-dependent way. The theory for one of them, the tearing mode, is given in Sect. 8.1, followed by extensions (Sect. 8.2), including cylindrical geometry, and nonlinear evolution (Sect. 8.2.1). In addition, when the diffusion region of a steadily reconnecting field becomes too long, it goes unstable to secondary tearing and an *impulsive bursty regime* of reconnection ensues (Priest 1986; Lee and Fu 1986a; Biskamp 1986; Forbes and Priest 1987); such secondary tearing has recently been studied extensively (Sect. 8.3).

Consider a current sheet or a sheared magnetic field, whose one-dimensional field is varying in the x-direction over a scale l with diffusion time $\tau_d = l^2/\eta$ and Alfvén travel-time $\tau_A = l/v_A$ across the field, such that $\tau_d \gg \tau_A$. Furth et al. (1963) discovered that, when diffusion couples to magnetic forces, it can drive three resistive instabilities on time-scales $\tau_d^{(1-\lambda)}\tau_A^{\lambda}$, where $0<\lambda<1$, that are much faster than diffusion alone (on a time τ_d). These instabilities create many small-scale magnetic islands in 2D or flux ropes in 3D, which later diffuse away and which may be important for coronal filamentation, diffusion and heating. The instabilities are called *gravitational modes*, *rippling modes* and *tearing modes*, with growth-rates ω_g, ω_r and ω_{tmi}, respectively.

Gravitational modes are driven by gradients in density $(\rho_0(x))$, whereas rippling modes come from gradients in diffusivity $(\eta(x))$ that may be caused by a temperature gradient (Fig. 42a). Such modes have short wavelengths, of order the transverse scale $(kl \simeq 1)$, and so they create fine-scale filamentary structure in sheets and sheared fields with growth-rates

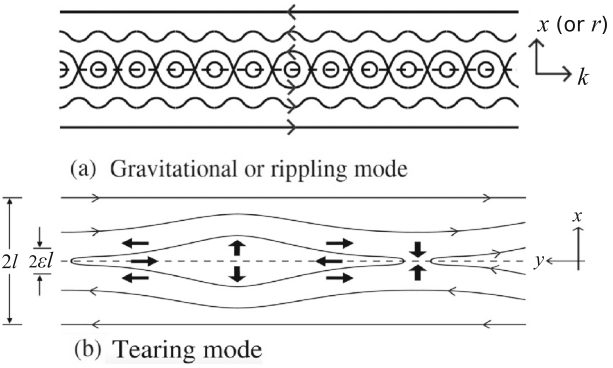

Fig. 42 Magnetic field lines and plasma velocity (solid arrows) for resistive instabilities of **a** small-wavelength and **b** long-wavelength in a one-dimensional magnetic field (i.e., a current sheet or a sheared field), with x (or r in a cylindrical geometry) as the coordinate across the field. Image reproduced with permission from Priest and Forbes (2000), copyright by CUP

$$\omega_g = \left(\frac{(kl)^2\,\tau_A^2}{\tau_d\,\tau_G^4}\right)^{1/3}, \qquad \omega_r = \left[\left(\frac{d\eta_0}{dx}\frac{l}{\eta_0}\right)^4\frac{(kl)^2}{\tau_d^3\tau_A^2}\right]^{1/3},$$

where $\tau_G = (-g/\rho_0\, d\rho_0/dx)^{-1/2}$ is the gravitational time-scale.

The wavelength for tearing mode instability is very long, much greater than the current sheet width ($kl \ll 1$), and so it can be more disruptive for a magnetic field than the other two modes (Fig. 42b). The growth-rate here is $\omega = [\tau_d^3\,\tau_A^2\,(kl)^2]^{-1/5}$ for $(\tau_A/\tau_d)^{1/4} < kl < 1$. The longest wavelength has the fastest growth-rate, namely,

$$\omega_{tmi} = \left(\frac{1}{\tau_d\,\tau_A}\right)^{1/2}.$$

Magnetic diffusion plays an important role only in a narrow region of width $\epsilon l = (kl)^{-3/5}(\tau_A/\tau_d)^{-2/5} l$. A perturbation such as in Fig. 42b, to a one-dimensional sheet with straight field lines, produces forces that make the perturbation grow. The magnetic tension tends to pull out the new loops of field away from the X-points along the sheet, while the magnetic pressure pushes plasma in from above and below towards them. The magnetic tension force due to large-scale curvature of the field lines produces a restoring force that is minimised for long wavelengths. The analysis of this instability is as follows.

8.1 Linear analysis of tearing-mode instability

Resistive instabilities can occur in any sheared magnetic field, not just a neutral current sheet, since the stability analysis is unaffected by the addition of a uniform field normal to the plane of Fig. 42. Sheared fields are, in general, resistively unstable at many thin sheaths throughout a structure. At any location the instabilities have a vector wavenumber ($\mathbf{k}$) perpendicular to the equilibrium field ($\mathbf{B}_0$), so that $\mathbf{k}\cdot\mathbf{B}_0 = 0$ and the crests of the perturbation lie in the plane of Fig. 42. Suppose the equilibrium plasma is at rest and the magnetic field has the form $\mathbf{B}_0 = B_{0y}(x)\,\hat{\mathbf{y}} + B_{0z}(x)\,\hat{\mathbf{z}}$, with field lines that lie in yz-planes but rotate with x.

When the diffusivity (η) is uniform and the plasma incompressible, the MHD induction equation and the curl of the equation of motion become

$$\frac{\partial \mathbf{B}}{\partial t} = \nabla\times(\mathbf{v}\times\mathbf{B}) + \eta\nabla^2\mathbf{B}, \tag{74}$$

$$\rho\frac{d}{dt}(\nabla\times\mathbf{v}) = \nabla\times\left[\frac{(\nabla\times\mathbf{B})\times\mathbf{B}}{\mu}\right]. \tag{75}$$

Small perturbations are made in the form

$$\mathbf{v}_1(x)\exp[i(k_y y + k_z z) + \omega t], \qquad \mathbf{B}_1(x)\exp[i(k_y y + k_z z) + \omega t],$$

while $\nabla\cdot\mathbf{B} = 0$ and $\nabla\cdot\mathbf{v} = 0$ are used to eliminate v_{1y} and B_{1y}. Then, after nondimensionalising the variables $(\bar{\mathbf{B}} = \mathbf{B}/B_0, \bar{\mathbf{v}}_1 = -\mathbf{v}_1 ikl^2/\eta, \bar{k} = kl,$

$\bar{\omega} = \omega l^2/\eta, \bar{x} = x/l$), the x-component of Eq. (74) and z-component of Eq. (75) become

$$\bar{\omega}\bar{B}_{1x} = -\bar{v}_{1x} f + (\bar{B}''_{1x} - \bar{k}^2 \bar{B}_{1x}), \tag{76}$$

$$\omega(\bar{v}''_{1x} - \bar{k}^2 \bar{v}_{1x}) = R_m^2 \bar{k}^2 f\left[-\bar{B}_{1x} f''/f + (\bar{B}''_{1x} - \bar{k}^2 \bar{B}_{1x})\right], \tag{77}$$

where a dash represents a derivative with respect to $\bar{x}$ and $f = \mathbf{k} \cdot \bar{\mathbf{B}}_0/k$.

When the magnetic Reynolds number is large ($R_m = l v_A/\eta = \tau_d/\tau_A \gg 1$), magnetic diffusion is negligible except in thin sheets (of width $2\epsilon l$, say) where $\mathbf{k} \cdot \mathbf{B}_0 = kf = 0$ and reconnection occurs. If the centre of the sheet is located at $x = 0$ and $k_z = 0$, then $\mathbf{k} \cdot \mathbf{B}_0 = 0$ reduces to $B_{0y}(x) = 0$ or $x = 0$. Solutions to Eqns.(76) and (77) are then found in an outer region ($|\bar{x}| > \epsilon$) and an inner region ($|\bar{x}| < \epsilon$) and matched at the boundary ($\bar{x} = \epsilon$) between them.

In the *outer region* diffusion is negligible and Eqns.(76) and (77) reduce to

$$\begin{aligned} \bar{\omega}\bar{B}_{1x} &= -\bar{v}_{1x}\bar{B}_{0y} + (\bar{B}''_{1x} - \bar{k}^2 \bar{B}_{1x}), \\ 0 &= -\bar{B}_{1x}\bar{B}''_{0y}/\bar{B}_{0y} + (\bar{B}''_{1x} - \bar{k}^2 \bar{B}_{1x}), \end{aligned} \tag{78}$$

whose solution for $\bar{B}_{1x}$ depends on the equilibrium field $\bar{B}_{0y}(\bar{x})$. For example, a step-profile ($\bar{B}_{0y} = 1$ for $\bar{x} > 1$, $\bar{x}$ for $|\bar{x}| < 1$, and -1 for $\bar{x} < -1$) leads to

$$\bar{B}_{1x} = \begin{cases} a_1 \sinh \bar{k}\bar{x} + b_1 \cosh \bar{k}\bar{x} & \bar{x} < 1, \\ a_0 \exp(-\bar{k}\bar{x}) & \bar{x} > 1, \end{cases} \tag{79}$$

for $\bar{x} > 0$, where conditions at $\bar{x} = 1$ determine the constants a_1 and b_1 for $\bar{x} > 0$. The corresponding solution for $\bar{x} < 0$ has the same value of b_1 but the opposite sign (same magnitude) of a_1, which leads to a jump in the value of $\bar{B}'_{1x}/\bar{B}_{1x}$, known as *delta prime*, given by $\Delta' = [\bar{B}'_{1x}/\bar{B}_{1x}]_{0-}^{0+} = 2a_1\bar{k}/b_1$.

The *inner region*, in which diffusion is important, has a width of order ϵl, where $\epsilon^4 = \bar{\omega}/(4\bar{k}^2 R_m^2)$. After defining inner variables $X = \bar{x}/\epsilon$, $V_{1x} = \bar{v}_{1x}(4\epsilon/\bar{\omega})$, Eqns.(76) and (77) reduce to

$$\ddot{\bar{B}}_{1x} = \epsilon^2 \bar{k}^2 \bar{B}_{1x} + \epsilon^2 \bar{\omega}(\bar{B}_{1x} + \tfrac{1}{4} V_{1x} X), \tag{80}$$

$$\ddot{V}_{1x} = V_{1x}(\bar{k}^2 \epsilon^2 + \tfrac{1}{4} X^2) + \bar{B}_{1x} X, \tag{81}$$

where dots represent X-derivatives. For long wavelengths $\bar{k} \ll 1$, Eq. (80) implies $\ddot{\bar{B}}_{1x} \sim \epsilon^2\, \bar{\omega}\, \bar{B}_{1x}$, so that $\Delta' = 2(\bar{B}'_{1x}/\bar{B}_{1x})_{x=\epsilon} = 2[\dot{\bar{B}}_{1x}/(\epsilon \bar{B}_{1x})]_{X=1} \sim \epsilon\, \bar{\omega}$.

If $\bar{B}_{1x}$ is assumed to be constant in the inner region (the so-called *constant-psi approximation*), Eq. (80) can be solved analytically and implies $\Delta' = 3\,\epsilon\,\bar{\omega}$ when $\bar{k}\epsilon \ll 1$. Equating the two expressions for Δ' enables the outer and inner regions to be matched (Fig. 43) and gives a growth-rate of $\bar{\omega} = [(8R_m)/(9\bar{k})]^{2/5}$, which lies between the diffusion ($\omega_d = \eta/l^2$) and Alfvén ($\omega_A = v_A/l$) rates. Eqns. (80) and (81) may also be solved when $\bar{k} \ll 1$ without assuming $\bar{B}_{1x}$ to be uniform in the internal region. The resulting dispersion relation has a growth-rate for the fastest-

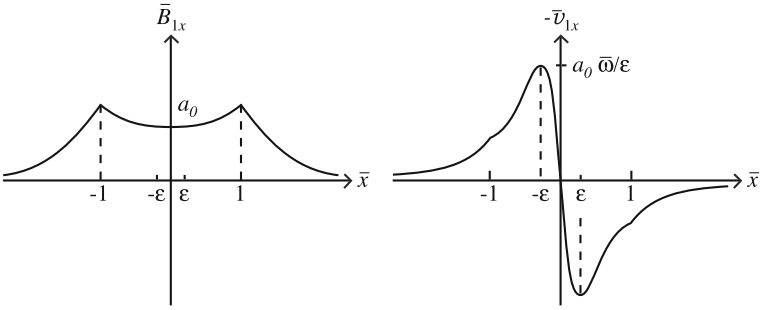

Fig. 43 The tearing mode instability produces the magnetic field ($\bar{B}_{1x}$) and velocity ($\bar{v}_{1x}$) profiles shown, as functions of distance ($\bar{x} = x/l$) normal to a current sheet, where l is the half-width of the sheet and ϵl is the half-width of the inner diffusive layer. Image reproduced with permission from Priest and Forbes (2000), copyright by CUP

growing mode of $\bar{\omega}_{\max} \simeq 0.6\,R_m^{1/2}$ and a corresponding wave-number of $\bar{k}_{\max} \simeq 1.4\,R_m^{-1/4}$. In other words, the growth time ($\tau_m = (\tau_d\,\tau_A)^{1/2}$) is the geometric mean of the diffusion and Alfvén times, so that long narrow islands are formed.

8.2 Extensions to the simple tearing-mode analysis

The above theory for tearing-mode instability has been extended in many different ways, which are reviewed in detail in Priest and Forbes (2000). These include the effects of different initial equilibrium profiles, the addition of a flow or an extra magnetic field component to the initial state, and a viscous force. Also, tearing may be driven faster by fast magnetoacoustic waves or small-scale MHD turbulence.

Ideal and resistive instabilities of a curved magnetic flux tube (*major radius R* and *minor radius* $a \ll R$) with both poloidal $B_p(r)$ and toroidal $B_\phi(r)$ components that vary with distance (r) from the axis, have been studied at length (e.g., Furth et al. 1973; Bateman 1978; Wesson 1997). Resistive modes can allow the magnetic field to slip through the plasma in a narrow layer around a *resonant surface* where $\mathbf{k}\cdot\mathbf{B} = 0$. Radial perturbations of the form $\boldsymbol{\xi} = \boldsymbol{\xi}(r)\exp[i(m\theta - n\phi)]$ are studied and a key parameter is the amount $[\Phi_T(r) = 2\pi R\,B_p/(r\,B_\phi)]$ by which a field line is twisted around the axis as it goes from one end of a flux tube to the other. A related quantity is the *safety factor* $q(r) = 2\pi/\Phi_T$, namely, the number of turns that a field line makes around the major axis during one turn around the minor axis of a torus.

A flux tube has three ideal modes. *m=1 kink modes* arise when the twist is too large and are driven by the current gradient. *Internal interchange modes* are driven by a pressure gradient. A *ballooning mode* is driven by pressure gradients when the large-scale curvature of a torus is included.

When resistivity is included, the kink mode becomes a *tearing mode* when $q_a > m$, with the resonant surface inside the tube and a growth-rate $\tau_d^{-3/5}\tau_A^{-2/5}$. Also, an internal mode with $m > 1$ becomes a *resistive interchange* mode, with a growth-rate of $\tau_d^{-1/3}\tau_A^{-2/3}$, while increased pressure gradients produce *resistive ballooning modes* (e.g., Strauss 1981). The $m = 1$ *internal resistive kink mode* becomes

unstable when $q_0 < 1$. The effect of increasing the twist of a flux tube is therefore to introduce the tearing-mode first and then later the ideal kink mode.

For a coronal loop or solar flare with a twist ($\Phi_T = LB_p/(rB_\phi)$), an important feature is the presence of *line-tying* in the dense photosphere at the feet of the coronal magnetic fields. For the kink instability in a flux tube of uniform twist, the threshold for kink instability is $\Phi_T = 2.5\pi$ (Hood and Priest 1981). Its nonlinear development can make the flux tube highly kinked, with many reconnecting current sheets (see Sect. 14.2). However, the effect of a resistive kink instability with its lower threshold for a coronal loop with line-tying has not yet been explored, as far as we are aware.

8.2.1 Nonlinear evolution of tearing

The nonlinear development of tearing can proceed in different ways, depending on the magnetic Reynolds number R_m, and the form of the equilibrium and boundary conditions. It may just saturate nonlinearly or, especially in the solar atmosphere, it may develop rapidly, as detailed in Priest and Forbes (2000). We just give a brief summary here.

One possible pathway is for the instability at constant-psi to saturate nonlinearly (Rutherford 1973) due to inwards diffusion from the external region to produce wider magnetic islands and to slow the rate of energy release, eventually saturating at an island width of order $\Delta_1'(0)l^2$ (White et al. 1977). Numerical confirmation for $m = 2$ has been presented (Park et al. 1984). However, $m = 1$ tearing is very different, since ψ is no longer constant in the island. A heuristic argument by Kadomtsev (1975) suggested that reconnection continues to grow until the current density flattens off inside the $q = 1$ surface, which was confirmed in a numerical study by Schnack and Killeen (1979) (Fig. 44). A large magnetic island grows rapidly in the nonlinear phase and then slow reconnection eats it away and leads to a new set of nested surfaces with one O-point.

Another pathway is nonlinear *mode coupling* of different tearing modes (Waddell et al. 1976; Diamond et al. 1984), which can produce high-m turbulence that may extend across a significant fraction of the minor radius.

A third pathway is for a chain of magnetic islands to undergo an ideal *coalescence instability* (Finn and Kaw 1977; Longcope and Strauss 1993). The way in which nonlinear coalescence depends on island amplitude (ϵ) and R_m has been

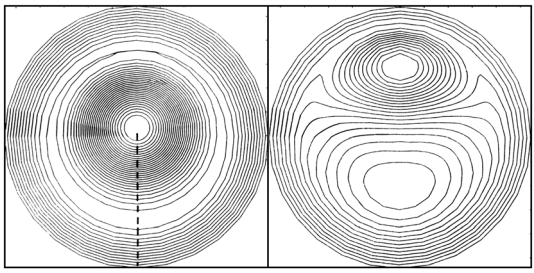

Fig. 44 Magnetic flux surfaces during the linear ($t = 10\tau_A$) and nonlinear ($t = 60\tau_A$) phases of $m = 1$ resistive kink instability. Image reproduced with permission from Priest and Forbes (2000), copyright by CUP, after Schnack and Killeen (1979)

studied by Pritchett and Wu (1979) and Biskamp (1982). In a numerical investigation of coalescence, Bhattacharjee et al. (1983) found that the islands first approach and form a current sheet, at which reconnection takes place, with the instability saturating after typically 30 τ_A and leaving a single island oscillating in response to its dynamic evolution.

A fourth pathway, especially at the extremely large values of R_m expected in the solar atmosphere, is for a current sheet to grow so long that it goes unstable to secondary tearing and enters a regime of *impulsive bursty reconnection*, as described below in Sect. 8.3.

In a solar current sheet with a large R_m that is line-tied at one end to the photosphere, tearing may develop at the neutral point closest to the surface, which may well develop fast nonlinear Petschek reconnection and subsequently possibly undergo secondary tearing and coalescence.

8.3 Fast impulsive bursty reconnection via the plasmoid instability

Reconnection in practice is not steady but is "impulsive and bursty", with reconnection rapidly switching on and off or changing between fast and slow in a quasi-periodic or random manner, as suggested by Priest (1986) and analysed by Biskamp (1986); Lee and Fu (1986b); Loureiro et al. (2007); Bhattacharjee et al. (2009). This may happen due to several scenarios, the first of which is the switching on or off of a turbulent magnetic diffusivity (η_{turb}) as the current density exceeds or falls below the critical current (j_{crit}) for the onset of microinstabilities. Other possibilities are that reconnection may switch on and off near a metastable state, as seen in some numerical experiments (Baty et al. 2009a), or that the nonlinear development of a resistive instability may lead to the formation, fragmentation and coalescence of magnetic islands. Indeed, in recent years there has been a resurgence of interest in this latter possibility, which we review in the remainder of this section.

In astrophysical plasmas, the extreme values of R_m mean that monolithic current layers provide very slow reconnection rates, at odds with the rapid energy release observed during, for example, solar flares. As described in Sect. 8.1, the tendency for such layers to fragment into a 'chain' of magnetic islands or plasmoids was established by Furth et al. (1963), although the growth-rate of the instability was initially thought to be too slow to explain fast reconnection onset.

8.3.1 Plasmoid instability in 2D planar current sheets

Building on earlier work by Bulanov et al. (1979), Biskamp (1986) suggested that a Sweet–Parker current sheet may be unstable for aspect ratios $L/l > 100$ (see also the discussion of Forbes and Priest 1987, and references therein). Our understanding of the importance of tearing for the onset of fast reconnection was then revolutionised by the discovery of what is now known as the "plasmoid instability", starting with the work of Loureiro et al. (2007) (see also Tajima and Shibata 1997) who made a stability analysis of a finite-length, Sweet–Parker current sheet (i.e., a current sheet with aspect ratio $l/L \sim S^{-1/2}$, where $S = Lv_A/\eta$ is the Lundquist

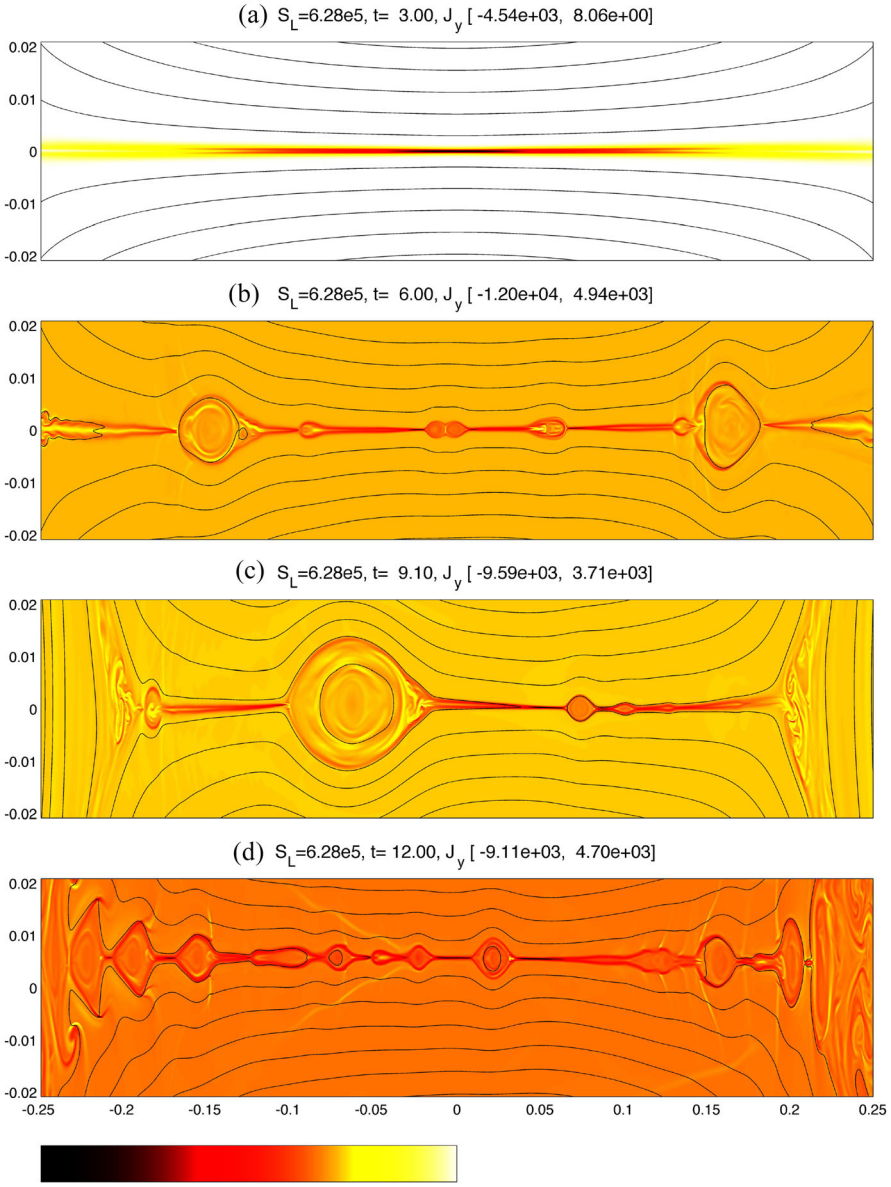

Fig. 45 Time evolution of 2D plasmoid instability simulations, showing the component of the current density out of the 2D plane (colour scale) and magnetic field lines (black), for a Lundquist number 6.28×10^5. Image reproduced with permission from Bhattacharjee et al. (2009), copyright by AIP

number; see Sect. 7.1). They solved the reduced MHD equations, matching the solutions in an "outer" ideal region and an "inner" region comprising the current layer. They discovered that the instability growth-rate (γ) for the fastest growing mode (namely, $\gamma_{\max}\tau_A \sim S^{1/4}$) *increases* with increasing S, where $\tau_A = L/v_A$ is the

Alfvén time-scale. The corresponding wavenumber k of the fastest growing mode scales as $k_{\max}L \sim S^{3/8}$.

Following these initial analyses, the theory has been extended to include the effects of plasma viscosity (Loureiro et al. 2013; Comisso et al. 2017), as well as three-dimensional effects (Baalrud et al. 2012). The scalings have been subsequently confirmed in various computational simulations, primarily beginning from 1D initial states such as Harris sheet configurations (e.g., Bhattacharjee et al. 2009; Samtaney et al. 2009; Loureiro et al. 2013). The critical current sheet aspect ratio for onset of tearing has been confirmed in simulations to be of order 100 (e.g., Loureiro et al. 2005; Samtaney et al. 2009). The fact that the growth-rate scales positively with the Lundquist number presents an issue in the limit $S \to \infty$, which has been considered by Pucci and Velli (2013) and Uzdensky and Loureiro (2016), who made slightly different arguments regarding saturation of the growth-rate for large S. An analogous instability with similar onset threshold values, for both S and the current sheet aspect ratio, was discovered for a current sheet formed by the collapse of a 3D null point by Wyper and Pontin (2014b).

The linear phase of the instability is characterised by the formation of plasmoids in the current layer. Due to the large growth-rate at large S, simulations rapidly access the nonlinear phase. It is in this nonlinear phase, when the plasmoids grow to sizes larger than the current sheet width, that the reconnection process becomes substantially affected by the plasmoid instability dynamics. Here the evolution becomes highly dynamic and "bursty", involving, for example, the nonlinear growth of plasmoids, their ejection from the current layer, coalescence of plasmoids, and associated "secondary tearing" of the current sheets that mediate this coalescence (see Fig. 45). This leads to a "fractal-like" structure for current sheets on a hierarchy of length scales (Shibata and Tanuma 2001).

While the reconnection rate in the nonlinear phase is found to fluctuate greatly in time, when these fluctuations are averaged, the overall reconnection rate (determined in 2D by the electric field at the "dominant" X-point) becomes nearly independent of the resistivity (e.g., Bhattacharjee et al. 2009; Loureiro et al. 2012). It is argued that this is because the reconnection rate can be approximated by applying the Sweet–Parker model to the smallest current sheets in the hierarchy, for which the reconnection rate scales as $\sqrt{S_c}$, where S_c is the critical Lundquist number, and is thus independent of the global Lundquist number (Uzdensky et al. 2010).

The statistical properties of the hierarchy of plasmoids that forms after the nonlinear stage has fully developed is important for describing the long-time dynamics. As such, a number of studies have addressed this plasmoid "spectrum" in some detail. Uzdensky et al. (2010) considered a typical plasmoid in some arbitrary level of the current sheet hierarchy, formed away from the current sheet centre, and ejected in the outflow while growing in size and flux due to the reconnection process. They showed that the distribution function for plasmoids of flux Ψ should be $f(\Psi) \sim \Psi^{-2}$, while their size (w) distribution should be $f(w) \sim w^{-2}$. In numerical simulations, the picture is found to be a little more complicated, with at least parts of the distribution of plasmoid fluxes and sizes having an exponent closer to -1 than

−2, and physical explanations have been proposed to account for these discrepancies (Huang and Bhattacharjee 2012; Loureiro et al. 2012).

Also predicted by Uzdensky et al. (2010) is the formation of rare "monster plasmoids", which are created when an island begins to grow by chance close to the centre of a current layer; such plasmoids are not entrained in a strong current layer outflow, and so are able to grow to "monster" sizes before being ejected from the current layer to coalesce with plasmoids further up the hierarchy. The formation of such monster plasmoids is confirmed in simulations (Loureiro et al. 2012; Nemati et al. 2017), and it is proposed that they may be associated with large, violent bursts during reconnection events.

8.3.2 Plasmoid instability in more complex geometries and in observations

The above analyses and simulations have focussed solely on the 2D case, while the nonlinear evolution in 3D has been much less explored. In 3D, the range of current sheet configurations that may be susceptible to a plasmoid-type instability is much richer. The simplest way to extend into 3D is to include a field component in the third dimension and to model a fully 3D domain. This was done by Huang and Bhattacharjee (2016) who simulated the coalescence instability in 3D. They observed that, following the initial tearing of the current sheet and formation of plasmoid-like structures, the reconnection layer quickly transitioned to a turbulent behaviour with fewer well-defined plasmoids (in cross-sections) than comparable 2D simulations—see Fig. 46.

This transition to turbulence is also present in the picture developed by Dahlburg and Einaudi (2002); Dahlburg et al. (2005) who considered tearing in a sheared magnetic field (though there are differences in the detailed interpretation). In their simulations, the twisted flux tubes formed by the initial tearing undergo a "secondary instability"—essentially an ideal kinking of those twisted flux tubes—for sufficiently large shear across the current layer, leading subsequently to a turbulent evolution. This secondary instability was proposed as an explanation for the "switch-on" nature of coronal heating events in Parker's braiding picture of coronal heating.

More recently, this has been revisited by Leake et al. (2020) who undertook a set of simulations for different current sheet lengths and magnetic shear angles. They discovered two different regimes of behaviour, distinguished by the relative values of the current sheet length L_s and the wavelength λ_f of the fastest growing parallel mode (in the corresponding infinite system). For $L_s > \lambda_f$, sub-harmonics of the fastest-growing parallel modes are present, and the nonlinear interaction of these sub-harmonics and the subsequent coalescence of 3D plasmoids dominates in the nonlinear phase. By contrast, for $L_s < \lambda_f$, the fastest growing parallel mode has no sub-harmonics, and rapid energy conversion only takes place when the magnetic shear is large, in which case oblique modes grow large enough to interact nonlinearly with the dominant parallel mode. There are discrepancies in the interpretation of the nonlinear behaviour with those of Dahlburg and Einaudi (2002); Dahlburg et al. (2005), and it is clear that further exploration is required.

Moreover, in order to determine the relevance for energy release in coronal current sheets, the stabilising effect of photospheric line-tying must in future be included.

A nonlinear tearing or plasmoid-type instability has also been discovered in a current sheet formed by the collapse of a 3D magnetic null by Wyper and Pontin (2014b, 2014a). The current sheet was formed by shear driving of the spine field lines as shown in the upper panel of Fig. 47. Tearing onset was observed to occur when the current sheet aspect ratio exceeds around 50, and the nonlinear dynamics

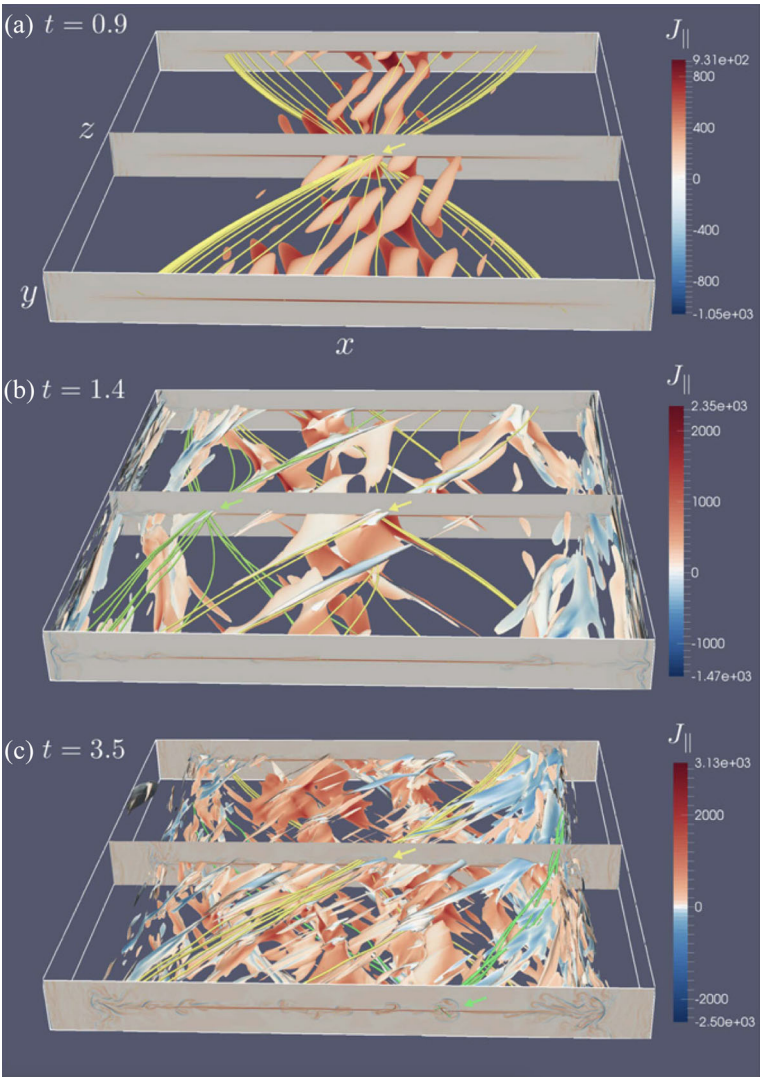

Fig. 46 Current density and magnetic field lines in a 3D MHD simulation of the plasmoid instability during coalescence instability with an initially uniform guide field. Image reproduced with permission from Huang and Bhattacharjee (2016), copyright by AAS

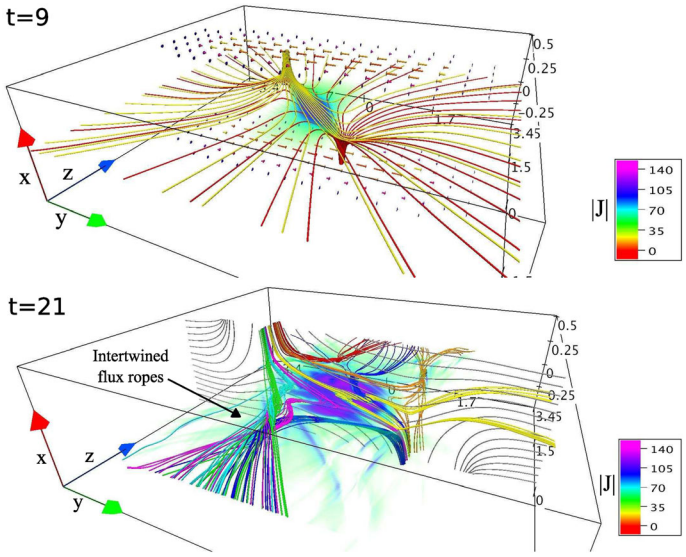

Fig. 47 Current density and magnetic field lines in a 3D MHD simulation of the plasmoid instability when a 3D magnetic null point is subjected to continuous shearing motions on the spine boundaries, which drives *spine-fan reconnection* (see Sect. 10.2.1). Image reproduced with permission from Wyper and Pontin (2014a), copyright by AIP

involves the formation of a plethora of 3D nulls due to multiple bifurcations (see Sect. 2.4) and accompanying twisted flux ropes. By contrast with plasmoids in 2D these flux ropes are not enclosed by magnetic flux surfaces, and field lines

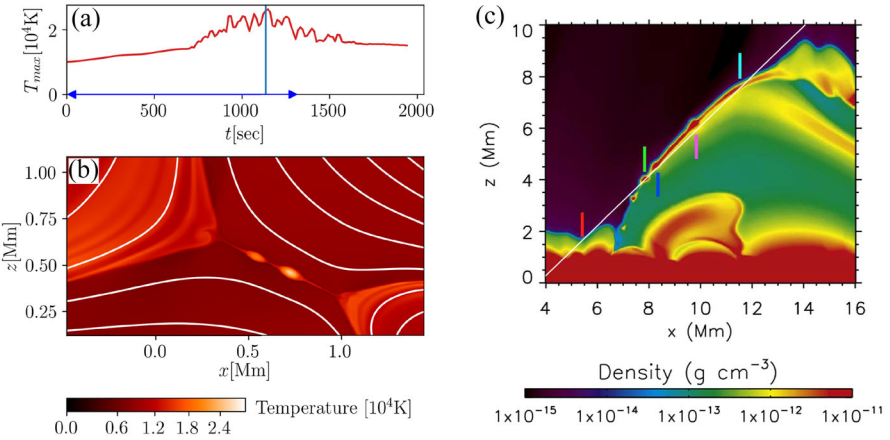

Fig. 48 Plasmoids in simulations of reconnection in the low solar atmosphere. **a**, **b** Temperature in the 2D MHD simulations of reconnection driven by a photospheric flow by Peter et al. (2019). In (**a**) the peak temperature in the reconnection region as a function of time is plotted, illustrating the bursty nature of the reconnection, while in (**b**) the temperature distribution is shown at the time illustrated by the blue vertical line in (**a**), in which two large plasmoids are clearly visible in the current sheet. **c** Density distribution in the 2.5D radiative MHD simulations of Rouppe van der Voort et al. (2017)

intertwine between multiple flux ropes as the nonlinear phase develops (Fig. 47). Since the magnetic shear angle goes from 180° at the null to small values further from the null, a detailed understanding of the dynamics in terms of perturbation modes is a formidable challenge.

Observations and simulations of dynamic events in various layers of the solar atmosphere are providing evidence for the importance of the plasmoid instability for energy release on the Sun. Rouppe van der Voort et al. (2017) present observations of bursty energy release in UV bursts in the chromosphere. These are compared with a reconnection event that was identified in a 2.5D radiative MHD simulation spanning from the upper convection zone to the corona. In the simulation, a localised flux emergence event drives the formation of a (curved) current sheet in the chromosphere, within which a series of plasmoids is formed (Fig. 48c). On the basis of synthesised spectral lines from the simulation the authors suggest diagnostics for plasmoid-mediated reconnection in observations. Peter et al. (2019) have developed a dedicated simulation for understanding UV bursts that begins from a 2D null dome topology, with a shear flow applied on the lower boundary leading to the collapse of the X-point and eventual formation of plasmoids in the current layer (Fig. 48a, b). They have explored different atmospheric stratifications, corresponding to different values of the plasma-β at the reconnection site. It turns out that when $\beta \geq 1$ the reconnection is not efficient, with only small increases in temperature and slow plasma flows being generated. For $\beta \ll 1$ an energetic reconnection process is observed, and the authors extrapolate to predict a maximum peak temperature that can be expected from such a process of around 0.2 MK. Plasmoid instability in the low solar atmosphere has also been modelled by Guo et al. (2020), who compare synthetic emissions with IRIS data, and by Ni et al. (2015); Ni and Lukin (2018), who consider the impact on the plasmoid instability of various effects associated with partial ionisation such as ambipolar diffusion and recombination.

Further observational evidence of bursty, plasmoid-mediated reconnection in small-scale reconnection events on the Sun has been reported by, e.g. Innes et al. (2015), while observed 'blobs' in jet/flare/CME current sheets have also been interpreted as plasmoids (e.g., Lin et al. 2005; Takasao et al. 2011; Kumar et al. 2019). These have been complemented by 3D simulations of jets that exhibit tearing and plasmoids in a current sheet formed about a coronal 3D null point (Moreno-Insertis and Galsgaard 2013; Wyper et al. 2016). 2D and 2.5D models of plasmoids in flare/CME current sheets include those by Bárta et al. (2011), Karpen et al. (2012), Lynch et al. (2016) and Hosteaux et al. (2018). Finally, formation of 3D flux ropes during impulsive, bursty reconnection in a current sheet in the laboratory has been reported at the MRX (Magnetic Reconnection eXperiment) by Dorfman et al. (2013).

To summarise, while there remain aspects of nonlinear MHD tearing that are poorly understood—especially in 3D—it provides a viable route to fast reconnection, and one that is expected to be relevant to energy release in many solar applications (Ji and Daughton 2011). It is also possible that MHD tearing creates a hierarchy of current sheets that eventually accesses kinetic scales, at which point additional physics beyond MHD is required to understand the details of

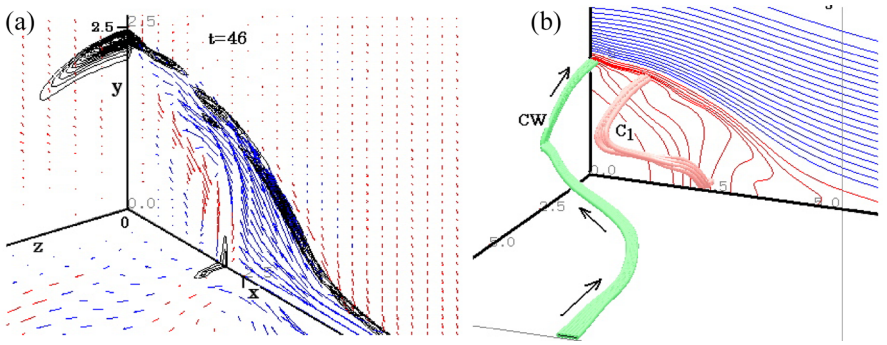

Fig. 49 **a** Plasma flow vectors and ohmic heating in the $x = 0$, $y = 0$ and $z = 0$ planes for fast 3D reconnection in a coronal arcade initiated by a local enhancement of anomalous resistivity. $x = 0$ represents the chromosphere in which the ohmic heating indicates the site of a flare ribbon, while $z = 0$ shows a vertical cut through the coronal arcade. Distances are normalised with respect to the half-width of the initial current sheet and time with respect to the corresponding Alfvén travel time. **b** The corresponding magnetic field lines in the $z = 0$ plane and the two main current channels, including the current wedge (*CW*) that flows to the chromospheric ribbons and a second current channel (C_1) that flows from the fast shock downstream of the reconnection jet. Image reproduced with permission from Ugai (2008), copyright by AIP

reconnection at these smallest scales (Sect. 9). While not the focus of this article, it is notable that fast reconnection mediated by the plasmoid instability has been explored using Hall MHD (Shepherd and Cassak 2010) and full particle-in-cell (e.g., Daughton et al. 2009b) approaches—see Sect. 9.2(ii)(c).

8.4 Response to a resistivity enhancement

Ugai has undertaken many experiments on the fast-reconnection response to a local resistivity enhancement, both in 2D and 3D. These have been performed in geomagnetic tail-like equilibria and in solar coronal arcade equilibria in order to model both geomagnetic substorms and solar flares. In a 2D model, Ugai (1999) allows the resistivity enhancement to depend on temperature. In an initial phase the reconnection grows slowly, but, after plasma and flux have been ejected from near the null point, this is followed by an explosive phase of much faster reconnection due to a positive feedback between the resistivity enhancement and the reconnection flow. The explosive phase sets up fast reconnection at the maximum reconnection rate, with standing slow shocks attached to a localized diffusion region and extending outwards in time. Ugai (2000) extended this analysis to the case in which the fields on both sides of the current sheet are different, finding the growth of an asymmetric plasmoid, predominantly in the region containing the weaker magnetic field. Ugai and Kondoh (2001) consider the effect of resistivity onset threshold (V_{c0}) and plasma beta (β). When V_{c0} is large enough, fast reconnection is set up, but when it is too small the diffusion region lengthens and reconnection becomes less effective. Furthermore, it is only when β is small enough that fast reconnection is set up.

Ugai and Wang (1998) and Ugai et al. (2004) extended the spontaneous fast reconnection model to three dimensions. Symmetry conditions were assumed on the xy, yz and zx planes and free boundary conditions on the other boundaries of the first quadrant. Qualitatively, the results are similar to those in 2D. 3D fast reconnection evolves explosively as a nonlinear instability due to a positive feedback between the anomalous resistivity and the reconnection flow. Slow shocks stand in the flow and ahead of the fast reconnection jet. A large-scale 3D plasmoid swells and propagates in the central current sheet, while a vortex flow is formed near the plasmoid side boundary.

Ugai and Zheng (2005) continued their 3D reconnection study and found that fast reconnection does not occur with classical resistivity, which decreases with temperature like $T^{3/2}$, but it does occur with an anomalous resistivity that increases with current when a threshold is exceeded. Here, resistivity is enhanced in the shock layer which thickens so that secondary tearing is more likely. When the anomalous resistivity increases with the electron-ion drift velocity, fast reconnection evolves rapidly and is sustained steadily. Ugai (2008) applied these ideas to a 3D model of a two-ribbon solar flare, in which the down-flowing fast reconnection jet causes impulsive chromospheric heating by a factor of 30 in two thin layers (or current wedges) near the separatrices, which move apart in time (Fig. 49). This is accompanied by chromospheric evaporation and expanding coronal loops.

9 Fast reconnection in a collisional or collisionless medium

Although this review deals mainly with a resistive collisional plasma, there have been many important discoveries recently concerning fast collisionless reconnection, and so we give here a brief overview of fast reconnection, in both a resistive plasma and a collisionless plasma. Apart from the plasmoid instability, we focus on steady-state reconnection. The chapter begins with some general principles for categorising reconnection (Sect. 9.1), which show that reconnection in two dimensions is much more diverse than often realised, so that general statements about reconnection need to have their domain of validity made clear. Then a summary of the results is presented (Sect. 9.2), mainly for 'almost-uniform' or local reconnection. Finally, the many unanswered questions that remain for two-dimensional reconnection are described (Sect. 9.3). For reviews of this subject, we have found Cassak et al. (2017) especially insightful, but see also Priest and Forbes (2000); Bhattacharjee (2004); Birn and Priest (2007); Daughton et al. (2009a); Yamada et al. (2010); Ji and Daughton (2011); Daughton and Roytershteyn (2012); Priest (2014); Comisso and Bhattacharjee (2016)

The conclusion detailed below is that three scenarios have been proposed for fast reconnection at a hundredth or a tenth of the Alfvén speed (v_A), each of which is likely to occur in the solar atmosphere under different circumstances, namely,

(a) Petschek reconnection when the plasma is collisional and the resistivity enhanced,

(b) Collisionless Hall reconnection when the current sheet width is of order the ion inertial length ($d^{(i)}$),
(c) Impulsive bursty or plasmoid reconnection when the current sheet goes unstable to tearing.

The apparent existence of a universal rate of reconnection of $(0.01-0.1)v_A$ has long been a puzzle, but we suggest that it arises because reconnection is usually dominated by the ideal MHD processes taking place in the region around the central current sheet (called the *diffusion region*) and depends only weakly on the microphysics of the current sheet and its length (Priest et al. 2021).

9.1 Principles for categorising fast reconnection

The following distinctions are important for classifying magnetic reconnection. They involve definitions which are common in a traditional solar MHD context, but differ from some definitions that have been adopted more recently in the kinetic plasma community.

(i) **Local or global reconnection rate**
Most of the plasma behaves in an ideal way, satisfying the ideal equations of MHD, regardless of whether the plasma is resistive or collisionless. In reconnection, one therefore considers an ideal region that surrounds a diffusion region, in which ideal MHD breaks down and the magnetic fields can slip through the plasma. In general, it is important to consider the physics of what is happening in both the ideal region and the diffusion region.
Regardless of whether the reconnection is resistive or collisionless, the first major point to make is that there is a distinction between the *local (or small-scale or microscale) reconnection rate*, namely, the speed v_i with which the plasma carries magnetic flux into the diffusion region, and the *global (or external or large-scale or macroscale) reconnection rate*, namely, the speed v_e with which plasma carries magnetic flux in from large distances towards the diffusion region, as indicated in Fig. 50a (e.g., Cassak et al. 2017). These are normally written in terms of the Alfvén speeds v_{Ai} at the inflow to the diffusion region and v_{Ae} at large distances to give corresponding Alfvén Mach numbers

$$M_i = \frac{v_i}{v_{Ai}} \qquad \text{and} \qquad M_e = \frac{v_e}{v_{Ae}}. \tag{82}$$

In addition, whereas the overall length-scale of the system being considered is L_e, say, the length of the diffusion region is L, which is often much smaller than L_e.

(ii) **Slow or fast reconnection**
Another important distinction is between *slow reconnection* at a rate very much slower than the Alfvén speed ($v_e \ll v_{Ae}$) and *fast reconnection* at an appreciable fraction of the Alfvén speed, say, $0.01 v_{Ae} < v_e < v_{Ae}$. Early in

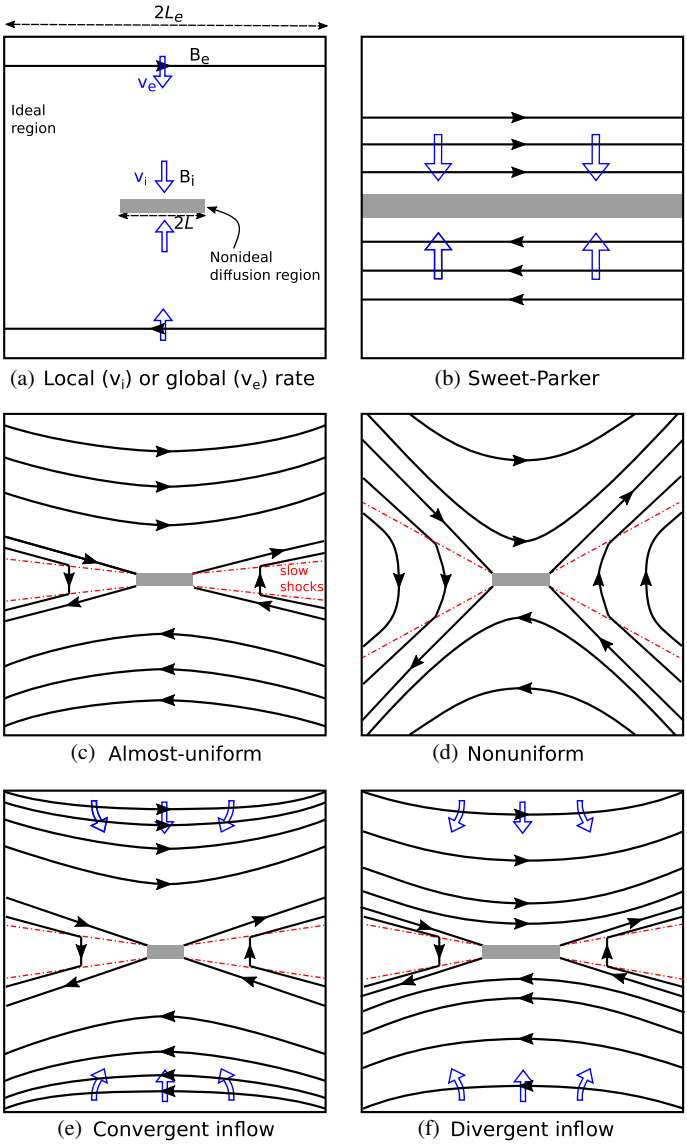

Fig. 50 Different types of reconnection in which a mainly ideal region surrounds a central current sheet or diffusion region (shaded), and separatrices (field lines extending out from the diffusion region) lie upstream of slow-mode shocks (dashed): **a** distinguishing between local (v_i) and global (v_e) rates of reconnection; **b** the Sweet–Parker model. Different initial conditions give **c** almost-uniform reconnection or **d** non-uniform reconnection. Different boundary conditions give **e** convergent inflow with short central current sheets or **f** divergent inflow with longer sheets

the development of the theory, the aim was to find mechanisms for fast reconnection, since they are needed to help explain a solar flare.

If the diffusion region stretches across the whole boundary of length L_e between opposing magnetic fields, and the plasma is resistive and steady state, then Sweet–Parker reconnection occurs (Fig. 50b), with the whole energy release in the diffusion region and a reconnection rate of

$$v_e = \frac{v_{Ae}}{R_{me}^{1/2}} \quad \text{or} \quad M_e = \frac{1}{R_{me}^{1/2}}, \tag{83}$$

where $R_{me} = L_e v_{Ae}/\eta$ is the *magnetic Reynolds number* based on the external or global length-scale (L_e) and the external or global Alfvén speed ($v_{Ae} = B_e/\sqrt{\mu\rho_e}$) in terms of the external magnetic field (B_e) and plasma density (ρ_e). It is also called the *Lundquist number*, designated by the symbol S, which is sometimes used instead of the local magnetic Reynolds number ($R_{mi} = L v_{Ai}/\eta$). Note that there are various modifications to this simple Sweet–Parker rate due to compressibility and different downstream conditions (Sect. 7.1). Since typical values of R_{me} lie in the range $10^6 - 10^{12}$, Sweet–Parker reconnection is slow. The width (l) of the current sheet for Sweet–Parker reconnection is

$$l = \frac{L_e}{R_{me}^{1/2}}. \tag{84}$$

Other regimes of reconnection illustrated in Fig. 50 possess an ideal region that surrounds the central current sheet. In the particular case when the central sheet is resistive, i.e., it is a Sweet–Parker sheet, the local reconnection rate at the sheet is given by Eq. (83) but with L_e replaced by L and external values by local inflow values, so that

$$v_i = \frac{v_{Ai}}{R_{mi}^{1/2}} \quad \text{or} \quad M_i = \frac{1}{R_{mi}^{1/2}} \quad \text{and} \quad l \equiv d_{SP} = \frac{L}{R_{mi}^{1/2}}, \tag{85}$$

where $R_{mi} = L v_{Ai}/\eta$.

Some of these other regimes are slow and others fast, but none should be referred to as "Sweet–Parker" reconnection, since, most of the energy release is often at slow-mode shock waves rather than the diffusion region, and also, even if their reconnection rate is proportional to $R_{me}^{-1/2}$, the constant of proportionality may be larger than 1. For these regimes, the values of B_i and L and therefore v_i are no longer imposed, but are determined in a coupled manner by the nature of the ideal MHD solution surrounding the diffusion region. In turn, this solution to the set of MHD partial differential equations depends (usually weakly) on L and also on both the initial and boundary conditions, which affect profoundly the behaviour of the MHD characteristics that carry information to and from

the boundaries (Forbes and Priest 1987). In particular, the solution in the ideal region depends on whether the reconnection is spontaneous or driven, almost-uniform or non-uniform, and whether the inflow at large distances is converging or diverging, as follows.

In the outflow region, it is the magnetic tension that accelerates the plasma to Alfvénic speeds, but it should be noted that this acceleration is focused in the two slow-mode shock waves that bound the outflowing jet and are emitted from the ends of the diffusion region.

(iii) **Spontaneous or driven**

Magnetic reconnection may be either *spontaneous* or *driven* (sometimes called "forced"). "Spontaneous" refers to reconnection that is initiated locally at a null point or in a current sheet or sheared magnetic field (or in 3D at a null point, a separator or a quasi-separator). It may occur due to a resistive instability such as the tearing mode or when conditions for the local onset of reconnection are reached, such as the resistivity suddenly being switched on. One example would be due to tearing in a current sheet that has formed in the preflare phase of an eruptive solar flare below a flux rope that has started to erupt and is stretching out the magnetic flux that arches over the flux rope. Another example would be in the geomagnetic tail during a substorm. In these cases, reconnection is likely to develop into a fast reconnection mode, with reconnection at the fastest allowed rate.

Alternatively, reconnection may be driven by motions of flux at large distances towards, for example, a neutral point or separator. Such motions may be the result of an ideal instability or may be part of the general evolution of a magnetic field. This may be what happens when new flux emerges from below the photosphere and interacts with the overlying coronal field or when opposite photospheric flux fragments move towards each other during flux cancellation and drive chromospheric or coronal heating events. In these cases, reconnection will occur at the rate at which the flux motions are driven—i.e., at any rate up to the maximum allowed one.

(iv) **Almost-uniform or nonuniform**

It is important to note that the magnetic field at large distances from the diffusion region for Petschek's mechanism is not that of an X-point, but rather it is a one-dimensional field, since Petschek theory assumes a small perturbation about a simple current sheet. It is an example of an *almost-uniform* regime of reconnection.

Since we are dealing with solutions of the nonlinear partial differential equations of plasma physics, both the initial and boundary conditions are crucial, as discussed in this and the next subsection. As far as the initial conditions are concerned, the most popular choice is to start with a one-dimensional current sheet having a unidirectional magnetic field,

$\mathbf{B}_0 = B_{0x}(y)\hat{\mathbf{x}}$, say, and current $\mathbf{j} = j_0(y)\hat{\mathbf{z}}$, where $j_0 = -\mu^{-1}dB_{0x}/dy$ from Ampère's law. Then reconnection can be initiated by a small magnetic or plasma perturbation or an enhancement of resistivity. This often leads ultimately to a steady state that is a perturbation to the initial field and tends to a unidirectional field at large distances: it is known as a regime of *almost-uniform reconnection* (e.g., Priest 2014) (Fig. 50c). This is relevant for reconnection below a rising flux rope in a solar flare, provided a non-reconnecting current sheet is formed and stretched out before reconnection is initiated, although this seems unlikely since reconnection may start as soon as the current sheet starts to form. It is also relevant for reconnection in the geomagnetic tail.

By contrast, for so-called *nonuniform reconnection* (e.g., Priest 2014) the magnetic field before the current sheet forms and at large distances from the reconnecting current sheet is that of an X-type null point, behaving like $\mathbf{B}_0 = y\hat{\mathbf{x}} - x\hat{\mathbf{y}}$, say (Fig. 50d). This regime would be relevant in several applications. One would be reconnection at a null point that forms below a rising flux rope in a solar flare without an extended current sheet first forming. Another would be during emerging or cancelling magnetic flux in a chromospheric or coronal heating event. For example, the length (L) of a reconnecting diffusion region together with its inflow velocity (v_i) and magnetic field (B_i) can be calculated in terms of the magnetic fluxes ($\pm F$) and plasma velocity (v_0) with which two opposite-polarity photospheric magnetic fragments approach and cancel in an overlying magnetic field (B_0) (Priest et al. 2018). Both almost-uniform and nonuniform reconnection could be either spontaneous or driven.

(v) **Convergent or divergent driven flow**

Boundary conditions also play an important role (Forbes and Priest 1987). In particular, on the inflow boundary it is found that the orientation of the plasma velocity vector affects the type of reconnection, in particular whether the inflow is converging or diverging and by how much it is doing so. If the inflow is converging, it tends to produce reconnection with smaller diffusion regions (Fig. 50e), whereas, if it is diverging, the diffusion regions tend to be much longer (Fig. 50f).

9.2 Fast reconnection: summary of results

In addition to the strength of the inflow and of the diffusion region, we are dealing with at least a five-parameter analysis, namely, depending on whether the reconnection is: spontaneous or driven; resistive or collisionless; local or global; almost-uniform or nonuniform; and converging or diverging. In addition, there is the question as to whether the system is steady or impulsive and bursty (due to secondary tearing or plasmoid instability) and also whether there is a magnetic field component (a "guide field") out of the plane. Finally, it should be stressed that we are here talking just about 2D reconnection, but 3D reconnection may well give quite different results.

Much of what has been discovered so far concerns only spontaneous almost-uniform reconnection or refers to the local rate of reconnection at an isolated diffusion region, so other regimes in different parts of parameter space await a full treatment.

Apart from the case when the diffusion region occupies the whole of the boundary between opposing fields, such as in Sweet–Parker reconnection, the diffusion region of length L and width l is immersed in an external region in most of which ideal MHD holds. Slow-mode MHD shock waves stand in the flow and are present because they are naturally generated by the presence of an obstacle (the diffusion region) in the flow in exactly the same way that a hydrodynamic shock is generated by a corner when a supersonic fluid flows round it. The shock turns the magnetic field towards the normal to the shock front and accelerates the plasma as magnetic energy is converted to plasma energy and heat. Most of the energy conversion in such reconnection takes place at the slow shocks, and the steady reconnection rate is then the value of v_e, which is imposed from outside for driven reconnection, but is determined by the solution itself for spontaneous reconnection.

Here the width (l) of the diffusion region is determined by the diffusion-region physics and its length (L) by mass continuity. The inflow field (B_i) is determined mainly by the nature of the inflow in the ideal region and weakly by the length (L) of the diffusion region. Thus, the presence of the slow-mode shocks in the otherwise ideal MHD region surrounding the diffusion region is a universal feature, regardless of whether the diffusion region is resistive or collisionless, since ideal MHD holds in both cases. As well as being a feature of early fast MHD reconnection models (Petschek 1964; Priest and Forbes 1986), it has also been observed in many numerical experiments, both MHD (e.g, Ugai and Tsuda 1977; Sato 1979; Biskamp 1986; Scholer 1989; Yan et al. 1992, 1993; Baty et al. 2009b) and large-domain collisionless PIC simulations (e.g., Liu et al. 2012; Innocenti et al. 2015).

(i) **Almost-uniform reconnection: resistive and collisionless**
Suppose the field B_e at large distances in the inflow is given. Then flux conservation determines the relationship between the reconnection rate v_e and the inflow speed v_i in a steady state by

$$v_i B_i = v_e B_e, \qquad \text{or in dimensionless variables} \qquad M_i = M_e \frac{B_e^2}{B_i^2}. \tag{86}$$

Furthermore, if the outflow speed from the diffusion region is the Alfvén speed (v_{Ai}), mass continuity determines the sheet length when the density is uniform as

$$\frac{L}{l} = \frac{v_{Ai}}{v_i} \qquad \text{or in dimensionless terms} \qquad \frac{L}{L_e} = \frac{1}{M_i}\frac{l}{L_e}. \tag{87}$$

(ii) **Spontaneous almost-uniform and nonuniform reconnection**
For spontaneous reconnection, the boundary conditions are free in some sense and v_e (or M_e) is determined as the maximum allowable

value for the solution.

For almost-uniform reconnection with a potential field in the ideal region, the field (B_i) at the inflow to the diffusion region is given (Priest 2014) in the simplest first treatment by

$$\frac{B_i}{B_e} = 1 - \frac{4M_e}{\pi} \log_e \frac{L_e}{L}. \tag{88}$$

The maximum reconnection rate (M_e^*) may then be estimated by assuming that B_i has reduced to roughly $\frac{1}{2}B_e$ and so is given by

$$M_e^* = \frac{\pi}{8 \log_e L_e/L}. \tag{89}$$

Thus, regardless of whether the diffusion region is resistive or collisionless, what matters is the length of the diffusion region at the maximum rate. If $L_e/L = 10^{12}$, then $M_e^* = 0.014$, whereas, if it is 10^6 or 10^3, then the maximum rate is 0.028 or 0.056, respectively, and if it is 10^2 or 10, then the maximum rate is 0.085 or 0.17, respectively.

(iii)(a) **Resistive diffusion region**

For a resistive diffusion region, we have Petschek's mechanism, provided there is an enhanced resistivity in the diffusion region. An enhanced resistivity may possibly be created by current-driven micro-instabilities, such as ion-acoustic or lower hybrid drift instabilities (e.g., Syrovatsky 1969; Smith and Priest 1972; Heyvaerts et al. 1977; Huba et al. 1977; Ugai 1984; Strauss 1988) or by a lowering of the temperature inside the diffusion region when cooling by radiation dominates ohmic heating (Heyvaerts and Priest 1976; Heyvaerts et al. 1977). In this case, for almost-uniform reconnection, the local reconnection rate is the Sweet–Parker rate $M_i = R_{mi}^{-1/2}$, while the maximum global rate is typically $M_e^* = 0.01$–0.1. Specifically, in this case, the width of the sheet is $l = \eta/v_i$ and so Eq. (87) implies that

$$\frac{L_e}{L} = R_{me} M_i^{3/2} M_e^{1/2}. \tag{90}$$

The maximum rate is therefore

$$M_e^* = \frac{\pi}{8 \log_e R_{me}}, \tag{91}$$

which gives $M_e^* = 0.014$, for $R_{me} = 10^{12}$, say, or $M_e^* = 0.028$, for $R_{me} = 10^6$.

On the other hand, if the Lundquist number R_{me} exceeds about 10^3 and the resistivity is uniform, numerical experiments (Biskamp 1986; Uzdensky and Kulsrud 2000) and theoretical considerations (Baty et al. 2014) show that the diffusion region grows in length to a value L that is a significant fraction (not yet properly determined) of L_e. In addition, the inflow becomes diverging rather than converging and so

we recover one of the flux pile-up regimes (Priest and Forbes 1986) with a reconnection rate of roughly

$$M_e = \frac{1.4}{R_{me}^{1/2}}, \tag{92}$$

somewhat faster than the Sweet–Parker rate.

In the alternative treatment of Priest and Forbes (1986), the magnetic field in a box with free conditions on three sides and the shock and diffusion region conditions on the fourth is calculated, and in particular the relation between B_i and B_e. Substituting it into Eq. (86) determines the relationship between M_i and M_e as

$$\frac{M_e^{1/2}}{M_i^{1/2}} = 1 - \frac{4M_e}{\pi}\left[0.83 - \log_e \tan\left(\frac{\pi}{4M_i}\frac{l}{L_e}\right)\right]. \tag{93}$$

instead of Eq. (88). If M_e is plotted as a function of M_i, the maximum occurs when $M_e M_i = 1/64$, and so, if for example the value of M_i at this maximum rate is, say, 0.1, then the maximum reconnection rate becomes $M_e^* = 0.16$.

Remaining questions about this topic are given in Sect. 9.3.1(i)

(iii)(b) **Collisionless diffusion region**

For collisionless Hall reconnection, the main focus has so far been on the local reconnection rate, and so in this section the Lundquist number (S) refers to the local magnetic Reynolds number (R_{mi})—see Sect. 9.1(ii). Some results are for almost-uniform reconnection, when the initial state is a one-dimensional current sheet, while others are for nonuniform reconnection, when it has an X-point between two flux rings. Here, after earlier studies (e.g., Drake and Kleva 1991; Aydemir 1992; Mandt et al. 1994; Kleva et al. 1995; Ma and Bhattacharjee 1996), Biskamp et al. (1997) clarified the nature of collisionless reconnection between two flux bundles that are drawn together by the magnetic tension of field lines that surround both bundles. They discovered with a two-fluid code that the diffusion region has a two-fold structure. There is an outer *ion diffusion region* where the electrons remain frozen-in to the magnetic field, while the ions are decoupled from the electrons and the magnetic field over a width equal to the ion inertial length (or skin depth), namely,

$$l = d^{(i)} = \frac{c}{\omega_p^{(i)}} \equiv \left(\frac{m^{(i)}}{\mu n e^2}\right)^{1/2}, \tag{94}$$

where ω_p is the plasma frequency and is a natural frequency of oscillation of charged particles. In addition, a much smaller *electron diffusion region* of width equal to the electron inertial length ($c/\omega_p^{(e)}$) allows the electrons to slip through the magnetic field. (Note that we are using superscripts (i) and (e) to represent ion and electron values,

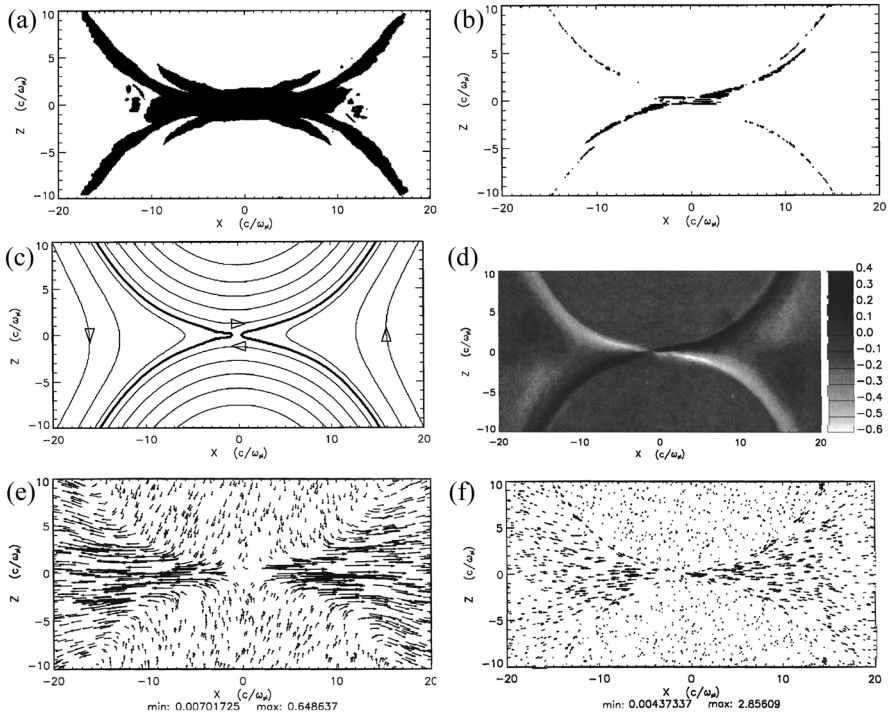

Fig. 51 Details of collisionless reconnection between two colliding flux rings, showing the regions where **a** the Hall current and **b** electron inertia is important. **c** The magnetic field lines in the *xy*-plane, together with **d** the magnetic field component out of the plane. **e** The ion flows and **f** the electron flows, with minimum and maximum values indicated. (From Shay et al. (1998) with permission, copyright AGU.)

since the normal notation (subscripts i and e) is being used to denote local inflow and external inflow values.) Although reconnection requires electron inertia, the reconnection rate is controlled by ion inertia and therefore the whistler mode.

This Hall reconnection occurs when the ion inertial length ($d^{(i)}$) exceeds the Sweet–Parker width ($d_{SP} = LR_{mi}^{-1/2}$ from Eq.(86)). Its behaviour was confirmed and investigated more thoroughly by Shay et al. (1998) with a 2.5D hybrid code, including Hall dyamics and electron inertia, in which the ions are modelled as particles and the electrons as a fluid (Fig. 51). The ions are accelerated to the Alfvén speed (v_{Ai}), while the electrons are ejected at a much higher speed but eventually slow down and join the ions. The local reconnection rate is of order

$$v_i = \frac{d^{(i)}}{L} v_{Ai} \approx 0.1 v_{Ai}, \tag{95}$$

and is controlled by the ions rather than the electrons. It is much faster than the Sweet–Parker rate because the ions are not constrained to flow

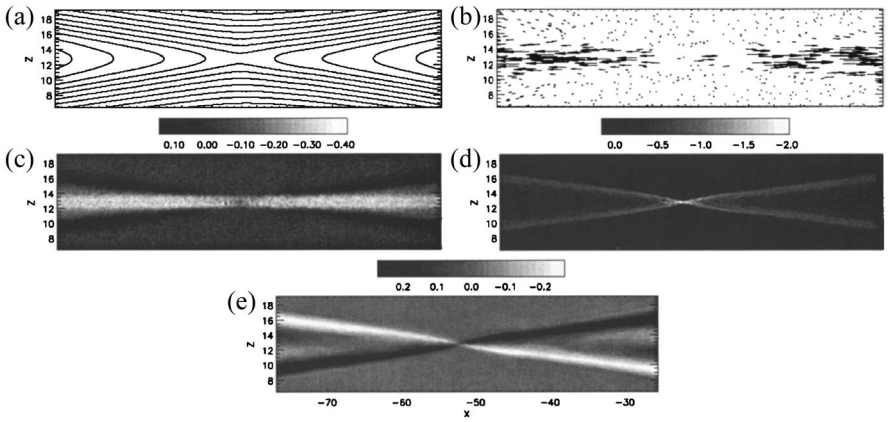

Fig. 52 Collisionless reconnection in a current sheet, showing the in-plane **a** magnetic field lines and **b** ion velocity, and the the out-of-plane **c** ion current, **d** electron current and **e** magnetic field. (From Shay et al. (1999) with permission, copyright AGU.)

through the very narrow electron region where the frozen-in constraint is broken.

Shay et al. (1999) used a hybrid code to consider a double current sheet initially rather than a pair of flux rings. Reconnection was initiated by perturbations in the form of magnetic islands. Fig. 52 shows a limited area of length 50 ion inertial lengths ($d^{(i)}$) about one of the X-points in a run of length $205d^{(i)}$. The ions form a layer about $2d^{(i)}$ wide and stretching over the whole length in Fig. 52c, with wings which separate at about $10d^{(i)}$ from the X-line downstream of the separatrix and fan outwards. On the other hand, the electrons form a tiny diffusion region of width $d^{(e)} = 0.2d^{(i)}$ and length $2d^{(i)}$ together with wings along the separatrices. The out-of-plane magnetic field has a quadrupolar structure due to Hall currents and whistler waves (Fig. 52e). The reconnection rate is $M_i = 0.1$, and they suggested that this is a universal rate. Indeed, a comparison of different codes, called the GEM challenge, in which the initial state was a one-dimensional current sheet with an initial perturbation as a set of magnetic islands, led to the conclusion that all models with a Hall effect, whether two-fluid, hybrid or full particle, produce the same reconnection rate for the nonlinear development of tearing (Birn et al. 2001).

Later, Shay et al. (2007) used a PIC code to study the electron diffusion region in more detail for reconnection in an initially one-dimensional current sheet. Reconnection approached a steady value of $M_i = 0.14$ with a steady diffusion region that did not form secondary islands, unlike earlier simulations such as Daughton et al. (2006). The ion diffusion region had a length of $7d^{(i)}$, and the surprising feature was that a high-velocity jet of electrons was accelerated to the electron

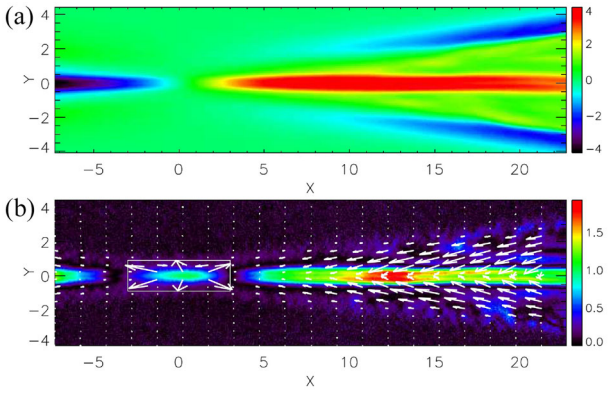

Fig. 53 Collisionless reconnection with a PIC code in a region of length $200 \times 100d^{(i)}$, showing **a** electron outflow velocity $v_x^{(e)}$ and **b** the momentum flux vectors in a region near the reconnection line. (From Shay et al. (2007) with permission, copyright AGU.)

Alfvén speed in the electron diffusion region and extended to large distances of several 10's of $d^{(i)}$, while the ions open out into the usual wedge-shaped jet characteristic of Hall reconnection and accelerated by the Hall effect (Fig. 53). Drake et al. (2008) stressed that the electron jet becomes a smaller fraction of the outflowing electrons in the bulk of the Hall jet with increasing distance downstream.

There is no theoretical model for this apparently universal local rate of 0.1 for collisionless reconnection, which depends purely on numerical experiments (Comisso and Bhattacharjee 2016). Various mechanisms have been proposed, such as Hall dissipation (Mandt et al. 1994; Rogers et al. 2001; Drake et al. 2008; Cassak and Shay 2008), off-diagonal pressure tensor terms (Hesse et al. 1999; Bessho and Bhattacharjee 2007; Ng et al. 2011; Cassak et al. 2015), and Wiebel instability (Swisdak et al. 2008). The same universal rate also occurs in other scenarios: in the absence of the Hall effect, when a large out-of-the-plane "guide field" is present (Liu et al. 2014; Cassak et al. 2015; Stanier et al. 2015); for asymmetric fields (Cassak and Shay 2008); in partially ionized plasmas (Jara-Almonte et al. 2019); and even in relativistic reconnection or for an electron-positron plasma (Bessho and Bhattacharjee 2005, 2012).

Extending these results to large domains, Shay et al. (2004) found that a large-scale initial current sheets develops reconnnection at the same local rate of 0.1 independent of the system size. Also, PIC and kinetic Riemann simulations have shown that to each of the Petschek slow-mode shocks is added a rotational discontinuity (which drives flows out of the plane) (Liu et al. 2012; Zhang et al. 2019). A similar evolution into a Petschek-type configuration was found by Comisso et al. (2013) with a gyrofluid model.

Remaining questions about this topic are given in Sect. 9.3.1(iii)

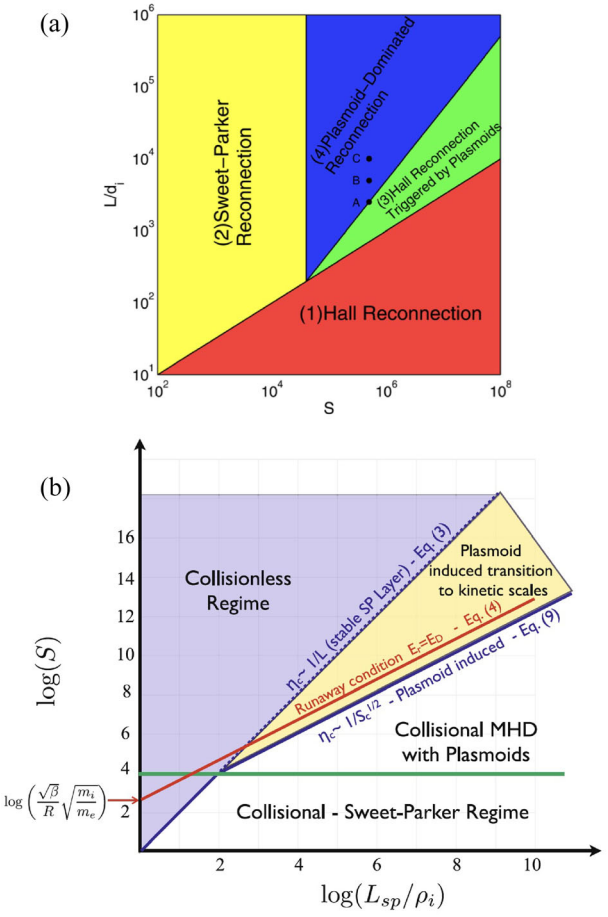

Fig. 54 Phase diagrams for the different regimes of reconnection, showing their dependency on the aspect ratio ($L/d^{(i)}$) of the current sheet and the Lundquist number (S): **a** in a Hall simulation of a neutral current sheet with no guide field, with permission from Huang et al. (2011), copyright by AIP; **b** in a collisional kinetic simulation of a current sheet with a strong guide field from Daughton and Roytershteyn (2012), copyright by Springer

(iii)(c) **Impulsive bursty reconnection—plasmoid instability**

When the diffusion region becomes too long, it can go unstable to tearing and the reconnection becomes impulsive and bursty, as described for a resistive plasma in Sect. 8.3, for which the linear growth rate is $S^{1/4}v_A/L$ and in the nonlinear regime the local reconnection rate is $M_i = 0.01$ (Biskamp 1986; Tajima and Shibata 1997; Loureiro et al. 2007; Bhattacharjee et al. 2009; Comisso and Bhattacharjee 2016; Huang et al. 2010; Uzdensky et al. 2010).

Daughton et al. (2009c) considered a Sweet–Parker diffusion region of length L_{SP} containing N secondary islands, each of length L_{SP}/N and

width $l_{SP}/\sqrt{N}$. They suggested that, since the original Sweet–Parker current sheet would have a local reconnection rate $M_i = 1\sqrt{S}$, when it is unstable to plasmoid instability with N islands, the local reconnection rate would increase to $M_i = 1\sqrt{NS}$, and this was later confirmed by numerical experiments (Cassak et al. 2009).

Similar results also arise for a collisionless plasma. Daughton et al. (2006) used a PIC code with open boundaries to study spontaneous reconnection in a current sheet initialised with a single X-point. The electron diffusion region grew in length and periodically went unstable to the formation and ejection of secondary islands (see also Karimabadi et al. 2007; Shay et al. 2007).

Daughton et al. (2009a, 2009c) then used a fully kinetic code with a Fokker-Planck collision operator to study the transition from collisional to kinetic regimes. They found that the current sheet goes unstable to the formation of plasmoids when the Lundquist number is large enough ($S > 10^3$), and there is an enhancement in the reconnection rate when the current sheet between two plasmoids becomes collisionless—i.e., its thickness becomes smaller than the ion inertial length ($d^{(i)}$). Later, Stanier et al. (2019) repeated the analysis with a 3D code, with similar results: in the nonlinear development of semi-collisional plasmoid instability, flux ropes are advected and rotated by reconnection outflow jets leading to a state in which super-Dreicer fields produce a transition to kinetic reconnection in the thin current sheets forming between the flux ropes.

Huang et al. (2011) conducted Hall simulations with system sizes up to 10^4 ion skin depths ($d^{(i)}$) and constructed a phase diagram (Fig. 54a) that shows how the presence of reconnection depends on the aspect ratio ($L/d^{(i)}$) of the current sheet and the Lundquist number (S). This includes Hall reconnection, plasmoid reconnection at multiple X-points, and reconnection at a single X-point (here called "Sweet–Parker reconnection"). The usual conditions for Hall reconnection are that $d^{(i)}$ exceed the Sweet–Parker current sheet width ($d_{SP} = S^{-1/2}$), and for plasmoid instability that S exceeds a critical value $S_c \approx 10^4$. When both are satisfied, the secondary current sheets cascade down to a width that may either exceed or reach the $d^{(i)}$ scale, so that reconnection is either resistive or Hall, respectively.

Previously, with smaller system sizes, Daughton et al. (2009b) had found a continual generation of copious plasmoids with a PIC code when $d^{(i)} > d_{SP}$, whereas Shepherd and Cassak (2010) had discovered with a Hall code that, after the plasmoids had been expelled, it settles down to a single stable X-point. Later, Daughton and Roytershteyn (2012) repeated their earlier simulations but added a strong "guide field" out of the plane, for which the condition for collisionless behaviour is changed to $d_{SP} > \rho_s$, where ρ_s is the ion sound radius

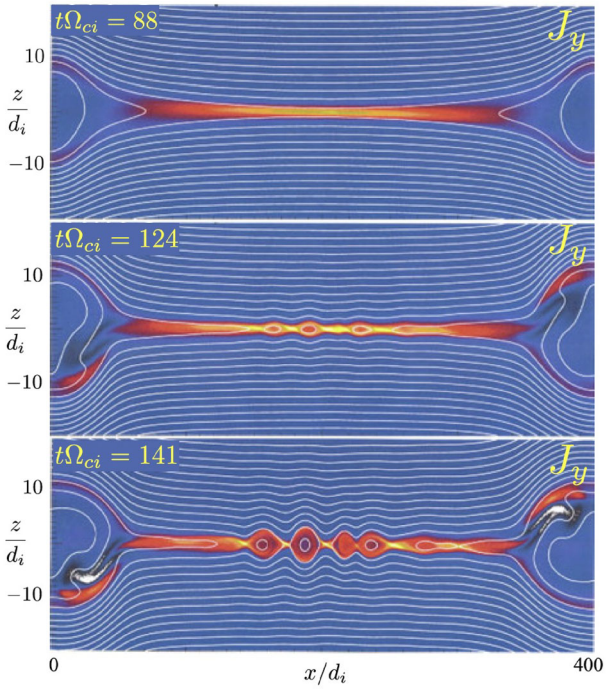

Fig. 55 Evolution of the out-of-plane current density (in colour) superimposed on the in-plane magnetic field lines during a collisional kinetic simulation. Image reproduced with permission from Daughton and Roytershteyn (2012), copyright by Springer

based on the total magnetic field (see also Stanier et al. 2017). This confirmed the onset of plasmoid instability when $S > 10^4$, as shown in Fig. 55, where at early times a long current layer develops, which subsequently goes unstable to the formation of plasmoids that induce a transition to a collisionless regime. They also produced a phase diagram (Fig. 54b): above the green line the current sheet is unstable to plasmoid formation; in the white region between the green and blue lines resistive MHD is valid; in the yellow region, plasmoid development induces a transition to kinetic scales, whereas in the purple regions the plasma is completely collisionless; below the red line the electric field remains below the runaway limit and two-fluid closures are valid.

From a 3D PIC simulation of double current sheet, Che et al. (2011) found that 3D reconnection is faster than 2D reconnection due to the onset of turbulence in the form of a complex web of filaments. With a guide field Liu et al. (2013) discovered that the dominant instability is collisionless tearing: in the nonlinear regime a turbulent state develops with oblique flux ropes, multiple electron diffusion regions and flow vortices (Daughton et al. 2014).

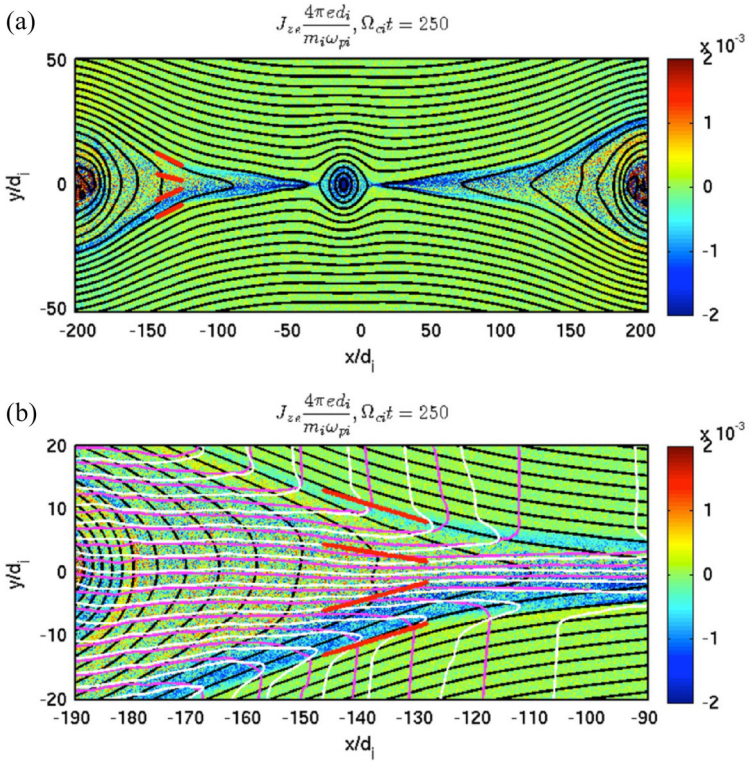

Fig. 56 A large-domain PIC simulation of collisionless reconnection, showing switch-off shocks after plasmoid instability has left a single large island in the centre of the sheet. **a** The magnetic field lines (black) and current (coloured). **b** A zoom of the left-hand outflow region, showing electron (white) and ion (purple) flow lines, together with two slow shocks in the outer part of the exhaust and two rotational discontinuities in the inner part. (Image reproduced with permission from Innocenti et al. (2015), copyright by AAS.)

When plasmoids are much larger than kinetic scales, the plasmoid flux ropes can bounce off one another or pile up and lower the reconnection rate (Karimabadi et al. 2011; Ng et al. 2015; Stanier et al. 2015), since the time-scale for interaction can be shorter than the reconnection time. Innocenti et al. (2015) found with a PIC simulation that a series of plasmoids at early times are replaced by a single plasmoid. It has Petschek shocks extending from it with a compound structure consisting of a slow shock and a rotational discontinuity (Fig. 56).

Several authors have modelled collisionless reconnection at the magnetopause with fully kinetic 3D codes. Nakamura et al. (2017) showed how Kelvin-Helmholtz instability can drive reconnection. Roytershteyn et al. (2012); Le et al. (2017, 2018) found enhanced transport of particles across separatrices due to lower hybrid drift turbulence. Furthermore, Egedal et al. (2019) modelled spacecraft data from NASA's Magnetospheric Multiscale (MMS) mission of an

electron diffusion region in the geomagnetic tail. They compared with 2.5D kinetic simulations and deduced that the off-diagonal electron pressure tensor was responsible for breaking the frozen-in condition for electrons.

Remaining questions about this topic are given in Sect. 9.3.1(iv)

(iv) **Driven almost-uniform reconnection**

As described in Sect. 7.3, driven reconnection gives rise to a whole family of almost-uniform regimes in which the inflow may be either converging or diverging, and the strength of the convergence or divergence may vary, depending on the inclination of the flow velocity on the inflow boundary. There is a continuum of solutions for the relation between the global (M_e) and local (M_i) reconnection rates, depending on how the reconnection is driven, as shown in Fig. 40b. Indeed, in some cases $M_e > M_i$ (especially converging flows) and in others $M_e < M_i$ (especially diverging flows and flux pileup solutions).

The above description refers to a resistive diffusion region, and so it needs to be investigated in detail for both collisionless and impulsive bursty regimes. For a converging flow the maximum local rate of reconnection is likely to be 0.1 (when $l/L = 0.1$) in both resistive and collisionless regimes, and so the maximum global rate is likely to be $M_e = 0.1$. For a diverging flow, on the other hand the maximum global rate is likely to be $M_e = S^{-1/2}$ for a resistive plasma, but 0.1 for a collisionless plasma.

Questions that need to be addressed here are set out in Sect. 9.3.2(i).

9.3 Questions to be addressed in future for 2D reconnection

9.3.1 Spontaneous almost-uniform reconnection

For spontaneous uniform reconnection several questions remain, depending on the nature of the diffusion region.

(i) **Enhanced resistivity**

For a resistive diffusion region, the key need in future is to investigate thoroughly whether or not the resistivity is enhanced in solar applications such as solar flares and coronal heating. For example, are current-induced micro-instabilities taking place, what is their nature and what is the resulting value of the anomalous resistivity? Does the enhanced resistivity remain enhanced or does it switch on and off? Also, the thermodynamics of a reconnecting current sheet needs to be re-evaluated in view of the fact that a simple such analysis by Heyvaerts and Priest (1976); Heyvaerts et al. (1977) suggested that in some situations the enhanced density in such a sheet can make the radiation dominate the ohmic heating and so raise the classical magnetic diffusivity (which is proportional to $T^{-3/2}$).

For both neutral sheet and guide-field reconnection, what is the role of plasma instabilities in the out-of-plane direction in altering the dynamical

evolution of the reconnecting layer and localising the diffusion region? The role of current-induced microinstabilities in producing a turbulent diffusivity and the effect of intense electron streaming, velocity shear, anisotropy and density gradients remain to be studied (e.g., Daughton et al. 2006).

An in-depth understanding of the nature of the behaviour of the MHD characteristics during spontaneous reconnection would be of value. It is thought that the slow-mode characteristics in the ideal inflow region are propagating information outwards from the diffusion region, but what about the fast-mode characteristics and their effect on the "free" boundary conditions at large distances? By contrast, in driven reconnection, both slow-mode and fast-mode characteristics are likely to propagate information inwards from the boundaries.

(ii) **Uniform resistivity**

When the resistivity remains uniform, so that the diffusion region grows in length, what is the ultimate length compared with the box size? What are the resulting details of the ideal region flow and what is the global reconnection rate (M_e)?

(iii) **Collisionless reconnection**

For Hall reconnection, the local reconnection rate is fast, but how is the diffusion region connected to the global environment? In other words, what is the nature of the global flow in the ideal region and what is the resulting global reconnection rate (M_e)? Since the local rate is $M_i \approx 0.1$, we expect the magnetic field in the ideal region to be roughly uniform and the global rate to be $M_e \approx 0.1$. But do numerical solutions bear that out?

(iv) **Impulsive bursty reconnection**

When the diffusion region is full of plasmoids, what is its length, the nature of the flow in the ideal region and the global reconnection rate (M_e)? Since the local rate is $M_i \approx 0.01$, we expect the magnetic field in the ideal region to decrease as the diffusion region is approached, similar to Petschek's mechanism, and the global rate to be $M_e \approx 0.1$. Is it possible to model this in terms an anomalous or eddy resistivity (e.g., Strauss 1988), and, if so, what are its value and its effects?

9.3.2 Driven or nonuniform reconnection

(i) **Driven reconnection**

For almost-uniform resistive driven reconnection, the theory is valid only when the Alfvén Mach number is much smaller than unity, and so it needs to be investigated numerically in order to be confident about the results as M_i or M_e approach unity. For both Hall reconnection and impulsive bursty reconnection, driven reconnection needs to be investigated thoroughly, paying careful attention to different initial and boundary conditions and the differences between local and global reconnection rates.

One important question here concerns the way in which the driving

boundary conditions interact with diffusion region physics to determine both the resulting diffusion region length and the nature of the inflow in the ideal region. Coupled with this is a determination of the maximum allowable global reconnection rate as the imposed value of M_e is increased.
Determining the details of the solution for given applications is also of great interest, such as flare reconnection driven by an erupting flux rope, or coronal heating driven by flux cancellation (when motions of photospheric flux fragments drives reconnection in the overlying atmosphere).

(ii) **Nonuniform reconnection**
For nonuniform reconnection, very little is known about either spontaneous or driven reconnection. The local solutions at the diffusion region are likely to remain the same as for almost-uniform reconnection, but what about the behaviour of the ideal region? A simple approximate solution exists for resistive spontaneous reconnection, but it needs to be checked numerically, in order to determine the global rate of reconnection with confidence.

9.3.3 Other major questions

(i) **Theory for ideal region coupled with the diffusion region**
Can a theory for the ideal region outside the diffusion region be developed, both for spontaneous and driven reconnection, along the lines of the original theory for almost-uniform theory (Priest and Forbes 1986) and nonuniform reconnection (Priest and Lee 1990)? What are the most appropriate boundary conditions? Can this be matched or patched to theories for collisionless and impulsive bursty diffusion regions in a similar way to a resistive region (Priest and Forbes 2000)? It is only if such a theory can be developed that we can be confident of extrapolating beyond the limited parameter range of current simulations to solar values (Priest et al. 2021).
Another way of addressing this question is to ask how the local reconnection picture fits into global large-scale physics (e.g., Cassak et al. 2017)? Can a theory be set up for bridging macroscales and microscales in the corona (e.g., Simakov et al. 2006; Liu et al. 2017)?

(ii) **Three dimensions**
Extending our understanding from two to three dimensions is only in its infancy and is heavily constrained by a much smaller range of parameters for numerical computations. This makes the need for in-depth theoretical understanding even higher. Especially complex is the effect of plasmoid instability, since the plasmoids correspond to magnetic flux ropes which may interact in highly complex ways (e.g., Daughton et al. 2014). Furthermore, the development of plasma instabilities in 3D may affect the nature of reconnection and the onset of microturbulence (e.g., Daughton and Roytershteyn 2012).

(iii) **The 0.1 reconnection rate**
It has been argued that $M_i = 0.1$ is a universal local rate of reconnection,

regardless of the nature of the diffusion region. Is this indeed the case? If so what is the theoretical reason? What is the resulting global reconnection rate (M_e)? Is it the same or different? Why is the local rate for plasmoid reconnection only 0.01 (e.g., Cassak et al. 2017)?

(iv) **Reconnection onset**
Are there conditions for the onset of reconnection or will it occur as soon as a current sheet forms? Can energy be stored in a preflare configuration only as long as there are no current sheets present or can it continue to be stored until a current sheet reaches a threshold? When photospheric fragments approach one another, does reconnection in the overlying magnetic field occur as soon as a null point or separator forms, or can energy be stored in the field while a current sheet is forming?

(v) **Partial ionisation**
Plasma in the lower solar atmosphere is partially ionised, so that the additional effect of ambipolar diffusion is present due to the friction between neutrals and ionised particles. Although ambipolar diffusion naturally leads to the formation of current sheets, it cannot by itself allow reconnection since it vanishes when $\mathbf{B} = \mathbf{0}$ (Zweibel 1994; Brandenburg and Zweibel 1994, 1995; Zweibel and Yamada 2009). It has been included in current MHD codes for the low-temperature solar plasmas (Leake and Arber 2006; Arber et al. 2007; Khomenko and Collados Vera 2012; Martínez-Sykora et al. 2012; Nóbrega-Siverio et al. 2020b, a), but a full account of its effect on reconnection has not yet been given.

(vi) **Magnetic turbulence**
The detailed nature of turbulence created by reconnection and its effect on reconnection and energy conversion needs further study in a wide variety of situations (see Sect. 16).

(vii) **Nonthermal particle acceleration**
The origin of particle acceleration in solar flares is not yet well understood, including the role of direct electric fields, shock waves of different types, and turbulence (see Sect. 17).

10 Magnetic reconnection at a three-dimensional null point

The focus of this review switches in the following sections to reconnection in fully 3D geometries. As mentioned in Sect. 4, in three dimensions magnetic reconnection is not restricted to occur only at null points (as in 2D), but it may in principle occur anywhere. What is required for reconnection is a concentration of parallel electric field, which in turn corresponds to an intense current concentration. In Sect. 5 we have described how such intense currents may form in 3D either at magnetic null points, along separators, or in the absence of nulls or separators, such as, for example, at a quasi-separator or hyperbolic flux tube (HFT). The details of the reconnection process turn out to be quite different in these different cases, and so we treat them here in turn in the following sections. First of all, in this section, we address reconnection at 3D null points. We begin by discussing ideal and resistive

kinematic modelling (Sect. 10.1), and then describe the reconnection regimes that have been discovered at a 3D null point (Sect. 10.2).

10.1 Results of early kinematic modelling

10.1.1 Ideal kinematic modelling for spine and fan reconnection

The pioneering work for the study of 3D null point reconnection was undertaken by Lau and Finn (1990) and Priest and Titov (1996). They employed steady-state, kinematic, ideal models (see Sect. 4.7.1), solving the kinematic equations for **v** and **E** (Eqns. 31–33) with **B** given by

$$(B_x, B_y, B_z) = \frac{B_0}{L_0}(x, y, -2z).$$

By imposing different boundary conditions, Priest and Titov (1996) found that two principal characteristic behaviours are possible. In the first, a plasma flow crosses the fan plane and in the second it crosses the spine (see Sect. 2.2). When a plasma flow across the fan is imposed, the solution exhibits singularities in **E** and **v** at the spine. For example, for a smooth boundary flow across the fan purely in the z-direction and an electric field of the form $E_\phi = v_e B_0 \sin\phi$, the velocity is

$$v_{\perp R} = \frac{2E_\phi L_0^2 z/B_0}{R(R^2 + 4z^2)}, \qquad v_{\perp z} = \frac{E_\phi L_0^2 z/B_0}{R^2 + 4z^2},$$

with $v_{\perp R}$ singular at the spine ($R = 0$). It was suggested that a similar evolution with the full dynamics included might lead to a strong current along the spine. Field lines traced from footpoints transported in the ideal flow across the fan are seen to jump from one spine direction to the other as the footpoint crosses the fan, with this behaviour being termed *spine reconnection* by Priest and Titov (1996).

By contrast, when a continuous plasma flow is imposed across the spine, **E** and **v** are found to exhibit singularities in the fan plane. Following field lines in that flow, only those that happen to pass exactly through the spine show a discontinuous jump, while all other field lines flip rapidly around in the fan. Again, it was speculated that dynamics would lead to a strong current localised to the fan, with the process termed *fan reconnection* (Priest and Titov 1996).

10.1.2 Resistive kinematic modelling

Priest and Titov (1996) were unable to resolve the singularities in their models with a finite resistivity, and it was later discovered that such isolated spine and fan reconnection modes seldom occur in practice. This was first realised through resistive kinematic modelling by Pontin et al. (2004, 2005), using the approach described in Sect. 4.7.2. They considered an isolated diffusion region centred on the null point, since this is the critical property of 3D reconnection (Sect 4). The equations to be solved are Eqns. (34)–(36), and, as with the solution described in Sect. 4.7.2, a localised resistivity is specified. It turns out that the properties of the

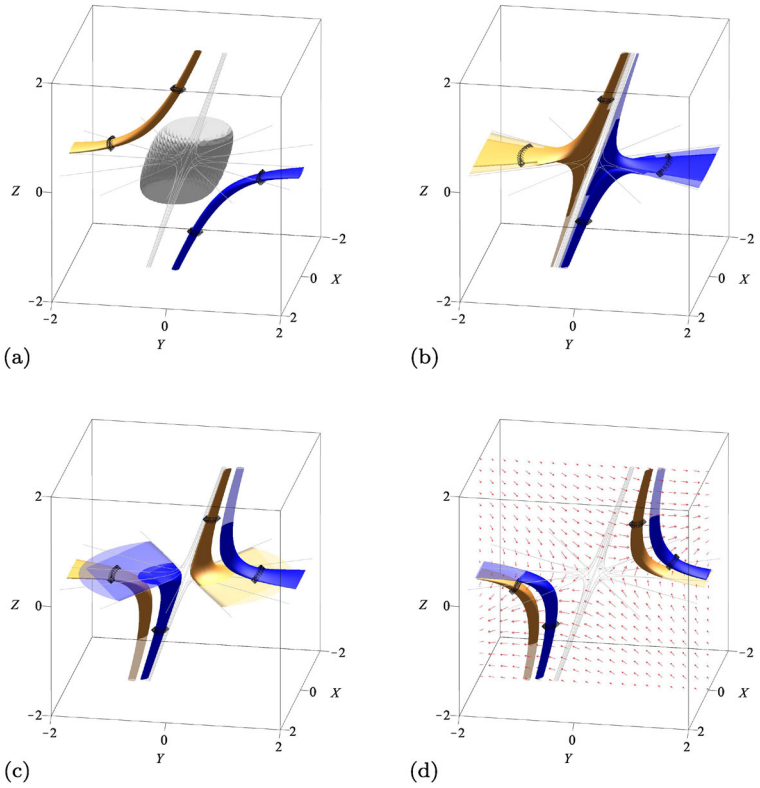

Fig. 57 Resistive, kinematic, spine-fan reconnection based on the solution of Pontin et al. (2005). Evolution of two arbitrarily chosen flux tubes in the magnetic field $\mathbf{B} = (x, y - jz, -2z)$, which has current directed parallel to the fan plane (with $j = 1$). A localised diffusion region is present around the null point, shown by the shaded surface in (**a**). Flux tubes are traced at each instant from a set of plasma elements—marked by black diamonds—that move with time at the flow velocity **v** in the ideal region (**v** is shown by the red arrows in (**d**)). Field lines traced through and beyond the diffusion region are rendered transparent. For a related movie see Supplementary Information

reconnection process depend critically on the orientation of the current density vector at the null.

When the current is non-zero at the null and oriented parallel to the fan surface, Pontin et al. (2005) found that the plasma must flow across both the spine and fan of the null-point. This transports flux both through and around the spine line, and across the fan surface (see Fig. 57), and it is therefore a combination of the 'spine' and 'fan' modes of Priest and Titov (1996). The reconnection rate—calculated as a maximal integrated $E_{\parallel}$ along fan field lines—measures the rate of transport of magnetic flux across the separatrix (fan) surface, much as in 2D X-point reconnection. Pontin et al. (2005) showed that the individual spine and fan reconnection modes can only be decoupled when the current is zero at the null point itself. However, this is unlikely in a full dynamic evolution, in which current tends

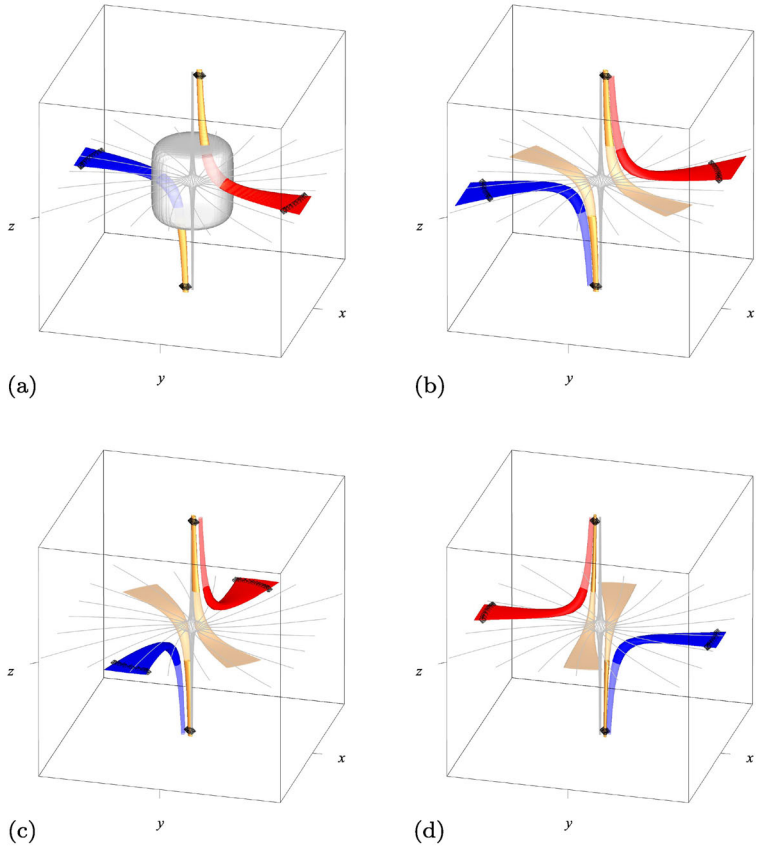

Fig. 58 Resistive, kinematic, torsional, null-point reconnection based on the solution of Pontin et al. (2004). Evolution of two arbitrarily chosen flux tubes in the magnetic field $\mathbf{B} = (R, jR/2, -2z)$ in cylindrical polar coordinates, which has current ($j = 1$) directed parallel to the spine. A localised diffusion region is present around the null point, shown by the shaded surface in the first frame. Flux tubes are traced at each instant from a set of plasma elements—marked by black diamonds—which move with time at the flow velocity $\mathbf{v}$ in the ideal region. Field lines traced through and beyond the diffusion region are rendered transparent. For a related movie see Supplementary Information

to accumulate at the null, as evidenced by the results described in Sect. 5.4 on null collapse, and the dynamic simulations described in Sect. 10.2.

By contrast, when the current at the null is parallel to the spine, then the field line connectivity change takes the form of a counter-rotational slippage, driven by rotational flows centred on the spine (Pontin et al. 2004; Wyper and Jain 2010)—see Figs. 58, 59. In this case there is no flux transport across either the spine or fan. The reconnection rate in this case (the integral of $E_{\parallel}$ along the spine) quantifies this slippage by measuring the difference between the rates of flux transport through the surfaces marked 'A' and 'B' in Fig. 59b.

In the kinematic models described in this section the solution is obtained by a method similar to that described in Sect. 4.7.1., namely, the non-ideal region is

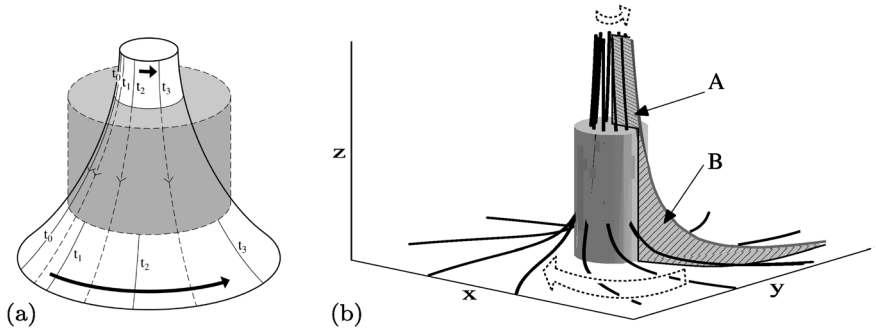

Fig. 59 **a** Rotational slippage of fields entering through the top of the diffusion region on a curved flux surface, showing as solid curves the locations of the plasma elements at $t = t_1$, $t = t_2$, $t = t_3$, that initially ($t = t_0$) lay on one field line. **b** The reconnection rate measures a rotational mismatching of flux threading the diffusion region, namely the difference between the rates of flux transport through surfaces A and B

localised artificially by prescribing a localised resistivity. The next natural step in the investigation of 3D null-point reconnection is to examine the self-consistent formation of localised non-ideal regions at the null through the dynamic formation of localised current concentrations. This has been investigated through a series of numerical MHD simulations, which have led to the discovery of the various modes of 3D null point reconnection described in Sect. 10.2.

10.2 Reconnection regimes at a 3D null point

The above-described models are all steady-state and kinematic, while simulations have revealed how the current layers required for 3D reconnection form dynamically. Early work by Rickard and Titov (1996), Galsgaard et al. (2003a) and Pontin and Galsgaard (2007) demonstrated that rotational perturbations (centred on the spine) lead to accumulation of currents along either the spine or fan of the null point. By contrast, perturbations that break the cylindrical symmetry tend to be refracted and lead to the accumulation of currents and free energy in the vicinity of the null. This behaviour is consistent with the propagation of Alfvén and magnetoacoustic waves around 2D nulls as reviewed by McLaughlin et al. (2011).

Complementary to these investigations of propagation of impulsive disturbances towards nulls are studies that investigate the long-time behaviour when systematic flows perturb the magnetic field. Such studies were discussed in Sect. 5.4, where it was described how boundary motions that displace the spine or fan footprints lead to a local collapse of the spine and fan towards one another in the vicinity of the null (since the Lorentz force acts to increase the applied displacement, just as at a 2D null), and the concomitant formation of an intense current sheet centred on the null (Pontin and Craig 2005). The implications of these different current density structures for the nature of the reconnection that ensues are explored in the following subsections.

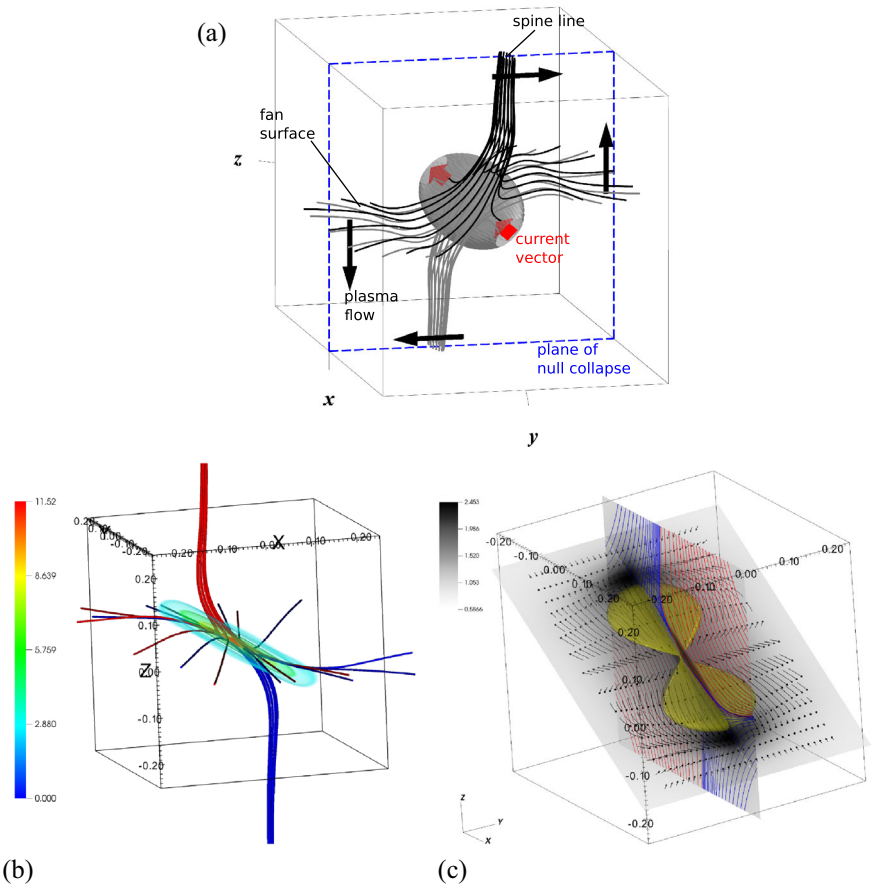

Fig. 60 Spine-fan reconnection. **a** Cartoon illustrating the qualitative structure of the magnetic field lines, current localisation (shaded) and plasma flow [modified from Pontin (2011), copyright by COSPAR]. **b**, **c** Two visualisations of *spine-fan reconnection* during impulsive 3D null collapse [reproduced from the simulations of Thurgood et al. (2017)]. **b** Magnetic field lines and contours of the current density component j_y. **c** Magnetic field lines in the "plane of collapse" (red in the inflow regions, blue in the outflow) together with plasma density (shaded) and plasma flow vectors in a plane containing the current sheet, illustrating the outflow jet. The yellow surface is the boundary of the fast outflow jet: within the yellow surface the flow speed exceeds the fast magnetosonic speed

10.2.1 Spine-fan reconnection

The most common form of reconnection to occur at a 3D null point is *spine-fan reconnection*. As we shall see below, the other modes of 3D null-point reconnection require a more organised form of driving flow, while spine-fan reconnection occurs whenever a perturbation displaces the locations of the spine and fan. This mode of reconnection was first studied in detail by Pontin et al. (2007a), who performed a systematic shearing of the spine (or fan) footpoints in a closed domain. As described

above, such a shear disturbance causes the spine and fan to collapse, with a current layer forming at the null as the shear stress accumulates in the weak-field region.

Tracing plasma elements moving in the ideal region, plasma—and thus magnetic flux—are found to be transported both across the fan and across or around the spine. As per the kinematic model of Pontin et al. (2005) discussed above, the rate of flux transport across the fan (separatrix) surface is quantified in 3D as usual by the maximal integral of $E_{\parallel}$ through the current layer, which occurs along a fan field line by symmetry.

The transfer of flux across both the spine and fan led Priest and Pontin (2009) to suggest the name *spine-fan reconnection*, and this behaviour distinguishes this type of reconnection from the other null point reconnection modes discussed below. Also, the current concentration is in the form of a localised sheet that is inclined at an intermediate angle between the spine and fan in such a way that the current sheet contains part of both the spine and the fan (see Fig. 60).

The direction in which the perturbation is applied determines the "plane of collapse", i.e., the plane in which the angle between the spine and fan is minimised, see Fig. 60a. In this plane of collapse, an inflow-outflow pattern is set up, with the current concentration, projected field lines, and plasma flow resembling closely the appearance of 2D X-point reconnection. Note, however, that the current layer and outflow jets have a fully three-dimensional character: moving away from the plane of collapse the magnetic field strength increases and the current weakens. While the expanding field lines in the fan plane cause the outflow jet to broaden moderately as it expands away from the null, the outflows remain fairly well collimated—see Fig. 60c. Note that Galsgaard and Pontin (2011a) have demonstrated that the plane of collapse may not be truly planar if the initial null point is not rotationally symmetric and the driving is not aligned with the strong or weak field eigenvectors in the fan (see Sect. 2.2).

While the qualitative properties of spine-fan reconnection described above are well understood, the quantitative properties are less well explored. Priest and Pontin (2009) analysed the case where the boundary driving is applied for a fixed period of time before being 'switched off', focusing on the scaling of the current sheet properties with resistivity and driving velocity. They found, for example, that the peak current has a power-law dependence on resistivity. These results were extended to the case of continual boundary driving by Galsgaard and Pontin (2011b), who sought to explore the properties of the asymptotic state. Scalings in the asymptotic state of the reconnection rate, peak current and peak outflow velocity with both the driving velocity (v_{drive}) and η are shown in Fig. 61. Clearly the reconnection rate decreases as both η and v_{drive} are decreased. The lines of best fit indicate scalings of $\sim\eta^{0.25}$ and $\sim {v_{\mathrm{drive}}}^{0.65}$, respectively. Note that corrections have been made to account for the numerical resistivity (triangle in frame (a)). The reconnection rate is then found to be faster than Sweet–Parker but slower than Petschek, within the limits of the restricted values of η accessible. Neither the peak current or peak velocity in the outflow jet is found to match a power-law scaling with v_{drive} (Fig. 61d, f). On the other hand, the peak current does show an approximate power-law scaling with η, although this scaling is different for different

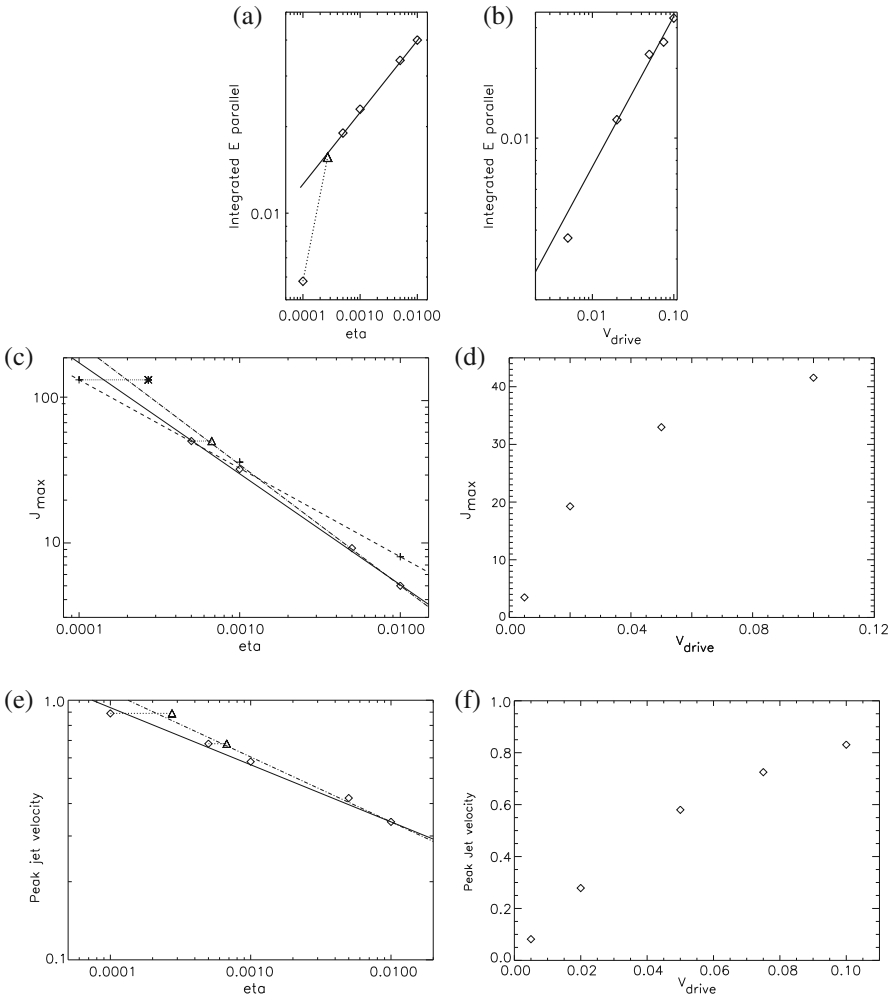

Fig. 61 Current sheet scalings during quasi-steady spine-fan reconnection. **a**, **b** Scaling of the reconnection rate with resistivity, η, (at $v_{\rm drive} = 0.05$) and the driving velocity $v_{\rm drive}$, (at $\eta = 10^{-3}$) together with lines of best fit. **c** Scaling of the peak current with η for $v_{\rm drive} = 0.1$ (crosses, dashed line) and $v_{\rm drive} = 0.05$ (diamonds, solid line). **d** Scaling of the peak current with driving velocity for $\eta = 10^{-3}$. **e**, **f** Scaling of the maximum velocity in the outflow jet with η and $v_{\rm drive}$ (for $v_{\rm drive} = 0.05$ and $\eta = 10^{-3}$, respectively). In (**a**, **c**, **e**) the triangles and asterisk represent values for which the effects of numerical dissipation have been approximated to correct the value of η from the one explicitly specified. Image reproduced with permission from Galsgaard and Pontin (2011b), copyright by ESO

$v_{\rm drive}$. Notably, the scaling $J_{\rm max} \sim \eta^{-0.6}$–$\eta^{-0.8}$ is comparable to the $J_{\rm max}$ predicted by the incompressible fan reconnective annihilation solution of Craig and Fabling (1998). Finally, as expected, the outflow jet velocity shows a scaling that mirrors the reconnection rate, namely, $v_{\rm max} \sim \eta^{-0.25}$.

The geometry of the field around a null point, where the field in the reconnection inflow regions will typically increase linearly away from the null, means that a truly

steady asymptotic state is unlikely to ever be reached. In any case, at values of the magnetic Reynolds number appropriate for the solar corona, continued driving is likely to cause the length of the current sheet to expand until the onset criterion for secondary tearing (or plasmoid) instability (Sects. 8.1–8.3) is reached, as observed by Wyper and Pontin (2014b).

Finally, it is worth noting the relation between spine-fan reconnection and the reconnective annihilation solutions discussed in Sect. 6.4. Pontin et al. (2007b) performed shear boundary driving at the spine footpoints in a series of simulations approaching the incompressible limit. They found that local null collapse is inhibited, with a current sheet instead forming all across the fan, and plasma flows and field line evolution reminiscent of the incompressible solutions of Craig et al. (1995). This implies that *fan reconnection* can be recovered as the incompressible limit of *spine-fan reconnection*. On the other hand, the same authors were unable to retrieve any behaviour resembling pure *spine reconnection* by shearing the fan surface. This suggests that such spine solutions are not recoverable in a dynamic evolution, or in other words are dynamically inaccessible, unlike the fan solutions (for further discussion, see Craig and Fabling 1998; Titov et al. 2004).

10.2.2 Torsional spine reconnection

In this and the following section, we describe two modes of reconnection that take place when the locations of the spine and fan are not disturbed. Both are induced when the equilibrium is perturbed by a rotational driving flow, with the axis of

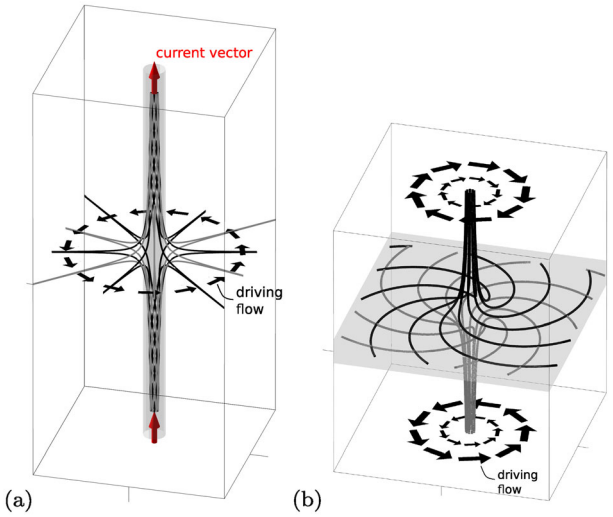

Fig. 62 Schematics of torsional spine and torsional fan reconnection at an isolated null. **a** Torsional spine reconnection. Black and grey lines are magnetic field lines, the shaded surface is a current density isosurface, the grey arrows indicate the direction of the current flow, while the black arrows indicate the driving plasma velocity. **b** Torsional fan reconnection, with the same notation. Images modified with permission from Pontin (2011), copyright by COSPAR

rotation coinciding with the spine line. First, when the rotational driving disturbs the field lines in the fan, the perturbation travels like a torsional Alfvén wave that approaches the spine. There is a corresponding accumulation of current in a tube around the spine whose radius decreases and intensity increases—as the field lines become increasingly tightly wound around the spine—until diffusion becomes important (Rickard and Titov 1996; Pontin and Galsgaard 2007). This configuration is illustrated in Fig. 62a. Once the current becomes sufficiently intense for the reconnection to take place, field lines experience a rotational slippage inside this current tube, which acts to decrease the stress induced by the twisting of the field lines. This is very different from the behaviour during the spine reconnection model of Priest and Titov (1996), and so it has been dubbed *torsional spine reconnection* (Priest and Pontin 2009).

The relative counter-rotation between selected bundles of field lines is illustrated in Fig. 58. This is detailed for a particular field line in Fig. 59a. Here the shaded cylinder represents the diffusion region, while solid lines represent field lines traced from a pair of plasma elements in the ideal region, on either side of the diffusion region. At $t = t_0$ the two field lines coincide so that the plasma elements are connected. At later times (t_1, t_2 and t_3) the plasma elements above and below (and their corresponding field lines) have rotated by different angles around the spine, and the field line connectivity has changed.

The kinematic solution of Priest and Pontin (2009) reproduces the qualitative behaviour observed in the simulations. In both the kinematic solution and early simulations, the magnetic field and driving were rotationally symmetric (independent of ϕ). When this rotational symmetry is broken, the qualitative behaviour of the system is retained, although the current layer is no longer circular in cross section. Specifically, the varying Alfvén speed in the fan plane means that the disturbance reaches the spine earlier in the strong-field direction, and the cross-section of the current concentration around the spine can be highly elliptical (Pontin et al. 2011a).

10.2.3 Torsional fan reconnection

If the external rotational flow acts in the vicinity of the spine (with the spine being the axis of rotation), then a magnetic disturbance propagates towards the fan plane. Here the hyperbolic field structure causes length scales perpendicular to the fan to decrease, creating a current front as the disturbance approaches the fan (Galsgaard et al. 2003b; Pontin and Galsgaard 2007). Moreover, a mis-match between the field lines on either side of the fan can be generated, depending on the relative rotations about either spine direction. The result is a current layer across the fan plane, within which again rotational slippage occurs, characteristic of *torsional fan reconnection*, 62(b), a kinematic model for which is presented by Priest and Pontin (2009).

In the early simulations of Galsgaard et al. (2003b) it was already clear that, when the rotational disturbance propagates towards the fan, the current is maximised at some distance from the null, owing to the hyperbolic field structure. This creates a current disc with a hole, as shown in Fig. 63. When the background null point magnetic field is not perfectly symmetric, the symmetry of the current

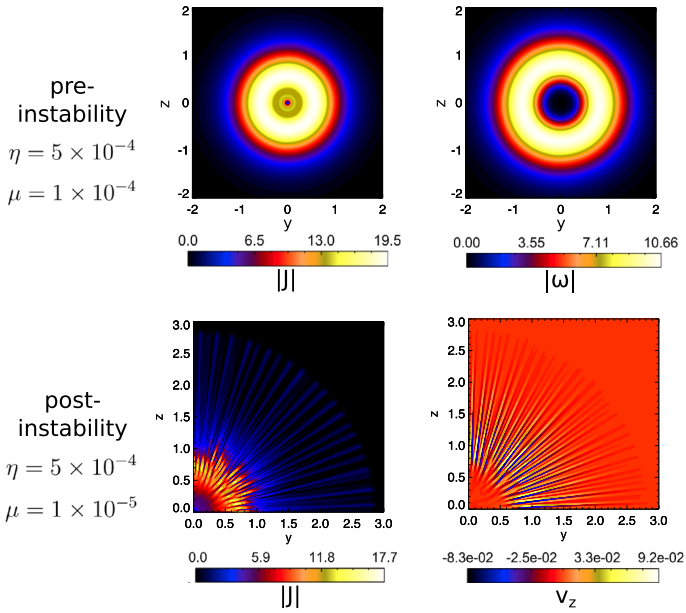

Fig. 63 Above: Distribution of the magnitudes of current density and vorticity in the fan plane in the simulations of Wyper and Pontin (2013), prior to instability of the current-vortex sheet. The fan plane is $x = 0$, the spine lies along the x-axis, and the null is at the origin. Below: After instability, in the same plane, current density and the normal component of the velocity. Clearly evident are the filaments and rolls generated during the instability, including some that branch outwards from the null. Note that the images in the top and bottom rows use slightly different plasma parameters. (Modified from Wyper and Pontin (2013), copyright by AIP.)

distribution is quickly lost, with the current instead being most intense in the weak field direction of the fan. This can be understood intuitively from the fact that the field lines must slip fastest in the weak field directions to maintain continuity of flux.

If the rotational flows associated with torsional fan reconnection do not exactly match on either side of the fan surface then the fan may host not only a current sheet but also a vortex sheet, associated with the mis-match of the rotational flows. Depending on parameters, such as the relative thicknesses of the current sheet and vortex sheet, this layer can be susceptible to tearing and/or Kelvin–Helmholtz instabilities (Einaudi and Rubini 1986; Wyper and Pontin 2013). Figure 63 illustrates the breakup of the current sheet in response to Kelvin–Helmholtz instability in the simulations of Wyper and Pontin (2013). During the nonlinear phase of the instability the flux evolution becomes much more complicated than before. Now, there is not only the rotational slippage associated with torsional fan reconnection, but also a transfer back and forth of flux across the fan surface. This flux transfer across the fan plane occurs in the many, thin, twisted flux tubes that are formed during the nonlinear evolution, leading to an increase in the net reconnection rate. The effects of different viscosity models and different relative values for the resistivity and viscosity have been explored by Quinn et al. (2021).

10.3 Time-dependent effects in spine-fan reconnection

As discussed above in Sect. 8.3, even under steady driving, spine-fan reconnection may become spontaneously bursty and time-dependent, in response to onset of plasmoid instability in the current layer. Another way in which the reconnection can be inherently time-dependent is through 'reconnection reversals', where the null point collapse reverses cyclically. In other words, the plane of collapse remains the same (Fig. 60a), but the orientation of the spine-fan collapse (orientation of the current vector at the null) reverses every half period. This may occur when the reconnection is driven by an impulsive external perturbation.

Such reconnection reversals were first observed for 2D X-points, in geometries for which the reversals were induced by the reflection of waves from the domain boundaries (Craig and McClymont 1991; Hassam 1992; McClymont and Craig 1996). However, subsequently it was realised that the reconnection reversals can be initiated self-consistently in the absence of reflections from boundaries through the mechanism described below. This was first observed for 2D X-point reconnection (McLaughlin et al. 2009, 2012) and then for 3D spine-fan reconnection (Thurgood et al. 2017), and the process has become known as *oscillatory reconnection*.

The phenomenon of oscillatory reconnection involves a number of key processes. First, the nonlinear evolution (assuming a perturbation of sufficient amplitude) of the wavefront approaching the null leads to a collapse of the null's spine and fan towards one another. This implosion drives the formation of a layer of hot, dense plasma co-spatial with the current layer. The implosion eventually stalls as either resistive or adiabatic heating creates a sufficiently strong outwards pressure ("back pressure") to halt the collapse (here an overshoot occurs leading to a net-outwards force and the launching of an outgoing wave, see Forbes et al. 1982; Thurgood et al. 2018a, b). The structure following this initial implosion is shown in Fig. 60c. Shortly afterwards, reverse current structures appear at the outflow ends of the current sheet (sometimes called deflection currents as they are associated with a fast-mode termination shock in the outflow region, see Forbes and Priest 1983; Forbes 1986). In the same location hot, dense plasma collects, and the associated pressure force chokes off the outflow. The reverse currents then propagate in toward the null point (see Fig. 64a) shortening the current sheet and prising the spine and fan field lines apart. This results in a shortening and widening of the current sheet (and corresponding decrease in the current density) until the opposite polarity currents merge at the null, forming a current sheet with long axis approximately perpendicular to the initial current sheet in the plane of collapse (Thurgood et al. 2017). This repeats cyclically, with each subsequent implosion having less energy than the last due to local dissipation and the outwards transport of energy by outgoing waves. The resulting oscillatory spine-fan reconnection results in flux being transported backwards and forward through the spine and fan (Fig. 64b).

Oscillatory reconnection periodically launches various types of wave outwards from the reconnection site, and has been proposed as a mechanism for explaining "quasi-periodic pulsations" in solar flares (McLaughlin et al. 2018). What is still required in order to relate the theory and simulation results to observations is to understand how the period of the oscillation is influenced by various plasma

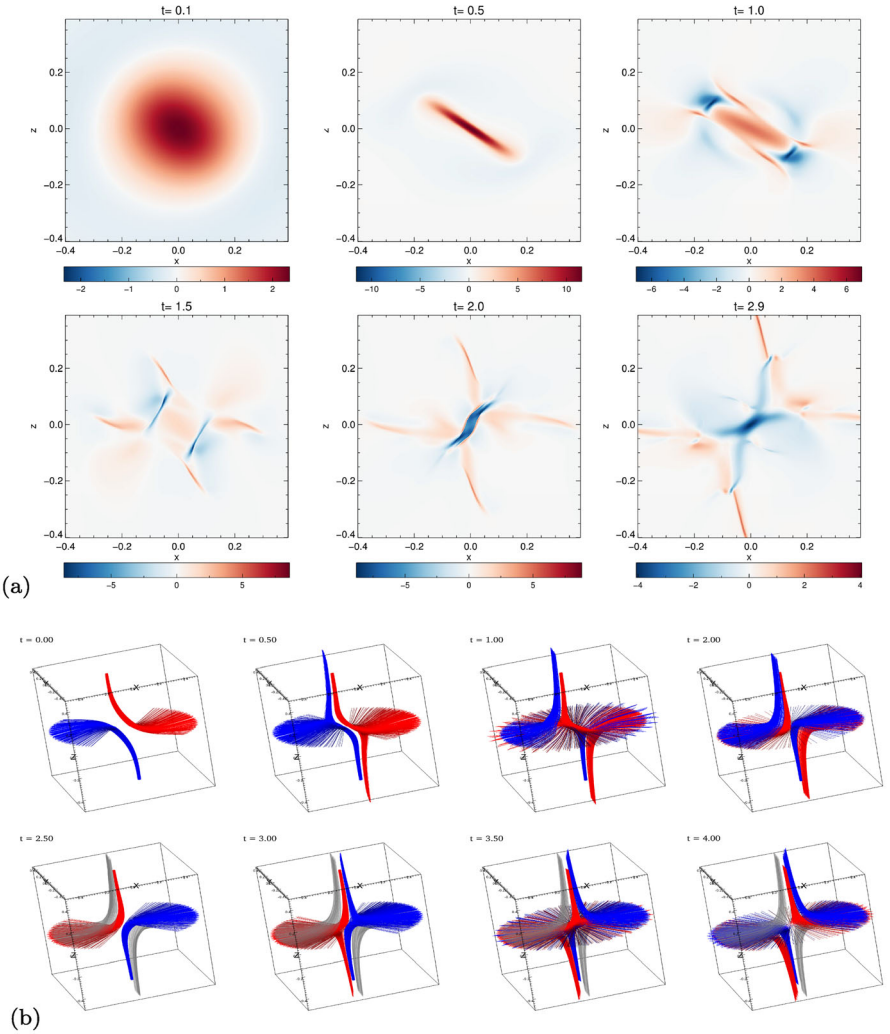

Fig. 64 Oscillatory reconnection simulations. **a** The current component (j_y) perpendicular to the plane of collapse in the plane of collapse ($y = 0$), illustrating the first current reversal. **b** Selected field lines traced from the ideal region, illustrating the cyclic nature of the spine-fan reconnection. Image reproduced with permission from Thurgood et al. (2017), copyright by AAS

parameters, and therefore what periodicities can be expected at coronal parameters. Despite initial studies by Thurgood et al. (2019) this remains an open problem.

10.4 3D null point reconnection in models and observations of the solar corona

The evidence from observations and models of coronal magnetic fields is that different modes of 3D magnetic reconnection (at 3D nulls, separators, QSLs and

otherwise) are important for understanding the dynamics of different phenomena in the solar atmosphere. In this section we highlight a few examples that demonstrate the importance of 3D null-point reconnection in the corona.

For solar flares, often separator or quasi-separator reconnection is involved (as in the new paradigm for solar flares, Sect. 13). However, sometimes the flare energy release site is found on the basis of magnetic field extrapolations to be located at a coronal null point (e.g., Fletcher et al. 2001b; Luoni et al. 2007). Moreover, the spine and fan structures can be directly related to observed emission features, indicating that the volume around the null is involved in the energy conversion (e.g.,

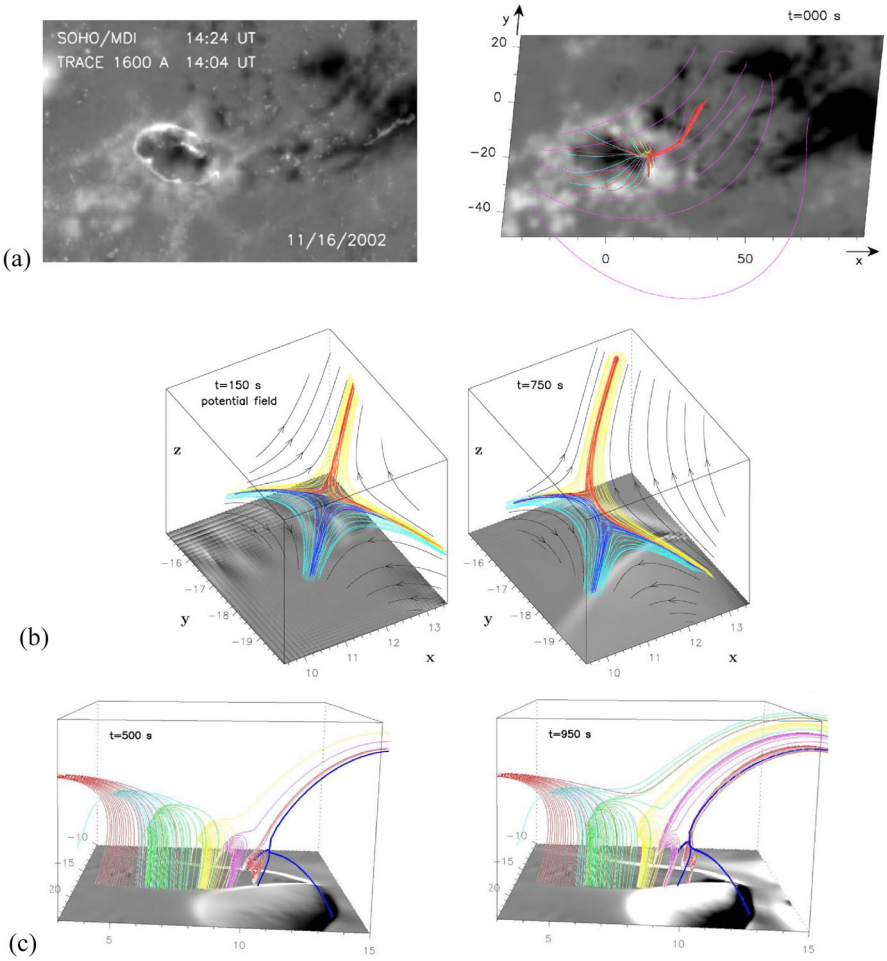

Fig. 65 Observation of a circular ribbon flare and an associated simulation. **a** Observed circular flare ribbon and kernels superimposed on magnetogram, together with field lines from a potential field extrapolation outlining the null. **b**, **c** Snapshots from a simulation starting from that potential field and applying boundary driving that mimicks the observed magnetogram evolution. **b** The collapse of the null during the simulation. **c** The reconnection of selected field lines from inside to outside the separatrix dome. Image reproduced with permission from Masson et al. (2009), copyright by AAS

Sun et al. 2013; Yang et al. 2015). These flares are often observed to exhibit circular flare ribbons, as well as bright "kernels". The circular flare ribbon is formed at the footprint of the null point separatrix dome (see e.g., Figs. 9, 65a), while the kernels are associated with the footpoints of the spine field lines, and are generically observed as elongated ribbons due to the generic asymmetry of the field about the null (Masson et al. 2009; Pontin et al. 2016). By employing boundary flows that mimicked the observed photospheric magnetic field evolution, Masson et al. (2009) demonstrated that the circular ribbon flare they described was likely associated with

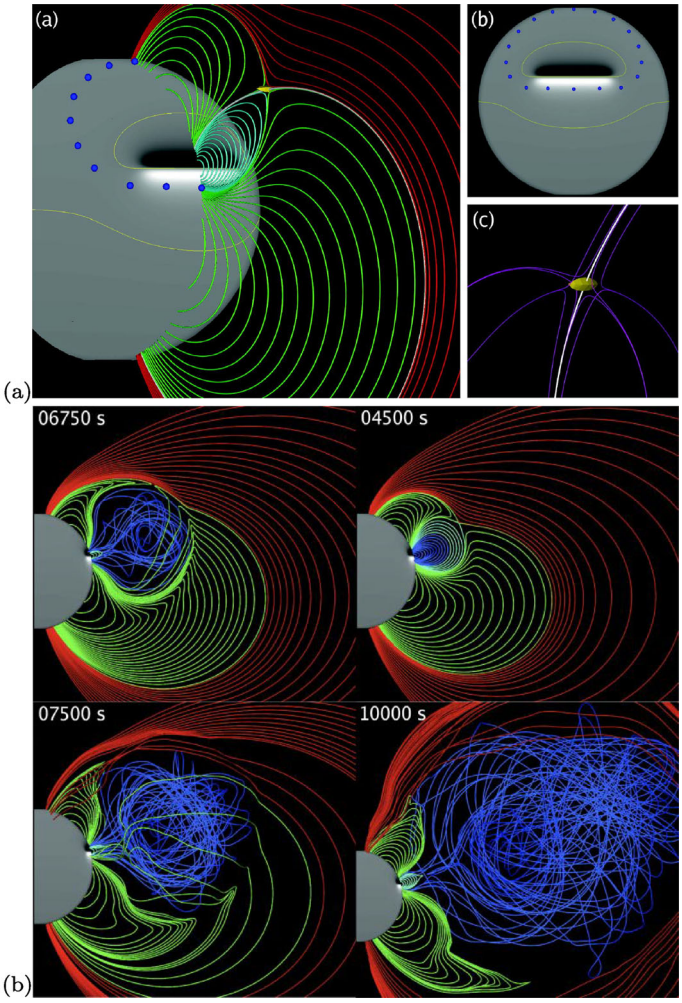

Fig. 66 Simulation of a coronal eruption by magnetic breakout. **a** Initial configuration showing the photospheric polarity distribution, polarity inversion lines, and local magnetic field structure around the null. **b** Frames showing selected field lines during the simulation. Field lines are colour-coded depending on their connectivity. Image reproduced with permission from Lynch et al. (2008), copyright by AAS

spine-fan reconnection and a transfer of flux into and out of the null dome (Fig. 65b, c).

Magnetic nulls have also been implicated in coronal eruptions. One of the leading candidate mechanisms for explaining such eruptions, which requires the presence of a null point topology, is *magnetic breakout*, first proposed by Antiochos et al. (1999). The mechanism involves a quadrupolar flux distribution with an overlying null point topology. During the breakout process, low-lying sheared flux (blue in Fig. 66) expands towards the null, reconnecting with the overlying flux (red) and thereby adding flux to two adjacent flux systems (green) within the quadrupolar topology. The removal of the overlying (or "strapping") flux allows for a more rapid expansion, creating a runaway process and the low-lying, sheared (stressed) flux erupts outwards. A number of observations have reported evidence supporting the breakout mechanism (e.g., Kumar et al. 2021), while studies employing magnetic field extrapolations showed that some erupting active regions support the required type of null point topology while others do not (e.g., Ugarte-Urra et al. 2007). A statistical study by Barnes (2007) revealed that active regions supporting magnetic nulls are more likely to produce eruptions.

The overwhelming majority of models for coronal jets involve null point reconnection in a dome-type topology (Fig. 9). For example, in the models of Török et al. (2009) and Moreno-Insertis and Galsgaard (2013) flux emergence from beneath the photosphere leads to the appearance of a coronal null from below the photosphere (whose separatrix encloses the emerging minority polarity) with the continued emergence of flux stressing the field beneath the dome leading to null collapse, spine-fan reconnection, and plasma outflow along newly opened field lines. A closely related jet model was first proposed by Pariat et al. (2009), and more recently developed further by Wyper and DeVore (2016); Wyper et al. (2016). This model supposes the pre-existence of a null point dome topology, with the field beneath the dome being stressed not by flux emergence but by boundary motions that twist or shear the enclosed flux, creating a filament channel or twisted flux rope beneath the dome. An instability in the system leads to spine-fan null point reconnection, with the twist or stress being transferred to open field lines and driving the jet.

The jet models involve reconnection in a dome topology between magnetic flux from inside and outside the dome. If the null dome is embedded in an "open field" region on the Sun (e.g., a polar coronal hole), then this reconnection is between open and closed magnetic flux, often termed *interchange reconnection* (see Sect. 15.2). This interchange process for an isolated null dome was studied in detail by Edmondson et al. (2010), who noted that the footprint of the null dome must be either entirely in the open field or entirely in the closed field, since topological arguments imply that all fan field lines must have the same connectivity as the (outer) spine field line. When the photospheric motions induce the parasitic polarity to move relative to the surrounding majority polarities, magnetic flux is reconnected into the dome on its "leading" side and out through the dome on the "trailing" side with the characteristic field line flipping of spine-fan reconnection (Fig. 57), as described by Pontin et al. (2013). Interchange reconnection was studied in a more complex geometry involving multiple null points and separators with a separatrix

curtain by Scott et al. (2021) as a model for the dynamic formation of pseudostreamers.

11 Separator reconnection

As described in Sect. 2.3, the fan of a null point consists of a surface of magnetic field lines that link to the null, and so, when two null points are present, the generic (i.e., topologically stable) configuration is one in which their two fans intersect in a special magnetic field line, called a *separator*, which links the two null points (Fig. 6). Such a separator is a natural location for the growth of a strong current, and so for the occurrence of a common type of reconnection, known as *separator reconnection*. Often, in a plane across the separator, the flow and field resemble those of classical two-dimensional reconnection, but the three-dimensional aspects add many new features.

An early ideal, kinematic solution (see Sect. 4.7.1) was presented by Priest and Titov (1996) who considered the field

$$(B_x, B_y, B_z) = [x(z-3), y(z+3), 1-z^2],$$

which has two null points at $z = (0, 0, \pm 1)$ and the z-axis as a separator. Suppose this configuration is bounded by a cuboid of size $2 \times 2 \times 4$, centred at the origin, and prescribe on the sides $y = \pm 1$ a horizontal flow in the x-direction with $v_z = 0$, which drives reconnection at both nulls. The field lines are given by

$$x(z-1)^{-1}(z+1)^2 = C, \quad y(z-1)^2(z+1)^{-1} = K, \tag{96}$$

where each field line has a different value for the constants C and K. For instance, a field line through the footpoint $(x_0, 1, z_0)$ has

$$C = \frac{x_0(z_0+1)^2}{z_0-1}, \qquad K = \frac{(z_0-1)^2}{z_0+1}. \tag{97}$$

If v_z vanishes on $y = 1$, then $E_x B_y = E_y B_x$, which implies a form for the potential of $\Phi = f[\frac{1}{2}x_0^2 + (z_0+1)^{1/2}(z_0-3)^{9/2}(z_0-1)^{-4}]$, where $x_0(C,K), z_0(C,K)$ are given by Eq. (97) and f is an arbitrary function.

11.1 Skeletons from photospheric magnetograms

The results from an early potential field extrapolation of a local photospheric magnetogram from SOHO/MDI are shown in Fig. 67, revealing the presence of many null points produced by the highly fragmented and mixed-polarity nature of the magnetic flux protruding through the solar surface, known as the *magnetic carpet* (Schrijver et al. 1998).

Subsequently, the global coronal topology was calculated by Platten et al. (2014) (Fig. 68). As a lower boundary condition they used SOLIS synoptic magnetograms for a global potential field using a maximum harmonic number of $l = 301$. This revealed 1964 nulls and 1946 separators at solar minimum, but 1131 nulls and 808

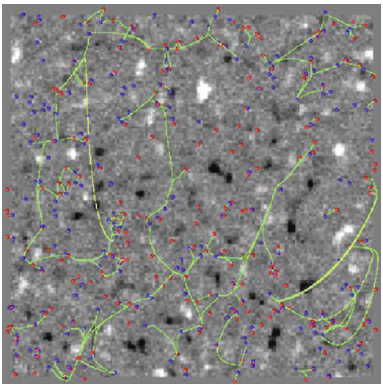

Fig. 67 Local skeleton for the magnetic carpet based on a SOHO/MDI photospheric magnetogram together with a potential field extrapolation. The following topological features are present: positive nulls (red dots), negative nulls (blue dots) and separators (green curves). Image reproduced with permission from Parnell et al. (2011), copyright by Springer

separators at solar maximum. During solar minimum one sees vast areas of the photosphere with small-scale mixed polarity that produce a highly complex network of nulls and separatrices (Fig. 68e).

If much higher-resolution extrapolations using magnetograms from SDO or the SUNRISE balloon were constructed, both local and global skeletons would certainly reveal even greater complexity, containing many more nulls and separators. Moreover, when dynamic configurations rather than equilibria are analysed, they tend to contain even greater topological complexity, as exemplified below.

11.2 Numerical experiments on separator reconnection

Numerical experiments complement analytical theory by allowing more realistic modelling and suggesting new theoretical ideas. 2D experiments are important in complementing 3D experiments, since they can be run at much higher values of the magnetic Reynolds number, but 3D experiments reveal many new features and richer behaviour that are not accessible in 2D or 2.5D.

Separator reconnection has been observed in many 3D MHD simulations. Here we just mention a few such examples that studied the separator reconnection process in detail. In particular, Galsgaard and Nordlund (1997) conducted a pioneering numerical experiment on the complex behaviour of a magnetic field containing eight null points (see below), while Parnell and colleagues determined how the coronal magnetic field reconnects above moving photospheric sources of magnetic field (Sect. 14.4.1). Furthermore, Longcope has discovered how separator current sheets form and dissipate (Longcope and Cowley 1996; Longcope 2001) and how this is likely to work during coronal heating (Priest et al. 2005). The ideas have been applied to the evolution and brightening of an active region (Longcope et al. 2005) and to solar flares (Sects. 11.3, 13).

The experiment by Galsgaard and Nordlund (1997) studied the evolution of a periodic force-free equilibrium with eight null points (Fig. 69a). Footpoint shearing was applied to two of the side boundaries, with periodic conditions on the remaining boundaries. During the evolution, the null points collapse to current sheets, which develop in weak-field tunnels along the separators joining nearby null points

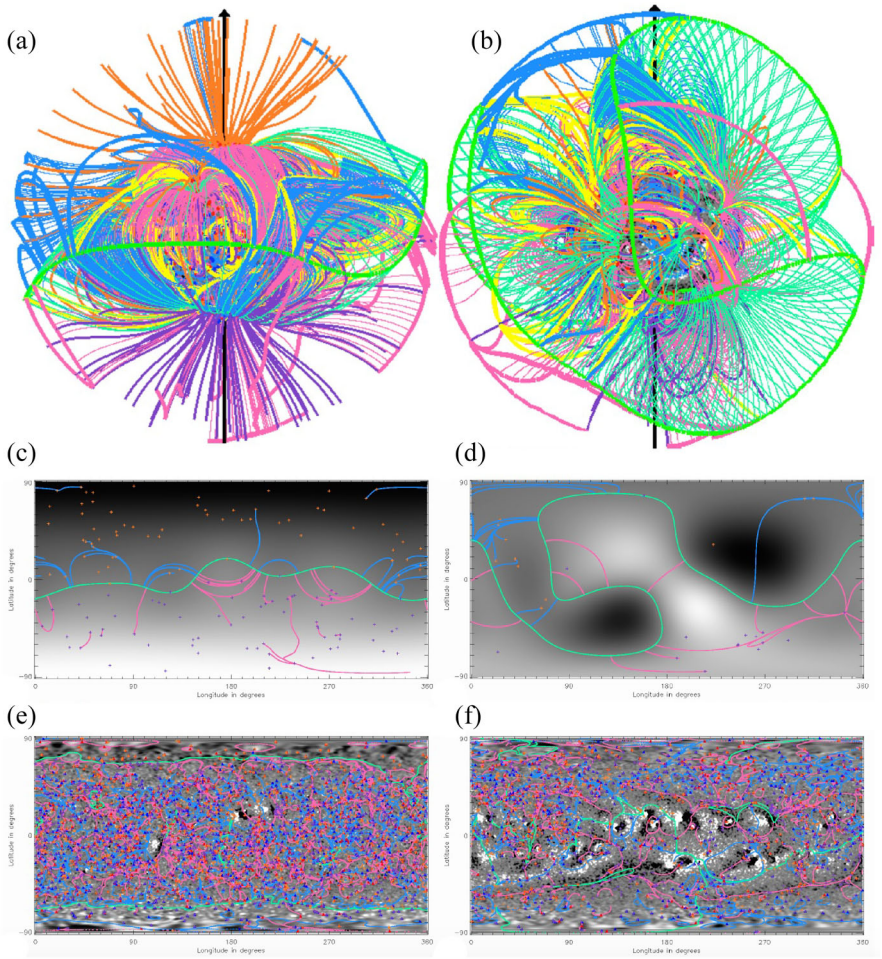

Fig. 68 Global magnetic skeleton using a synoptic photospheric magnetogram and a potential field extrapolation at **a** solar minimum and **b** solar maximum. The following topological features are present: positive nulls (red dots) with spines (purple) and separatrices (thin pink lines); negative nulls (blue dots) with spines (orange), separatrices (thin blue lines); and separators (green curves). The separatrices meet the source surface ($r = 2.5\,R_\odot$) in thick pink and blue curves, while the base of the heliospheric current sheet is indicated by thick green lines, with thin green lines extending down from them to map out the heliospheric current-sheet curtains dividing open and closed fields. (**c**, **d**) give cuts at a radius $r = 2.5\,R_\odot$, while (**e**, **f**) show cuts at $r = 1.005\,R_\odot$ together with the null points. Image reproduced with permission from Parnell et al. (2015), copyright by Royal Society

(Fig. 69b). Then separator reconnection takes place, with Alfvénic jets of plasma ejected from the sides of the sheets, accelerated by Lorentz and pressure gradient forces. Eventually, most of the magnetic connections between the two boundaries are destroyed and arcade-like structures remain, with small-scale current sheets continually forming and dissipating the energy supplied by boundary driving in a statistically steady manner.

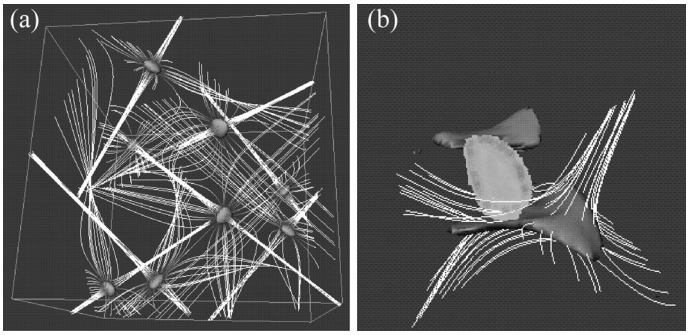

Fig. 69 **a** An initial magnetic field with eight null points. **b** The response to boundary motions is reconnection at the separator joining two of the nulls. For a related movie see Supplementary Information. Image reproduced with permission from Galsgaard and Nordlund (1997), copyright by AGU

11.3 Separators and solar flares

Applications of separator reconnection to coronal heating are described in Sect. 14.4. Here we describe their role in solar flares and in Sect. 13 in the new 3D paradigm for solar flares that has been emerging.

For many solar flares, separator reconnection is a natural explanation (Longcope and Silva 1998), in which energy is stored and liberated by separator reconnection that spreads through the domains of an active region (Longcope and Beveridge 2007; Kazachenko et al. 2010). Here we describe some aspects of modelling, which have played a key role in the development of a new "standard model" for solar flares in three dimensions (Sect. 13).

Longcope et al. (2007) predicted the flare energy release for several active regions, which compared favourably with observations. In practice, the coronal magnetic field is likely to evolve in time through a series of nonlinear force-free equilibria with current sheets along separators, but these are difficult to calculate, and so Longcope (2001) developed a simpler *Minimum Current Corona (MCC)* model. In this model, the photospheric magnetic field is divided into positive (P_i) and negative (N_j) unipolar flux patches, and the flux in the domain joining each patch P_i to every other patch N_j is evaluated. The configuration's *skeleton* is made up of separatrices, which bound the domains and intersect in separators. Reconnection between domains would in reality conserve the total magnetic helicity and create a force-free field in each domain, but, the MCC model assumes for simplicity that the field evolves through a series of *flux-constrained equilibria*, which possess the minimum energy that preserves the domain fluxes and which has current sheets along the separators. Separator reconnection then releases the free energy and transfers flux between domains as the field reduces to a potential one.

A particular active region (Longcope et al. 2007) was partitioned into 28 domains, whose initial skeleton is shown in Fig. 70 and contains 29 nulls and 32 separators. The changes in domain flux by a series of separator reconnections were deduced, which allowed reconnection to spread through the region. The currents lying along each separator were calculated from the flux changes. The released

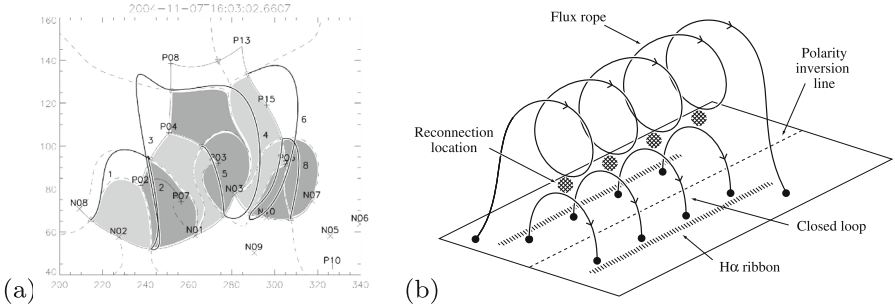

Fig. 70 **a** The skeleton footprint for an active region, showing: positive (+) and negative (×) sources; positive (**∇**) and negative (***Δ***) null points; spines (solid); fan footprints (dashed); separators (thick curves); and domains where flux is being gained (dark) or lost (light). **b** A 3D cartoon for the creation during a flare by reconnection at many locations above a polarity inversion line of a twisted flux rope together with an underlying 3D arcade of flare loops. Images reproduced with permission from Longcope et al. (2007), copyright by Springer

energy here amounted to 8×10^{31} ergs, or 6% of the active-region energy, and the resulting flare ribbons lay along a series of spines joining a set of nulls. The same idea was used by Titov et al. (2012) to understand how a sequence of flares and CMEs is triggered.

In 2D models of a solar flare, reconnection creates a closed field line or magnetic island, but, in 3D models, reconnection at a series of locations instead forms a twisted flux rope and a coronal arcade of flare loops, as indicated in Fig. 70.

However, two important questions about the three-dimensional aspects of a flare are: how do two bright flare knots grow during the rise phase into flare ribbons (Fletcher et al. 2004), while a single loop joining the knots develops into a flare arcade? And what is the nature and magnitude of the resulting twist in the erupting flux rope? These have been addressed in a model for *zipper reconnection* (Priest and Longcope 2017). The core of this is the *zippette process* (Fig. 71a, b) in which two untwisted flux tubes (X_+X_- and Y_+Y_-) overlie an initial flux rope (Z_+Z_-), which then, provided it is energetically favourable, reconnect below Z_+Z_- to create an underlying flux tube (U) from Y_+ to X_- together with a twisted flux rope (R) from X_+ to Y_- that wraps around Z_+Z_-. This process affects a conversion of magnetic shear at the polarity inversion line to twist in the overlying flux rope, as described by, e.g., van Ballegooijen and Martens (1989).

Then, the idea during zipper reconnection is that, before the flare the magnetic configuration in an active region consists of an arcade of coronal loops (A_+A_-, B_+B_-, C_+C_-, D_+D_-) overlying a filament or prominence Z_+Z_-, whose magnetic field is a flux tube that may be untwisted or only weakly twisted (Fig. 71c,i). Here the initiation of the flare, when it is energetically favourable, is due to reconnection starting at one point in the arcade. Thus, during the rise phase, zippette reconnection takes place first of all between, say, A_+A_- and B_+B_- to produce a flux rope A_+B_-, a flare loop B_+A_- and brightening at the feet A_+B_+ and A_- B_-. Next, the reconnection spreads along the polarity inversion line, gradually filling up the flare arcade and the flare ribbons (Fig. 71c,ii).

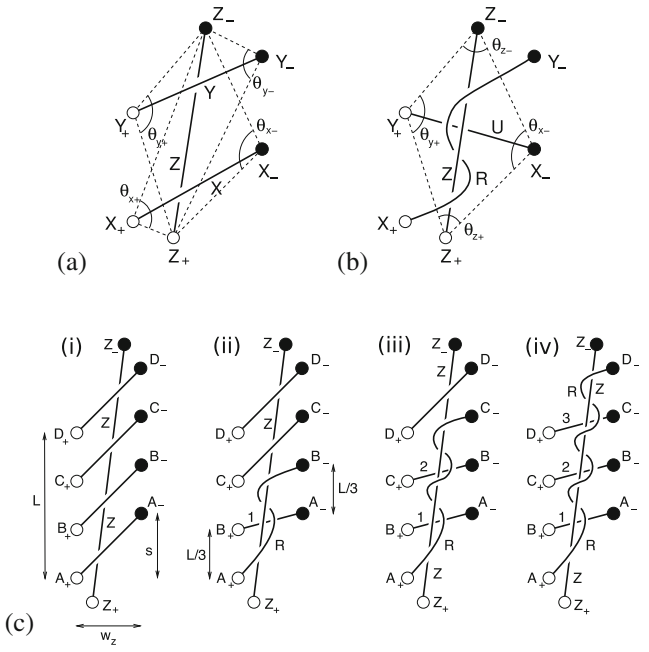

Fig. 71 The creation of twist by the zippette process, namely, reconnection of two coronal loops (X_+X_-,Y_+Y_-) overlying a prominence flux tube (Z_+Z_-) (**a**) to create a twisted flux rope X_+Y_-, whose core is Z_+Z_- (**b**). **c** A zipper model for the creation of flare ribbons and the build-up of twist in an erupting flux rope, by a series of zippette processes. Images reproduced with permission from Priest and Longcope (2017)

First of all, A_+B_- reconnects with C_+C_- to create the twisted rope A_+C_- (Fig. 71c,iii), and later A_+C_- reconnects with D_+D_- to create A_+D_-, and so on. Eventually (Fig. 71c,iv), the ribbons and arcade of hot loops have been created, together with a highly twisted flux rope, the core of which is the initial prominence field Z_+Z_- but whose main part is A_+D_-. After the flare ribbons have formed during the rise phase by zipper reconnection, the ribbons move apart during the main phase by a reconnection process (see Sect. 13) whose location increases in height.

The mechanism by which twist is increased during the 3D reconnection of two magnetic flux tubes, as well as its distribution within the tubes was then analysed in detail (Priest and Longcope 2020). One constraint on this process is provided by the conservation of total magnetic helicity (i.e., mutual helicity plus self-helicity), where mutual helicity can be converted to self-helicity and so create twist. Both a local and a global contribution to this process are present: the local effect is the way twist is added to the tubes by the above helicity equipartition; but there is an additional global effect, namely, that the location and orientation of the flux tube feet tend to add different extra self-helicities to the two flux tubes.

12 Quasi-separator (or HFT) reconnection

12.1 Basic theory of quasi-separator or HFT reconnection

As described in Sect. 2.6, a region in a magnetic configuration where the gradient of the footpoint mapping is large but not infinite is called a quasi-separatrix layer (QSL) (Priest and Démoulin 1995; Démoulin et al. 1996a; Titov et al. 2002); it is located where the squashing factor (Q) is finite but much larger than unity (Sect. 2.6.1). QSLs intersect in quasi-separators, which are surrounded by hyperbolic flux tubes (HFT's) (Sect. 2.6.2). Two examples have been proposed by Titov (2007) of simple configurations that contain QSLs and have been used for modelling flares (Sect. 2.6.2).

Current sheets tend to form in QSLs and in particular at quasi-separators, and so reconnection is likely to take place at them. Indeed, Démoulin et al. (1996a) demonstrated that, when a coronal quasi-separator is present, most smooth motions of the photospheric footpoints will create current sheets, while Titov et al. (2003) proved that a stagnation-point flow at a quasi-separator generates strong currents. This was confirmed by Aulanier et al. (2005) and others with resistive MHD simulations.

When no nulls or separators are present, quasi-separators are preferential locations for reconnection. Thus, in order to study quasi-separator reconnection, it is important first to carefully ensure that no nulls or separators are present. Note that the squashing degree Q, which is used to find QSL locations (Titov et al. 2002; Pariat and Démoulin 2012), does not distinguish between separators and quasi-separators.

Once a QSL has been located, kinematic reconnection may be used satisfying Eq. (31) to deduce the potential (Φ) and field-line velocity Eq. (33). Thus, suppose field-line velocity components $v_{\perp 1x}$ and $v_{\perp 1y}$ are prescribed at a point $(x_1, y_1, 1)$ on the top side $(z = 1)$ of a cube (see Fig. 72). Then the potential $\Phi(x_1, y_1)$ throughout the cube may be calculated, from which follow the electric field $\mathbf{E}$ and plasma velocity $\mathbf{v}_\perp$. On the base $(z = 0)$ of the cube, the resulting electric field components have the form

$$E_{x0} = -\frac{\partial \Phi \partial x_1}{\partial x_1 \partial x_0} - \frac{\partial \Phi \partial y_1}{\partial y_1 \partial x_0}, \qquad E_{y0} = -\frac{\partial \Phi \partial x_1}{\partial x_1 \partial y_0} - \frac{\partial \Phi \partial y_1}{\partial y_1 \partial y_0}.$$

These depend on the imposed electric field ($E_{x1} = -\partial \Phi / \partial x_1$, $E_{y1} = -\partial \Phi / \partial y_1$) at the top boundary, but also on the gradients of the mapping functions $(x_1(x_0, y_0)$ and $y_1(x_0, y_0))$. This implies that $\mathbf{E}_0$ becomes large where the mapping gradients are large—i.e., in quasi-separatrix layers,—and is the key reason why quasi-separators are important locations of reconnection (Priest and Démoulin 1995; Démoulin et al. 1996a; Titov 2007).

As an example, suppose that the magnetic field inside the cube is $\mathbf{B} = (B_x, B_y, B_z) = (x, y, l)$ with l constant (see Fig. 72). Suppose flows with $v_{\perp 1x} = 0, \quad v_{\perp 1y} = v_0 x_1$ are prescribed on the top $(z = 1)$ of the cube and $v_{\perp 1x} = 0, \quad v_{\perp 1y} = \frac{1}{2} v_0$ on the side $(x = \frac{1}{2})$. The resulting flow on the base $(z = 0)$ along $y = 0$ is then

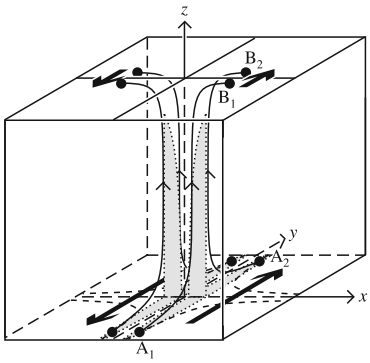

Fig. 72 A magnetic field consisting of an X-type field in the xy-plane together with a uniform field in the z-direction. Quasi-separatrix layers (shaded) are revealed by the large displacement on the bottom of the cube produced by a small footpoint displacement on the top of the cube. Image reproduced with permission from Priest (2014), copyright by CUP

$$v_{\perp y0} = \begin{cases} v_0 x_0/\epsilon^2 & \text{if} \quad |x_0| < \frac{1}{2}\epsilon, \\ v_0/(4x_0) & \text{if} \quad x_0 > \frac{1}{2}\epsilon, \end{cases}$$

(where $\epsilon = \exp(-1/l) \ll 1$) which has a maximum of $v_0/(2\epsilon)$ at $x_0 = \frac{1}{2}\epsilon$. If this exceeds the Alfvén speed, then the approximation of an ideal flow will break down and diffusive layers will tend to form about $x_0 = \pm\frac{1}{2}\epsilon$, where the field lines are likely to slip and flip rapidly through the plasma at speeds quicker than the plasma (Priest and Forbes 1992; Priest and Démoulin 1995). Such flipping is also present in null-point and separator reconnection, and so physically the behaviour of quasi-separator and separator reconnection are very similar. This philosophy has been used in models for solar flares with twisted flux tubes (Démoulin et al. 1996a, 1997a).

Another example is the magnetic flux tube configuration with components $B_x = -(z-a)^2 + b^2(1-y^2/c^2), B_y = d, B_z = x$, where a, b, c, d are constants, as described by Démoulin et al. (1996b). Three kinds of field line are present, namely, below the flux tube, within it and above it, as well as quasi-separatrix layers, with ends that curl up and increase in complexity as the twist increases.

Aulanier et al. (2006) and Pariat et al. (2006) refer to quasi-separator reconnection as *slip-running reconnection*, in view of the *magnetic flipping* process (Priest and Forbes 1992) that is a common feature of all three-dimensional reconnection. They use the term *slip-running* rather than *slipping* or *flipping* in order to emphasise that, when the flux velocity is large enough (i.e., $w > v_A$), the system is likely to generate fast jets of plasma. This flipping or slipping or slip-running can be seen in several movies of the process (Fig. 75).

12.1.1 Slip-squashing factors as a measure of 3D reconnection

Titov et al. (2009) used a time-sequence of magnetic fields and their tangential boundary flows to develop a powerful method for describing reconnection in three-dimensional configurations. The idea is to extend the concept of a squashing factor (Q) to analyze ideal or nonideal evolution. They define two "slip-squashing

factors", namely, a slip-forth squashing factor (Q_{sf}) whose large value identifies flux tubes that are about to be reconnected and a slip-back squashing factor (Q_{sb}) for those that have just been reconnected over a given period of time. The areas swept by such reconnection fronts correspond to the footprints of reconnecting flux tubes.

The rate of change of reconnected magnetic flux is proportional to the voltage drop along field lines (Schindler et al. 1988), but Titov et al. (2009) realised that this can be found at each time from only the initial magnetic field and the boundary flows. They applied it to ideal flows and also to nonideal flows with a slippage between boundary plasma elements and magnetic footpoints. For 2D configurations Forbes and Priest (1984b) had noticed that the electric field at the reconnection site can be found from the speed with which the photosphere is swept by a separatrix field line, and what Titov et al. (2009) did was essentially to generalise this principle to 3D and to QSLs.

Suppose the magnetic field lines have start and end locations at boundary points with coordinates (u^1, u^2) and (w^1, w^2). The corresponding mapping is given by a function $(W^1(u^1, u^2), W^2(u^1, u^2))$ with Jacobian matrix

$$D = \left[\frac{\partial W^i}{\partial u^j}\right]. \tag{98}$$

(a) Ideal evolution

For an ideal evolution, the initial magnetic connection of plasma elements is conserved, and so the field-line mapping Π_t^{ie} at any time t can be written as:

$$\Pi_t^{\mathrm{ie}} = F_t \circ \Pi_0 \circ F_{-t}, \tag{99}$$

where F_t and F_{-t} are tangential boundary flows, forward and backward in time, respectively.

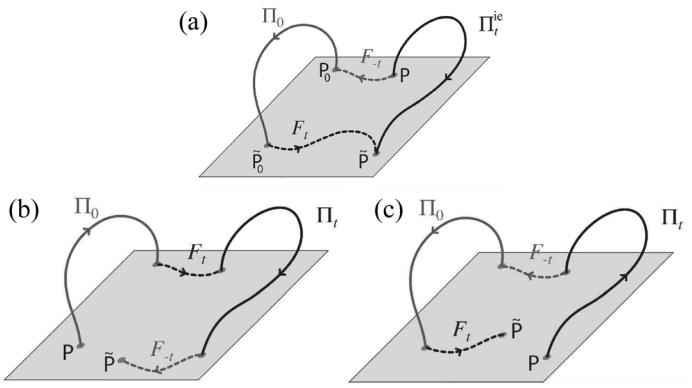

Fig. 73 Illustration of the slip-squashing factor. **a** For ideal evolution, the field-line mapping Π_t^{ie} at any time t may be expressed in terms of the initial field-line mapping Π_0 and the forward and backward boundary flows F_t and F_{-t}. **b** For non-ideal evolution, these are replaced by slip-forth and **c** slip-back mappings acting on the footpoints of field lines. The field lines and trajectories of the footpoints are shown by solid and dashed curves, respectively. Image reproduced with permission from Titov et al. (2009); copyright by AAS

This implies that, for a footpoint P of a given field line, the other footpoint $\tilde{\mathrm{P}} \equiv \Pi_t^{\mathrm{ie}}(\mathrm{P})$ can be found by first tracing the trajectory of P backward in time to find its initial location P_0, then following the field line of the initial configuration to $\tilde{\mathrm{P}}_0$, and finally tracing the trajectory from $\tilde{\mathrm{P}}_0$ forward in time to $\tilde{\mathrm{P}}$ (as shown in Fig. 73a).

The Jacobian matrix D_{ie} of the composite "ideal" mapping (99) is the product of the Jacobian matrices of the three individual mappings $(W^i(w_0), W^p(u_0), W^s(u))$, namely

$$D_{\mathrm{ie}} = \underbrace{\left[\frac{\partial W^i}{\partial w_0^p}\right]^{**}}_{M^{**}} \underbrace{\left[\frac{\partial W_0^p}{\partial u_0^s}\right]^{*}}_{D_0^*} \underbrace{\left[\frac{\partial U_0^s}{\partial u^j}\right]}_{M^{-1}},$$

which enables the corresponding squashing factor Q_{ie} to be written

$$Q_{\mathrm{ie}} = \frac{\mathrm{tr}(D_{\mathrm{ie}}^{\mathrm{T}}\, G^{***}\, D_{\mathrm{ie}}\, G^{-1})}{|\det(D_{\mathrm{ie}}^{\mathrm{T}}\, G^{***}\, D_{\mathrm{ie}}\, G^{-1})|^{1/2}}$$

in terms of the matrix

$$G = \left[\frac{\partial \boldsymbol{R}}{\partial u^i} \cdot \frac{\partial \boldsymbol{R}}{\partial u^j}\right] \tag{100}$$

associated with the footpoint motion, where double and triple asterisks denote double and triple pullbacks referred to conjugate footpoints. For details, see Titov et al. (2009).

This three-part calculation of the Jacobian matrix and squashing degree may at first seem complex, but it has the key advantage over the normal method (Eq. 98) that the magnetic field data is used only for the initial state, without calculating the evolution of the new magnetic configuration in time.

(b) Nonideal evolution

When the evolution is nonideal, the footpoints slip relative to their motion in the ideal MHD mapping. The resulting behaviour may be described in terms of a *slip-forth mapping* for a slippage (S_t) *forward* in time from 0 and t (Fig. 73b)

$$S_t = \Pi_0^{\mathrm{ie}} \circ \Pi_0,$$

and a *slip-back mapping*, describing a slippage (S_{-t}) backward in time from t to 0 (Fig. 73c)

$$S_{-t} = \Pi_t^{\mathrm{ie}} \circ \Pi_t.$$

The slip-forth mapping S_t highlights differences in magnetic connectivity between the non-ideal and ideal configurations for the initial observer, whereas the slip-back mapping S_{-t} does so for the final observer. The footpoint slippage in a time t is determined simply by the magnetic field at the initial or final time and the footpoint displacements. Furthermore, the resulting squashing factors allow us to identify

reconnecting magnetic flux tubes in any evolving configuration, even if its evolution involves a substantial resistive diffusion.

The corresponding Jacobian matrices may be determined and the resulting squashing factors are

$$Q_{\rm sf} = \left(\frac{g^{***}g_0^{*}}{g^{**}g_0^{****}}\right)^{1/2}\left|\frac{B_n^{***}B_{n0}^{*}}{B_n^{**}B_{n0}}\right|\frac{\mathrm{tr}\left(D_{\rm sf}^{\rm T}\,G_0^{****}\,D_{\rm sf}\,G_0^{-1}\right)}{\det\left(M^{-1***}\,M^{*}\right)}$$

for the slip-forth mapping and

$$Q_{\rm sb} = \left(\frac{g_0^{***}g^{*}}{g_0^{**}g^{****}}\right)^{1/2}\left|\frac{B_{n0}^{***}B_{n}^{*}}{B_{n0}^{**}B_{n}}\right|\frac{\mathrm{tr}\left(D_{\rm sb}^{\rm T}\,G^{****}\,D_{\rm sb}\,G^{-1}\right)}{\det\left(M^{***}\,M^{-1*}\right)}.$$

for the slip-back mapping.

Titov et al. (2009) applied the theory to two examples. The first was the rise of a flux rope without null points and the second was reconnection in a sheared force-free field, which forms flux tubes with narrow, ribbon-like footprints. The theory has advantages over general magnetic reconnection (GMR) theory (Schindler et al. 1988; Hesse et al. 2005), since it treats regions with small or large amounts of reconnected flux on an equal footing and also discriminates between reconnection and simple diffusion much better.

12.2 Quasi-separator reconnection in solar flares

Investigating the role of quasi-separator reconnection in eruptive and confined flares has been pioneered by Démoulin and colleagues, with both observations and numerical simulations. For example, Démoulin et al. (1997a) compared observed solar flares with calculated QSLs and found that chromospheric knots and ribbons often lie along the QSLs. Also, Démoulin et al. (1996b) showed analytically that QSLs tend to wrap around flux ropes and represent a boundary between different classes of field line (Fig. 74). Their intersection with the lower boundary forms a shape that is typical of observed flare ribbons (Chandra et al. 2009).

Comparisons of QSL locations with Hα flare brightenings have been performed using both linear (Démoulin et al. 1997a; Schmieder et al. 1997; Bagalá et al. 2000; Mandrini et al. 2006; Chandra et al. 2011) and nonlinear (Savcheva et al. 2012, 2015; Zhao et al. 2016; Su et al. 2018) force-free extrapolations. The intersections of QSLs with the photosphere are often double J-shaped and match well the locations of chromospheric flare ribbons, and the 3D structure of QSLs surrounds a flux rope and resembles an S-shaped sigmoid.

Flipping or slipping of field lines takes place in all 3D reconnection models. It has been clearly demonstrated in, for example, a 3D numerical resistive experiment on quasi-separator reconnection (Aulanier et al. 2006), as shown in Fig. 75. The distant footpoints of red and black field lines are held fixed, and it can be seen that the near red footpoints flip from right to left, while the black footpoints flip from left to right. A similar process occurs with cyan and green field lines.

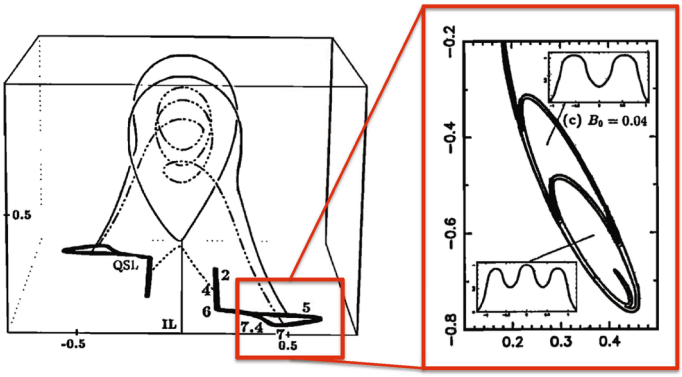

Fig. 74 A model of a twisted flux rope, indicating field lines at its edge (solid) and near its central part (dash-dotted), together with a small underlying arcade (dotted). Also shown are the QSL footprints forming two elongated strips either side of the polarity inversion line and a zoom of the hook-shaped part which encloses the footprints of the flux rope. Image reproduced with permission from Démoulin et al. (1996b), copyright by AGU

Janvier et al. (2013) have simulated a solar flare driven by the eruption of a flux rope containing a QSL (Fig. 76). The slippage speed of the footpoints is proportional to the strength of the QSL. Such simulations and observations led Aulanier and colleagues (Aulanier et al. 2012, 2013; Kliem et al. 2013; Janvier et al. 2014) to propose some 3D additions (see Sect. 13) to the standard 2D CSHKP flare model (Fig. 77). During the expansion of the flux rope, high current surfaces are formed along the separatrices or QSLs of the flux rope which form a cusp-shaped HFT, while their footprints produce flare ribbons that have a double J shape. Reconnection within the current layers creates flipping within the flare ribbons (Savcheva et al. 2012; Zhao et al. 2016).

Separator and quasi-separator models of flares both imply flipping or slipping of loop footpoints in both directions along flare ribbons. One direction towards the ribbon hook builds up the twist in the erupting flux rope, while the opposite direction gives rise to slippage of flare loops. Many observations of these features have now been made, especially with SDO. Aulanier et al. (2007) observed fast

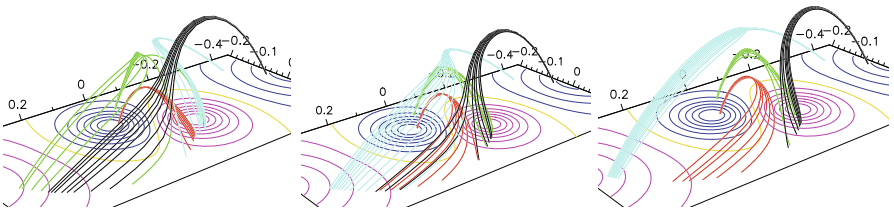

Fig. 75 The flipping or slipping of field lines in a numerical simulation of quasi-separator reconnection. Positive (negative) polarity magnetic fields are indicated by pink (blue) contours. Four sets of magnetic field lines (red, black, cyan and green lines) are integrated from fixed footpoints and their conjugate footpoints gradually flip or slip along arc-shaped trajectories. For related movies see Supplementary Information. Image reproduced with permission from Aulanier et al. (2006), copyright by Springer

bidirectional slippage of coronal loops. Dudík et al. (2014) reported slipping speeds along ribbons of several tens of km s^{-1}. Li and Zhang (2014) found one end of an eruptive flux rope was fixed, while the other end showed a slippage along a hook-shaped flare ribbon. Li and Zhang (2015) compared observations from SDO and IRIS and found small-scale bright knots moving along flare ribbons in quasi-periodic patterns with a period 3–6 minutes, together with slippage of the flare loops along the ribbon at a speed of 20–110 km s^{-1}. Dudík et al. (2016) observed flare loops slipping in opposite directions at speeds of 20–40 km s^{-1}, but even faster velocities (400–450 km s^{-1}) have sometimes been seen (Zheng et al. 2016; Lörinčík et al. 2019a). In addition, Jing et al. (2017) saw ribbon slippage in a long-duration flare over a long distance (~ 60 Mm).

In eruptive flares, the 3D reconnection geometries are more complex than in 2D. During the rise, the flare ribbons are formed by sequential brightening along the polarity inversion line before they begin to move apart during the main phase (Fletcher 2009; Li and Zhang 2014; Li et al. 2016; Chen et al. 2019a; Lörinčík et al. 2019b; Zemanová et al. 2019; Dudík et al. 2019; Aulanier and Dudík 2019). This process of ribbon formation has been modelled by Priest and Longcope (2017) in terms of zipper reconnection (Sect. 11.3).

In confined solar flares, both separator and quasi-separator reconnection have been shown to play a role (Li et al. 2019, 2020), through, for example, the observation of bi-directional slippage along the ribbons (Li et al. 2018). Furthermore, both separators and quasi-separators may be important for coronal heating (Wang et al. 2000; Fletcher et al. 2001a; Schrijver et al. 2010). For example, a study by Schrijver et al. (2010) compared bright loops fanning out from active regions with maps of the squashing degree (Q), which suggest magnetic energy release at separators or quasi-separators.

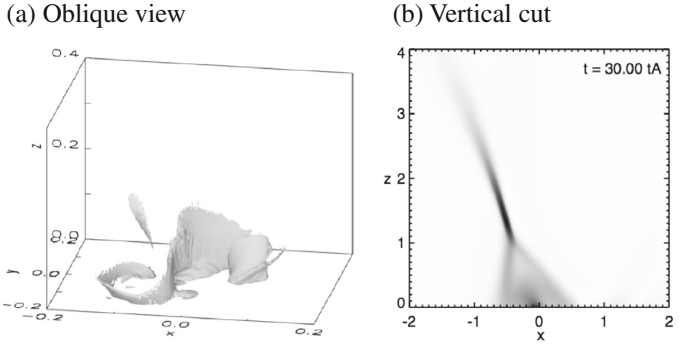

Fig. 76 A numerical simulation of an erupting flux rope, showing **a** the isosurface of a current sheet underlying the flux rope, and **b** a vertical section through the electric current. Images reproduced with permission from (**a**) Kliem et al. (2013), copyright by AAS; and (**b**) Janvier et al. (2013), copyright by ESO

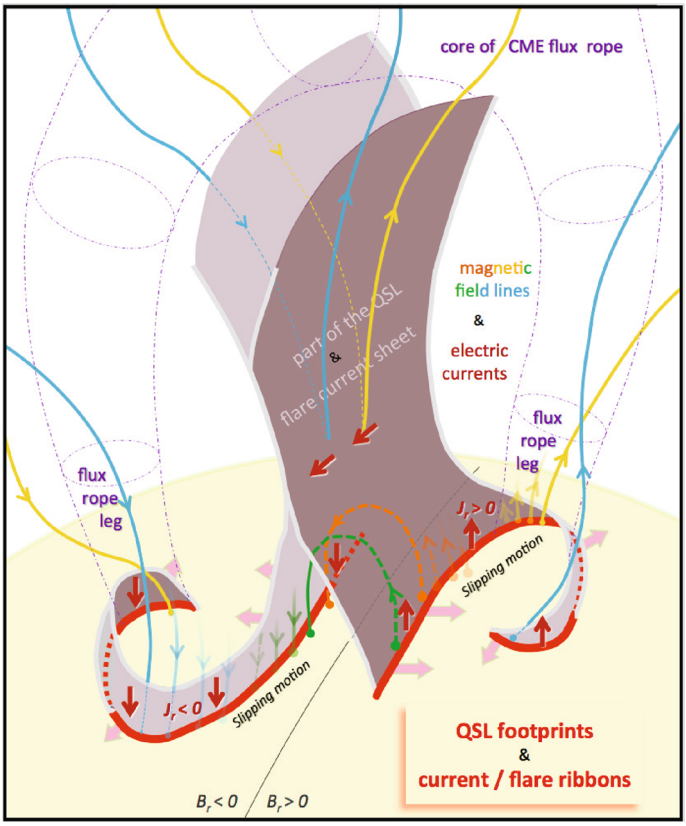

Fig. 77 A cartoon for a 3D model of eruptive flares, showing a QSL (grey) wrapping around an erupting flux rope, together with the outer envelope of the flux rope (blue and yellow) and flare loops that are newly formed by reconnection (green and orange). Image reproduced with permission from Janvier et al. (2014), copyright by AAS

13 New 3D paradigm for solar flares

For many years the CSHKP "standard model" for solar flares (Carmichael 1964; Sturrock 1966; Hirayama 1974; Kopp and Pneuman 1976) has been based on an essentially two-dimensional understanding of magnetic topology and the reconnection process. More recently, modelling of flares in 3D geometries and the associated properties of the 3D reconnection processes has led to a substantial refinement of these ideas, leading to a "standard model in 3D" or a "new paradigm" for solar flares. This new picture has emerged through a range of observational, theoretical and computational studies [see e.g., Sects. 10.4, 11.3, 12.2 and, for a more complete review Janvier (2017)] and has been synthesised into a complete picture in a series of papers by Aulanier and colleagues (Aulanier et al. 2012, 2013; Janvier et al. 2013, 2014), and by Li et al. (2021).

In some cases the flare is eruptive, and in others the overlying magnetic field is strong enough to inhibit the eruption and produce a confined fare. In some cases the

basic magnetic configuration is bipolar and in others it is multipolar. In the latter case, the basic process of eruption may be similar to the former case but the resulting field more complex, or the multipolar nature may be crucial to some aspects of the flare process, as in the breakout model (e.g., Antiochos et al. 1999). Whether the boundary conditions for modelling are assumed to be smooth or source-like does not greatly effect the resulting flare process, since in the former case quasi-separators are more common, but the resulting reconnection is very similar to the separator reconnection that is more common in the latter case.

The basic picture of the new 3D paradigm for flares is described below. The first two properties are taken over from the standard 2D paradigm, while later properties come from detailed comparisons of observed flares with flare models involving separator reconnection or quasi-separator reconnection. The properties apply equally to both scenarios. By contrast, flares involving 3D null-point reconnection exhibit circular ribbons, so that certain properties, such as (viii) are less relevant.

(i) A magnetic flux rope erupts and drives the formation of a current sheet below the flux rope; the eruption itself is probably caused by magnetic nonequilibrium or instability, although there remains some debate about this (e.g., Aulanier 2013), in particular whether the cause is an ideal process such as torus or kink instability (e.g., Kliem and Török 2006) or whether reconnection itself is integral to the early stages of the eruption (e.g., Antiochos et al. 1999);

(ii) Magnetic field reconnects at the current sheet, creating an arcade of flare loops with chromospheric ribbons at their feet; the arcade rises and the ribbons separate as the height of the reconnection location increases;

(iii) At low spatial and temporal resolution, the reconnection may appear quasi-steady and laminar, but, at high resolution, it is often impulsive and bursty in time and fragmented in space (e.g., Karpen et al. 2012; Naus et al. 2021); for example, during the main phase, supra-arcade downflows are often present (McKenzie and Savage 2009; Longcope et al. 2009, 2018);

(iv) Since reconnection starts at one location in the current sheet, it first creates two kernels of chromospheric emission; then, during the flare rise phase, reconnection spreads along the sheet above the polarity inversion line; this gradually energises the whole coronal arcade and forms the flare ribbons by zipper reconnection (Priest and Longcope 2017); then, during the main phase, the ribbons move apart;

(v) Some of the twist in an erupting flux rope may have been present before the eruption, but most of it is created during the process of 3D reconnection due to the conversion of mutual magnetic helicity into self-helicity (Wright and Berger 1989; Priest and Longcope 2020), or in other words conversion of magnetic shear at the polarity inversion line to twist in the overlying flux rope (van Ballegooijen and Martens 1989);

(vi) Two main types of 3D reconnection may occur during flares, namely, null-point reconnection, which tends to create flare ribbons that are roughly circular in shape (see Sect. 10.4), and separator (or quasi-separator) reconnection, which creates ribbons that are roughly straight or S-shaped;

(vii) Active regions can possess a topology (or quasi-topology) that is highly complex and split into many different domains (or quasi-domains) bounded by

separatrix (or quasi-separatrix) surfaces. Magnetic reconnection between different domains (or quasi-domains) occurs at separators (or quasi-separators), which allows the energy release to spread from one domain (or quasi-domain) to another; the flare ribbons follow a sequence of spines (or quasi-spines) (Longcope and Beveridge 2007; Kazachenko et al. 2012); similarly, a series of coronal eruptions may be understood as a series of separator (or quasi-separator) reconnections between different regions (Titov et al. 2012);

(viii) Flare ribbons can possess hook-like ends (see Fig. 74 and Démoulin et al. 1996b; Li and Zhang 2014), which represent the ends of flux ropes that are bounded by quasi-separatrix (or separatrix) surfaces (Janvier et al. 2014);

(ix) Flipping or slipping of magnetic fields is a property of all 3D reconnection mechanisms (see Sect. 4.4 for the general result and Sects. 10–12 for explicit descriptions) and can be observed in the behaviour of flare loops and their footpoints (Mandrini et al. 1991; Dudík et al. 2016).

14 Chromospheric and coronal heating by reconnection

In this section, we discuss models for explaining chromospheric and coronal heating by reconnection in braided (Sect. 14.1) or kink-unstable twisted fields (Sect. 14.2), by flux tube tectonics at separatrices or QSLs (Sect. 14.3), and, finally, by separators and flux cancellation (Sect. 14.4).

14.1 Reconnection in braided magnetic fields

Reconnection in braided magnetic fields has been studied in detail for some time in the context of the coronal heating model proposed by Parker (1972). A detailed review is provided by Pontin and Hornig (2020), and we limit ourselves to a brief discussion here. In this context a *magnetic braid* is a field in which all field lines connect two simply-connected polarity regions on the boundary (often opposite, plane-parallel boundaries) without nulls points or separatrices. Usually we have in mind some configuration in which the field lines are tangled around one another in some non-trivial way. Quantifying this tangling requires a measure of the mutual winding of field lines around one another (e.g., the *winding number* Prior and Yeates 2014; Candelaresi et al. 2018) or the rate of separation of neighbouring trajectories, such as the *finite-time topological entropy* (e.g., Budišić and Thiffeault 2015; Candelaresi et al. 2017, and references therein). The former is related to the field line helicity (see Sect. 4.6.4), which can be obtained from the winding number by weighting it with respect to the magnetic flux (in an appropriate gauge). Broadly speaking, larger values of the winding number with variations over shorter length scales correspond to high braid complexity. The complexity can also be revealed qualitatively by visualising gradients of the field line mapping, e.g., by plotting Q, as in the lower panels of Fig. 30.

14.1.1 Flux braiding simulations: continuous driving

In one class of model, the two opposite magnetic polarity regions on the boundaries are subjected to driving flows that are applied continually. Different driving flows that mimic, in some sense, observed photospheric flows have been employed, ranging from shearing flows to arrays of vortices. In all such simulations, thin ribbons of current rapidly form (for the reasons discussed in Sect. 5.5.3) and then dissipate throughout the domain. These current ribbons are always elongated in the direction along the field—see Fig. 78.

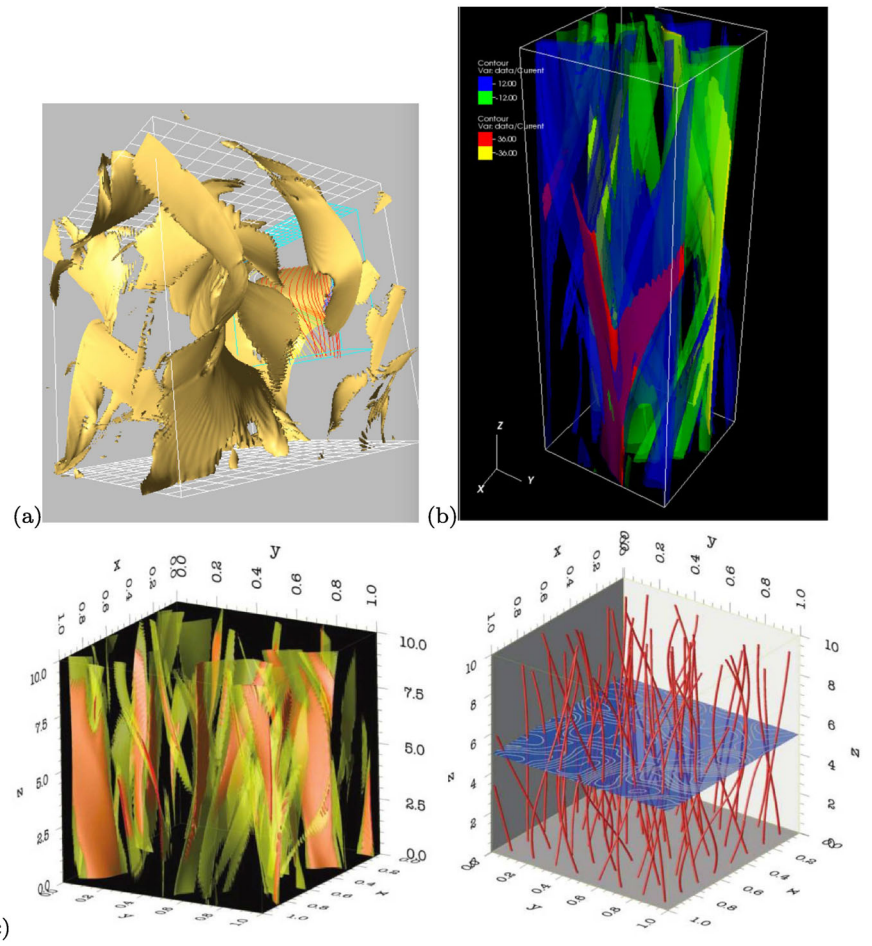

Fig. 78 Illustrations of the statistically steady state attained in three flux braiding simulations. **a** Current isosurfaces and magnetic field lines in the simulation of Galsgaard and Nordlund (1996) (for a unit cube). **b** Current isosurfaces in the simulation of Ng et al. (2012). **c** Current isosurfaces (left) and magnetic field lines (right) in the simulation of Rappazzo et al. (2007, 2008). Images are reproduced with permission from the corresponding papers, copyright by AGU and AAS

Within the current ribbons that form throughout the domain, magnetic reconnection takes place. The net effect of these reconnection processes is to relieve the stress that is added to the system by the driving flows. Qualitatively, the driving flows tend to increase the field line tangling (see above), while the reconnection tends to reduce the tangling. Eventually, a statistically steady state is reached in which (for example) the magnetic and kinetic energies fluctuate about some mean value, and the aim of many such studies is to examine the properties of this steady state.

A handful of flux braiding simulation studies solve the full MHD equations (e.g., Galsgaard and Nordlund 1996; Dahlburg et al. 2012; Ritchie et al. 2016), while many others solve the reduced MHD equations (e.g., Longcope and Strauss 1994; Dmitruk and Gómez 1999; Ng et al. 2012; Rappazzo et al. 2007, 2008) or make other simplifications such as assuming a constant density (e.g., Hendrix and Van Hoven 1996). While the different approaches yield some detailed differences, the broad understanding gained from these simulations can be summarised as follows. First, an anisotropic turbulent cascade develops (the anisotropy being introduced by the dominant field component along the loop). The properties of the turbulence—for example the scaling exponents in the inertial range—depend on various properties of the system, including but not limited to the length of the "loop" and the axial field strength (e.g., Dmitruk and Gómez 1999; Rappazzo et al. 2007, 2008). While the magnetic energy in the domain is dominated by the axial field, a "free" magnetic energy builds up associated with the field line tangling (i.e., the free magnetic energy is the energy in excess of the initial potential field energy). In the statistically-steady state this free magnetic energy is greater by a factor of 10–40 than the kinetic energy (e.g., Rappazzo et al. 2007; Ng et al. 2012; Ritchie et al. 2016). However, the free magnetic energy is also found to scale with R_m, as well as with the driving speed (e.g., Galsgaard and Nordlund 1996).

Crucial for understanding the implications for coronal heating is to determine the way in which the energy dissipation scales with various parameters, notably R_m, which is many orders of magnitude larger in the corona than in the simulations. Based on a dimensional analysis, Rappazzo et al. (2007, 2008) argue that the dissipation should scale with

$$f = \frac{l_\perp v_A}{L u_{ph}}, \tag{101}$$

and, on the basis of a phenomenological model of the turbulence, they propose a coronal heating dissipation rate with the following scaling

$$\epsilon \sim l_\perp^2 \rho v_A u_{ph}^2 \left(\frac{l_\perp v_A}{L u_{ph}}\right)^{\alpha/(\alpha+1)}, \tag{102}$$

where α is the scaling index for the turbulence model, $l_\perp$ and L are the loop diameter and length, respectively, and u_{ph} and v_A are the driving speed and Alfvén speed in the loop, respectively. α is found to be $\alpha \approx -5/3$ for weak axial magnetic fields and large L, whereas $\alpha < -5/3$ for strong axial magnetic fields and small L. Like Galsgaard and Nordlund (1996), they argue that the energy dissipation is likely to be

independent of R_m for $R_m \geq 10^3$. Also, Ng et al. (2012) argue that this should be the case if the energy dissipation time-scale is larger than the correlation time of the driving flow.

The specific geometrical pattern of the driving flow has minimal effect on the energy dissipation (Rappazzo et al. 2010). However, global properties of the driving such as the helicity injection rate or correlation/turnover time may affect the characteristics of the energy release events. Both Ritchie et al. (2016) and Knizhnik et al. (2019) show that, when the net helicity injection is non-zero, large-scale twist builds up in the domain. In the simulations of Ritchie et al. (2016), this leads to intermittent large energy release events that are probably due to a generalised kink instability.

In considering the implications for heating the corona, it is important to note that much of the complexity of the coronal field is absent from the models so far. In particular, on the Sun magnetic flux does not penetrate through the photosphere in a homogeneous field (as in the models) but in concentrated flux fragments, and this may contribute substantially to chromospheric and coronal heating, making it highly inhomogeneous in space and time (Priest et al. 2002). Furthermore, Klimchuk and Antiochos (2021) argue that the heating of the corona in response to braiding-type motions should not be considered as a traditional turbulent cascade. Instead they argue that the coronal field evolves largely quasi-statically, with occasional bursts of energy conversion taking place in myriad small current sheets that form and dissipate throughout the volume in response to processes distinct from a turbulent inertial range.

14.1.2 Flux braiding simulations: relaxation approach

The studies described in the previous section attain a statistical balance between energy injection by boundary motions and energy dissipation (mediated by reconnection). However, there is a large disparity between the plasma properties in the corona and in the simulations (especially R_m), so that any conclusions rely on the uncertain extrapolation of parameter space. A complementary approach is to separate the field line braiding process from the energy release allowing a deeper understanding of each process.

As described in Sect. 5.5.3, various ideal MHD flux braiding studies revealed the exponential thinning of current sheets as boundary driving proceeds, in the absence of reconnection. On the basis of one such study, Pontin and Hornig (2015) estimated the degree of tangling required to initiate reconnection in these current sheets at coronal parameters (appealing, for example, to the onset criterion for nonlinear tearing).

The details of the flux evolution during a resistive MHD relaxation process—commencing from an initially braided magnetic field—were studied in a series of papers by Wilmot-Smith et al. (2010, 2011) and Pontin et al. (2011b). In these simulations, the magnetic field is line-tied at the boundaries, where the flow is set to zero. The field and plasma evolution proceed via a decaying turbulent cascade (with a power-law slope close to $-5/3$; Pontin et al. 2016) with many current sheets

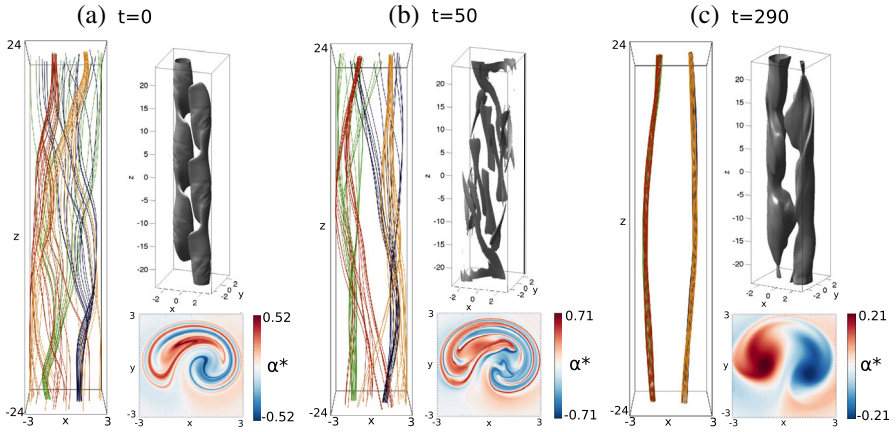

Fig. 79 Magnetic field lines and currents during the resistive relaxation (turbulent decay) of a magnetic braid. Shown at each time are magnetic field lines traced from two fixed rings of points on the line-tied boundaries (red and orange from $z = 24$, green and black from $z = -24$), a current isosurface (at 50% of the spatial maximum at that time), and the distribution of $\alpha^\star = \mathbf{j} \cdot \mathbf{B}/B^2$ on $z = -24$. At the initial and final times the currents are on large spatial scales, while at $t = 50$ many individual current layers are present. The simplification in the field line structure ("unbraiding") can be seen qualitatively from the field lines, and also by examining $\alpha^\star$ (which is constant along field lines in a force-free equilibrium, which the initial and final states at $t = 0$ and $t = 290$ approximate). For related movies see Supplementary Information. Image reproduced with permission from Pontin et al. (2016), copyright by AIP

forming and dissipating, until the system attains a new equilibrium (see also Rappazzo and Parker 2013). The final equilibrium has a much simpler field line topology, with tangling of field lines absent, but instead a large-scale twist remains in the field (see Fig. 79). The presence of this large-scale twist is inconsistent with the relaxation hypothesis of Taylor (1974), in which the only constraint on a turbulent relaxation is the total magnetic helicity. This implies that the total helicity (which is zero by symmetry for the braids considered) cannot be used to predict the final state, and has led to the discovery of additional topological constraints, such as the *topological degree* of the braid (Yeates et al. 2010, 2015) and the field line helicity spectrum (Russell et al. 2015) (see Sect. 4.6.4). Indeed, in Fig. 79 the final state has two twisted flux tubes which are predicted by conservation of the topological degree and field line helicity but not by conservation of helicity alone.

To determine the global reconnection rate during the simulations, Pontin et al. (2011b) identified the local reconnection rate associated with each current layer (maximal integrated $E_\parallel$ along field lines threading each current layer, see Eq. 44). The net effect of all of these reconnection events is that field lines traced from either end of the domain are seen to "wander" across the opposite boundary (see Fig. 79 and associated animation)—recall that the plasma velocity is zero on the boundaries, so this motion is entirely associated with the flipping of field lines in 3D reconnection. Explicitly, the red and orange field lines are traced from fixed points anchored in the plasma on the upper boundary, with their motion on the lower boundary exhibiting the flipping field line velocity (say $\mathbf{w}_{\text{in}}$, see Sect. 4.7.2) created by the multiple reconnection events within the loop. Conversely, the green and

black (yellow in the animation) field lines are anchored in the plasma on the lower boundary, and flip at the virtual velocity $\mathbf{w}_{\text{out}}$ on the upper boundary.

It is noteworthy that the net flux reconnected during the evolution (found by integrating the reconnection rate over time) is found to be larger than the total flux associated with the field line tangling at $t = 0$. This indicates that each flux bundle is reconnected multiple times in order for the global field to unbraid (cf. the multiply reconnected flux in the fly-by experiments described in Sect. 14.4.1). Simulations with different values of R_m reveal that the number of current layers, total relaxation time, and total flux reconnected all increase with R_m. The peak reconnection rate in any one current layer is smaller for larger R_m, but there are more individual current layers formed, and the global reconnection rate depends at most weakly on R_m.

14.2 Reconnection following a kink instability

Reconnection in or between loops in the corona may be initiated by an ideal instability. In the case of the coalescence instability the reconnection occurs in a pre-existing HFT (hyperbolic flux tube). By contrast, in the kink instability there is no special feature in the field line mapping prior to reconnection. The detailed evolution following a kink instability in a resistive plasma was explored by Browning et al. (2008). They described the fragmentation of the initial helical current sheet, leading to the formation of many current sheets located at different radii from the loop axis, and consequently a relatively uniform heating of the loop plasma. The reconnection of field lines at many locations in the loop results in the same qualitative behaviour as in the braid relaxation simulations discussed in the previous section, with field lines traced from one end of the loop appearing to wander across the opposite boundary.

These results have been extended to consider multiple adjacent twisted flux tubes, both for initially twisted loops (Hood et al. 2016) and for the case where the twist is injected by discrete vortical driving flows on the boundaries (Reid et al. 2018). It turns out that the onset of the kink instability in one loop can add twist to a second adjacent loop (previously stable to the kink mode) in such a way as to induce instability in the second loop. The ensuing evolution takes the form of an *avalanche*, as each instability triggers adjacent flux tubes, and has been proposed as a mechanism for producing "nanoflare storms" (Klimchuk 2015). Later in the evolution, the field lines from the individual tubes are found to have been efficiently mixed together by the numerous reconnection events, as shown in Fig. 80.

14.3 Reconnection and nanoflare heating by flux tube tectonics

14.3.1 Flux tube tectonics: concepts

A popular model for explaining the hot corona is that of *nanoflares* created by Parker braiding (Parker 1972) (Sect. 14.1), in which an initially uniform magnetic field is braided by complex footpoint motions, so that the corona is filled with myriads of tiny current sheets that are continually being created and dissipated by reconnection.

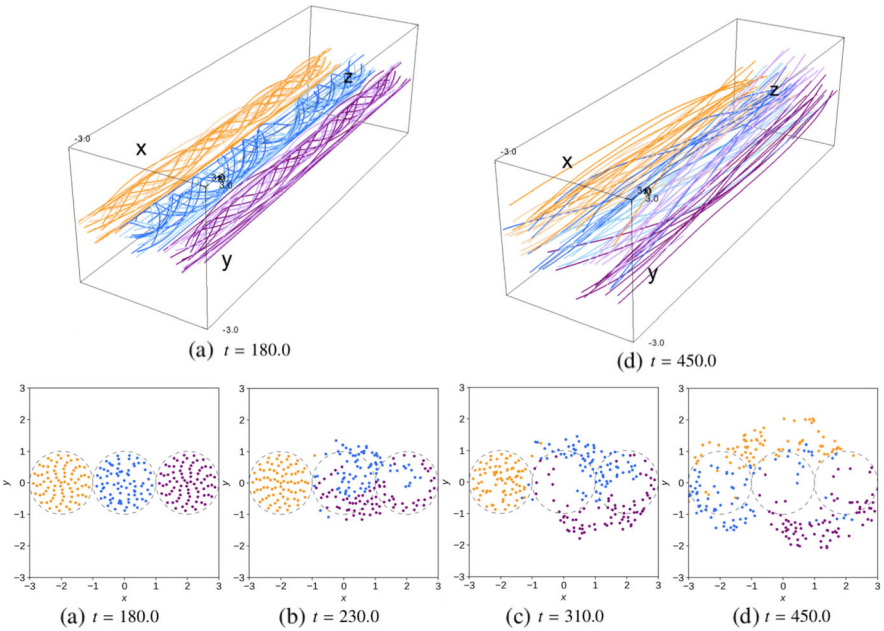

Fig. 80 Illustration of the field line evolution in the kink instability simulations. Initially only the central tube is kink-unstable. The top two images show a 3D view at early and late times, with the darker field lines traced from the same plasma elements on the far boundary at each time, while the lighter field lines are traced from the near boundary. The lower panel shows the evolution of the field-line intersections at $z = -L$ that are anchored in the footprints of the three flux tubes at $z = L$ (with colours as shown in the left-hand frame). Their motion outside their respective dashed circles illustrates the flipping field line motion, say $\mathbf{w}_{\text{in}}$. If the field lines had instead been traced from $z = -L$, then the feet at $z = L$ would have shown flipping at $\mathbf{w}_{\text{out}}$. Image reproduced with permission from Reid et al. (2018), copyright by ESO

The *Flux Tube Tectonics Model* (Priest et al. 2002) is a development of Parker's nanoflare heating ideas, based on the discovery of the *magnetic carpet* (Schrijver et al. 1998), namely, the fact that the photospheric magnetic sources of chromospheric and coronal magnetic field are not smoothly varying structures over large scales (as in Parker's model), but are instead intense flux tubes in the form of highly concentrated and localised magnetic fragments (Figs. 67, 68, 81). This realisation that very strong magnetic field protrudes through the photosphere into the chromosphere and corona at many tiny locations makes the chromospheric and coronal magnetic field much more complex than in Parker's original model (Fig. 82a,b), since it contains myriads of null points, separators and quasi-separators, at which current sheets can form and reconnection take place (Fig. 82c,d) (Priest et al. 2005; De Moortel and Galsgaard 2006b). Furthermore, in the tectonics model, complex braiding flows are not necessary, since even the simplest photospheric motions lead to current sheet formation.

In a first step, Priest et al. (2002) considered tiny footpoint sources localised in the boundaries of supergranules. In the Quiet Sun, such magnetic flux begins in ephemeral regions, which fragment, move to the boundaries and junctions of

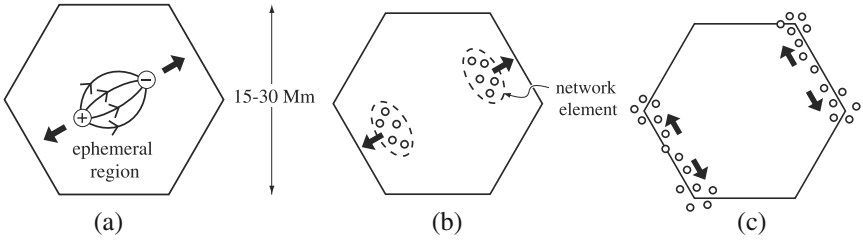

Fig. 81 Scenario for the flux in the magnetic carpet that comes from ephemeral regions: **a** an ephemeral region is born in a supergranule cell of diameter 15–30 Mm, with a flux of 3×10^{19} Mx; **b** each polarity moves towards the boundary at 0.5 km s^{-1} and fragments into 10 network elements; **c** the elements move along the boundary at 0.1 km s^{-1} and eventually cancel. Image reproduced with permission from Priest (2014), copyright by CUP

supergranule cells (the network), merge and cancel over a time of 10–40 hours (Fig. 81). Since the network flux is highly concentrated in units of 10^{17} Mx or smaller, the highly fragmented photospheric magnetic fields produce myriads of separatrix surfaces in the chromosphere and corona. Furthermore, the relative motions of the photospheric sources will cause the field lines to slip (hence "tectonics") and form current sheets on those surfaces.

In a second step, it was realised that the tiny footpoint sources are much more common and are located in and around most granules. Smitha et al. (2017) discovered from SUNRISE observations that, in the Quiet Sun, magnetic flux is emerging and cancelling at a rate of 1100 Mx cm^{-2} day^{-1}, namely, a factor of 10 higher than realised before (Sect. 14.4.2). Most of the flux is emerging in granules with fluxes of only 10^{15} Mx, much smaller than the ephemeral regions considered by Priest et al. (2002), and so the resulting chromospheric and coronal field is very much more complex than thought before, with many more separatrices, which makes flux tube tectonics even more effective.

Fig. 82a shows magnetic field lines (viewed from the side) calculated from an observed magnetogram, illustrating that most of the field lines close low down in the atmosphere. However, this was based on a SoHO magnetogram, and so magnetograms with much higher resolution that are now available (such as SUNRISE or DKIST) will lead to even greater complexity, with probably many more field lines closing low down. Figure 82b is an artist's impression of the complexity of chromospheric and coronal loops, with each magnetic source connecting to many different loops. Figure 82c is a schematic from the side of many separatrices (thick curves) separating the flux from different photospheric magnetic fragments, while Fig. 82d illustrates the fact that even the finest coronal loop currently visible will reach down to the photosphere in many, many feet, so that the interior of the loop will consist of a web of separatrices separating the magnetic flux from each tiny photospheric source.

The basic units of magnetic flux in the photosphere are likely to be tiny intense flux tubes with fields of 500–1200 G, diameters of 100 km or less and fluxes of 10^{15}–10^{17} Mx. An X-ray bright point therefore has hundreds or thousands of

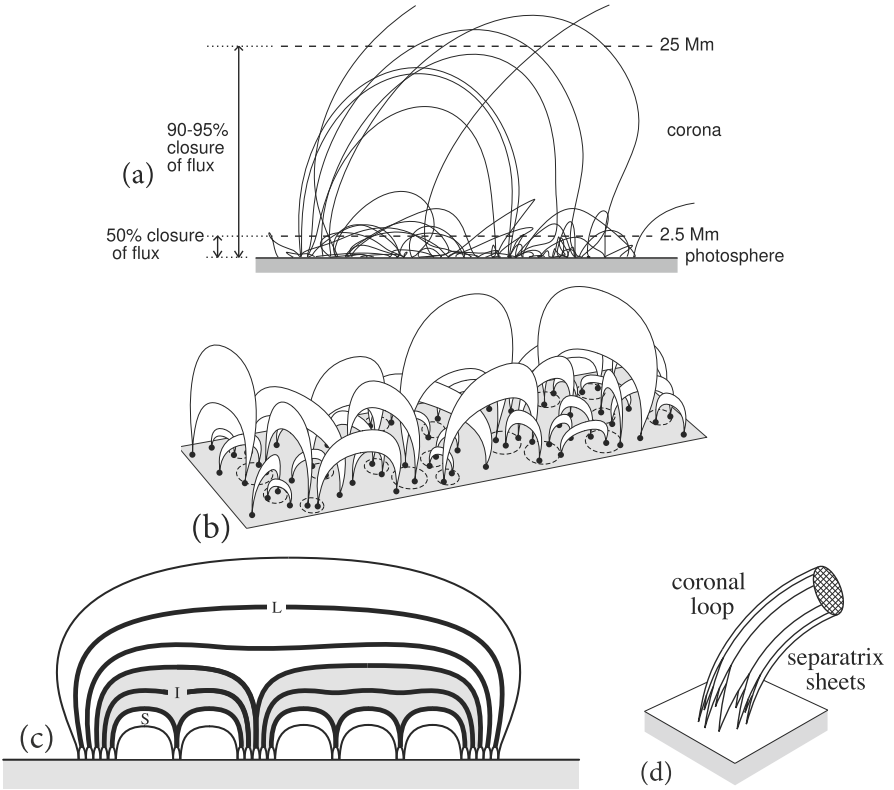

Fig. 82 **a** Side view of a typical magnetic carpet field calculated from an observed photospheric magnetogram. Image reproduced with permission from Close et al. (2003), copyright by Springer. **b** A schematic of chromospheric and coronal loops, whose photospheric magnetic flux elements (dashed ovals) are in general connected to a range of neighbours, although in reality each loop will join to many more neighbours than shown here. **c** A schematic of a chromospheric or coronal loop from the side, which consists of many parts, each joining to a separate source and separated from one another by separatrix surfaces (thick curves). **d** Single coronal loops connect down to the photosphere in many tiny sources separated by a web of separatrix surfaces at which current sheets form and dissipate. Image reproduced with permission from Priest (2014), copyright by CUP

photospheric sources, and each fine coronal loop seen with, say, TRACE is likely to comprise 10–100 much finer, unresolved loops (Fig. 82d).

Priest et al. (2002) considered the effect of simple motions on a simple array of flux tubes, anchored in discrete sources. They showed how smooth shearing motions form current sheets and estimated the heating (Fig. 83). In their model the coronal field is initially potential, with lateral motions of the sources producing opposite signs of the horizontal field on either side of the coronal separatrix surfaces (explicitly, opposite signs of B_y in the example of Fig. 83). The resulting current is singular on the separatrix. In this model the dissipation of current along a separatrix leads to fairly uniform heating along each flux tube, so that each (sub-resolution) coronal flux tube would be heated uniformly. However, at least 95% of the flux closes low down and only 5% forms large-scale connections (Fig. 82a) (Close et al.

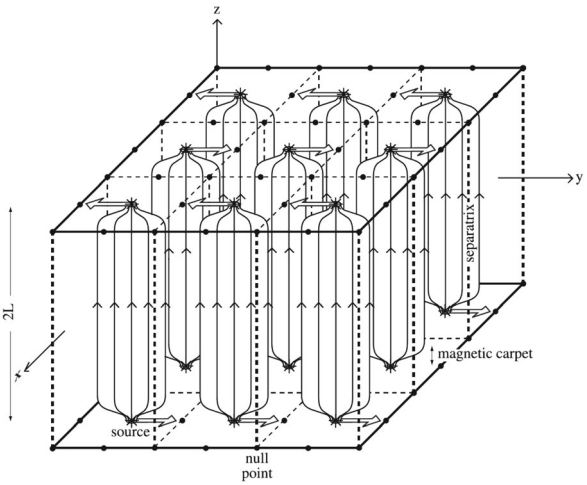

Fig. 83 Representations of coronal loops having concentrated magnetic sources (asterisks) in planes $z = \pm L$, from the flux tube tectonics model of Priest et al. (2002). Null points are indicated by filled circles and separatrices by dashed lines. Image reproduced with permission from Priest (2014), copyright by CUP

2003), so the magnetic carpet will be heated more effectively than the large-scale corona. This implies that unresolved coronal loops would possess enhanced heating near their feet in the carpet, whereas the upper parts of the loops would be heated uniformly but less strongly.

The flux tube tectonics model needs to be developed in several ways to make it more realistic, although the basic principles are unlikely to change. First of all, starting with asymmetrically placed sources would enable each source to be connected to several others and would create many more separatrices. Furthermore, it is important to replace the two parallel photospheric planes by one plane with a realistic complex initial distribution of sources and realistic photospheric flows. Simulations of a simple configuration of two flux tubes anchored at either end in discrete sources have been undertaken by De Moortel and Galsgaard (2006a). Current sheets form as expected along the separators, or when a weak background field is superposed, the quasi-separators. These sheets become highly fragmented and heat the plasma extremely efficiently. This was followed by another experiment that compares the effect of large-scale rotation of the flux tube with small-scale spinning (De Moortel and Galsgaard 2006b). With no background field, the heating due to both types of motion is similar, in agreement with the theory of Priest et al. (2005), but, when a background field is added, the small-scale spinning is more efficient.

14.3.2 Large-scale coronal heating simulations

Around the time that the flux tube tectonics model was introduced, the first large-scale coronal heating simulations were undertaken. These models aimed to reproduce the observed structure of the corona by computationally solving the full set of MHD equations including an energy equation that accounts for thermal conduction and radiative losses. Some approaches of this type use a parameterised heating function, but in most cases the heating is directly by ohmic (and possibly

viscous) dissipation. For a comprehensive review of the successes and caveats of these models, see Peter (2015).

The first models of this type were presented by Gudiksen and Nordlund (2002, 2005a, b) (see Fig. 84). The initial condition comprises a gravitationally stratified atmosphere and an initial potential magnetic field extrapolated from a SOHO/MDI magnetogram. This initial equilibrium is then disturbed by a driving flow on the lower (photospheric) boundary that is designed to mimic some properties of the incompressible component of photospheric granulation. In these simulations a loop-dominated corona was formed, with synthetic emission patterns with an appearance (on large scales) that matches the observations (see Fig. 84). Given that the spatial and temporal scales that can be resolved in the simulations are large, it can be concluded that the heating responsible for these few-million-degree loops is of DC-type heating, i.e. of the type envisaged in the tectonics and braiding mechanisms.

Due to the computational limits on numerical resolution, loop structures formed in these models tend to be created by Ohmic dissipation of one (or a small number of related) current concentration(s). It is expected that at higher resolution these would resolve into many localised current ribbons and therefore heated strands. In order to investigate the nature of the energy release events in studies of this type, Kanella and Gudiksen (2018) modelled a continually evolving region of the quiet Sun, employing an intensive and sophisticated algorithm to pick out individual

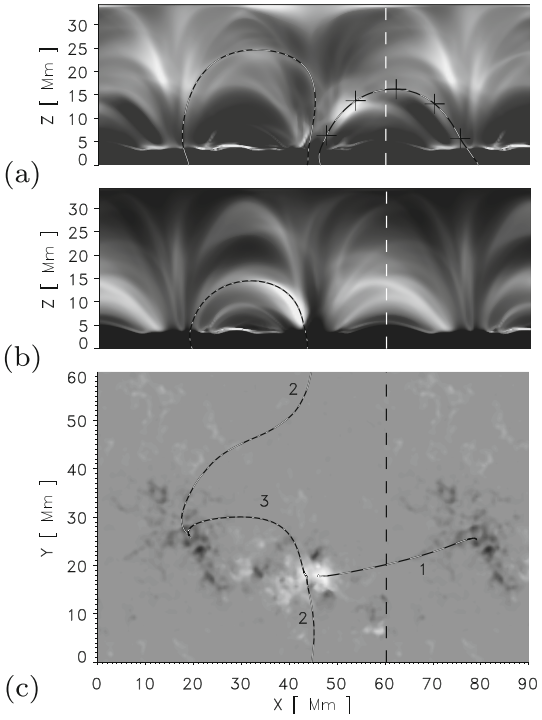

Fig. 84 Hot corona produced by 'DC' heating in large-scale MHD simulations. Simulated TRACE 171 (**a**) and 195 (**b**) images, together with a simulated magnetogram (**c**), showing three identified bright loops. Image reproduced with permission from Gudiksen and Nordlund (2005b), copyright by AAS

(ohmic) heating events in space and time. These simulations (using the Bifrost code) model the region from the upper convection zone up to 14.3 Mm above the photosphere. A horizontal field is injected from the bottom of the simulation domain which is brought up to the solar surface by the convection and helps to maintain the "salt and pepper" quiet Sun photospheric flux distribution. Heating events are then identified in the part of the domain above 3.28 Mm above the photosphere (this is the height at which $T \approx 1$ MK). The individually identified heating events are found to have a power law distribution in both energy and duration. The vast majority of the events ($> 93\%$) are found to be of "pico" size, having total energy release less than 10^{24} ergs (10^{17} J), and so smaller than the typical size of a nanoflare proposed by Parker (1988). However, in an earlier study Bingert and Peter (2013) found that the energy flux into the coronal plasma peaks for event energies around 10^{17} J. Additionally, in studies that analyse the height distribution of the temperature and energy deposition—see for example Hansteen et al. (2010), Bingert and Peter (2011)—the energy input per particle (defined as the energy input divided by the mass density) peaks somewhere near the transition region, consistent with observations.

Warnecke and Peter (2019) undertook a "data-driven" approach to a coronal heating simulation. They simulated the emission from an active region, with the aim of determining whether the observed emission patterns could be reproduced. They began from a potential magnetic field extrapolated from an SDO/HMI line-of-sight magnetogram, and updated the boundary values for the vertical magnetic field using a time sequence of these observed magnetograms. An additional photospheric flow was used to drive a granulation-type pattern, as in the simulations by Gudiksen and Nordlund (2002, 2005a, b). A comparison between the observed and simulated emission patterns is shown in Fig. 85, with a relatively good match being obtained.

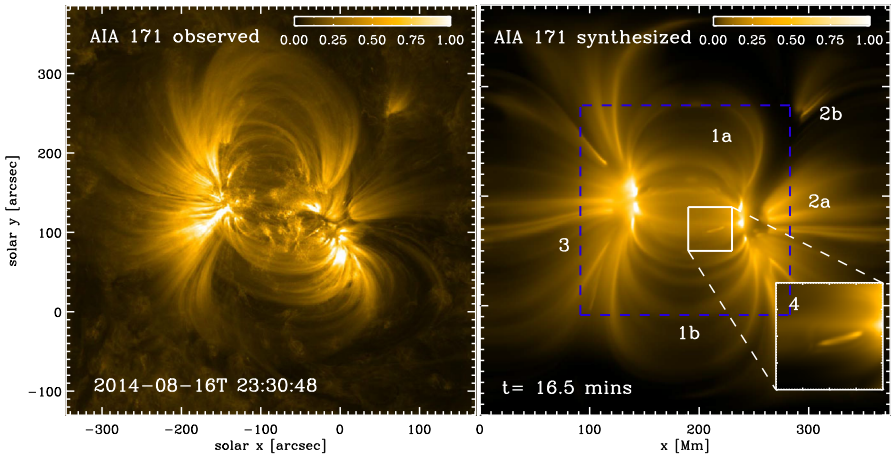

Fig. 85 Comparison of observed emission and synthesised emission from the study of Warnecke and Peter (2019). Note that the peak count value in the observations (corresponding to 1.00) is 3500 DN/pixel, which is a factor of six higher than in the model. The inset in the right-hand image shows a bright, relatively short-lived, low-lying loop

Loop structures are visible in many of the same locations, super-imposed upon a diffuse background emission. There are some marked discrepancies as well, for example the simulated emission exhibits an absence of small-scale structure in the active region core, which the authors attribute to a lack of resolution of the magnetogram data used. In addition, the simulations under-estimate the shear of the loops on the active region scale, which may be improved by making use of the observed horizontal components of the magnetic field. The fact that the observed coronal emission is so well reproduced by such simulations driven by footpoint shuffling is a strong indication that the braiding/flux-tube tectonics model is a key part of active-region heating.

The large-scale MHD simulations discussed above are able to reproduce quite closely the energy fluxes and temperatures required to maintain a hot corona. This might be surprising, given that the simulations drastically under-resolve the photospheric field and flows, and the coronal resistivity is many orders of magnitude larger than the true value. Since small spatial and temporal scales are missing from the modelling, the heating is of a 'DC' type consistent with the tectonics and

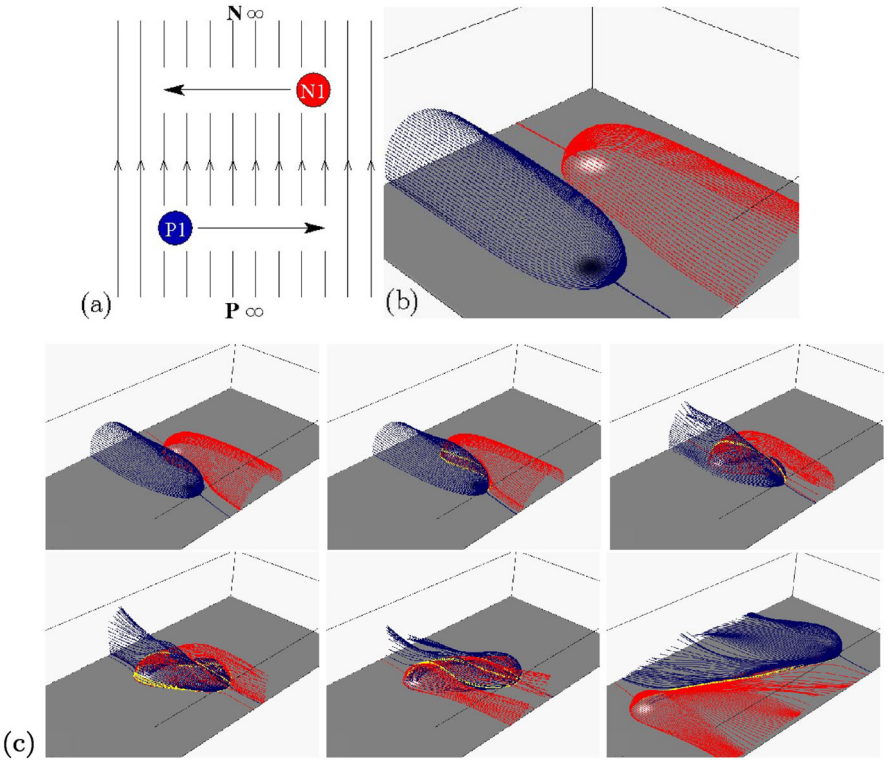

Fig. 86 Initial configuration for a flyby numerical experiment showing **a** the view from above and **b** the magnetic skeleton. **c** Time evolution showing the interaction of the red and blue separatrix surfaces at yellow separator field lines. For related movies see Supplementary Information. Images reproduced with permission from Parnell and Haynes (2009), copyright by Springer

braiding pictures—albeit the loops are produced by Ohmic heating in one or a handful of current layers, which would likely be resolved into many current layers on smaller spatial and temporal scales were the resolution increased. It is possible that 'AC' or wave heating would also contribute if smaller spatio-temporal scales were included. However, it is worth noting that, while the overall heating rates are reproduced in these models, many more detailed features of the observations are not: for example the non-thermal broadening of synthesised spectral lines is much smaller than typically observed. It was recently demonstrated by Pontin et al. (2020) that turbulent heating induced by small-scale braiding within the loops—absent in the large-scale simulations—reproduces the principal observed spectral properties of loops, and is thus a candidate to account for this discrepancy.

For the above simulations, it would be interesting to analyse carefully the quasi-skeleton and skeleton, and to determine what type of 3D reconnection is involved in the heating events. Finally, it is worth noting that both the braiding and tectonics pictures exclude flux emergence and cancellation for simplicity. Recent startling observations of magnetic flux cancellation in the photosphere show that flux cancellation is very much more frequent than thought before and is present over the whole solar disc. This presents the possibility that flux cancellation may be an important component in heating many chromospheric and coronal structures, as summarised in Sect. 14.4.2.

14.4 Separators and chromospheric or coronal heating

The suggestion that the solar atmosphere is filled with thousands of current sheets that are continually being created and reconnected to produce *nanoflares* was put forward by Parker (1972) and has usually been modelled in terms of braiding an initially uniform magnetic field by footpoint motions (see Sect. 14.1).

Later, however, the *flux tube tectonics model* (Priest et al. 2002) (Sect. 14.3) was proposed as a modern development of Parker's nanoflare heating ideas. It incorporates the fact that the photospheric magnetic sources of chromospheric and coronal magnetic field are highly concentrated and localised magnetic fragments (Figs. 67,68), which makes the chromospheric and coronal magnetic field quite different from Parker's original model. Thus, Parker's model requires complex braiding motions to create current sheets, but for flux tube tectonics simple observed motions will create myriads of dissipating current sheets throughout the chromosphere and corona at separators, quasi-separators and null points in ways that are probably more effective than with Parker braiding.

Many of the consequences of this new approach still need to be worked out. One that has been considered is that, as neighbouring magnetic fragments in the photosphere move past one another, their chromospheric and coronal fields reconnect (Sect. 14.4.1). Another, from recent observations, is that flux cancellation is much more common than previously realised and that this may be driving heating of the overlying atmosphere (Sect. 14.4.2).

14.4.1 "Flyby" of magnetic flux fragments

A natural way for flux tube tectonics to heat the corona has been modelled numerically by Galsgaard et al. (2000), Parnell and Galsgaard (2004), Parnell et al. (2010), namely, a so-called *flyby*, the elementary interaction between two photospheric magnetic fragments. This drives reconnection at a collection of coronal separators when the source separation is small enough. The initial setup (Fig. 86a) consists of two opposite-polarity photospheric flux sources ($P1$ moving to the right and $N1$ moving to the left) in an overlying uniform field that is perpendicular to the motion of the sources. Initially, the two sources are not magnetically connected, as can be seen from the magnetic skeleton, namely, the web of separatrix surfaces that separate the corona into its topologically distinct parts (Fig. 86b). Two photospheric null points possess fans that form open separatrix surfaces extending along the direction of the overlying field. The blue separatrix encloses all the flux from the positive source extending out through one side boundary, and the red surface encloses flux from the negative source extending out through the opposite boundary. These fluxes are called *open*, whereas the flux that later links one source to the other is designated *closed*.

The subsequent evolution of the skeleton (Fig. 86c) shows how the two separatrices intersect in several reconnecting separators that vary in number as the simulation progresses. Furthermore, plots of the current reveal that the new flux tube is twisted and contains a twisted current sheet at its core. The twist is a consequence of magnetic helicity conservation. The unexpected topological complexity of the interaction is revealed when a vertical section through the skeleton of Fig. 86c is taken (Fig. 87) (Haynes et al. 2007). The magnetic field evolves through a sequence of 6 different topologies, with the number of coronal separators changing from 0 to

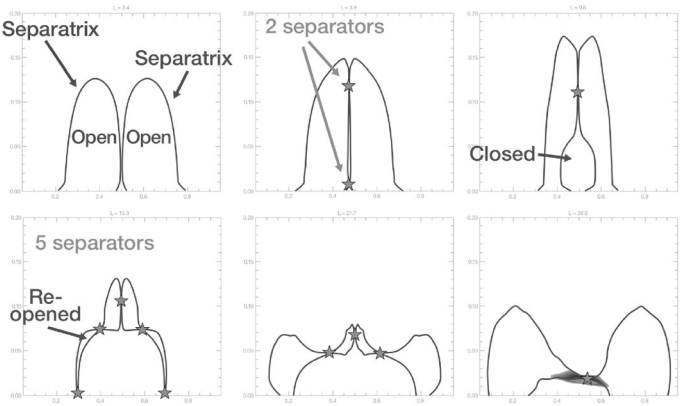

Fig. 87 The evolution of a vertical section across the skeleton at the mid-plane $y = 0.5$ of the flyby simulation. "Open" refers to flux that links one of the sources with a side boundary of the numerical box, while "Closed" denotes flux that joins the two sources. For a related movie see Supplementary Information. Image reproduced with permission from Priest (2014), copyright by CUP

2 to 1 to 5 to 3 and finally to 1. The dissipation mechanism is separator reconnection at multiple separator current sheets.

As mentioned above, the two separatrix surfaces are at first completely separate. Then they touch and a so-called *global double-separator bifurcation* takes place. This creates a new coronal domain containing magnetic flux that joins the photospheric fragments and is bounded by separatrix surfaces that intersect in a pair of new separators (Fig. 87b). The lower separator moves down through the lower boundary, leaving one separator (Fig. 87c), where reconnection has the effect of building up the closed flux that links the two sources. Next, the separatrix surface bounding the closed flux touches and then intersects the side separatrices in another bifurcation that creates two new separators on one side and two more on the other (Fig. 87d). The lower two separators move down through the lower boundary to leave behind three separators. Reconnection at the two lateral locations re-opens the flux, so that eventually the two sources become disconnected again.

Parnell et al. (2010) discovered that, when the separator current is strong enough, the magnetic field near the separator becomes that of a twisted flux rope, so that the field component in transverse planes changes from X-type to O-type (Fig. 88), a property that can vary spatially as one moves along a separator. At the same time, the parallel electric field and current vary along a separator, with the reconnection regions located between counter-rotating flow regions (see Sect. 4.7.2 and Hornig and Priest 2003).

Parnell et al. (2008) reaffirmed the importance of the skeleton for understanding the nature of 3D reconnection. They analysed in detail the flux evolution during a phase of the flyby simulations with three reconnection sites, one of which closes the flux (converts open flux to closed), while the other two reopen it. They observed *recursive reconnection*, with flux closing and reopening simultaneously, so that the same flux may be closed and opened several times (Fig. 89). This increases the global rate of reconnection and enables heating to continue longer and over a larger area than the single-separator case.

The plasma heating in a particular flyby event depends on the magnetic flux of the fragments, their speed and direction of movement, and the strength of the overlying magnetic field. The effect of decreasing the resistivity is to increase both the duration of the interaction and the ohmic heating (Parnell and Haynes 2009). Recursive reconnection is also possible when several separators link the same two

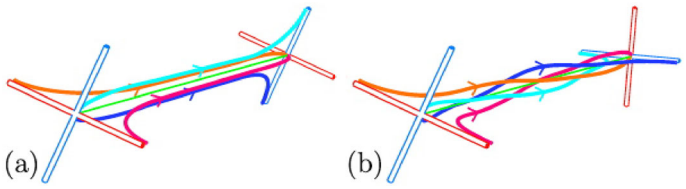

Fig. 88 Cartoons of the magnetic field lines around a separator with a structure that is **a** hyberbolic with X-type field lines in planes perpendicular to the separator and **b** elliptic with O-type field lines. Image reproduced with permission from Parnell et al. (2010), copyright by AGU

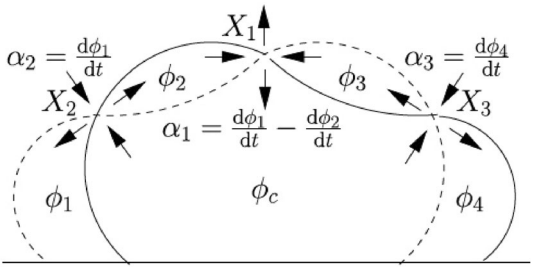

Fig. 89 A sketch of a vertical cross-section of the skeleton during recursive reconnection, in which fluxes can pass through the separators X_1, X_2 and X_3 several times. Arrows indicate the directions of flux transfer between different lobes, in which the rates of change (α_1, α_2, α_3) are written in terms of the reopened fluxes (ϕ_1,ϕ_4) and open fluxes (ϕ_2,ϕ_3). Image reproduced with permission from Parnell et al. (2008), copyright by AAS

null points, so that the nulls are *multiply connected* (Parnell 2007), which can occur in potential, force-free and non-force-free fields. In addition, recursive reconnection involves a greater spread of energy, repeated heating of the plasma and a longer duration of heating. Multiply reconnected magnetic flux has also been found in simulations of braided fields (see Sect. 14.1).

14.4.2 Heating driven by photospheric flux cancellation

Photospheric flux cancellation was earlier thought to occur only occasionally—mainly at the boundaries of supergranule cells, where the magnetic flux in the magnetic carpet, after emerging as ephemeral regions and fragmenting, is reprocessed by cancellation and submergence (Schrijver et al. 1998; Parnell 2001) (Fig. 81). It was also thought that occasionally such flux cancellation drives reconnection in the corona to produce X-ray bright points (Priest et al. 1994; Parnell and Priest 1995). Furthermore, photospheric reconnection was thought sometimes to produce Ellerman bombs as transient brightenings in the wings of Hα near sunspots, although later Rouppe van der Voort et al. (2016), using the Swedish Solar Telescope (SST), discovered Ellerman bombs are sometimes also present in the quiet Sun. However, a recent landmark discovery has been the realisation that flux cancellation is very much more common than thought before (Smitha et al. 2017; Joshi et al. 2020), and may well be responsible for chromospheric and coronal heating (Priest et al. 2018).

The key discovery from SUNRISE balloon observations (Solanki et al. 2010) is that the photospheric magnetic field is much more complex than realised before, with quiet-Sun flux emerging and cancelling at a rate that is a factor of ten higher than before, namely, 1100 Mx cm^{-2} day^{-1} (Smitha et al. 2017). An image of the corona (Fig. 90a) and the underlying magnetogram from SDO/HMI (Fig. 90b), suggest that coronal loop feet are unipolar. However, the corresponding much higher-resolution SUNRISE magnetogram (Fig. 90c) reveals instead many tiny regions of cancelling flux of mixed polarity.

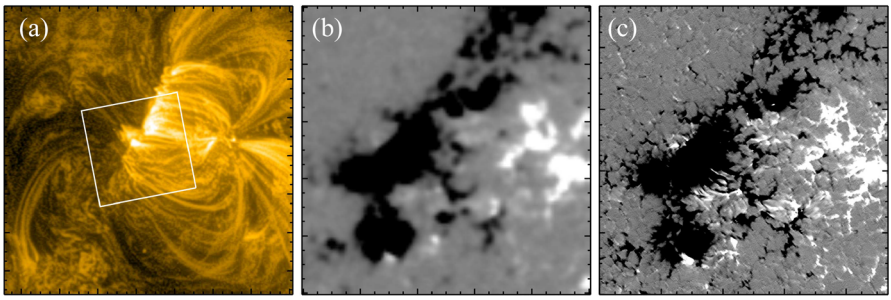

Fig. 90 **a** A coronal image of an active region from the SDO/Atmospheric Imaging Assembly (AIA) 171 Å filter in a 150 × 150 arcsec field of view. The white box encloses footpoints of several coronal loops. **b** The underlying magnetic field from an SDO/HMI photospheric magnetogram for the white box region of panel (**a**). **c** The corresponding SUNRISE/IMaX observations for the same region. Image reproduced with permission from Priest et al. (2018), copyright by AAS

Several observational consequences of this ubiquitous flux cancellation have been discovered. Firstly, more observations with the SST have been undertaken. At a spatial resolution of 0.1 arcsec, Joshi et al. (2020) discovered that quiet-Sun Ellerman bombs produced by flux cancellation are ubiquitous and uniformly distributed across the quiet Sun, predominantly occurring in intergranular lanes. Typically, half a million are present at any one time. Also, simultaneous SST and IRIS observations in emerging flux regions (Rouppe van der Voort et al. 2017; Ortiz et al. 2020; Vissers et al. 2019) showed that in the chromosphere and transition region above an Ellerman bomb there are UV bursts that indicate heating, as well as acceleration of jets and sometimes small rapidly moving brightenings suggestive of plasmoids.

Secondly, observations at coronal temperatures from AIA on SDO have revealed new features. Chitta et al. (2019) found, by comparing with Swedish Solar Telescope observations, that coronal loops in active regions have flux cancellation at the feet of the loops. The observations and 3D radiative MHD simulations with the MURAM code suggest that often opposite-polarity magnetic field brought up by tiny transient flux emergence in granules cancels with the surrounding plage field. Chitta et al. (2020) then focused on coronal loops in the cores of active regions that are heated to 5 MK, and found that at least one footpoint of such loops is located in a region of mixed magnetic polarity; indeed, when simultaneous IRIS observations are available there is spectroscopic evidence of reconnection there.

The initial discovery by Smitha et al. (2017) led Priest et al. (2018) to propose a *flux cancellation model* for heating, in which nanoflares are created by photospheric flux cancellation driving reconnection in the overlying atmosphere (Fig. 91). In their simple model, they suppose two opposite-polarity magnetic fragments of flux $\pm F$ approach one another in an overlying horizontal field B_0 and eventually cancel (Fig. 91). At first, when the half-distance d between them is large, no flux joins one fragment to the other, but, as soon as $d < d_0$, where

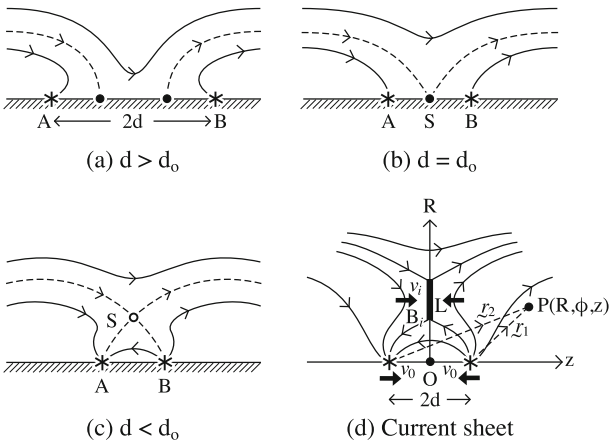

Fig. 91 The flux cancellation model of Priest and Syntelis (2021) for chromospheric and coronal heating, in which two photospheric flux sources ($\pm F$) a distance $2d$ apart approach at speed $v_0\hat{\mathbf{x}}$ in an overlying field $B_0\hat{\mathbf{x}}$. The magnetic topology when **a** $d > d_0 \equiv [F/(\pi B_0)]^{1/2}$, **b** $d = d_0$, a separator S is formed, **c** $d < d_0$ and reconnection is driven at the separator S. **d** The current sheet of length L, with plasma inflow v_i and magnetic field B_i, at which the energy is converted. Image reproduced with permission, copyright by ESO

$$d_0 = \left(\frac{F}{\pi B_0}\right)^{1/2} \tag{103}$$

is the interaction distance (Longcope 1998), reconnection begins at a separator.

The energy release occurs in a first phase as the separator rises to a maximum height that depends on d_0 and then falls to the photosphere. It continues in a second phase as the fragments cancel. The maximum height of energy release can be located in the chromosphere, transition region or corona, depending on the parameter values, and in both cases energy is released as the heat and kinetic energy of hot fast jets, as well as fast particles.

The inflow speed (v_i) and magnetic field (B_i) at a current sheet of length L were calculated in terms of the approach speed (v_0) of the fragments, their fluxes (F) and the overlying field (B_0). For observed values of these parameters, the energy release in the model is found to be sufficient to heat the chromosphere and corona. More recently, the model has been extended by analysing reconnection at a 3D separator current sheet (Priest and Syntelis 2021), and by numerical simulations (Syntelis et al. 2019; Syntelis and Priest 2020).

15 Other examples of reconnection at work in the Sun and Magnetosphere

Here we describe briefly some other examples of the key role of magnetic reconnection, namely, of isolated tubes and their role in flux emergence (Sect. 15.1.2), in the formation of the slow solar wind (Sect. 15.2) and in the Earth's magnetosphere (Sect. 15.3)

15.1 Reconnection of isolated flux tubes

The preceding sections describe modes of 3D reconnection at different features of a space-filling 3D magnetic field. In certain applications it is relevant to consider the magnetic field as being localised into isolated magnetic flux tubes (outside which the magnetic field is approximately zero). We describe such models here, first for reconnection between two such isolated tubes, and then reconnection driven by the emergence of a flux tube through the photosphere.

15.1.1 Reconnection of colliding isolated flux tubes

Linton and colleagues have studied numerically the collision and interaction of two isolated magnetic flux tubes (Dahlburg et al. 1997; Linton et al. 2001; Linton and

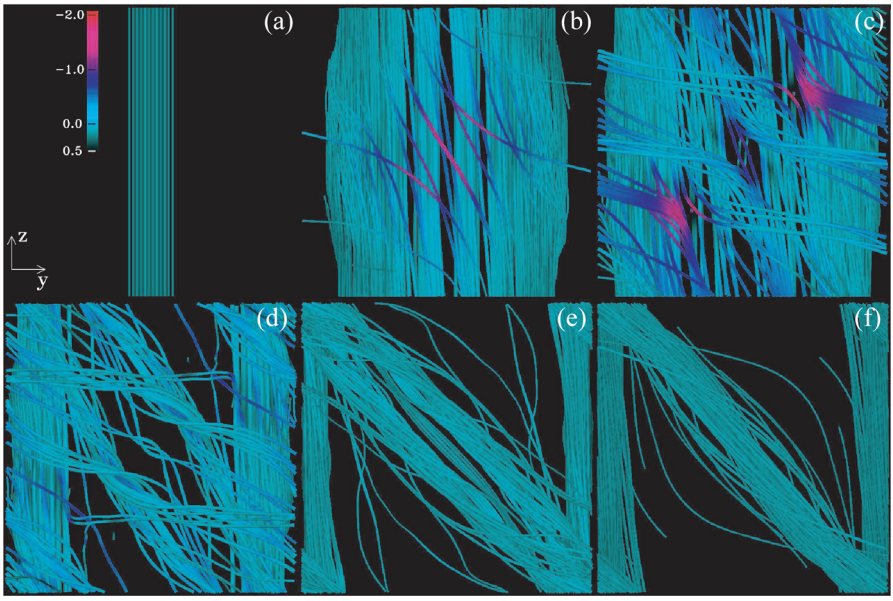

Fig. 92 The reconnection of two untwisted flux tubes in a stagnation-point flow, with the colour indicating the value of $j_{\parallel}/j_0$, where $j_0 = B_0/(4\mu R)$: **a** initial field, **b** reconnection beginning near the centre, **c** reconnection continuing at two new locations to the lower left and upper right, **d**–**f** later evolution of the two slanting reconnected tubes. For related movies see Supplementary Information. Image reproduced with permission from Linton and Priest (2003), copyright by AAS

Priest 2003; Linton and Antiochos 2005; Linton 2007). Initially, the tubes are surrounded by field-free plasma and have a variety of twists and relative inclination angles, and are carried towards one another by a stagnation-point flow.

Linton and Priest (2003) considered two perpendicular untwisted flux tubes that are forced together by a stagnation-point flow inside a periodic simulation domain with a maximum velocity amplitude $v_0 = v_A/30$ (in terms of the initial Alfvèn speed (v_A) on the axis of the tube). In terms of v_A and the tube radius (R), the viscous Reynolds number is $R_e = v_A R/(\pi v) = 560$ and the magnetic Reynolds number $R_m = v_A R/(\pi \eta) = 5600$.

They followed the evolution with a 3D visco-resistive pseudo-spectral MHD code (Dahlburg and Antiochos 1995), as shown in Fig. 92. In this figure, only field lines that connect to the top and bottom boundaries are shown. Fig. 92a shows the initial magnetic field, which in Fig. 92b is flattened out by the stagnation-point flow into a thin flux sheet, near whose centre reconnection starts. In Fig. 92c two new reconnection locations have been created by tearing instability either side of the original location. These locations show up as regions of strong parallel electric field (a signature of 3D reconnection—see Sect.4), shaded pink. Finally, in Fig. 92d–f two slanting tubes that have been created by the reconnection are pulled together by magnetic tension and coalesce to produce a single twisted flux tube. Roughly a third of the total flux has reconnected, while two-thirds has been carried to the sides by the flow, to produce purely vertical field lines.

Linton (2007) extended these studies by considering the approach of twisted flux tubes (Fig. 93). The presence of twist has three effects: the stagnation-point flow no

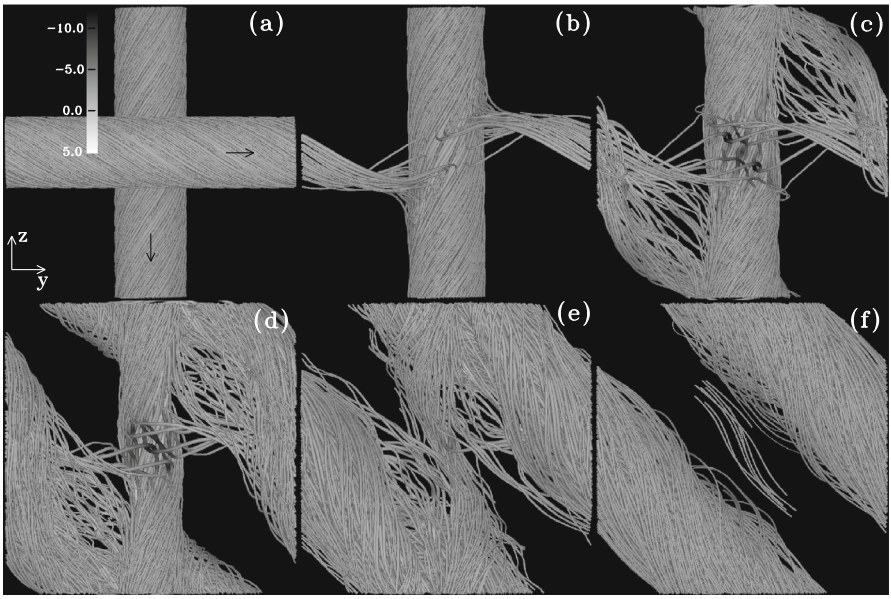

Fig. 93 Slingshot reconnection of slightly twisted ($\Phi = 1$) flux tubes to form two slanted tubes with half their initial twist. Image reproduced with permission from Linton (2007), copyright by CUP

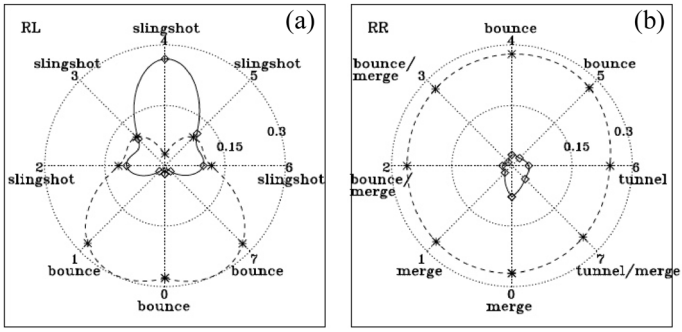

Fig. 94 Energy diagram for flux tubes whose twist is oppositely (left) or like (right) directed, with a twist of $\Phi = 10$. The distance from the origin is the energy divided by the initial magnetic energy, while the azimuthal coordinate is the inclination ($\theta = N\pi/4$) of the two tubes, labeled with the value of N. Twice the peak kinetic energy is the solid curve, and the final magnetic energy (when $tv_A/R = 150$) is the dashed curve. Image reproduced with permission from Linton et al. (2001), copyright by AAS

longer spreads out and flattens the flux tubes, since the tension force associated with the twist binds them together; tearing no longer takes place and so reconnection occurs at only one location; and the twist keeps the tubes coherent so that all their flux reconnects.

They found that the nature of the reconnection depends on the twists in the two tubes and the angle $\theta = N\pi/4$ at which they collide (Fig. 94). They studied like-twisted and oppositely twisted flux tubes with N varying between $N = 0$ and $N = 7$. They discovered four different types of interaction when the twist is large. The tubes either *bounce* elastically off one another without reconnecting; or they undergo classical *slingshot reconnection*; or they pass through each other (in so-called *tunnel reconnection*) (Dahlburg et al. 1997); or they combine together to form a single flux tube (*merge reconnection*).

Slingshot reconnection (Fig. 92) occurs when the angle of inclination lies between $\pi/2$ and $3\pi/2$ provided the tubes are oppositely twisted. When the tubes are anti-parallel ($\theta = \pi$), nearly all the magnetic energy is released, whereas when they are only slightly inclined, the tubes bounce with little reconnection and little energy release. At other angles, slingshot reconnection is highly energetic and releases over half of the magnetic energy, with the energy release being due to both shortening of the axial field lines and cancelling of opposite twists (Linton et al. 2001; Ozaki and Sato 1997). For like-twisted tubes, much less energy is released during reconnection, and merge, bounce or tunnel reconnection occur depending on N (Fig. 95). Interactions of parallel, like-twisted flux tubes exhibit such reconnection, as has been found in numerical experiments (Lau and Finn 1996; Kondrashov et al. 1999; Linton et al. 2001) and also laboratory experiments (Yamada et al. 1990).

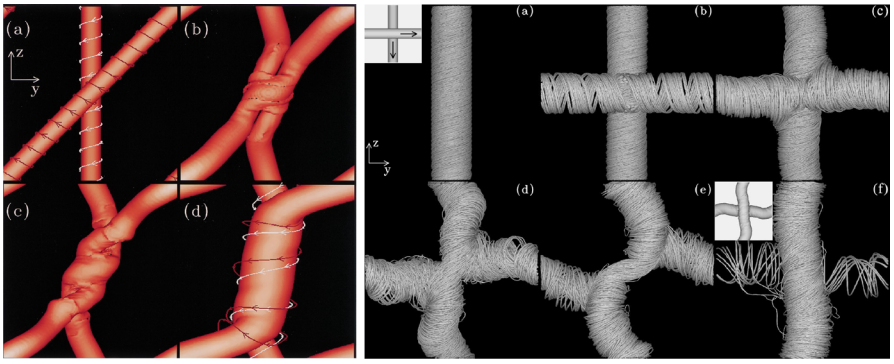

Fig. 95 Left: Merge reconnection of like-twisted flux tubes at an inclination of $\theta = \pi/4$ and with a large twist ($\Phi = 10$). Right: tunnel reconnection of like-twisted tubes at an inclination of $\theta = 6\pi/4$ and a twist of $\Phi = 5.5$, showing (b)–(d) a slingshot reconnection, and (e)–(f) a rebound and second reconnection. Images reproduced with permission from [left] Linton et al. (2001), and from [right] Linton and Antiochos (2005); copyright by AAS

15.1.2 Reconnection driven by flux emergence

The emergence of magnetic flux from below the photosphere has long been known to be a trigger of dynamic phenomena in the chromosphere and corona. Typical models of this process involve a coherent, subsurface magnetic flux tube that breaks through the photosphere. Numerous detailed reviews of this phenomenon exist, including Cheung and Isobe (2014), and so we only touch briefly on a few aspects specific to the associated reconnection here.

There are many unknowns related to the process of flux emergence, such as the properties of the sub-surface magnetic flux structures, whether they remain coherent as they rise through the convection zone, and how much of the flux breaks through the surface compared to what is trapped below (Stein 2012; Cheung and Isobe 2014). Isolated rising flux tubes may be shredded as they rise through the convection zone; a coherent twist may permit a flux tube to retain its identity, but there remains debate about whether a threshold for this twist exists, and whether such a twist is consistent with observations.

It is very likely that sub-photospheric reconnection plays a role in configuring the flux that eventually emerges into the corona, though direct evidence is scarce. Such sub-photospheric reconnection was noted in simulations by Tortosa-Andreu and Moreno-Insertis (2009). Recently Baker et al. (2020) have proposed that sub-photospheric reconnection of flux bundles may influence the composition of the coronal plasma.

Once a portion of a flux tube breaks through the photosphere, it will come into contact with pre-existing field in the atmosphere, and the resulting dynamics depends on the relative orientations of the emerging and pre-existing fields. Heyvaerts et al. (1977) were the first to propose flux emergence as a possible trigger for solar flares, while Forbes and Priest (1984a) and Shibata et al. (1992) demonstrated that flux emergence can drive reconnection with a pre-existing

horizontal field in the corona in 2D MHD simulations. Similar simulations in 3D indicate that, when the angle between the emerging field and the horizontal field of the corona is sufficiently large, reconnection ensues producing hot jets of plasma (Archontis et al. 2005). MacTaggart and Haynes (2013) analysed the magnetic topology of this interaction, identifying the presence of separator reconnection.

Another class of simulations takes the pre-existing coronal field to be inclined at a uniform angle. Yokoyama and Shibata (1995, 1996) demonstrated that reconnection between the oblique and emerging fields drives both hot and cool jets upwards along the oblique field direction (Fig. 96a). Similar simulations in 3D show that the reconnection takes place at a 3D null point that sits above the emerging minority polarity, with the jet flowing outwards along the null point's spine (Fig. 96b) (Moreno-Insertis and Galsgaard 2013). Still more complex and realistic coronal fields have been considered such as potential or force-free arcades (MacTaggart 2011; Kusano et al. 2012). In particular Kusano et al. (2012) performed a series of simulations varying the angle of the emerging flux relative to the force-free arcade, identifying the range of parameters for which an eruption is triggered. A large number of works have studied the potential link between flux emergence and flux rope eruptions (e.g., Manchester et al. 2004; Fan and Gibson 2004; Leake et al. 2014). In some models the emerging flux rope itself erupts, while more commonly the flux emergence drives coronal reconnection leading to the formation of a coronal flux rope which subsequently erupts. Theoretical, computational and observational approaches to understanding the link between flux emergence and dynamic atmospheric phenomena involving reconnection are reviewed in more detail by Cheung and Isobe (2014), Green et al. (2018) and Archontis and Syntelis (2019).

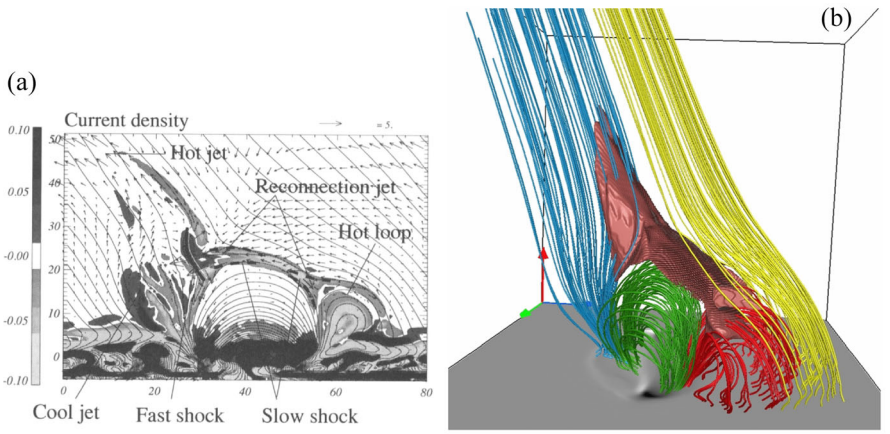

Fig. 96 MHD simulations of flux emergence into a pre-existing inclined coronal field, triggering reconnection between the emerging and overlying flux. **a** 2D simulations of Yokoyama and Shibata (1996) with the shading showing current density, solid lines magnetic field lines and arrows the plasma flow. **b** Flux systems formed in the 3D simulation of Moreno-Insertis and Galsgaard (2013), where the red isosurface shows the high-temperature region around the collapsed null point, extending outwards along the open spine as a hot jet

15.2 Interchange reconnection and the slow solar wind

Section 14 dealt with models for heating the closed corona by reconnection. Reconnection between open and closed magnetic field lines—called *interchange reconnection* (Crooker et al. 2002)—is also a leading candidate for explaining the origin and structure of the slow solar wind. This is summarised briefly here, while more complete reviews can be found in Abbo et al. (2016); Viall and Borovsky (2020). Note that further examples of interchange reconnection, e.g., in models of coronal jets, are discussed in Sect. 10.4.

While it is well established that the fast, steady wind emanates from coronal holes, the origin of the slow solar wind (SSW) remains unexplained. Any model must account for the SSW's relatively low speed, strong and continuous variability, distinct difference in composition from the fast wind, and broad observed latitudinal extent (up to 60° at solar minimum). The strongly fluctuating speed, density, and elemental and ion-charge-state abundances are hard to reconcile with direct acceleration of plasma along open magnetic field lines; indeed, the composition of the SSW suggests that the plasma has some component that originates in the closed magnetic field regions of the corona (Zhao et al. 2017). However, plasma cannot normally move from a closed to an open magnetic field line. This apparent paradox can be resolved through interchange reconnection, which allows closed-field plasma to escape along newly opened magnetic field lines. First proposed by Fisk et al. (1998), this idea gained wider attention with the development of a new model for the Sun's global magnetic field proposed by Antiochos et al. (2011). They demonstrated that when the full complexity of the coronal magnetic field is included, the separatrices and quasi-separatrix layers—collectively called the *S-Web*—associated with the boundary between open and closed magnetic flux in the corona, map out an extended latitudinal band around the heliospheric current sheet, consistent with observations of the SSW (see also Sect. 2.7). This provides a resolution to the apparent contradiction that plasma with closed-corona properties is observed at high latitudes. Further evidence for the association between S-Web structures dividing open and closed flux and SSW production comes from observations of SSW at pseudo-streamers (Owens et al. 2013) and upflows at the edges of active regions (Brooks et al. 2015; Macneil et al. 2019). Coronal magnetic field extrapolations often reveal the presence of the separatrices and QSLs of the S-Web in close proximity to these upflows (e.g., Del Zanna et al. 2011; van Driel-Gesztelyi et al. 2012; Mandrini et al. 2015).

Interchange reconnection (see Sect. 2.7) between closed and open field lines by definition requires some form of separatrix surface (that separates the open flux from the closed), and thus typically involves null points or separators. The open-closed boundary turns out to be composed of a range of different such separatrices associated with bald patches and coronal nulls and separators in various different configurations including multi-null systems with series of separatrix curtains (see the discussion of Sect. 2 and Titov et al. 2011; Platten et al. 2014; Scott et al. 2018, 2019). The full complexity of this bounding surface and its implications remain to be explored. As pointed out by Rappazzo et al. (2012) and by Pontin and Wyper (2015), a combination of turbulence and current layer fragmentation means

that the interchange reconnection process itself will further increase the topological complexity beyond that present in the equilibrium field.

As discussed earlier in Sect. 10.4, interchange reconnection in a dome topology with single and multiple nulls can release plasma onto open field lines. Such reconnection occurs throughout coronal holes where regions of minority polarity are enclosed beneath separatrix domes. The size of the minority (or parasitic) polarity region determines the height of the associated null, and therefore of the reconnection. Jets and plumes are commonly observed, and the associated outflows may lead to observed fluctuations, including "micro-streams" in the solar wind (e.g., Neugebauer 2012; Raouafi et al. 2016, and references therein). The production of solar energetic particles through such events is well documented—see Sect. 17. It is also proposed that interchange reconnection events might be the source of magnetic field "switchbacks" found in the solar wind and recently discovered to be ubiquitous in the data from Parker Solar Probe (see Owens et al. 2020, and references therein). Indeed, it has been suggested that the strongly curved magnetic field line geometry in the vicinity of the null point at which the interchange reconnection takes place may be critical in forming the radial magnetic field reversal associated with the switchback (e.g., Fisk and Kasper 2020). At the time of writing, the origin of switchbacks is a very active topic of investigation due to the new data being obtained from Parker Solar Probe and Solar Orbiter, and so further progress in the coming years is anticipated.

While many simulation studies have addressed interchange reconnection in the local vicinity of a separatrix dome (see Sect. 10.4), simulating interchange reconnection on a larger scale to include the boundaries of coronal holes is substantially more challenging computationally. Interchange reconnection in a global coronal geometry has been simulated by Higginson et al. (2017a, 2017b). They considered the displacement of the base of the global helmet streamer by a large-scale vortical flow, both for a spherically symmetric initial coronal field and a coronal field involving a narrow corridor of open flux (forming a HFT). They tracked the magnetic field line connectivity and observed episodes of interchange reconnection (Fig. 97) and opening and closing of flux (as the helmet streamer expands or contracts), as well as reconnection occurring purely in the open field region. In the latter case, field lines are shown to slip along the "S-Web" arc over time (Higginson et al. 2017b), a signature of 3D non-null reconnection in the open field of the associated HFT (Antiochos et al. 2011; Scott et al. 2018). This expected field line slippage along the S-Web arc (open separatrix or quasi-separatrix curtain) was also described by Masson et al. (2014) for a pseudo-streamer topology. They compared EUV emissions at a pseudo-streamer with a static magnetic field extrapolation and some simulations in a separatrix dome topology, and concluded that interchange reconnection plays a determining role in pseudo-streamer emission patterns.

Moreover, Higginson and Lynch (2018) describe the 3D plasmoid structures formed during "pinch-off" reconnection in the heliospheric current sheet, which occurs between open field lines and can create disconnected magnetic flux. That is, the reconnection involves purely open field lines, which is the complement of the work described earlier in this section, as well as in Sect. 12, on reconnection in the absence of null points in which all the participating magnetic flux is closed

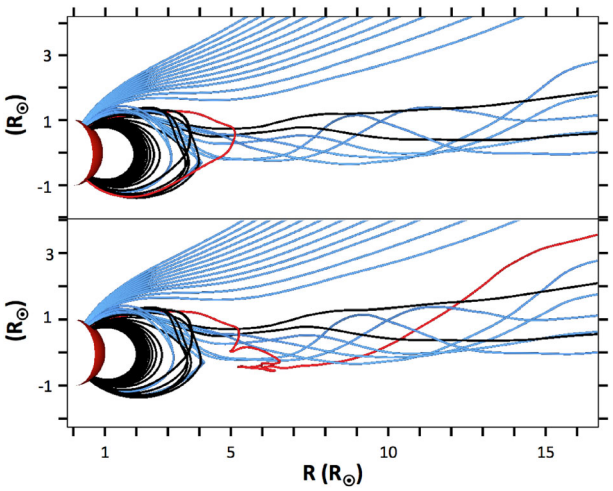

Fig. 97 Illustration of interchange reconnection in the simulations of Higginson et al. (2017a), reproduced with permission, copyright by AAS. Vortical driving of the footprint of the global helmet streamer leads the red field line to open up between the two times (while a counterpart field line is closed)

(anchored at both ends to the Sun's surface). These studies have been extended to include interchange reconnection at pseudo-streamers by Scott et al. (2021) and Aslanyan et al. (2021). In particular Aslanyan et al. (2021) drove both the helmet streamer and pseudo-streamer boundaries of a coronal hole with a driving pattern representative of the Sun's supergranulation. They described how the photospheric driving leads to the formation of filaments of newly-opened flux in the supergranular lanes due to interchange reconnection, leaving an imprint of the supergranulation in the heliosphere, previously reported in observations by Borovsky (2008, 2016).

15.3 3D reconnection in the Earth's magnetosphere

Reconnection is a crucial ingredient of magnetospheric dynamics, as described in the "open" model of the magnetosphere first proposed by Dungey (1961). In this model the magnetosphere is open in the sense that a finite amount of flux connects the Earth to interplanetary space. Reconnection occurs on the day-side between the interplanetary magnetic field (IMF) and Earth's magnetic field, leading predominantly to magnetic energy storage. There is a quasi-continuous reconnection process when the orientation of the IMF is favourable (with a strong southward component), as well as bursty *flux transfer events*. On the night-side, reconnection in the magnetotail releases the stored magnetic energy, most notably during *substorms*. Traditionally, reconnection in the magnetosphere has been interpreted in terms of 2D models. A 3D understanding has not been developed as fully as in the solar context, most likely in large part because of the *in situ* nature of the observations,

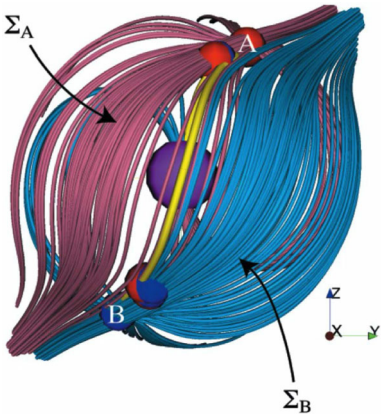

Fig. 98 Magnetic skeleton during a global MHD simulation of the magnetosphere. Red and blue spheres are A-type (negative) and B-type (positive) nulls, respectively, and separators are marked in yellow. Bundles of red and blue field lines pass close to the nulls of the corresponding colour and outline the spine and fan (Σ) surfaces of the nulls. Image reproduced with permission from Dorelli et al. (2007), copyright by AGU

which make an appreciation of the full 3D topology impossible without recourse to computational models.

The categorisation of reconnection has been based on 2.5D rather than 3D concepts, which is potentially misleading since a 2.5D magnetic field is often topologically unstable. The standard categorisation includes *anti-parallel merging* and *component merging*, depending on whether a non-zero magnetic field component exists in the plane perpendicular to a so-called *X-line*. In this context an X-line is a line along which any perpendicular cut exhibits an X-type hyperbolic field. However, as pointed out by, for example, Priest and Forbes (1989), in general in a 3D hyperbolic field, the X-lines are non-unique, since there is a continuum of X-lines, depending on the orientation of the perpendicular cut, implying that such definitions are fraught with ambiguities. Thus, in practice, antiparallel merging is likely to refer to null-point reconnection, whereas component merging could refer to either separator reconnection or quasi-separator reconnection. Furthermore, the term "X-line" is best avoided, since it could be mistaken with an X-type null line, namely, a continuum stack of 2D X-points on top of each other to form a line of X-type null points, which is topologically unstable (see Sect. 2.4).

Following the development of fully 3D models of the magnetosphere, it was realised that magnetospheric cusp regions are in fact the locations of 3D magnetic nulls (or perhaps more generically clusters of 3D nulls), and that the separatrix (fan) surfaces of these nulls intersect along one or more separator lines at the dayside magnetopause (sometime called null-null lines in the literature)—see Fig. 98 and Dorelli et al. (2007). A number of studies have demonstrated that reconnection is typically observed along these separators in global magnetospheric simulations (Dorelli et al. 2007; Glocer et al. 2016). Observationally such reconnection would be classed as component merging. Dorelli et al. (2007) also identify reconnection at the null point clusters in the cusps, which would be classed as anti-parallel merging.

The topology of flux transfer events turns out to be highly complex and is yet to be fully explored. Dorelli and Bhattacharjee (2009) demonstrated the existence of multiple separator lines in a simulated flux transfer event (see also Fedder et al. 2002). Other 3D models have interpreted FTEs in terms of "interlaced" magnetic

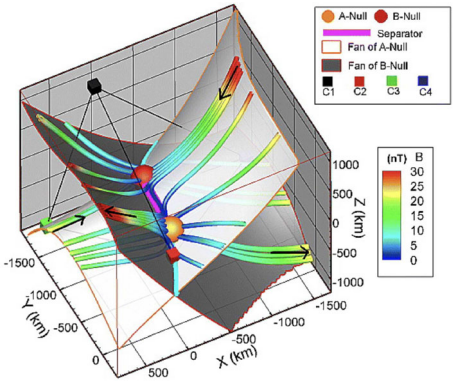

Fig. 99 Reconstructed magnetic field configuration based on Cluster data from the magnetotail. Orange and red spheres are A-type (negative) and B-type (positive) nulls, respectively, and the pink curve is the separator. Magnetic field lines are coloured by the local field strength, while the positions of the four Cluster spacecraft are shown with the cubes. Image reproduced with permission from He et al. (2008b), copyright by AGU

flux tubes (e.g., Kacem et al. 2018). An interesting open question is whether separators are the initial sites of the reconnection process in the FTE, or whether their formation is a secondary effect.

In recent years the presence of magnetic nulls has been inferred using spacecraft data (both Cluster and the Magnetospheric Multiscale Mission) from the magnetotail (e.g., Xiao et al. 2006; He et al. 2008a; Deng et al. 2009; Guo et al. 2016), magnetopause (Xiao et al. 2007; Fu et al. 2019), magnetosheath (Wendel and Adrian 2013; Chen et al. 2017), and bow shock (Chen et al. 2019b). Different techniques have been employed for identifying the null points and reconstructing the local 3D topology using the data (for a comparison see Olshevsky et al. 2020). The presence of separators is usually inferred in observations by separately identifying nearby magnetic nulls whose fan surfaces are oriented in such a way that they will intersect. This is because most methods reconstruct only the linear field structure around the null (though see Liu et al. 2019). Some methods though choose to fit a restricted field geometry with higher-order terms allowing for a separator joining a null pair to appear in the reconstructed field, as shown for example in Fig. 99.

In many cases, the magnetic nulls and separators identified in the field reconstructions are found to be collocated with signatures of ongoing reconnection. For example, Deng et al. (2009) identified whistler waves and electron beams in the vicinity of a null pair, while Wendel and Adrian (2013) compared the current distribution with the reconstructed field to infer ongoing torsional spine and torsional fan reconnection (see Sect. 10.2). The majority of the nulls identified turn out to be spiral nulls (see Fig. 4). These spiral nulls are found to be associated with twisted flux ropes and signatures of energy dissipation (Deng et al. 2009; Guo et al. 2016, 2019), and the flux ropes are important sites for particle acceleration in kinetic simulations (Zhou et al. 2018). A possible explanation for the production of these

spiral nulls and flux ropes is current sheet tearing as described by Wyper and Pontin (2014b) and shown in Fig. 47. We expect that future observational and theoretical developments will shed further light on the role of null points and separators in energy dissipation in the magnetosphere.

16 Reconnection and turbulence

Given the extreme values of the magnetic Reynolds number in astrophysical plasmas, the phenomena of reconnection and turbulence are inextricably linked. We saw in Sect. 8.3 how an initially laminar current layer can undergo nonlinear tearing, leading to a turbulent evolution (e.g., Loureiro and Boldyrev 2020). Furthermore, a smooth initial field with braided magnetic field lines was shown to develop a turbulent cascade of many inter-related reconnection events (Sect. 14.1.2). We briefly describe some aspects of the relation between reconnection and turbulence here. Further details on aspects of the problem are reviewed by Lazarian et al. (2020).

16.1 Breakdown of the frozen flux theorem

Boozer (2012) developed a description for stochastic magnetic field lines, describing how the cross-section of an infinitesimal flux tube deforms into a network of thin filaments as one follows the field lines (see also Rechester and Rosenbluth 1978). He argues that a breakdown in ideal motion will be triggered when the field-line separation becomes sufficiently large that the filaments of the deformed flux tubes reach kinetic length scales. These ideas were developed further by Boozer (2019), who used a Lagrangian description for field line evolution. He considered the case of a magnetic field with stochastic field lines and a small but non-vanishing non-ideal term. He demonstrated that the deviation of the field line evolution from exactly ideal motion grows exponentially with the characteristic field line separation. In this picture, fast scaling in the breakdown of ideal evolution with η is mediated not by a (parallel) current density that grows to ensure $\eta j_{\parallel}$ is large, but by field line exponentiation. Specifically, ideal evolution tends to produce an exponentially increasing field line separation (along field lines), and this leads to an exponential increase in sensitivity (in the departure of the local field vector from the ideally evolving value) to small non-ideal effects. By drawing a parallel with thermal equilibration in a gas, Boozer (2021) argued that the exponential separation of field lines implies that a current density of order $\ln(R_m)$ (rather than R_m) is required for reconnection to be dynamically significant.

These results offer an alternative perspective that is nevertheless consistent in two respects with our understanding of reconnection in braided fields described above: first, reconnection onset occurs for a sufficiently tangled field (as in Sect. 5.5.3); and second, once a burst of reconnection-mediated heating is triggered, the global reconnection rate for that heating burst is almost independent of the dissipation, this being due to an increase in the number of reconnection locations

with increasing R_m (see Sect. 14.1.2), rather than a local increase in the current density.

A related perspective has been developed by Eyink and collaborators. Our understanding of reconnection concepts is built on the foundations of Alfvén's flux freezing theorem for ideal MHD (Sect. 3.1). In most reconnection models, reconnection occurs when flux freezing breaks down in a localised layer of intense current density. However, Eyink (2009) and Eyink et al. (2011) have proposed an alternative scenario due to the breakdown of flux freezing in a turbulent plasma. They showed that a stochastic version of the frozen flux theorem can be derived, by considering stochastic Lagrangian trajectories of fluid particles. They argue that, if all solution fields of the equations remain smooth in the limit $R_m \to \infty$, then these stochastic trajectories collapse to the unique deterministic trajectory, and magnetic flux is frozen to the fluid in the deterministic sense. On the other hand, Chaves et al. (2003) have argued that the solution fields should be rough in the limit $R_m \to \infty$, so that, in turbulent plasmas with high R_m, flux freezing does not strictly hold. Instead, it is valid only in a statistical sense, namely, that the magnetic flux through a surface at a given time is the average of the magnetic fluxes through an ensemble of surfaces traced backward in time in the stochastic flow.

This stems from the idea that in a turbulent flow particles separate at a super-ballistic rate; so-called Richardson two-particle diffusion (Richardson 1926). In this picture, fluid particles 'forget' their initial position, and their trajectories are intrinsically random. The (Lagrangian) dynamics of the plasma elements (particles) are said to exhibit "spontaneous stochasticity" (Eyink et al. 2011). As a result, we must modify the concept of a magnetic field line being frozen to a unique plasma element: the stochasticity of the flow means that infinitely many particle trajectories bring infinitely many field lines to a given point at a given time (Figs. 100, 101). The result is that magnetic field line topology conservation (and the frozen-flux theorem) breaks down in a strict, deterministic sense—without having to appeal to resistive diffusion.

The extension of the ideas of magnetic flux conservation and field-line conservation (Sect. 3) to the picture of a plasma with stochastic field lines is

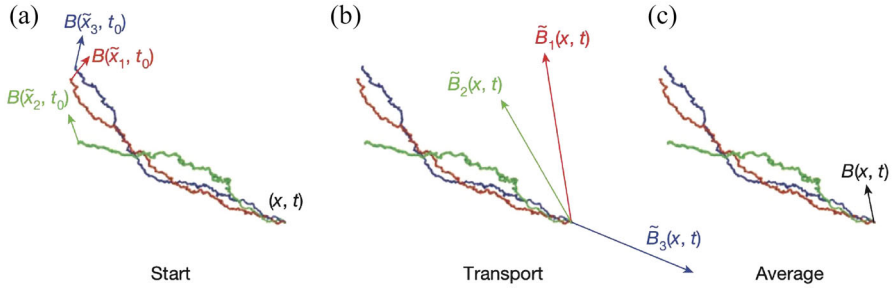

Fig. 100 Illustration of stochastic flux freezing, in which three different stochastic trajectories are traced back in time to t_0 from $(\mathbf{x}, t)$. The three field vectors at $t = t_0$ are transported along the stochastic trajectories, such that $\mathbf{B}(\mathbf{x}, t)$ is the average of the transported field vectors. Image reproduced with permission from Eyink et al. (2013), copyright by Springer

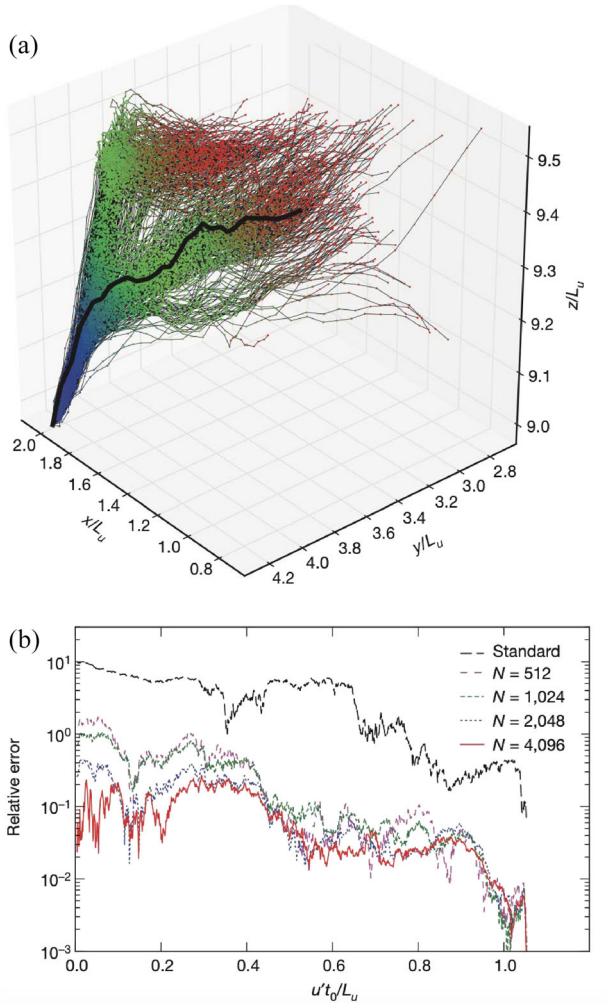

Fig. 101 **a** Realisation of stochastic flux freezing as per Fig. 100 in 3D MHD turbulence simulations. All of the plotted stochastic trajectories arrive at the same space-time point, and are coloured red–green–blue from early to late time. **b** Errors in flux transport of the magnetic field vector along the single black "deterministic" trajectory in (**a**), versus averages over different sized ensembles of stochastic trajectories (numbers as per the legend). Image reproduced with permission from Eyink et al. (2013), copyright by Springer

discussed explicitly by Eyink (2015), who develops a "turbulent generalisation" of *general magnetic reconnection*. On the basis of an Ohm's law

$$\mathbf{E} + \mathbf{v} \times \mathbf{B} = \mathbf{N} \tag{104}$$

he defines a "slip velocity source" $\mathbf{\Sigma} = -(\nabla \times \mathbf{N})_{\perp}/|\mathbf{B}|$ with the corresponding field line slip velocity

$$\Delta \mathbf{w}_\perp = \frac{\hat{\mathbf{B}} \times (\nabla V - \mathbf{N})}{|\mathbf{B}|}, \tag{105}$$

where V is a Hamiltonian for the evolution of Euler potentials in the ideal limit (denoted by $-\psi$ in Hesse and Schindler 1988). Consistent with the derivations discussed in Sect. 3.2, field line conservation now requires $\mathbf{\Sigma} = 0$, while $\mathbf{\Sigma} \neq 0$ implies a change of field line connectivity. Now, they argue that for turbulent eddies of length scale ℓ and below, $|\nabla \times \mathbf{N}_\ell^T| \sim |\delta\mathbf{v}(\ell) \times \delta\mathbf{B}(\ell)|$ with $\delta\mathbf{v}(\ell)$ and $\delta\mathbf{B}(\ell)$ being variations in $\mathbf{v}$ and $\mathbf{B}$ over length-scale ℓ. Now, for decreasing ℓ in the inertial range, this term grows, and typically dominates the effect of the "true" non-idealness. The "coarse-grained" (or low-pass filtered) magnetic field $\bar{\mathbf{B}}_\ell$ experiences a connectivity change not due to $\nabla \times \bar{\mathbf{N}}_\ell$ but due to the turbulence-induced slippage term $(\nabla \times \mathbf{N}_\ell^T)_\perp / |\bar{\mathbf{B}}_\ell|$. The reader is referred to Eyink (2015) for full details. The study

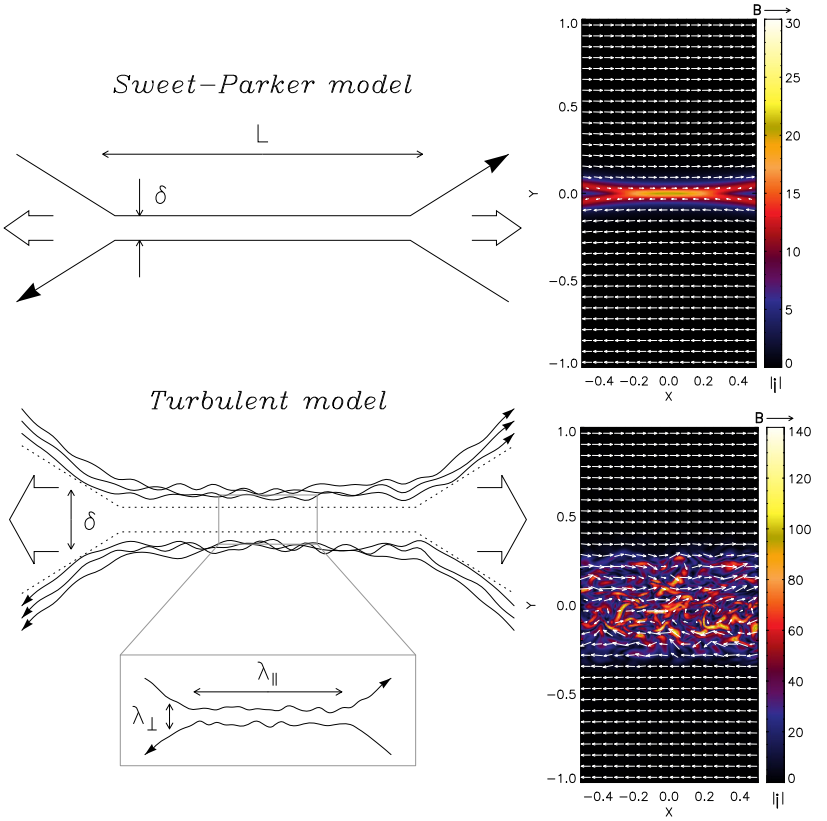

Fig. 102 Left: The upper plot shows a schematic of a Sweet–Parker current layer with laminar fields, as described in Sect. 7.1. The lower plot shows an equivalent current layer in a field characterised by stochastic field line wandering induced by turbulent fluctuations. In the inset is a small, localised reconnection region, many of which are assumed to be present within the large-scale structure, such that the net reconnection rate is independent of resistivity. Right: current density in the 3D MHD simulations of Kowal et al. (2009) showing reconnection in the absence (above) and presence (below) of turbulent fluctuations. Image reproduced with permission from Kowal et al. (2009), copyright by AAS

goes on to discuss the relevance for interpreting observables associated with turbulence in the solar wind. The impact of stochastic field line wandering on observables associated with magnetic reconnection has been addressed for tokamak plasmas by Firpo et al. (2016).

16.2 The rate of reconnection in a turbulent plasma

The effect of turbulent fluctuations on the rate of reconnection was considered in the groundbreaking study by Lazarian and Vishniac (1999), wherein they envisaged such fluctuations modifying the reconnection properties of a global-scale current layer (Fig. 102). Conceptually, what they showed is that the presence of the turbulent fluctuations removes the restriction of the narrow outflow channel in the Sweet–Parker model (which in Sweet–Parker limits the inflow speed and thus the reconnection rate, due to mass conservation). Rather than a laminar, collimated reconnection exhaust, the width δ of the outflow jet is limited by the field line wandering, not by the value of the resistivity. Many localised reconnection events occur within the large-scale layer that replaces the single, monolithic reconnection site (Fig. 102). In this way, the global reconnection rate is argued to be determined not by any detailed microphysics (such as resistivity) but instead by the degree of field line stochasticity, itself a property of the turbulent cascade. The authors discuss scalings based on different turbulence models, with the slowest possible reconnection rate being

$$M_i \sim R_m^{-3/16}, \tag{106}$$

which is substantially faster than the Sweet–Parker scaling of $R_m^{-1/2}$ described in Sect. 7.1. It was subsequently demonstrated by Eyink et al. (2011) that the predictions of Lazarian and Vishniac (1999) can also be derived within a stochastic flux freezing framework in the presence of a large-scale field reversal (Sect. 16.1).

The theory developed by Lazarian and Vishniac (1999) was tested in numerical simulations of MHD turbulence by Kowal et al. (2009), which involved simulating an initial system-scale Harris sheet equilibrium with the addition of a perturbation to initialise the reconnection and turbulent fluctuations. The current distribution in the presence and absence of turbulent fluctuations is shown in the right panel of Fig. 102. It is clear that in the presence of turbulent fluctuations the "reconnection layer" is substantially broadened, and reconnection occurs at many localised sites throughout the layer. They confirm the prediction that the rate of reconnection is essentially independent of resistivity and scales with the injected turbulent power.

Here we have only scratched the surface of the intimate connection between reconnection and turbulence. This will be an important topic for development in future. In particular, at present there remains debate on how to synthesise this picture with the developing understanding of nonlinear tearing (Sect. 8.3). In addition, there is a need to form a bridge with the understanding developed for globally 3D geometries (Sects. 10–14). In 3D, particularly in the absence of null points, the interpretation of the reconnection rate is not so straightforward as a simple inflow speed, even in the case of a single, isolated reconnection process (e.g.,

Sects. 4.7.2, 10–13). Wyper and Hesse (2015) developed a framework for quantifying the rate of reconnection in 3D when many, inter-related reconnection events occur within the same volume. In this extension of *general magnetic reconnection* (Sect. 4.5), they describe how the collective rate at which the connectivity changes can be quantified in two ways. The first is a total rate, which measures the true rate at which new connections are formed, and the second is a net rate which measures the net change of connection seen by the global field (external to the volume of interest) due to the influence of many non-ideal regions.

17 Non-thermal particle acceleration during reconnection

The concept of reconnection was first introduced as a way to explain non-thermal particle acceleration in solar flares, and indeed, since then, reconnection has become a leading candidate for explaining non-thermal particle acceleration for many astrophysical plasmas. It is known that a substantial fraction of the energy released during reconnection may often be released in the form of non-thermal particles, although the fraction is likely to depend on many factors such as the local and global geometries and the plasma parameters. Several acceleration mechanisms associated with reconnection exist, and the relative contribution of each in different scenarios remains to be determined. A vast literature on the topic exists, which we do not attempt to review here. Rather we make note of a few important concepts and results as they relate to the MHD description of reconnection discussed in this review, and refer the reader to more complete reviews of particle acceleration in solar flares (Zharkova et al. 2011; Gordovskyy et al. 2019; Kontar et al. 2019) and more broadly in astrophysics (Marcowith et al. 2020).

Within the framework of MHD modelling, particle acceleration can be studied using the "test particle" approach, in which individual particle trajectories are traced through the (evolving) electromagnetic fields from the MHD solution or simulation. Often the particle gyro-motion around the field lines is averaged out by using the guiding centre approximation (Northrop 1961), which substantially reduces the computation time. This is a good approximation unless the field is weak (such as close to a null point) or the parallel electric field is large—in which case the full Lorentz equation of motion must be used—or a significant percentage of the particles making up the plasma is accelerated when a full kinetic treatment is needed. The test particles are treated as independent of one another so that collisions are excluded, although some studies have sought to include scattering, for example due to Coulomb collisions (e.g., Borissov et al. 2017). While the test particle approach has severe limitations, a number of important insights can be drawn.

The primary limitation of the test particle approach is the absence of feedback between the particles and the electromagnetic field. If the number of particles accelerated is small then the test particle approach remains reasonable. However, if a large number of particles is accelerated (as in, e.g., a large solar flare) then the magnetic field induced by the flow of particles (current) may be sufficiently large that it would modify significantly the magnetic field from what MHD gives, at which point self-consistency is lost. Additionally, if substantial numbers of protons

and electrons are accelerated in opposite directions then charge separation would set up an electric field that is absent from an MHD description. As a result of these limitations, a complementary approach is to employ a kinetic simulation method such as particle-in-cell (PIC). This solves the self-consistency problem, but it comes at a high computational expense, which severely limits the scale of the domain that can be considered (usually the global geometry is excluded so that only the near vicinity of the reconnection site is modelled). Other compromises may also be made such as in the value of the electron-to-proton mass ratio. As a result, hybrid fluid-kinetic models have been developed that seek a compromise between the benefits of the MHD and kinetic descriptions. For much more detail, see the reviews by Zharkova et al. (2011), Gordovskyy et al. (2019), Marcowith et al. (2020).

In the classical 2D reconnection picture, one fundamental process is direct particle acceleration along the current sheet by the reconnection electric field, which may occur until the particles escape from the current sheet (Speiser 1965; Litvinenko 1996). Depending on the global geometry, acceleration can also occur at shocks that are associated with the reconnection process, including standing shocks such as those described in Sect. 7.2 and "termination shocks" that form ahead of a reconnection outflow jet where it encounters the ambient plasma. Additionally, stochastic acceleration may occur due to turbulence in the outflow region. These latter effects only partly mitigate the issue of accelerating a sufficient number of particles though a single, small diffusion region. However, it may be possible to alleviate these concerns by appealing to a fragmented or turbulent reconnection process (Sects. 8.4, 16), which both increases the overall volume of the non-ideal region and allows for the possibility of particles encountering multiple acceleration sites (for a detailed discussion see, e.g., Cargill et al. 2012; Kowal et al. 2012). There has been particular recent focus on particles being accelerated in contracting and colliding magnetic islands or flux ropes (e.g., Drake et al. 2006; Arnold et al. 2021).

3D modelling of particle acceleration in coronal geometries has so far relied predominantly on the MHD plus test particles approach. Implementation of test particles into 3D MHD simulations is nevertheless useful for understanding the geometry of particle trajectories and the expected particle deposition patterns. In such modelling, particles are generally found to follow the topological structures of the magnetic field at which the reconnection is taking place, such as QSLs or the spine and fan field lines of magnetic nulls. This has been used to help explain flare ribbon geometry in different 3D magnetic topologies (e.g., Démoulin et al. 1997a; Masson et al. 2009; Rosdahl and Galsgaard 2010; Baumann et al. 2013; Janvier et al. 2013; Savcheva et al. 2015). In addition, Masson et al. (2013, 2019) have discussed the importance of interchange reconnection (Sect. 15.2) for facilitating the escape of solar energetic particles from the corona into the heliosphere. As one further example, particle acceleration at the many reconnection sites that form following the onset of kink instability has been studied as a model for particle acceleration within coronal loops (e.g., Pinto et al. 2016).

18 Summary and outlook

Magnetic reconnection theory has come a long way since the early work in the middle of the last century. Early efforts, aimed initially at explaining energy release in solar flares, focussed on 2D, steady-state, resistive MHD modelling (Sect. 6, 7). More recently the field has developed in two principal directions, the first being to understand the mechanism that permits a rapid energy conversion (high reconnection rate) in different plasmas. Such studies have been primarily restricted to two dimensions—due to the computational expense and challenges for interpretation in three dimensions—and have focussed either on detailed micro-physics (largely outside the scope of this review—see Sect. 9), or time-dependent effects such as impulsive bursty reconnection due to, e.g., the plasmoid instability (Sect. 8). The result is that rapid reconnection at a tenth or a hundredth of the Alfén speed is likely in three cases (Sect. 9), namely: by Petschek or almost uniform reconnection (Sect. 7) when the resistivity is enhanced; by Hall effects; or by impulsive bursty reconnection.

The second main focus of the development of reconnection theory has been the exploration of the rich properties of 3D reconnection, relevant for astrophysical systems such as the Sun which do not have special symmetries. We now know that many fundamental properties of reconnection are very different in 3D from 2D (Sect. 4). For example, in 3D, reconnection is not restricted to null points, and indeed does not occur at a point (as in 2D) but throughout a finite diffusion region. As a consequence, all 3D reconnection is characterised by field line flipping (or slipping or slip-running), and by a non-one-to-one rejoining of field line pairs.

With reconnection in 3D not restricted to occur at null points, it is critical to understand where and how intense current concentrations can form in complex 3D magnetic fields, in order to determine where reconnection will take place. It transpires that there are several magnetic features that are preferential sites for current sheet formation (Sect. 5), including: magnetic null points; separators; quasi-separators (or hyperbolic flux tubes), together with their associated separatrix surfaces and QSLs; and magnetic braids. While reconnection processes within current layers at each of these features share the key properties of 3D reconnection described above, there are also some important differences, and so a framework for understanding 3D reconnection modes at null points (Sect. 10), separators (Sect. 11), quasi-separators or HFTs (Sect. 12), and braids (Sect. 14.1) has been developed.

In solar physics, reconnection is a key component for understanding several of the biggest unsolved problems in the field, such as the origin of the Sun's field (the dynamo problem), the origin of solar flares and eruptions, heating of the solar corona and formation of the (slow) solar wind. Reconnection now seems certain to contribute substantially to coronal heating. Several mechanisms have been identified, including Parker braiding (Sect. 14.1), flux tube tectonics (Sect. 14.3) and flux cancellation (Sect. 14.4.2). All of these mechanisms are likely play some role, though their relative magnitudes in different parts of the solar atmosphere remain to be determined.

Solar flares and eruptions continue to be a key motivation in driving forward our understanding of reconnection. Recent 3D modelling has led to a new paradigm for flares, incorporating 3D reconnection theory (Sect. 13). Observational evidence suggests that flares may be triggered either at separators or quasi-separators (two-ribbon flares) or at null points (circular ribbon flares). Reconnection at these 3D magnetic structures also drives smaller-scale dynamic events in the corona such as jets and X-ray bright points (Sects. 10.4, 14.4.2), and releases plasma onto open field lines to contribute to the solar wind (Sect. 15.2).

Great advances have been made in our understanding of magnetic reconnection. However, there remain many open questions to be addressed in future. Here we list some of the most pressing. The first two of these can be summarised under the theme of "cross-scale coupling".

Current sheet formation in complex 3D magnetic fields: How do the global plasma dynamics determine where current sheets form in complex 3D magnetic fields? Consequently, which 3D reconnection regimes—described in Sects. 10–12—are most prevalent?

Relation between the MHD scale and kinetic scale: How is the magnetic field topology at large scales (external to the current sheet) coupled with the micro-physics in the diffusion region? What is the role of the large-scale structure in determining the kinetic physics. Conversely, what detailed mechanisms are at play in the electron dissipation region, and how does the micro-scale physics feed back onto the macro-scale dynamics?

Quantitative properties in 3D: What are the quantitative properties of each of the 3D reconnection regimes described in Sects. 10–12? It is critical to understand how the different plasma, flow and field parameters combine to influence, for example, the diffusion region dimensions, and the resulting reconnection rate.

Reconnection in a fragmented dissipation region: At large R_m, the dissipation region tends to break up, producing an array of inter-related reconnection processes. How do we interpret and understand the reconnection rate and energy conversion in such a state? What is the relation between reconnection and turbulence?

Observational signatures: What are the different observational signatures for each of the 3D reconnection regimes described in Sects. 10–12? For all but the largest reconnection events on the Sun, the dynamics in the vicinity of the current layer itself will not be spatially resolved for the foreseeable future, so of particular interest are secondary effects that can be observed at larger scales, such as bulk flows of plasma in outflow jets as well as non-thermal particle acceleration spectra, in order to allow diagnosis via, e.g., spectroscopic measurements.

Energy conversion: In 3D reconnection in the various different regimes, what determines the rate of energy conversion, into which forms, and what is the mechanism by which the energy is ultimately dissipated?

Progress in answering these questions will require a combination of the development of fundamental theory, large-scale numerical simulations, and new observations with cutting edge instruments.

Supplementary Information The online version contains supplementary material available at https://doi.org/10.1007/s41116-022-00032-9.

Acknowledgements We are delighted to acknowledge continual help and support from colleagues in St Andrews and Dundee working in the field of reconnection, notably Alan Hood, Gunnar Hornig, Duncan Mackay, Ineke De Moortel, Thomas Neukirch, Clare Parnell and Antonia Wilmot-Smith. Also, many colleagues around the world have been most helpful, especially Guillaume Aulanier, Hubert Baty, Joachim Birn, Allen Boozer, Terry Forbes, Michael Hesse, Dana Longcope, Karl Schindler and Slava Titov. ERP is also pleased to acknowledge support from the Leverhulme Trust during his emeritus fellowship.

Open Access This article is licensed under a Creative Commons Attribution 4.0 International License, which permits use, sharing, adaptation, distribution and reproduction in any medium or format, as long as you give appropriate credit to the original author(s) and the source, provide a link to the Creative Commons licence, and indicate if changes were made. The images or other third party material in this article are included in the article's Creative Commons licence, unless indicated otherwise in a credit line to the material. If material is not included in the article's Creative Commons licence and your intended use is not permitted by statutory regulation or exceeds the permitted use, you will need to obtain permission directly from the copyright holder. To view a copy of this licence, visit http://creativecommons.org/licenses/by/4.0/.

References

Abbo L, Ofman L, Antiochos SK, Hansteen VH, Harra L, Ko YK, Lapenta G, Li B, Riley P, Strachan L, von Steiger R, Wang YM (2016) Slow solar wind: observations and modeling. Space Sci Rev 201(1–4):55–108. https://doi.org/10.1007/s11214-016-0264-1

Albright BJ (1999) The density and clustering of magnetic nulls in stochastic magnetic fields. Phys Plasmas 6(11):4222–4228. https://doi.org/10.1063/1.873689

Amari T, Aly JJ (1990) Current sheets in two-dimensional potential magnetic fields. II. Asymptotic limits of indefinitely sheared force-free fields. Astron Astrophys 227:628

Antiochos SK (1987) The topology of force-free magnetic fields and is implications for coronal activity. Astrophys J 312:886. https://doi.org/10.1086/164935

Antiochos SK (1996) Solar drivers of space weather. In: Balasubramaniam KS, Keil SL, Smartt RN (eds) Solar drivers of the interplanetary and terrestrial disturbances. Proceedings of the 16th internationnal workshop National Solar Observatory/Sacramento Peak, Sunspot, New Mexico, USA, 16–20 October 1995. ASP Conf. Ser., vol 95. Astronomical Society of the Pacific, San Francisco, p 1

Antiochos SK, DeVore CR, Klimchuk JA (1999) A model for solar coronal mass ejections. Astrophys J 510(1):485–493. https://doi.org/10.1086/306563. arXiv:astro-ph/9807220 [astro-ph]

Antiochos SK, Mikić Z, Titov VS, Lionello R, Linker JA (2011) A model for the sources of the slow solar wind. Astrophys J 731(2):112. https://doi.org/10.1088/0004-637X/731/2/112

Arber TD, Haynes M, Leake JE (2007) Emergence of a flux tube through a partially ionized solar atmosphere. Astrophys J 666(1):541–546. https://doi.org/10.1086/520046. arXiv:0706.4223 [astro-ph]

Archontis V, Syntelis P (2019) The emergence of magnetic flux and its role on the onset of solar dynamic events. Philos Trans R Soc London Ser A 377(2148):20180387. https://doi.org/10.1098/rsta.2018.0387

Archontis V, Moreno-Insertis F, Galsgaard K, Hood AW (2005) The three-dimensional interaction between emerging magnetic flux and a large-scale coronal field: reconnection, current sheets, and jets. Astrophys J 635(2):1299–1318. https://doi.org/10.1086/497533

Arnol'd VI (1974) The asymptotic Hopf invariant and its applications. Sel Math Sov 5:327–345

Arnold H, Drake JF, Swisdak M, Guo F, Dahlin JT, Chen B, Fleishman G, Glesener L, Kontar E, Phan T, Shen C (2021) Electron acceleration during macroscale magnetic reconnection. Phys Rev Lett 126(13):135101. https://doi.org/10.1103/PhysRevLett.126.135101

Aslanyan V, Pontin DI, Wyper PF, Scott RB, Antiochos SK, DeVore CR (2021) Effects of pseudostreamer boundary dynamics on heliospheric field and wind. Astrophys J 909(1):10. https://doi.org/10.3847/1538-4357/abd6e6

Aulanier G (2013) The physical mechanisms that initiate and drive solar eruptions. Proc Int Astron Union 8(S300):184–196. https://doi.org/10.1017/S1743921313010958
Aulanier G, Dudík J (2019) Drifting of the line-tied footpoints of CME flux-ropes. Astron Astrophys 621:A72. https://doi.org/10.1051/0004-6361/201834221. arXiv:1811.04253 [astro-ph.SR]
Aulanier G, Schmieder B (2002) The magnetic nature of wide EUV filament channels and their role in the mass loading of CMEs. Astron Astrophys 386:1106–1122. https://doi.org/10.1051/0004-6361:20020179
Aulanier G, Schmieder B, van Driel-Gesztelyi L, Kucera T, Démoulin P, Fang C, Mein N, Vial J, Mein P, Tang YH, Deforest C (2000) 3-D magnetic configurations for filaments and flares: the role of "magnetic dips" and "bald patches". Adv in Space Res 26:485–488. https://doi.org/10.1016/S0273-1177(99)01100-X
Aulanier G, Pariat E, Démoulin P (2005) Current sheet formation in quasi-separatrix layers and hyperbolic flux tubes. Astron Astrophys 444:961–976. https://doi.org/10.1051/0004-6361:20053600
Aulanier G, Pariat E, Démoulin P, Devore CR (2006) Slip-running reconnection in quasi-separatrix layers. Sol Phys 238:347–376. https://doi.org/10.1007/s11207-006-0230-2
Aulanier G, Golub L, DeLuca EE, Cirtain JW, Kano R, Lundquist LL, Narukage N, Sakao T, Weber MA (2007) Slipping magnetic reconnection in coronal loops. Science 318(5856):1588. https://doi.org/10.1126/science.1146143
Aulanier G, Janvier M, Schmieder B (2012) The standard flare model in three dimensions. I. Strong-to-weak shear transition in post-flare loops. Astron Astrophys 543:A110. https://doi.org/10.1051/0004-6361/201219311
Aulanier G, Démoulin P, Schrijver CJ, Janvier M, Pariat E, Schmieder B (2013) The standard flare model in three dimensions. II. Upper limit on solar flare energy. Astron Astrophys 549:A66. https://doi.org/10.1051/0004-6361/201220406. arXiv:1212.2086 [astro-ph.SR]
Aydemir AY (1992) Nonlinear studies of m=1 modes in high-temperature plasmas. Phys Fluids B 4(11):3469–3472. https://doi.org/10.1063/1.860355
Baalrud SD, Bhattacharjee A, Huang YM (2012) Reduced magnetohydrodynamic theory of oblique plasmoid instabilities. Phys Plasmas 19(2):022101. https://doi.org/10.1063/1.3678211
Bagalá LG, Mandrini CH, Rovira MG, Démoulin P (2000) Magnetic reconnection: a common origin for flares and active region interconnecting arcs. Astron Astrophys 363:779–788
Bajer K (1990) Flow, kinematics and magnetic equilibria. PhD thesis, Cambridge University, Cambridge
Baker D, van Driel-Gesztelyi L, Brooks DH, Démoulin P, Valori G, Long DM, Laming JM, To ASH, James AW (2020) Can subphotospheric magnetic reconnection change the elemental composition in the solar corona? Astrophys J 894(1):35. https://doi.org/10.3847/1538-4357/ab7dcb
Barnes G (2007) On the relationship between coronal magnetic null points and solar eruptive events. Astrophys J Lett 670(1):L53–L56. https://doi.org/10.1086/524107
Bárta M, Büchner J, Karlický M, Skála J (2011) Spontaneous current-layer fragmentation and cascading reconnection in solar flares. I. Model and analysis. Astrophys J 737(1):24. https://doi.org/10.1088/0004-637X/737/1/24
Bateman G (1978) MHD instabilities. MIT Press, Cambridge
Baty H, Priest ER, Forbes TG (2006) Effect of nonuniform resistivity in Petschek reconnection. Phys Plasmas 13:022312/1–7. https://doi.org/10.1063/1.2172543
Baty H, Priest ER, Forbes TG (2009a) Petschek-like reconnection with uniform resistivity. Phys Plasmas 16:060701. https://doi.org/10.1063/1.3155087
Baty H, Priest ER, Forbes TG (2009b) Petschek reconnection with a nonlocalized resistivity. Phys Plasmas 16:012102/1–6. https://doi.org/10.1063/1.3062833
Baty H, Forbes TG, Priest ER (2014) The formation and stability of Petschek reconnection. Phys Plasmas 21(11):112111. https://doi.org/10.1063/1.4901918
Baum PJ, Bratenahl A (1980) Flux linkages of bipolar sunspot groups: a computer study. Sol Phys 67:245–258. https://doi.org/10.1007/BF00149805
Baumann G, Galsgaard K, Nordlund Å (2013) 3D solar null point reconnection MHD simulations. Sol Phys 284(2):467–487. https://doi.org/10.1007/s11207-012-0168-5
Berger MA (1984) Rigorous new limits on magnetic helicity dissipation in the solar corona. Geophys Astrophys Fluid Dyn 30:79–104. https://doi.org/10.1080/03091928408210078
Berger MA (1988) An energy formula for nonlinear force-free magnetic fields. Astron Astrophys 201:355–361

Berger MA (1999) Magnetic helicity in space physics. In: Brown MR, Canfield RC, Pevtsov AA (ed) Magnetic helicity in space and laboratory plasmas. American Geophysical Union, Washington, pp 1–11. https://doi.org/10.1029/GM111p0001
Berger MA, Field GB (1984) The topological properties of magnetic helicity. J Fluid Mech 147:133–148. https://doi.org/10.1017/S0022112084002019
Bessho N, Bhattacharjee A (2005) Collisionless reconnection in an electron-positron plasma. Phys Rev Lett 95(24):245001. https://doi.org/10.1103/PhysRevLett.95.245001
Bessho N, Bhattacharjee A (2007) Fast collisionless reconnection in electron-positron plasmasa. Phys Plasmas 14(5):056503. https://doi.org/10.1063/1.2714020
Bessho N, Bhattacharjee A (2012) Fast magnetic reconnection and particle acceleration in relativistic low-density electron-positron plasmas without guide field. Astrophys J 750(2):129. https://doi.org/10.1088/0004-637X/750/2/129
Beveridge C, Priest ER, Brown DS (2002) Magnetic topologies due to two bipolar regions. Sol Phys 209:333–347. https://doi.org/10.1023/A:1021210127598
Beveridge C, Priest ER, Brown DS (2003) Magnetic topologies in the solar corona due to four discrete photospheric flux regions. Geophys Astrophys Fluid Dyn 98:429–455. https://doi.org/10.1023/A:1026102820634
Bhattacharjee A (2004) Impulsive magnetic reconnection in the Earth's magnetotail and the solar corona. Annu Rev Astron Astrophys 42(1):365–384. https://doi.org/10.1146/annurev.astro.42.053102.134039
Bhattacharjee A, Brunel F, Tajima T (1983) Magnetic reconnection driven by the coalescence instability. Phys Fluids 26:3332–3337. https://doi.org/10.1063/1.864070
Bhattacharjee A, Huang YM, Yang H, Rogers B (2009) Fast reconnection in high-Lundquist-number plasmas due to the plasmoid instability. Phys Plasmas 16(11):112102
Bineau M (1972) Existence of force-free magnetic-fields. Commun Pure Appl Math 25(1):77
Bingert S, Peter H (2011) Intermittent heating in the solar corona employing a 3D MHD model. Astron Astrophys 530:A112. https://doi.org/10.1051/0004-6361/201016019
Bingert S, Peter H (2013) Nanoflare statistics in an active region 3D MHD coronal model. Astron Astrophys 550:A30. https://doi.org/10.1051/0004-6361/201220469
Birn J, Priest ER (2007) Reconnection of magnetic fields: MHD and collisionless theory and observations. Cambridge University Press, Cambridge
Birn J, Drake JF, Shay MA, Rogers BN, Denton RE, Hesse M, Kuznetsova M, Ma ZW, Bhattacharjee A, Otto A, Pritchett PL (2001) Geospace environmental modeling GEM magnetic reconnection challenge. J Geophys Res 106:3715–3720. https://doi.org/10.1029/1999JA900449
Biskamp D (1982) Effect of secondary tearing instability on the coalescence of magnetic islands. Phys Lett 87A:357–360. https://doi.org/10.1016/0375-9601(82)90844-1
Biskamp D (1986) Magnetic reconnection via current sheets. Phys Fluids 29:1520
Biskamp D (1993) Nonlinear magnetohydrodynamics. Cambridge University Press, Cambridge
Biskamp D, Schwarz E, Drake JF (1997) Two-fluid theory of collisionless magnetic reconnection. Phys Plasmas 4(4):1002–1009. https://doi.org/10.1063/1.872211
Boozer AH (2012) Separation of magnetic field lines. Phys Plasmas 19(11):112901. https://doi.org/10.1063/1.4765352
Boozer AH (2019) Fast magnetic reconnection and the ideal evolution of a magnetic field. Phys Plasmas 26(4):042104. https://doi.org/10.1063/1.5081828
Boozer AH (2021) Magnetic reconnection and thermal equilibration. Phys Plasmas 28(3):032102032102. https://doi.org/10.1063/5.0031413
Borissov A, Kontar EP, Threlfall J, Neukirch T (2017) Particle acceleration with anomalous pitch angle scattering in 2D magnetohydrodynamic reconnection simulations. Astron Astrophys 605:A73. https://doi.org/10.1051/0004-6361/201731183
Borovsky JE (2008) Flux tube texture of the solar wind: Strands of the magnetic carpet at 1 au? J Geophys Res 113(A8). https://doi.org/10.1029/2007JA012684
Borovsky JE (2016) The plasma structure of coronal hole solar wind: origins and evolution. J Geophys Res 121(6):5055–5087. https://doi.org/10.1002/2016JA022686
Brandenburg A, Zweibel EG (1994) The formation of sharp structures by ambipolar diffusion. AstrophysJ Lett 427:L91. https://doi.org/10.1086/187372
Brandenburg A, Zweibel EG (1995) Effects of pressure and resistivity on the ambipolar diffusion singularity: too little, too late. Astrophys J 448:734. https://doi.org/10.1086/176001

Brooks DH, Ugarte-Urra I, Warren HP (2015) Full-Sun observations for identifying the source of the slow solar wind. Nat Commun 6:5947. https://doi.org/10.1038/ncomms6947
Brown DS, Priest ER (1999) Topological bifurcations in 3D magnetic fields. Proc R Soc London Ser A 455:3931–3951. https://doi.org/10.1098/rspa.1999.0484
Brown DS, Priest ER (2001) The topological behaviour of 3D null points in the Sun's corona. Astron Astrophys 367:339–346. https://doi.org/10.1051/0004-6361:20010016
Browning PK, Gerrard C, Hood AW, Kevis R, van der Linden RAM (2008) Heating the corona by nanoflares: simulations of energy release triggered by a kink instability. Astron Astrophys 485:837–848. https://doi.org/10.1051/0004-6361:20079192
Budišić M, Thiffeault JL (2015) Finite-time braiding exponents. Chaos 25(8):087407087407. https://doi.org/10.1063/1.4927438
Bulanov SV, Olshanetsky MA (1984) Magnetic collapse near zero points of the magnetic field. Phys Lett 100A:35–38. https://doi.org/10.1016/0375-9601(84)90349-9
Bulanov SV, Sakai J (1997) Magnetic collapse in incompressible plasma flows. J Phys Soc Jpn 66(11):3477–3483. https://doi.org/10.1143/JPSJ.66.3477
Bulanov SV, Sakai DI, Syrovatsky SI (1979) Tearing instability in quasi-stationary magnetohydrodynamic configurations. Sov J Plasma Phys 5:280–290
Bulanov SV, Shasharaina SG, Pegoraro F (1990) MHD modes near the X-line of a magnetic configuration. Plasma Phys Control Fusion 32:377–389. https://doi.org/10.1088/0741-3335/32/5/006
Bungey TN, Priest ER (1995) Current sheet configurations in potential and force-free fields. Astron Astrophys 293:215–224
Bungey TN, Titov VS, Priest ER (1996) Basic topological elements of coronal magnetic fields. Astron Astrophys 308:233–247
Candelaresi S, Pontin DI, Hornig G (2014) Mimetic methods for Lagrangian relaxation of magnetic fields. SIAM J Sci Comput 36:B952–B968
Candelaresi S, Pontin DI, Hornig G (2015) Magnetic field relaxation and current sheets in an ideal plasma. Astrophys J 808:134
Candelaresi S, Pontin DI, Hornig G (2017) Quantifying the tangling of trajectories using the topological entropy. Chaos 27(9):093102. https://doi.org/10.1063/1.5000812
Candelaresi S, Pontin DI, Yeates AR, Bushby PJ, Hornig G (2018) Estimating the rate of field line braiding in the solar corona by photospheric flows. Astrophys J 864:157
Cargill PJ, Vlahos L, Baumann G, Drake JF, Nordlund Å (2012) Current fragmentation and particle acceleration in solar flares. Space Sci Rev 173(1–4):223–245. https://doi.org/10.1007/s11214-012-9888-y
Carmichael H (1964) A process for flares. In: Hess WN (ed) NASA special publication, vol 50. NASA, Washington, p 451
Cassak PA, Shay MA (2008) Scaling of asymmetric Hall magnetic reconnection. Geophys Res Lett 35(19):L19102. https://doi.org/10.1029/2008GL035268
Cassak PA, Shay MA, Drake JF (2009) Scaling of Sweet-Parker reconnection with secondary islands. Phys Plasmas 16(12):120702. https://doi.org/10.1063/1.3274462
Cassak PA, Baylor RN, Fermo RL, Beidler MT, Shay MA, Swisdak M, Drake JF, Karimabadi H (2015) Fast magnetic reconnection due to anisotropic electron pressure. Phys Plasmas 22(2):020705. https://doi.org/10.1063/1.4908545. arXiv:1502.01781 [physics.plasm-ph]
Cassak PA, Liu YH, Shay MA (2017) A review of the 0.1 reconnection rate problem. J Plasma Phys 83(5):715830501. https://doi.org/10.1017/S0022377817000666
Chandra R, Schmieder B, Aulanier G, Malherbe JM (2009) Evidence of magnetic helicity in emerging flux and associated flare. Sol Phys 258(1):53–67. https://doi.org/10.1007/s11207-009-9392-z. arXiv:0906.1210 [astro-ph.SR]
Chandra R, Schmieder B, Mandrini CH, Démoulin P, Pariat E, Török T, Uddin W (2011) Homologous flares and magnetic field topology in active region NOAA 10501 on 20 November 2003. Sol Phys 269(1):83–104. https://doi.org/10.1007/s11207-010-9670-9. arXiv:1011.1187 [astro-ph.SR]
Chaves M, Gawedzki K, Horvai P, Kupiainen A, Vergassola M (2003) Lagrangian dispersion in Gaussian self-similar velocity ensembles. J Stat Phys 113:643–692. https://doi.org/10.1023/A:1027348316456
Che H, Drake JF, Swisdak M (2011) A current filamentation mechanism for breaking magnetic field lines during reconnection. Nature 474(7350):184–187. https://doi.org/10.1038/nature10091
Chen XH, Fu HS, Liu CM, Cao D, Wang Z, Dunlop MW, Chen ZZ, Peng FZ (2017) Magnetic nulls in the reconnection driven by turbulence. Astrophys J 852(1):17. https://doi.org/10.3847/1538-4357/aa9991

Chen H, Yang J, Ji K, Duan Y (2019a) Observational analysis on the early evolution of a CME flux rope: preflare reconnection and flux rope's footpoint drift. Astrophys J 887(2):118. https://doi.org/10.3847/1538-4357/ab527e. arXiv:1911.00257 [astro-ph.SR]

Chen ZZ, Fu HS, Wang Z, Liu CM, Xu Y (2019b) Evidence of magnetic nulls in the reconnection at bow shock. Geophys Res Lett 46(17–18):10209–10218. https://doi.org/10.1029/2019GL084360

Cheung MCM, Isobe H (2014) Flux emergence (theory). Living Rev Sol Phys 11:3. https://doi.org/10.12942/lrsp-2014-3

Chitta LP, Sukarmadji ARC, Rouppe van der Voort L, Peter H (2019) Energetics of magnetic transients in a solar active region plage. Astron Astrophys 623:A176. https://doi.org/10.1051/0004-6361/201834548. arXiv:1902.01650 [astro-ph.SR]

Chitta LP, Peter H, Priest ER, Solanki SK (2020) Impulsive coronal heating during the interaction of surface magnetic fields in the lower solar atmosphere. Astron Astrophys 644:A130. https://doi.org/10.1051/0004-6361/202039099. arXiv:2010.12560 [astro-ph.SR]

Chodura R, Schlueter A (1981) A 3D code for MHD equilibrium and stability. J Comput Phys 41:68–88

Close RM, Parnell CE, Mackay DH, Priest ER (2003) Statistical flux tube properties of 3D magnetic carpet fields. Sol Phys 212(2):251–275. https://doi.org/10.1023/A:1022961913168

Comisso L, Bhattacharjee A (2016) On the value of the reconnection rate. J Plasma Phys 82(6):595820601. https://doi.org/10.1017/S002237781600101X. arXiv:1609.02998 [physics.plasm-ph]

Comisso L, Grasso D, Waelbroeck FL, Borgogno D (2013) Gyro-induced acceleration of magnetic reconnection. Phys Plasmas 20(9):092118. https://doi.org/10.1063/1.4821840. arXiv:1309.1753 [physics.plasm-ph]

Comisso L, Lingam M, Huang YM, Bhattacharjee A (2017) Plasmoid instability in forming current sheets. Astrophys J 850(2):142. https://doi.org/10.3847/1538-4357/aa9789

Cowley SC, Longcope DW, Sudan RN (1997) Current sheets in MHD turbulence. Phys Rep 283:227–251. https://doi.org/10.1016/S0370-1573(96)00064-6

Cowling TG (1953) Solar electrodynamics. In: Kuiper G (ed) The Sun. University of Chicago Press, Chicago, pp 532–591

Craig IJD, Fabling RB (1996) Exact solutions for steady-state spine and fan magnetic reconnection. Astrophys J 462:969–976. https://doi.org/10.1063/1.871932

Craig IJD, Fabling RB (1998) Dynamic magnetic reconnection in three space dimensions: fan current solutions. Phys Plasmas 5:635–644

Craig IJD, Henton SM (1995) Exact solutions for steady state incompressible magnetic reconnection. Astrophys J 450:280–288. https://doi.org/10.1086/176139

Craig IJD, Litvinenko YE (2005) Current singularities in planar magnetic X-points of finite compressibility. Phys Plasmas 12:032301. https://doi.org/10.1063/1.1854154

Craig IJD, McClymont AN (1991) Dynamic magnetic reconnection at an X-type neutral point. Astrophys J 371:L41–L44. https://doi.org/10.1086/185997

Craig IJD, McClymont AN (1993) Linear theory of fast reconnection at an X-type neutral point. Astrophys J 405:207–215. https://doi.org/10.1086/172354

Craig IJD, Pontin DI (2014) Current singularities in line-tied three-dimensional magnetic fields. Astrophys J 788:177. https://doi.org/10.1088/0004-637X/788/2/177

Craig IJD, Sneyd AD (1986) A dynamic relaxation technique for determining the structure and stability of coronal magnetic fields. Astrophys J 311:451–459. https://doi.org/10.1086/164785

Craig IJD, Sneyd AD (1990) Non-linear development of the kink instability in coronal flux tubes. Astrophys J 357:653–661

Craig IJD, Sneyd AD (2005) The Parker problem and the theory of coronal heating. Sol Phys 232(1–2):41–62. https://doi.org/10.1007/s11207-005-1582-8

Craig IJD, Fabling RB, Henton SM, Rickard GJ (1995) An exact solution for steady state magnetic reconnection in three dimensions. Astrophys J Lett 455:L197. https://doi.org/10.1086/309822

Crooker NU, Gosling JT, Kahler SW (2002) Reducing heliospheric magnetic flux from coronal mass ejections without disconnection. J Geophys Res A 107:1028. https://doi.org/10.1029/2001JA000236

Dahlburg RB, Antiochos SK (1995) Reconnection of antiparallel magnetic flux tubes. J Geophys Res 100(A9):16991–16998. https://doi.org/10.1029/95JA01613

Dahlburg RB, Einaudi G (2002) MHD unstable modes in the 3D evolution of 2D MHD structures and the diminished role of coalescence instabilities. Phys Lett A 294:101–107. https://doi.org/10.1016/S0375-9601(02)00027-0

Dahlburg RB, Antiochos SK, Norton D (1997) Magnetic flux tube tunneling. Phys Rev E 56:2094–2103. https://doi.org/10.1103/PhysRevE.56.2094

Dahlburg RB, Klimchuk JA, Antiochos SK (2005) An explanation for the "switch-on" nature of magnetic energy release and its application to coronal heating. Astrophys J 622:1191–1201. https://doi.org/10.1086/425645

Dahlburg RB, Einaudi G, Rappazzo AF, Velli M (2012) Turbulent coronal heating mechanisms: coupling of dynamics and thermodynamics. Astron Astrophys 544:L20. https://doi.org/10.1051/0004-6361/201219752

Daughton W, Roytershteyn V (2012) Emerging parameter space map of magnetic reconnection in collisional and kinetic regimes. Space Sci Rev 172(1–4):271–282. https://doi.org/10.1007/s11214-011-9766-z

Daughton W, Scudder J, Karimabadi H (2006) Fully kinetic simulations of undriven magnetic reconnection with open boundary conditions. Phys Plasmas 13(7):072101. https://doi.org/10.1063/1.2218817

Daughton W, Roytershteyn V, Albright BJ, Karimabadi H, Yin L, Bowers KJ (2009a) Influence of Coulomb collisions on the structure of reconnection layers. Phys Plasmas 16(7):072117. https://doi.org/10.1063/1.3191718

Daughton W, Roytershteyn V, Albright BJ, Karimabadi H, Yin L, Bowers KJ (2009b) Transition from collisional to kinetic regimes in large-scale reconnection layers. Phys Rev Lett 103(6):065004. https://doi.org/10.1103/PhysRevLett.103.065004

Daughton W, Roytershteyn V, Albright BJ, Karimabadi H, Yin L, Bowers KJ (2009c) Transition from collisional to kinetic regimes in large-scale reconnection layers. Phys Rev Lett 103(6):065004. https://doi.org/10.1103/PhysRevLett.103.065004

Daughton W, Nakamura TKM, Karimabadi H, Roytershteyn V, Loring B (2014) Computing the reconnection rate in turbulent kinetic layers by using electron mixing to identify topology. Phys Plasmas 21(5):052307. https://doi.org/10.1063/1.4875730

De Moortel I, Galsgaard K (2006a) Numerical modelling of 3D reconnection due to rotational footpoint motions. Astron Astrophys 451:1101–1115. https://doi.org/10.1051/0004-6361:20065716

De Moortel I, Galsgaard K (2006b) Numerical modelling of 3D reconnection. II. Comparison between rotational and spinning footpoint motions. Astron Astrophys 459:627–639

Del Zanna G, Aulanier G, Klein KL, Török T (2011) A single picture for solar coronal outflows and radio noise storms. Astron Astrophys 526:A137. https://doi.org/10.1051/0004-6361/201015231

Delannée C, Aulanier G (1999) CME associated with transequatorial loops and a bald patch flare. Sol Phys 190:107–129. https://doi.org/10.1023/A:1005249416605

Démoulin P (2006) Extending the concept of separatrices to QSLs for magnetic reconnection. Adv in Space Res 37:1269–1282. https://doi.org/10.1016/j.asr.2005.03.085

Démoulin P, Henoux JC, Priest ER, Mandrini CH (1996a) Quasi-separatrix layers in solar flares. I. Method. Astron Astrophys 308:643–655

Démoulin P, Priest ER, Lonie DP (1996b) 3D magnetic reconnection without null points. II. Application to twisted flux tubes. J Geophys Res 101:7631–7646. https://doi.org/10.1029/95JA03558

Démoulin P, Bagala LG, Mandrini CH, Hénoux JC, Rovira MG (1997a) Quasi-separatrix layers in solar flares. II. Observed magnetic configurations. Astron Astrophys 325:305–317

Démoulin P, Henoux JC, Mandrini CH, Priest ER (1997b) Can we extrapolate a magnetic field when its topology is complex? Sol Phys 174:73–89. https://doi.org/10.1023/A:1004926513260

Deng XH, Zhou M, Li SY, Baumjohann W, Andre M, Cornilleau N, Santolík O, Pontin DI, Reme H, Lucek E, Fazakerley AN, Decreau P, Daly P, Nakamura R, Tang RX, Hu YH, Pang Y, Büchner J, Zhao H, Vaivads A, Pickett JS, Ng CS, Lin X, Fu S, Yuan ZG, Su ZW, Wang JF (2009) Dynamics and waves near multiple magnetic null points in reconnection diffusion region. J Geophys Res 114(A7):A07216. https://doi.org/10.1029/2008JA013197

Diamond PH, Hazeltine RD, An ZG, Carreras BA, Hicks HR (1984) Theory of anomalous tearing mode growth and the major tokamak disruption. Phys Fluids 27:1449–1462. https://doi.org/10.1063/1.864766

Dmitruk P, Gómez DO (1999) Scaling law for the heating of solar coronal loops. Astrophys J 527:L63

Dorelli JC, Bhattacharjee A (2009) On the generation and topology of flux transfer events. J Geophys Res 114(A6):A06213. https://doi.org/10.1029/2008JA013410

Dorelli JC, Bhattacharjee A, Raeder J (2007) Separator reconnection at Earth's dayside magnetopause under generic northward interplanetary magnetic field conditions. J Geophys Res 112:A02202. https://doi.org/10.1029/2006JA011877

Dorfman S, Ji H, Yamada M, Yoo J, Lawrence E, Myers C, Tharp TD (2013) Three-dimensional, impulsive magnetic reconnection in a laboratory plasma. Geophys Res Lett 40(2):233–238. https://doi.org/10.1029/2012GL054574

Drake JF, Kleva RG (1991) Collisionless reconnection and the sawtooth crash. Phys Rev Lett 66(11):1458–1461. https://doi.org/10.1103/PhysRevLett.66.1458

Drake JF, Swisdak M, Che H, Shay MA (2006) Electron acceleration from contracting magnetic islands during reconnection. Nature 443(7111):553–556. https://doi.org/10.1038/nature05116

Drake JF, Shay MA, Swisdak M (2008) The Hall fields and fast magnetic reconnection. Phys Plasmas 15(4):042306. https://doi.org/10.1063/1.2901194

Dudík J, Janvier M, Aulanier G, Del Zanna G, Karlický M, Mason HE, Schmieder B (2014) Slipping magnetic reconnection during an X-class solar flare observed by SDO/AIA. Astrophys J 784(2):144. https://doi.org/10.1088/0004-637X/784/2/144. arXiv:1401.7529 [astro-ph.SR]

Dudík J, Polito V, Janvier M, Mulay SM, Karlický M, Aulanier G, Del Zanna G, Dzifčáková E, Mason HE, Schmieder B (2016) Slipping magnetic reconnection, chromospheric evaporation, implosion, and precursors in the 2014 September 10 X1.6-class solar flare. Astrophys J 823(1):41. https://doi.org/10.3847/0004-637X/823/1/41. arXiv:1603.06092 [astro-ph.SR]

Dudík J, Lörinčík J, Aulanier G, Zemanová A, Schmieder B (2019) Observation of all pre- and post-reconnection structures involved in three-dimensional reconnection geometries in solar eruptions. Astrophys J 887(1):71. https://doi.org/10.3847/1538-4357/ab4f86. arXiv:1910.08620 [astro-ph.SR]

Dungey JW (1953) Conditions for the occurrence of electrical discharges in astrophysical systems. Philos Mag 44:725–738

Dungey JW (1961) Interplanetary magnetic field and the auroral zones. Phys Rev Lett 6:47–48. https://doi.org/10.1103/PhysRevLett.6.47

Edmondson JK, Antiochos SK, DeVore CR, Lynch BJ, Zurbuchen TH (2010) Interchange reconnection and coronal hole dynamics. Astrophys J 714:517–531. https://doi.org/10.1088/0004-637X/714/1/517

Edwards SJ, Yeates AR, Bocquet FX, Mackay DH (2015) Influence of non-potential coronal magnetic topology on solar-wind models. Sol Phys 290(10):2791–2808. https://doi.org/10.1007/s11207-015-0795-8

Effenberger F, Thust K, Arnold L, Grauer R, Dreher J (2011) Numerical simulation of current sheet formation in a quasi-separatrix layer using adaptive mesh refinement. Phys Plasmas 18(3):032902. https://doi.org/10.1063/1.3565018

Egedal J, Ng J, Le A, Daughton W, Wetherton B, Dorelli J, Gershman D, Rager A (2019) Pressure tensor elements breaking the frozen-in law during reconnection in Earth's magnetotail. Phys Rev Lett 123(22):225101. https://doi.org/10.1103/PhysRevLett.123.225101

Einaudi G, Rubini F (1986) Resistive instabilities in a flowing plasma. I. Inviscid case. Phys Fluids 29:2563–2568. https://doi.org/10.1063/1.865548

Eyink GL (2009) Stochastic line motion and stochastic flux conservation for nonideal hydromagnetic models. J Math Phys 50(8):225101. https://doi.org/10.1063/1.3193681

Eyink GL (2015) Turbulent general magnetic reconnection. Astrophys J 807(2):137. https://doi.org/10.1088/0004-637x/807/2/137

Eyink GL, Lazarian A, Vishniac ET (2011) Fast magnetic reconnection and spontaneous stochasticity. Astrophys J 743(1):51. https://doi.org/10.1088/0004-637X/743/1/51

Eyink G, Vishniac E, Lalescu C, Aluie H, Kanov K, Bürger K, Burns R, Meneveau C, Szalay A (2013) Flux-freezing breakdown in high-conductivity magnetohydrodynamic turbulence. Nature 497(7450):466–469. https://doi.org/10.1038/nature12128

Fan Y, Gibson SE (2004) Numerical simulations of three-dimensional coronal magnetic fields resulting from the emergence of twisted magnetic flux tubes. Astrophys J 609(2):1123–1133. https://doi.org/10.1086/421238

Fedder JA, Slinker SP, Lyon JG, Russell CT (2002) Flux transfer events in global numerical simulations of the magnetosphere. J Geophys Res 107(A5):SMP 1–1–SMP 1–10. https://doi.org/10.1029/2001JA000025

Finn JM, Kaw PK (1977) Coalescence instability of magnetic islands. Phys Fluids 20:72–78. https://doi.org/10.1063/1.861709

Firpo MC, Ettoumi W, Lifschitz AF, Retino A, Farengo R, Ferrari HE, García-Martínez PL (2016) Impact of the Eulerian chaos of magnetic field lines in magnetic reconnection. Phys Plasmas 23(12):122905. https://doi.org/10.1063/1.4972544

Fisk LA, Kasper JC (2020) Global circulation of the open magnetic flux of the sun. Astrophys J 894(1):L4. https://doi.org/10.3847/2041-8213/ab8acd

Fisk LA, Schwadron NA, Zurbuchen TH (1998) On the slow solar wind. Space Sci Rev 86(1):51–60
Fletcher L (2009) Ultra-violet footpoints as tracers of coronal magnetic connectivity and restructuring during a solar flare. Astron Astrophys 493:241–250
Fletcher L, López Fuentes MC, Mandrini CH, Schmieder B, Démoulin P, Mason HE, Young PR, Nitta N (2001a) A relationship between transition region brightenings, abundances, and magnetic topology. Sol Phys 203(2):255–287. https://doi.org/10.1023/A:1013302317042
Fletcher L, Metcalf TR, Alexander D, Brown DS, Ryder LA (2001b) Evidence for the flare trigger site and three-dimensional reconnection in multi-wavelength observations of a solar flare. Astrophys J 554:451–463. https://doi.org/10.1086/321377
Fletcher L, Pollock JA, Potts HE (2004) Tracking of TRACE ultraviolet flare footpoints. Sol Phys 222:279–298
Forbes TG (1986) Fast-shock formation in line-tied magnetic reconnection models of solar flares. Astrophys J 305:553–563
Forbes TG (2001) The nature of Petschek-type reconnection. Earth Planets Space 53:423–429. https://doi.org/10.1186/BF03353252
Forbes TG, Priest ER (1983) A numerical experiment relevant to line-tied reconnection in two-ribbon flares. Sol Phys 84(1–2):169–188. https://doi.org/10.1007/BF00157455
Forbes TG, Priest ER (1984a) Numerical simulation of reconnection in an emerging magnetic flux region. Sol Phys 94(2):315–340. https://doi.org/10.1007/BF00151321
Forbes TG, Priest ER (1984b) Reconnection in solar flares. In: Butler D, Papadopoulos K (eds) Solar terrestrial physics: present and future. NASA RP-1120, Washington, pp 1–35
Forbes TG, Priest ER (1987) A comparison of analytical and numerical models for steadily-driven magnetic reconnection. Rev Geophys 25:1583–1607. https://doi.org/10.1029/RG025i008p01583
Forbes TG, Priest ER, Hood AW (1982) Evolution of current sheets following the onset of enhanced resistivity. J Plasma Phys 27(1):157–176. https://doi.org/10.1017/S0022377800026453
Freed MS, Longcope DW, McKenzie DE (2015) Three-year global survey of coronal null points from potential-field-source-surface (PFSS) modeling and Solar Dynamics Observatory (SDO) observations. Sol Phys 290:467–490. https://doi.org/10.1007/s11207-014-0616-5
Fu HS, Cao JB, Cao D, Wang Z, Vaivads A, Khotyaintsev YV, Burch JL, Huang SY (2019) Evidence of magnetic nulls in electron diffusion region. Geophys Res Lett 46(1):48–54. https://doi.org/10.1029/2018GL080449
Fuentes-Fernández J, Parnell CE (2012) Magnetohydrodynamic dynamical relaxation of coronal magnetic fields. III. 3D spiral nulls. Astron Astrophys 544:A77. https://doi.org/10.1051/0004-6361/201219190
Fuentes-Fernández J, Parnell CE (2013) Magnetohydrodynamic dynamical relaxation of coronal magnetic fields. IV. 3D tilted nulls. Astron Astrophys 554:A145. https://doi.org/10.1051/0004-6361/201220346
Furth HP, Killeen J, Rosenbluth MN (1963) Finite-resistivity instabilities of a sheet pinch. Phys Fluids 6:459–484. https://doi.org/10.1063/1.1706761
Furth HP, Rutherford PH, Selberg H (1973) Tearing mode in the cylindrical tokamak. Phys Fluids 16:1054–1063. https://doi.org/10.1063/1.1694467
Galsgaard K, Nordlund Å (1996) The heating and activity of the solar corona: I. Boundary shearing of an initially homogeneous magnetic field. J Geophys Res 101:13445–13460. https://doi.org/10.1029/96JA00428
Galsgaard K, Nordlund Å (1997) Heating and activity of the solar corona. III. Dynamics of a low-beta plasma with 3D null points. J Geophys Res 102:231–248. https://doi.org/10.1029/96JA02680
Galsgaard K, Pontin DI (2011a) Current accumulation at an asymmetric 3D null point caused by generic shearing motions. Astron Astrophys 534:A2. https://doi.org/10.1051/0004-6361/201117532
Galsgaard K, Pontin DI (2011b) Steady state reconnection at a single 3D magnetic null point. Astron Astrophys 529:A20. https://doi.org/10.1051/0004-6361/201014359
Galsgaard K, Priest ER, Nordlund Å (2000) Three-dimensional separator reconnection: how does it occur? Sol Phys 193:1–16. https://doi.org/10.1023/A:1005248811680
Galsgaard K, Priest ER, Titov VS (2003a) Numerical experiments on wave propagation towards a 3D null point due to rotational motions. J Geophys Res 108(A1):SSH 10.1–10.9. https://doi.org/10.1029/2002JA009393
Galsgaard K, Titov VS, Neukirch T (2003b) Magnetic pinching of hyperbolic flux tubes. II. Dynamic numerical model. Astrophys J 595:506–516. https://doi.org/10.1086/377258

Giovanelli RG (1947) Magnetic and electric phenomena in the Sun's atmosphere associated with sunspots. Mon Not Ry Astron Soc 107:338–355. https://doi.org/10.1093/mnras/107.4.338
Glocer A, Dorelli J, Toth G, Komar CM, Cassak PA (2016) Separator reconnection at the magnetopause for predominantly northward and southward IMF: techniques and results. J Geophys Res 121(1):140–156. https://doi.org/10.1002/2015JA021417
Gorbachev VS, Somov BV (1988) Photospheric vortex flows as a cause for two-ribbon flares: a topological model. Sol Phys 117:77–88. https://doi.org/10.1007/BF00148574
Gordovskyy M, Browning P, Pinto RF (2019) Combining MHD and kinetic modelling of solar flares. Adv Space Res 63(4):1453–1465. https://doi.org/10.1016/j.asr.2018.09.024
Green RM (1965) Modes of annihilation and reconnection in magnetic fields. In: Lust R (ed) Stellar and solar magnetic fields. North-Holland, Amsterdam, pp 398–404
Green LM, Török T, Vršnak B, Manchester W, Veronig A (2018) The origin, early evolution and predictability of solar eruptions. Space Sci Rev 214(1):46. https://doi.org/10.1007/s11214-017-0462-5
Gudiksen BV, Nordlund Å (2002) Bulk heating and slender magnetic loops in the solar corona. Astrophys J 572(1):L113–L116. https://doi.org/10.1086/341600
Gudiksen BV, Nordlund Å (2005a) An ab initio approach to the solar coronal heating problem. Astrophys J 618:1020. https://doi.org/10.1086/426063
Gudiksen BV, Nordlund Å (2005b) An ab initio approach to solar coronal loops. Astrophys J 618(2):1031–1038. https://doi.org/10.1086/426064
Guo LJ, De Pontieu B, Huang YM, Peter H, Bhattacharjee A (2020) Observations and modeling of the onset of fast reconnection in the solar transition region. Astrophys J 901(2):148. https://doi.org/10.3847/1538-4357/abb2a7
Guo R, Pu Z, Chen LJ, Fu S, Xie L, Wang X, Dunlop M, Bogdanova YV, Yao Z, Xiao C, He J, Fazakerley AN (2016) In-situ observations of flux ropes formed in association with a pair of spiral nulls in magnetotail plasmas. Phys Plasmas 23(5):052901. https://doi.org/10.1063/1.4948415
Guo R, Pu Z, Yao Z, Dunlop M, Bogdanova YV, Wei Y, Wang X, Xiao C, He J, Fu S, Xie L, Fazakerley AN, Wan W (2019) A three-dimensional model of spiral null pair to form ion-scale flux ropes in magnetic reconnection region observed by cluster. Phys Plasmas 26(11):112901. https://doi.org/10.1063/1.5114620
Hansteen VH, Hara H, Pontieu BD, Carlsson M (2010) On redshifts and blueshifts in the transition region and corona. Astrophys J 718(2):1070–1078. https://doi.org/10.1088/0004-637x/718/2/1070
Hassam AB (1992) Reconnection of stressed magnetic fields. Astrophys J 399:159–163. https://doi.org/10.1086/171911
Haynes AL, Parnell CE (2007) A trilinear method for finding null points in a three-dimensional vector space. Phys Plasmas 14(8):082107082107. https://doi.org/10.1063/1.2756751
Haynes AL, Parnell CE (2010) A method for finding three-dimensional magnetic skeletons. Phys Plasmas 17(9):092903. https://doi.org/10.1063/1.3467499
Haynes AL, Parnell CE, Galsgaard K, Priest ER (2007) Magnetohydrodynamic evolution of magnetic skeletons. Proc R Soc A 463:1097–1115. https://doi.org/10.1098/rspa.2007.1815
He JS, Tu CY, Tian H, Xiao CJ, Wang XG, Pu ZY, Ma ZW, Dunlop MW, Zhao H, Zhou GP, Wang JX, Fu SY, Liu ZX, Zong QG, Glassmeier KH, Reme H, Dandouras I, Escoubet CP (2008a) A magnetic null geometry reconstructed from cluster spacecraft observations. J Geophys Res 113(A5). https://doi.org/10.1029/2007JA012609
He JS, Zong QG, Deng XH, Tu CY, Xiao CJ, Wang XG, Ma ZW, Pu ZY, Lucek E, Pedersen A, Fazakerley A, Cornilleau-Wehrlin N, Dunlop MW, Tian H, Yao S, Tan B, Fu SY, Glassmeier KH, Reme H, Dandouras I, Escoubet CP (2008b) Electron trapping around a magnetic null. Geophys Res Lett 35(14):L14104. https://doi.org/10.1029/2008GL034085
Hendrix DL, Van Hoven G (1996) Magnetohydrodynamic turbulence and implications for solar coronal heating. Astrophys J 467:887–893
Hesse M, Schindler K (1988) A theoretical foundation of general magnetic reconnection. J Geophys Res 93:5539–5567. https://doi.org/10.1029/JA093iA06p05559
Hesse M, Schindler K, Birn J, Kuznetsova M (1999) The diffusion region in collisionless magnetic reconnection. Phys Plasmas 6:1781–1795. https://doi.org/10.1063/1.873436
Hesse M, Forbes TG, Birn J (2005) On the relation between connected magnetic flux and parallel electric fields in the solar corona. Astrophys J 631:1227–1238. https://doi.org/10.1086/432677
Heyn MF (1996) Rapid reconnection in compressible plasma. Phys Plasmas 3:2725–2741. https://doi.org/10.1063/1.871723

Heyvaerts J, Priest ER (1976) Thermal evolution of current sheets and flash phase of solar flares. Sol Phys 47:223–231. https://doi.org/10.1007/BF00152260
Heyvaerts J, Priest ER (1984) Coronal heating by reconnection in DC current systems: a theory based on Taylor's hypothesis. Astron Astrophys 137:63–78
Heyvaerts J, Priest ER, Rust DM (1977) An emerging flux model for the solar flare phenomenon. Astrophys J 216:123–137. https://doi.org/10.1086/155453
Hide R (1979) On the magnetic flux linkage of an electrically conducting fluid. Geophys Astrophys Fluid Dyn 12:171–176. https://doi.org/10.1080/03091927908242682
Higginson AK, Lynch BJ (2018) Structured slow solar wind variability: streamer-blob flux ropes and torsional Alfvén waves. Astrophys J 859(1):6. https://doi.org/10.3847/1538-4357/aabc08
Higginson AK, Antiochos SK, DeVore CR, Wyper PF, Zurbuchen TH (2017a) Dynamics of coronal hole boundaries. Astrophys J 837(2):113. https://doi.org/10.3847/1538-4357/837/2/113
Higginson AK, Antiochos SK, DeVore CR, Wyper PF, Zurbuchen TH (2017b) Formation of heliospheric arcs of slow solar wind. Astrophys J Lett 840(1):L10. https://doi.org/10.3847/2041-8213/aa6d72
Hirayama T (1974) Theoretical model of flares and prominences. I: evaporating flare model. Sol Phys 34(2):323–338. https://doi.org/10.1007/BF00153671
Hood AW, Priest ER (1979) Kink instability of solar coronal loops as the cause of solar flares. Sol Phys 64:303–321. https://doi.org/10.1007/BF00151441
Hood AW, Priest ER (1981) Critical conditions for magnetic instabilities in force-free coronal loops. Geophys Astrophys Fluid Dyn 17:297–318. https://doi.org/10.1080/03091928108243687
Hood AW, Cargill PJ, Browning PK, Tam KV (2016) An MHD avalanche in a multi-threaded coronal loop. Astrophys J 817(1):5. https://doi.org/10.3847/0004-637X/817/1/5
Hornig G (1997) The covariant transport of electromagnetic fields and its relation to magnetohydrodynamics. Phys Plasmas 4(3):646–654. https://doi.org/10.1063/1.872161
Hornig G (2001) The geometry of reconnection. In: Ricca RL (ed) An introduction to the geometry and topology of fluid flows. Kluwer, Dordrecht, pp 295–313
Hornig G, Priest ER (2003) Evolution of magnetic flux in an isolated reconnection process. Phys Plasmas 10:2712–2721. https://doi.org/10.1063/1.1580120
Hornig G, Rastätter L (1998) The magnetic structure of B≠0 reconnection. Phys Scr 74:34–39. https://doi.org/10.1088/0031-8949/1998/T74/006
Hornig G, Schindler K (1996) Magnetic topology and the problem of its invariant definition. Phys Plasmas 3:781–791. https://doi.org/10.1063/1.871778
Hosteaux S, Chané E, Decraemer B, Talpeanu DC, Poedts S (2018) Ultrahigh-resolution model of a breakout CME embedded in the solar wind. Astron Astrophys 620:A57. https://doi.org/10.1051/0004-6361/201832976
Huang YM, Bhattacharjee A (2012) Distribution of plasmoids in high-Lundquist-number magnetic reconnection. Phys Rev Lett 109:265002. https://doi.org/10.1103/PhysRevLett.109.265002
Huang YM, Bhattacharjee A (2016) Turbulent magnetohydrodynamic reconnection mediated by the plasmoid instability. Astrophys J 818(1):1–11. https://doi.org/10.3847/0004-637X/818/1/20
Huang YM, Bhattacharjee A, Zweibel EG (2010) Effects of line-tying on magnetohydrodynamic instabilities and current sheet formation. Phys Plasmas 17(5):055707
Huang YM, Bhattacharjee A, Sullivan BP (2011) Onset of fast reconnection in Hall magnetohydrodynamics mediated by the plasmoid instability. Phys Plasmas 18(7):072109
Huba JD (2003) A tutorial on Hall MHD. In: Scholer M, Dum C, Büchner J (eds) Space simulations. Springer, New York, pp 170–197
Huba JD, Gladd NT, Papadopoulos K (1977) The lower-hybrid-drift instability as a source of anomalous resistivity for magnetic field line reconnection. Geophys Res Lett 4(3):125–128. https://doi.org/10.1029/GL004i003p00125
Innes DE, Guo LJ, Huang YM, Bhattacharjee A (2015) IRIS Si IV line profiles: an indication for the plasmoid instability during small-scale magnetic reconnection on the sun. Astrophys J 813(2):86. https://doi.org/10.1088/0004-637X/813/2/86
Innocenti ME, Goldman M, Newman D, Markidis S, Lapenta G (2015) Evidence of magnetic field switch-off in collisionless magnetic reconnection. Astrophys J Lett 810(2):L19. https://doi.org/10.1088/2041-8205/810/2/L19
Inverarity GW, Priest ER (1999) Magnetic null points due to multiple sources of solar photospheric flux. Sol Phys 186:99–121. https://doi.org/10.1023/A:1005129931992

Inverarity GW, Titov VS (1997) Formation of current layers in three-dimensional, inhomogeneous coronal magnetic fields by photospheric motions. J Geophys Res 102:22285–22294. https://doi.org/10.1029/97JA01674

Janse AM, Low BC (2009) The topological changes of solar coronal magnetic fields. I. Spontaneous current sheets in three-dimensional fields. Astrophys J 690(2):1089–1104

Janvier M (2017) Three-dimensional magnetic reconnection and its application to solar flares. J Plasma Phys 83(1):535830101. https://doi.org/10.1017/S0022377817000034

Janvier M, Aulanier G, Pariat E, Démoulin P (2013) The standard flare model in three dimensions. III. Slip-running reconnection properties. Astron Astrophys 555:A77. https://doi.org/10.1051/0004-6361/201321164. arXiv:1305.4053 [astro-ph.SR]

Janvier M, Aulanier G, Bommier V, Schmieder B, Démoulin P, Pariat E (2014) Electric currents in flare ribbons: observations and three-dimensional standard model. Astrophys J 788(1):60. https://doi.org/10.1088/0004-637X/788/1/60. arXiv:1402.2010 [astro-ph.SR]

Jara-Almonte J, Ji H, Yoo J, Yamada M, Fox W, Daughton W (2019) Kinetic simulations of magnetic reconnection in partially ionized plasmas. Phys Rev Lett 122(1):015101. https://doi.org/10.1103/PhysRevLett.122.015101

Ji H, Daughton W (2011) Phase diagram for magnetic reconnection in heliophysical, astrophysical, and laboratory plasmas. Phys Plasmas 18(11):111207. https://doi.org/10.1063/1.3647505

Jing J, Liu R, Cheung MCM, Lee J, Xu Y, Liu C, Zhu C, Wang H (2017) Witnessing a large-scale slipping magnetic reconnection along a dimming channel during a solar flare. Astrophys J Lett 842(2):L18. https://doi.org/10.3847/2041-8213/aa774d. arXiv:1706.01355 [astro-ph.SR]

Joshi J, Rouppe van der Voort LHM, de la Cruz Rodríguez J (2020) Signatures of ubiquitous magnetic reconnection in the lower solar atmosphere. Astron Astrophys 641:L5. https://doi.org/10.1051/0004-6361/202038769. arXiv:2006.14975 [astro-ph.SR]

Kacem I, Jacquey C, Génot V, Lavraud B, Vernisse Y, Marchaudon A, Le Contel O, Breuillard H, Phan TD, Hasegawa H, Oka M, Trattner KJ, Farrugia CJ, Paulson K, Eastwood JP, Fuselier SA, Turner D, Eriksson S, Wilder F, Russell CT, Øieroset M, Burch J, Graham DB, Sauvaud JA, Avanov L, Chandler M, Coffey V, Dorelli J, Gershman DJ, Giles BL, Moore TE, Saito Y, Chen LJ, Penou E (2018) Magnetic reconnection at a thin current sheet separating two interlaced flux tubes at the Earth's magnetopause. J Geophys Res 123(3):1779–1793. https://doi.org/10.1002/2017JA024537

Kadomtsev BB (1975) Disruptive instability in tokamaks. Sov J Plasma Phys 1:389–391

Kanella C, Gudiksen BV (2018) Investigating 4D coronal heating events in magnetohydrodynamic simulations. Astron Astrophys 617:A50. https://doi.org/10.1051/0004-6361/201732494. arXiv:1806.04495 [astro-ph.SR]

Karimabadi H, Daughton W, Scudder J (2007) Multi-scale structure of the electron diffusion region. Geophys Res Lett 34(13):L13104. https://doi.org/10.1029/2007GL030306

Karimabadi H, Dorelli J, Roytershteyn V, Daughton W, Chacón L (2011) Flux pileup in collisionless magnetic reconnection: bursty interaction of large flux ropes. Phys Rev Lett 107(2):025002. https://doi.org/10.1103/PhysRevLett.107.025002

Karpen JT, Antiochos SK, DeVore CR (2012) The mechanisms for the onset and explosive eruption of coronal mass ejections and eruptive flares. Astrophys J 760(1):81. https://doi.org/10.1088/0004-637X/760/1/81

Kazachenko MD, Canfield RC, Longcope DW, Qiu J (2010) Sunspot rotation, flare energetics, and flux rope helicity: the Halloween flare on 2003 October 28. Astrophys J 722:1539–1546

Kazachenko MD, Canfield RC, Longcope DW, Qiu J (2012) Predictions of energy and helicity in four major eruptive solar flares. Sol Phys 277:165–183

Khomenko E, Collados Vera M (2012) Heating of the magnetized solar chromosphere by partial ionization effects. Astrophys J 747:87

Kippenhahn R, Schluter A (1957) Eine Theorie der Solaren Filamente. Z Astrophys 43:36–62

Klapper I, Rado A, Tabor M (1996) A Lagrangian study of dynamics and singularity formation at magnetic null points in ideal three-dimensional magnetohydrodynamics. Phys Plasmas 3(11):4281–4283. https://doi.org/10.1063/1.871559

Kleva RG, Drake JF, Waelbroeck FL (1995) Fast reconnection in high temperature plasmas. Phys Plasmas 2(1):23–34. https://doi.org/10.1063/1.871095

Kliem B, Török T (2006) Torus instability. Phys Rev Lett 96(25):255002. https://doi.org/10.1103/PhysRevLett.96.255002

Kliem B, Su YN, van Ballegooijen AA, DeLuca EE (2013) Magnetohydrodynamic modeling of the solar eruption on 2010 April 8. Astrophys J 779(2):129. https://doi.org/10.1088/0004-637X/779/2/129. arXiv:1304.6981 [astro-ph.SR]

Klimchuk JA (2015) Key aspects of coronal heating. Philos Trans R Soc Lond Ser A 373(2042):20140256–20140256. https://doi.org/10.1098/rsta.2014.0256

Klimchuk JA, Antiochos SK (2021) How turbulent is the magnetically closed corona? Front Astron Space Sci 8:83. https://doi.org/10.3389/fspas.2021.662861

Klimchuk JA, Sturrock PA, Yang WH (1988) Coronal magnetic fields produced by photospheric shear. Astrophys J 335:456–467. https://doi.org/10.1086/166939

Knizhnik KJ, Antiochos SK, Klimchuk JA, DeVore CR (2019) The role of magnetic helicity in coronal heating. Astrophys J 883(1):26. https://doi.org/10.3847/1538-4357/ab3afd

Kondrashov D, Feynman J, Liewer PC, Ruzmaikin A (1999) Three-dimensional magnetohydrodynamic simulations of the interaction of magnetic flux tubes. Astrophys J 519:884–898. https://doi.org/10.1086/307383

Kontar EP, Jeffrey NLS, Emslie AG (2019) Determination of the total accelerated electron rate and power using solar flare hard X-ray spectra. Astrophys J 871(2):225. https://doi.org/10.3847/1538-4357/aafad3. arXiv:1812.09474 [astro-ph.SR]

Kopp RA, Pneuman GW (1976) Magnetic reconnection in the corona and the loop prominence phenomenon. Sol Phys 50(1):85–98. https://doi.org/10.1007/BF00206193

Kowal G, Lazarian A, Vishniac ET, Otmianowska-Mazur K (2009) Numerical tests of fast reconnection in weakly stochastic magnetic fields. Astrophys J 700:63–85. https://doi.org/10.1088/0004-637X/700/1/63

Kowal G, de Gouveia Dal Pino EM, Lazarian A (2012) Particle acceleration in turbulence and weakly stochastic reconnection. Phys Rev Lett 108(24):241102. https://doi.org/10.1103/PhysRevLett.108.241102

Kruskal MD, Johnson JL, Gottlieb MB, Goldman LM (1958) Hydromagnetic instability in a stellarator. Phys Fluids 1:421–429. https://doi.org/10.1063/1.1724359

Kulsrud RM (2001) Magnetic reconnection: Sweet-Parker versus Petschek. Earth Planets Space 53:417–422. https://doi.org/10.1186/BF03353251

Kumar P, Karpen JT, Antiochos SK, Wyper PF, DeVore CR (2019) First detection of plasmoids from breakout reconnection on the sun. Astrophys J 885(1):L15. https://doi.org/10.3847/2041-8213/ab45f9

Kumar P, Karpen JT, Antiochos SK, Wyper PF, DeVore CR, Lynch BJ (2021) From pseudostreamer jets to coronal mass ejections: observations of the breakout continuum. Astrophys J 907(1):41. https://doi.org/10.3847/1538-4357/abca8b

Kusano K, Bamba Y, Yamamoto TT, Iida Y, Toriumi S, Asai A (2012) Magnetic field structures triggering solar flares and coronal mass ejections. Astrophys J 760(1):31. https://doi.org/10.1088/0004-637X/760/1/31

Lau YT, Finn JM (1990) Three-dimensional kinematic reconnection in the presence of field nulls and closed field lines. Astrophys J 350:672–691. https://doi.org/10.1086/168419

Lau YT, Finn JM (1996) Magnetic reconnection and the topology of interacting twisted flux tubes. Phys Plasmas 3(11):3983. https://doi.org/10.1063/1.871571

Lazarian A, Vishniac ET (1999) Reconnection in a weakly stochastic field. Astrophys J 517:700–718. https://doi.org/10.1086/307233

Lazarian A, Eyink GL, Jafari A, Kowal G, Li H, Xu S, Vishniac ET (2020) 3D turbulent reconnection: theory, tests, and astrophysical implications. Phys Plasmas 27(1):012305. https://doi.org/10.1063/1.5110603

Le A, Daughton W, Chen LJ, Egedal J (2017) Enhanced electron mixing and heating in 3-D asymmetric reconnection at the Earth's magnetopause. Geophys Res Lett 44(5):2096–2104. https://doi.org/10.1002/2017GL072522. arXiv:1703.10246 [physics.plasm-ph]

Le A, Daughton W, Ohia O, Chen LJ, Liu YH, Wang S, Nystrom WD, Bird R (2018) Drift turbulence, particle transport, and anomalous dissipation at the reconnecting magnetopause. Phys Plasmas 25(6):062103. https://doi.org/10.1063/1.5027086. arXiv:1802.10205 [physics.plasm-ph]

Leake JE, Arber TD (2006) The emergence of magnetic flux through a partially ionised solar atmosphere. Astron Astrophys 450:805–818

Leake JE, Linton MG, Antiochos SK (2014) Simulations of emerging magnetic flux. II. The formation of unstable coronal flux ropes and the initiation of coronal mass ejections. Astrophys J 787(1):46. https://doi.org/10.1088/0004-637X/787/1/46

Leake JE, Daldorff LKS, Klimchuk JA (2020) The onset of 3D magnetic reconnection and heating in the solar corona. Astrophys J 891(1):62. https://doi.org/10.3847/1538-4357/ab7193

Lee DT, Brown DS (2020) Topology of coronal magnetic fields: extending the magnetic skeleton using null-like points. Sol Phys 295(12):168. https://doi.org/10.1007/s11207-020-01729-6. arXiv:2011.10272 [astro-ph.SR]

Lee LC, Fu Z (1986a) Multiple X-line reconnection. I. A criterion for the transition from a single X-line to a multiple X-line reconnection. J Geophys Res 91:6807–6815. https://doi.org/10.1029/JA091iA06p06807

Lee LC, Fu ZF (1986b) A simulation study of magnetic reconnection: transition from a fast mode to a slow mode expansion. J Geophys Res 91:4551–4556. https://doi.org/10.1029/JA091iA04p04551

Li T, Zhang J (2014) Slipping magnetic reconnection triggering a solar eruption of a triangle-shaped flag flux rope. Astrophys J Lett 791(1):L13. https://doi.org/10.1088/2041-8205/791/1/L13. arXiv:1407.4180 [astro-ph.SR]

Li T, Zhang J (2015) Quasi-periodic slipping magnetic reconnection during an X-class solar flare observed by the Solar Dynamics Observatory and Interface Region Imaging Spectrograph. Astrophys J Letts 804(1):L8. https://doi.org/10.1088/2041-8205/804/1/L8. arXiv:1504.01111 [astro-ph.SR]

Li T, Yang K, Hou Y, Zhang J (2016) Slipping magnetic reconnection of flux-rope structures as a precursor to an eruptive X-class solar flare. Astrophys J 830(2):152. https://doi.org/10.3847/0004-637X/830/2/152. arXiv:1608.02057 [astro-ph.SR]

Li T, Hou Y, Yang S, Zhang J (2018) Three-dimensional magnetic reconnection triggering an X-class confined flare in active region 12192. Astrophys J 869(2):172. https://doi.org/10.3847/1538-4357/aaefee. arXiv:1811.03302 [astro-ph.SR]

Li T, Liu L, Hou Y, Zhang J (2019) Two types of confined solar flare. Astrophys J 881(2):151. https://doi.org/10.3847/1538-4357/ab3121

Li T, Hou Y, Yang S, Zhang J, Liu L, Veronig AM (2020) Magnetic flux of active regions determining the eruptive character of large solar flares. Astrophys J 900(2):128. https://doi.org/10.3847/1538-4357/aba6ef. arXiv:2007.08127 [astro-ph.SR]

Li T, Priest ER, Guo R (2021) Three-dimensional magnetic reconnection in astrophysical plasmas. Proc R Soc A 477:20200949. https://doi.org/10.1098/rspa.2020.0949

Lin J, Ko YK, Sui L, Raymond JC, Stenborg GA, Jiang Y, Zhao S, Mancuso S (2005) Direct observations of the magnetic reconnection site of an eruption on 2003 November 18. Astrophys J 622(2):1251–1264. https://doi.org/10.1086/428110

Linton M (2007) Three-dimensional flux-tube reconnection. In: Birn J, Priest ER (eds) Reconnection of magnetic fields: MHD and collisionless theory and observations. Cambridge University Press, Cambridge, pp 74–86

Linton MG, Antiochos SK (2005) Magnetic flux tube reconnection: tunneling versus slingshot. Astrophys J 625:506–521. https://doi.org/10.1086/429585

Linton MG, Priest ER (2003) Three-dimensional reconnection of untwisted magnetic flux tubes. Astrophys J 595:1259–1276. https://doi.org/10.1086/377439

Linton MG, Dahlburg RB, Antiochos SK (2001) Reconnection of twisted flux tubes as a function of contact angle. Astrophys J 553:905–921. https://doi.org/10.1086/320974

Litvinenko YE (1996) Particle acceleration in reconnecting current sheets with a nonzero magnetic field. Astrophys J 462:997. https://doi.org/10.1086/177213

Liu YH, Drake JF, Swisdak M (2012) The structure of the magnetic reconnection exhaust boundary. Phys Plasmas 19(2):022110–022110. https://doi.org/10.1063/1.3685755. arXiv:1111.7039 [physics.-plasm-ph]

Liu YH, Daughton W, Karimabadi H, Li H, Roytershteyn V (2013) Bifurcated structure of the electron diffusion region in three-dimensional magnetic reconnection. Phys Rev Lett 110(26):265004. https://doi.org/10.1103/PhysRevLett.110.265004

Liu YH, Daughton W, Karimabadi H, Li H, Peter Gary S (2014) Do dispersive waves play a role in collisionless magnetic reconnection? Phys Plasmas 21(2):022113. https://doi.org/10.1063/1.4865579

Liu YH, Hesse M, Guo F, Daughton W, Li H, Cassak PA, Shay MA (2017) Why does steady-state magnetic reconnection have a maximum local rate of order 0.1? Phys Rev Lett 118(8):085101. https://doi.org/10.1103/PhysRevLett.118.085101. arXiv:1611.07859 [physics.plasm-ph]

Liu YY, Fu HS, Olshevsky V, Pontin DI, Liu CM, Wang Z, Chen G, Dai L, Retino A (2019) SOTE: a nonlinear method for magnetic topology reconstruction in space plasmas. Astrophys J Suppl Ser 244(2):31. https://doi.org/10.3847/1538-4365/ab391a

Longbottom AW, Rickard GJ, Craig IJD, Sneyd AD (1998) Magnetic flux braiding: force-free equilibria and current sheets. Astrophys J 500:471–482. https://doi.org/10.1086/305694

Longcope DW (1996) Topology and current ribbons: a model for current, reconnection and flaring in a complex, evolving corona. Sol Phys 169:91–121. https://doi.org/10.1007/BF00153836

Longcope DW (1998) A model for current sheets and reconnection in X-ray bright points. Astrophys J 507:433–442. https://doi.org/10.1086/306319

Longcope DW (2001) Separator current sheets: generic features in minimum-energy magnetic fields subject to flux constraints. Phys Plasmas 8:5277–5289. https://doi.org/10.1063/1.1418431

Longcope DW (2005) Topological methods for the analysis of solar magnetic fields. Living Rev Sol Phys 2:7. https://doi.org/10.12942/lrsp-2005-7

Longcope DW, Beveridge C (2007) A quantitative, topological model of reconnection and flux rope formation in a two-ribbon flare. Astrophys J 669:621–635. https://doi.org/10.1086/521521

Longcope DW, Cowley SC (1996) Current sheet formation along three-dimensional magnetic separators. Phys Plasmas 3:2885–2897

Longcope DW, Parnell CE (2009) The number of magnetic null points in the quiet-Sun corona. Sol Phys 254:51–75. https://doi.org/10.1007/s11207-008-9281-x

Longcope DW, Silva AVR (1998) A current ribbon model for energy storage and release with application to the flare 1992 Jan. 7. Sol Phys 179:349–377. https://doi.org/10.1023/A:1005071122577

Longcope DW, Strauss HR (1993) The coalescence instability and the development of current sheets in two-dimensional magnetohydrodynamics. Phys Fluids B 5:2858–2869

Longcope DW, Strauss HR (1994) The form of ideal current layers in line-tied magnetic fields. Astrophys J 437:851–859. https://doi.org/10.1086/175045

Longcope DW, Brown DS, Priest ER (2003) On the distribution of magnetic null points above the solar photosphere. Phys Plasmas 10:3321–3334. https://doi.org/10.1063/1.1590983

Longcope DW, McKenzie D, Cirtain J, Scott J (2005) Observations of separator reconnection to an emerging active region. Astrophys J 630:596–614. https://doi.org/10.1086/432039

Longcope DW, Beveridge C, Qiu J, Ravindra B, Barnes G, Dasso S (2007) Modeling and measuring the flux reconnected and ejected by the two-ribbon flare/ CME event on 7 November 2004. Sol Phys 244:45–73. https://doi.org/10.1007/s11207-007-0330-7

Longcope DW, Guidoni SE, Linton MG (2009) Gas-dynamic shock heating of post-flare loops due to retraction following localized, impulsive reconnection. Astrophys J Lett 690:L18–L22

Longcope D, Unverferth J, Klein C, McCarthy M, Priest E (2018) Evidence for downflows in the narrow plasma sheet of 2017 September 10 and their significance for flare reconnection. Astrophys J 868(2):148. https://doi.org/10.3847/1538-4357/aaeac4

Lörinčík J, Aulanier G, Dudík J, Zemanová A, Dzifčáková E (2019a) Velocities of flare kernels and the mapping norm of field line connectivity. Astrophys J 881(1):68. https://doi.org/10.3847/1538-4357/ab298f. arXiv:1906.01880 [astro-ph.SR]

Lörinčík J, Dudík J, Aulanier G (2019b) Manifestations of three-dimensional magnetic reconnection in an eruption of a quiescent filament: filament strands turning to flare loops. Astrophys J 885(1):83. https://doi.org/10.3847/1538-4357/ab4519. arXiv:1909.03825 [astro-ph.SR]

Loureiro NF, Boldyrev S (2020) Nonlinear reconnection in magnetized turbulence. Astrophys J 890(1):55. https://doi.org/10.3847/1538-4357/ab6a95

Loureiro NF, Cowley SC, Dorland WD, Haines MG, Schekochihin AA (2005) X-point collapse and saturation in the nonlinear tearing mode reconnection. Phys Rev Lett 95(23):235003. https://doi.org/10.1103/PhysRevLett.95.235003

Loureiro NF, Schekochihin AA, Cowley SC (2007) Instability of current sheets and formation of plasmoid chains. Phys Plasmas 14(10):100703

Loureiro NF, Samtaney R, Schekochihin AA, Uzdensky DA (2012) Magnetic reconnection and stochastic plasmoid chains in high-Lundquist-number plasmas. Phys Plasmas 19(4):042303. https://doi.org/10.1063/1.3703318

Loureiro NF, Schekochihin AA, Uzdensky DA (2013) Plasmoid and Kelvin-Helmholtz instabilities in Sweet-Parker current sheets. Phys Rev E 87(1):013102. https://doi.org/10.1103/PhysRevE.87.013102

Low BC (1981) Eruptive solar magnetic fields. Astrophys J 251:352–363. https://doi.org/10.1086/159470

Low BC (1986) Models of partially open magnetospheres with and without magnetodisks. Astrophys J 310:953–965. https://doi.org/10.1086/164746
Low BC (2001) Coronal mass ejections, magnetic flux ropes, and solar magnetism. J Geophys Res 106(A11):25141–25164. https://doi.org/10.1029/2000JA004015
Low BC (2006) Spontaneous current sheets in an ideal hydromagnetic fluid. Astrophys J 649(2):1064–1077. https://doi.org/10.1086/506586
Low BC, Flyer N (2007) The topological nature of boundary value problems for force-free magnetic fields. Astrophys J 668(1):557–570. https://doi.org/10.1086/520503
Low BC, Wolfson R (1988) Spontaneous formation of electric current sheets and the origin of solar flares. Astrophys J 324:574–581. https://doi.org/10.1086/165918
Luoni ML, Mandrini CH, Cristiani GD, Démoulin P (2007) The magnetic field topology associated with two M flares. Adv Space Res 39:1382–1388. https://doi.org/10.1016/j.asr.2007.02.005
Lynch BJ, Antiochos SK, DeVore CR, Luhmann JG, Zurbuchen TH (2008) Topological evolution of a fast magnetic breakout CME in three dimensions. Astrophys J 683(2):1192–1206. https://doi.org/10.1086/589738
Lynch BJ, Edmondson JK, Kazachenko MD, Guidoni SE (2016) Reconnection properties of large-scale current sheets during coronal mass ejection eruptions. Astrophys J 826(1):43. https://doi.org/10.3847/0004-637X/826/1/43
Ma ZW, Bhattacharjee A (1996) Fast impulsive reconnection and current sheet intensification due to electron pressure gradients in semi-collisional plasmas. Geophys Res Lett 23(13):1673–1676. https://doi.org/10.1029/96GL01600
Macneil AR, Owen CJ, Baker D, Brooks DH, Harra LK, Long DM, Wicks RT (2019) Active region modulation of coronal hole solar wind. Astrophys J 887(2):146. https://doi.org/10.3847/1538-4357/ab5586
MacTaggart D (2011) Flux emergence within mature solar active regions. Astron Astrophys 531:A108. https://doi.org/10.1051/0004-6361/201117099
MacTaggart D, Haynes AL (2013) On magnetic reconnection and flux rope topology in solar flux emergence. Mon Not R Astron Soc 438(2):1500–1506. https://doi.org/10.1093/mnras/stt2285
Malherbe JM, Priest ER (1983) Current sheet models for solar prominences. I. Magnetohydrostatics of support and evolution through quasi-static models. Astron Astrophys 123:80–88
Manchester IW, Gombosi T, DeZeeuw D, Fan Y (2004) Eruption of a buoyantly emerging magnetic flux rope. Astrophys J 610(1):588–596. https://doi.org/10.1086/421516
Mandrini CH, Demoulin P, Henoux JC, Machado ME (1991) Evidence for the interaction of large-scale magnetic structures in solar flares. Astron Astrophys 250:541–547
Mandrini CH, Demoulin P, Schmieder B, Deluca EE, Pariat E, Uddin W (2006) Companion event and precursor of the X17 flare on 28 October 2003. Sol Phys 238(2):293–312. https://doi.org/10.1007/s11207-006-0205-3
Mandrini CH, Baker D, Démoulin P, Cristiani GD, van Driel-Gesztelyi L, Vargas Domínguez S, Nuevo FA, Vásquez AM, Pick M (2015) Parallel evolution of quasi-separatrix layers and active region upflows. Astrophys J 809(1):73. https://doi.org/10.1088/0004-637X/809/1/73. arXiv:1507.01264 [astro-ph.SR]
Mandt ME, Denton RE, Drake JF (1994) Transition to whistler mediated magnetic reconnection. Geophys Res Lett 21(1):73–76. https://doi.org/10.1029/93GL03382
Marcowith A, Ferrand G, Grech M, Meliani Z, Plotnikov I, Walder R (2020) Multi-scale simulations of particle acceleration in astrophysical systems. Living Rev Comput Astrophys 6:1. https://doi.org/10.1007/s41115-020-0007-6
Martínez-Sykora J, De Pontieu B, Hansteen V (2012) Two-dimensional radiative magnetohydrodynamic simulations of the importance of partial ionization in the chromosphere. Astrophys J 753:161
Masson S, Pariat E, Aulanier G, Schrijver CJ (2009) The nature of flare ribbons in coronal null-point topology. Astrophys J 700:559–578. https://doi.org/10.1088/0004-637X/700/1/559
Masson S, Aulanier G, Pariat E, Klein KL (2012) Interchange slip-running reconnection and sweeping SEP beams. Sol Phys 276:199–217. https://doi.org/10.1007/s11207-011-9886-3
Masson S, Antiochos SK, DeVore CR (2013) A Model for the Escape of Solar-flare-accelerated Particles. Astrophys J 771(2):82. https://doi.org/10.1088/0004-637X/771/2/82
Masson S, McCauley P, Golub L, Reeves KK, DeLuca EE (2014) Dynamics of the transition corona. Astrophys J 787(2):145. https://doi.org/10.1088/0004-637X/787/2/145
Masson S, Antiochos SK, DeVore CR (2019) Escape of flare-accelerated particles in solar eruptive events. Astrophys J 884(2):143. https://doi.org/10.3847/1538-4357/ab4515

McClymont AN, Craig IJD (1996) Dynamical finite-amplitude magnetic reconnection at an X-type neutral point. Astrophys J 466:487. https://doi.org/10.1086/177526
McKenzie DE, Savage SL (2009) Quantitative examination of supra-arcade downflows in eruptive solar flares. Astrophys J 697:1569–1577
McLaughlin JA, De Moortel I, Hood AW, Brady CS (2009) Nonlinear fast magnetoacoustic wave propagation in the neighbourhood of a 2D magnetic X-point: oscillatory reconnection. Astron Astrophys 493(1):227–240. https://doi.org/10.1051/0004-6361:200810465. arXiv:0901.1781 [astro-ph.SR]
McLaughlin JA, Hood AW, de Moortel I (2011) Review article: MHD wave propagation near coronal null points of magnetic fields. Space Sci Rev 158(2–4):205–236. https://doi.org/10.1007/s11214-010-9654-y
McLaughlin JA, Thurgood JO, MacTaggart D (2012) On the periodicity of oscillatory reconnection. Astron Astrophys 548:A98. https://doi.org/10.1051/0004-6361/201220234. arXiv:1212.1000 [astro-ph.SR]
McLaughlin JA, Nakariakov VM, Dominique M, Jelínek P, Takasao S (2018) Modelling quasi-periodic pulsations in solar and stellar flares. Space Sci Rev 214(1):45. https://doi.org/10.1007/s11214-018-0478-5
Mellor C, Titov VS, Priest ER (2003) Linear collapse of spatially linear 3D potential null points. Geophys Astrophys Fluid Dyn 97:489–505. https://doi.org/10.1080/0309192032000141483
Metcalf TR, De Rosa ML, Schrijver CJ, Barnes G, van Ballegooijen AA, Wiegelmann T, Wheatland MS, Valori G, McTtiernan JM (2008) Nonlinear force-free modeling of coronal magnetic fields. II. Modeling a filament arcade and simulated chromospheric and photospheric vector fields. Sol Phys 247(2):269–299. https://doi.org/10.1007/s11207-007-9110-7
Mikić Z, Schnack DD, Hoven GV (1989) Creation of current filaments in the solar corona. Astrophys J 338:1148–1157. https://doi.org/10.1086/167265
Moffatt HK (1985) Magnetostatic equilibria and analogous Euler flows of arbitrarily complex topology. Part 1 Fundamentals. J Fluid Mech 159:359–378. https://doi.org/10.1017/S0022112085003251
Moraitis K, Pariat E, Valori G, Dalmasse K (2019) Relative magnetic field line helicity. Astron Astrophys 624:A51. https://doi.org/10.1051/0004-6361/201834668
Moraitis K, Patsourakos S, Nindos A (2021) Relative field line helicity of a large eruptive solar active region. Astron Astrophys 649:A107. https://doi.org/10.1051/0004-6361/202140384. arXiv:2103.03643 [astro-ph.SR]
Moreno-Insertis F, Galsgaard K (2013) Plasma jets and eruptions in solar coronal holes: a three-dimensional flux emergence experiment. Astrophys J 771(1):20. https://doi.org/10.1088/0004-637X/771/1/20. arXiv:1305.2201 [astro-ph.SR]
Nakamura TKM, Hasegawa H, Daughton W, Eriksson S, Li WY, Nakamura R (2017) Turbulent mass transfer caused by vortex induced reconnection in collisionless magnetospheric plasmas. Nat Commun 8:1582. https://doi.org/10.1038/s41467-017-01579-0
Naus SJ, Qiu J, DeVore CR, Antiochos SK, Dahlin JT, Drake JF, Swisdak M (2021) Correlated spatiotemporal evolution of extreme-ultraviolet ribbons and hard x-rays in a solar flare. arXiv e-prints arXiv:2109.15314 [astro-ph.SR]
Nemati MJ, Wang ZX, Wei L (2017) Dynamics of the plasmoid-unstable regime in different multiple-current plasmas. Astrophys J 835(2):191. https://doi.org/10.3847/1538-4357/835/2/191
Neugebauer M (2012) Evidence for polar X-ray jets as sources of microstream peaks in the solar wind. Astrophys J 750(1):50. https://doi.org/10.1088/0004-637x/750/1/50
Ng J, Egedal J, Le A, Daughton W, Chen LJ (2011) Kinetic structure of the electron diffusion region in antiparallel magnetic reconnection. Phys Rev Lett 106(6):065002. https://doi.org/10.1103/PhysRevLett.106.065002
Ng CS, Lin L, Bhattacharjee A (2012) High-Lundquist number scaling in three-dimensional simulations of Parker's model of coronal heating. Astrophys J 747(2):109
Ng J, Huang YM, Hakim A, Bhattacharjee A, Stanier A, Daughton W, Wang L, Germaschewski K (2015) The island coalescence problem: scaling of reconnection in extended fluid models including higher-order moments. Phys Plasmas 22(11):112104. https://doi.org/10.1063/1.4935302. arXiv:1511.00741 [physics.plasm-ph]
Ni L, Lukin VS (2018) Onset of secondary instabilities and plasma heating during magnetic reconnection in strongly magnetized regions of the low solar atmosphere. Astrophys J 868(2):144. https://doi.org/10.3847/1538-4357/aaeb97

Ni L, Kliem B, Lin J, Wu N (2015) Fast magnetic reconnection in the solar chromosphere mediated by the plasmoid instability. Astrophys J 799(1):79. https://doi.org/10.1088/0004-637X/799/1/79
Nóbrega-Siverio D, Martínez-Sykora J, Moreno-Insertis F, Carlsson M (2020a) Ambipolar diffusion in the Bifrost code. Astron Astrophys 638:A79. https://doi.org/10.1051/0004-6361/202037809. arXiv:2004.11927 [astro-ph.SR]
Nóbrega-Siverio D, Moreno-Insertis F, Martínez-Sykora J, Carlsson M, Szydlarski M (2020b) Nonequilibrium ionization and ambipolar diffusion in solar magnetic flux emergence processes. Astron Astrophys 633:A66. https://doi.org/10.1051/0004-6361/201936944. arXiv:1912.01015 [astro-ph.SR]
Northrop TG (1961) The guiding center approximation to charged particle motion. Ann Phys 15(1):79–101. https://doi.org/10.1016/0003-4916(61)90167-1
Olshevsky V, Pontin DI, Williams B, Parnell CE, Fu HS, Liu Y, Yao S, Khotyaintsev YV (2020) A comparison of methods for finding magnetic nulls in simulations and in situ observations of space plasmas. Astron Astrophys 644:A150. https://doi.org/10.1051/0004-6361/202039182
Ortiz A, Hansteen VH, Nóbrega-Siverio D, Rouppe van der Voort L (2020) Ellerman bombs and UV bursts: reconnection at different atmospheric layers. Astron Astrophys 633:A58. https://doi.org/10.1051/0004-6361/201936574. arXiv:1910.10736 [astro-ph.SR]
Owens MJ, Crooker NU, Lockwood M (2013) Solar origin of heliospheric magnetic field inversions: evidence for coronal loop opening within pseudostreamers. J Geophys Res 118:1868–1879. https://doi.org/10.1002/jgra.50259
Owens M, Lockwood M, Macneil A, Stansby D (2020) Signatures of coronal loop opening via interchange reconnection in the slow solar wind at 1 AU. Sol Phys 295(3):37. https://doi.org/10.1007/s11207-020-01601-7
Ozaki M, Sato T (1997) Interactions of convecting magnetic loops and arcades. Astrophys J 481:524–531. https://doi.org/10.1086/304036
Pariat E, Démoulin P (2012) Estimation of the squashing degree within a three-dimensional domain. Astron Astrophys 541:A78. https://doi.org/10.1051/0004-6361/201118515
Pariat E, Aulanier G, Schmieder B, Georgoulis MK, Rust D, Bernasconi PN (2004) Resistive emergence of undulatory flux tubes. Astrophys J 614:1099–1112. https://doi.org/10.1086/423891
Pariat E, Aulanier G, Démoulin P (2006) A new concept for magnetic reconnection: slip-running reconnection. In: Barret D, Casoli F, Lagache G, Lecavelier A, Pagani L (eds) SF2A-2006: Semaine d'Astrophysique Francaise. Société Francoise d'Astronomie et dAstrophysique, Paris, pp 559–562
Pariat E, Antiochos SK, DeVore CR (2009) A model for solar polar jets. Astrophys J 691:61–74. https://doi.org/10.1088/0004-637X/691/1/61
Park W, Monticello DA, B WR (1984) Reconnection rates of magnetic fields including the effects of viscosity. Phys Fluids 27:137–149. https://doi.org/10.1063/1.864502
Parker EN (1957) Sweet's mechanism for merging magnetic fields in conducting fluids. J Geophys Res 62:509–520. https://doi.org/10.1029/JZ062i004p00509
Parker EN (1963) The solar flare phenomenon and the theory of reconnection and annihilation of magnetic fields. Astrophys J 8:177–212. https://doi.org/10.1086/190087
Parker EN (1972) Topological dissipation and the small-scale fields in turbulent gases. Astrophys J 174:499–510. https://doi.org/10.1086/151512
Parker EN (1973) Comments on the reconnection rate of magnetic fields. J Plasma Phys 9:49–63. https://doi.org/10.1017/S0022377800007327
Parker EN (1979) Cosmical magnetic fields. Oxford University Press, Oxford
Parker EN (1988) Nanoflares and the solar X-ray corona. Astrophys J 330:474–479. https://doi.org/10.1086/166485
Parker EN (1989) Spontaneous tangential discontinuities and the optical analogy for static magnetic fields. Geophys Astrophys Fluid Dyn 45:159–168. https://doi.org/10.1080/03091928908208897
Parker EN (1994) Spontaneous current sheets in magnetic fields. Oxford University Press, New York
Parnell CE (2001) A model of the solar magnetic carpet. Sol Phys 200:23–45
Parnell CE (2007) Multiply connected source and null pairs. Sol Phys 242:21–41. https://doi.org/10.1007/s11207-007-0329-0
Parnell CE, Galsgaard K (2004) Elementary heating events—interaction between two flux sources. II. Rates of flux reconnection. Astron Astrophys 428:595–612. https://doi.org/10.1051/0004-6361:20034350

Parnell CE, Haynes AL (2009) Three-dimensional magnetic reconnection. In: Magnetic coupling between the interior and atmosphere of the sun. Springer, Heidelberg, pp 261–276. https://doi.org/10.1007/978-3-642-02859-5_20

Parnell CE, Priest ER (1995) A converging flux model for the formation of an X-ray bright point above a supergranule cell. Geophys Astrophys Fluid Dyn 80(3):255–276. https://doi.org/10.1080/03091929508228958

Parnell CE, Smith JM, Neukirch T, Priest ER (1996) The structure of 3D magnetic neutral points. Phys Plasmas 3:759–770. https://doi.org/10.1063/1.871810

Parnell CE, Neukirch T, Smith JM, Priest ER (1997) Structure and collapse of 3D magnetic neutral points. Geophys Astrophys Fluid Dyn 84:245–271. https://doi.org/10.1080/03091929708208979

Parnell CE, Haynes AL, Galsgaard K (2008) Recursive reconnection and magnetic skeletons. Astrophys J 675:1656–1667. https://doi.org/10.1086/527532

Parnell CE, Haynes AL, Galsgaard K (2010a) The structure of magnetic separators and separator reconnection. J Geophys Res 115:2102. https://doi.org/10.1029/2009JA014557

Parnell CE, Maclean RC, Haynes AL (2010b) The detection of numerous magnetic separators in a three-dimensional magnetohydrodynamic model of solar emerging flux. Astrophys J Lett 725:L214–L218. https://doi.org/10.1088/2041-8205/725/2/L214

Parnell CE, Haynes AL, Maclean RC (2011) Three-dimensional magnetic reconnection at null points and separators. In: Miralles MP, Sánchez Almeida J (eds) The sun, the solar wind, and the heliosphere. vol 4, p 147

Parnell CE, Stevenson JEH, Threlfall J, Edwards SJ (2015) Is magnetic topology important for heating the solar atmosphere? Philos Trans R Soc Lond A 373:20140264. https://doi.org/10.1098/rsta.2014.0264

Peter H (2015) What can large-scale magnetohydrodynamic numerical experiments tell us about coronal heating? Philos Trans R Soc Lond Ser A 373:20150055. https://doi.org/10.1098/rsta.2015.0055

Peter H, Huang Y-M, Chitta LP, Young PR (2019) Plasmoid-mediated reconnection in solar UV bursts. Astron Astrophys 628:A8. https://doi.org/10.1051/0004-6361/201935820

Petschek HE (1964) Magnetic field annihilation. In: The physics of solar flares. NASA Special Publication, vol SP-50. NASA, Washington DC, pp 425–439

Pinto RF, Gordovskyy M, Browning PK, Vilmer N (2016) Thermal and non-thermal emission from reconnecting twisted coronal loops. Astron Astrophys 585:A159. https://doi.org/10.1051/0004-6361/201526633

Platten SJ, Parnell CE, Haynes AL, Priest ER, Mackay DH (2014) The solar cycle variation of topological structures in the global solar corona. Astron Astrophys 565:A44. https://doi.org/10.1051/0004-6361/201323048

Pontin DI (2011) Three-dimensional magnetic reconnection regimes: a review. Adv Space Res 47:1508–1522. https://doi.org/10.1016/j.asr.2010.12.022

Pontin DI, Craig IJD (2005) Current singularities at finitely compressible three-dimensional magnetic null points. Phys Plasmas 12(7):072112. https://doi.org/10.1063/1.1987379

Pontin DI, Galsgaard K (2007) Current amplification and magnetic reconnection at a three-dimensional null point: physical characteristics. J Geophys Res 112:A03103. https://doi.org/10.1029/2006JA011848

Pontin DI, Hornig G (2015) The structure of current layers and degree of field-line braiding in coronal loops. Astrophys J 805:47. https://doi.org/10.1088/0004-637X/805/1/47

Pontin DI, Hornig G (2020) The Parker problem: existence of smooth force-free fields and coronal heating. Living Rev Sol Phys 17:5. https://doi.org/10.1007/s41116-020-00026-5

Pontin DI, Huang YM (2012) On the formation of current sheets in response to the compression or expansion of a potential magnetic field. Astrophys J 756(1):7. https://doi.org/10.1088/0004-637X/756/1/7. arXiv:1207.1127 [astro-ph.SR]

Pontin DI, Wyper PF (2015) The effect of reconnection on the structure of the Sun's open-closed flux boundary. Astrophys J 805:39. https://doi.org/10.1088/0004-637X/805/1/39. arXiv:1502.01311 [astro-ph.SR]

Pontin DI, Hornig G, Priest ER (2004) Kinematic reconnection at a magnetic null point: spine-aligned current. Geophys Astrophys Fluid Dyn 98:407–428. https://doi.org/10.1080/0309192042000272324

Pontin DI, Hornig G, Priest ER (2005) Kinematic reconnection at a magnetic null point: fan-aligned current. Geophys Astrophys Fluid Dyn 99:77–93. https://doi.org/10.1080/03091920512331328071

Pontin DI, Bhattacharjee A, Galsgaard K (2007a) Current sheet formation and nonideal behavior at three-dimensional magnetic null points. Phys Plasmas 14:052106. https://doi.org/10.1063/1.2722300

Pontin DI, Bhattacharjee A, Galsgaard K (2007b) Current sheets at three-dimensional magnetic nulls: effect of compressibility. Phys Plasmas 14:052109. https://doi.org/10.1063/1.2734949
Pontin DI, Hornig G, Wilmot-Smith AL, Craig IJD (2009) Lagrangian relaxation schemes for calculating force-free magnetic fields, and their limitations. Astrophys J 700:1449–1455
Pontin DI, Al-Hachami AK, Galsgaard K (2011a) Generalised models for torsional spine and fan magnetic reconnection. Astron Astrophys 533:A78. https://doi.org/10.1051/0004-6361/201117250
Pontin DI, Wilmot-Smith AL, Hornig G, Galsgaard K (2011b) Dynamics of braided coronal loops. II. Cascade to multiple small-scale reconnection events. Astron Astrophys 525:A57. https://doi.org/10.1051/0004-6361/201014544
Pontin DI, Priest ER, Galsgaard K (2013) On the nature of reconnection at a solar coronal null point above a separatrix dome. Astrophys J 774:154. https://doi.org/10.1088/0004-637X/774/2/154
Pontin DI, Candelaresi S, Russell AJB, Hornig G (2016) Braided magnetic fields: equilibria, relaxation and heating. Plasma Phys Control Fusion 58(5):054008. https://doi.org/10.1088/0741-3335/58/5/054008
Pontin DI, Peter H, Chitta LP (2020) Non-thermal line broadening due to braiding-induced turbulence in solar coronal loops. Astron Astrophys 639:A21. https://doi.org/10.1051/0004-6361/202037582
Priest ER (1986) Magnetic reconnection on the Sun. Mitteil Astron Ges 65:41–51
Priest ER (2014) Magnetohydrodynamics of the sun. Cambridge University Press, Cambridge
Priest ER, Démoulin P (1995) 3D reconnection without null points. J Geophys Res 100:23,443-23,463
Priest ER, Forbes TG (1986) New models for fast, steady-state reconnection. J Geophys Res 91:5579–5588
Priest ER, Forbes TG (1989) Steady magnetic reconnection in three dimensions. Sol Phys 119:211–214. https://doi.org/10.1007/BF00146222
Priest ER, Forbes TG (1992) Magnetic flipping—reconnection in three dimensions without null points. J Geophys Res 97:1521–1531. https://doi.org/10.1029/91JA02435
Priest ER, Forbes TG (2000) Magnetic reconnection: MHD theory and applications. Cambridge University Press, Cambridge
Priest ER, Lee LC (1990) Nonlinear magnetic reconnection models with separatrix jets. J Plasma Phys 44:337–360. https://doi.org/10.1017/S0022377800015221
Priest ER, Longcope DW (2017) Flux-rope twist in eruptive flares and CMEs: due to zipper and main-phase reconnection. Sol Phys 292:25. https://doi.org/10.1007/s11207-016-1049-0
Priest ER, Longcope DW (2020) The creation of twist by reconnection of flux tubes. Sol Phys 295(3):48. https://doi.org/10.1007/s11207-020-01608-0
Priest ER, Pontin DI (2009) Three-dimensional null point reconnection regimes. Phys Plasmas 16(12):122101–122101. https://doi.org/10.1063/1.3257901
Priest ER, Raadu MA (1975) Preflare current sheets in the solar atmosphere. Sol Phys 43:177–188. https://doi.org/10.1007/BF00155152
Priest ER, Syntelis P (2021) Chromospheric and coronal heating and jet acceleration due to reconnection driven by flux cancellation. I. At a three-dimensional current sheet. Astron Astrophys 647:A31. https://doi.org/10.1051/0004-6361/202038917. arXiv:2101.04600 [astro-ph.SR]
Priest ER, Titov VS (1996) Magnetic reconnection at three-dimensional null points. Philos Trans R Soc A 355:2951–2992. https://doi.org/10.1098/rsta.1996.0136
Priest ER, Parnell CE, Martin SF (1994) A converging flux model of an X-ray bright point and an associated canceling magnetic feature. Astrophys J 427:459–474
Priest ER, Titov VS, Rickard GK (1995) The formation of magnetic singularities by nonlinear time-dependent collapse of an X-type magnetic field. Philos Trans R Soc A 351:1–37. https://doi.org/10.1098/rsta.1995.0024
Priest ER, Bungey TN, Titov VS (1997) The 3D topology and interaction of complex magnetic flux systems. Geophys Astrophys Fluid Dyn 84:127–163. https://doi.org/10.1080/03091929708208976
Priest ER, Heyvaerts J, Title A (2002) A Flux Tube Tectonics model for solar coronal heating driven by the magnetic carpet. Astrophys J 576:533–551. https://doi.org/10.1086/341539
Priest E, Hornig G, Pontin DI (2003) On the nature of three-dimensional magnetic reconnection. J Geophys Res 108(A7):SSH 6.1–6.8. https://doi.org/10.1029/2002JA009812
Priest ER, Longcope DW, Heyvaerts J (2005) Coronal heating at separators and separatrices. Astrophys J 624:1057–1071. https://doi.org/10.1086/429312
Priest ER, Chitta LP, Syntelis P (2018) A cancellation nanoflare model for solar chromospheric and coronal heating. Astrophys J 862:L24. https://doi.org/10.3847/2041-8213/aad4fc. arXiv:1807.08161 [astro-ph.SR]

Priest ER, Cassack PA, Forbes TG (2021) The global rate of reconnection in collisional and collisionless plasmas. Phys Plasmas (in Preparation)
Prior C, Yeates AR (2014) On the helicity of open magnetic fields. Astrophys J 787(2):100. https://doi.org/10.1088/0004-637x/787/2/100
Pritchett PL, Wu CC (1979) Coalescence of magnetic islands. Phys Fluids 22:2140–2146. https://doi.org/10.1063/1.862507
Pucci F, Velli M (2013) Reconnection of quasi-singular current sheets: the "ideal" tearing mode. Astrophys J 780(2):L19. https://doi.org/10.1088/2041-8205/780/2/l19
Quinn J, MacTaggart D, Simitev RD (2021) Kelvin-Helmholtz instability and collapse of a twisted magnetic null point with anisotropic viscosity. Astron Astrophys 650:A143. https://doi.org/10.1051/0004-6361/202140460. arXiv:2102.00761 [astro-ph.SR]
Raouafi NE, Patsourakos S, Pariat E, Young PR, Sterling AC, Savcheva A, Shimojo M, Moreno-Insertis F, DeVore CR, Archontis V, Török T, Mason H, Curdt W, Meyer K, Dalmasse K, Matsui Y (2016) Solar coronal jets: observations, theory, and modeling. Space Sci Rev 201(1–4):1–53. https://doi.org/10.1007/s11214-016-0260-5
Rappazzo AF, Parker EN (2013) Current sheets formation in tangled coronal magnetic fields. Astrophys J Lett 773(1):L2–6. https://doi.org/10.1088/2041-8205/773/1/L2
Rappazzo AF, Velli M, Einaudi G, Dahlburg RB (2007) Coronal heating, weak MHD turbulence, and scaling laws. Astrophys J 657:L47. https://doi.org/10.1086/512975
Rappazzo AF, Velli M, Einaudi G, Dahlburg RB (2008) Nonlinear dynamics of the Parker scenario for coronal heating. Astrophys J 677:1348–1366. https://doi.org/10.1086/528786
Rappazzo AF, Velli M, Einaudi G (2010) Shear photospheric forcing and the origin of turbulence in coronal loops. Astrophys J 722(1):65–78. https://doi.org/10.1088/0004-637X/722/1/65
Rappazzo AF, Matthaeus WH, Ruffolo D, Servidio S, Velli M (2012) Interchange reconnection in a turbulent corona. Astrophys J 758(1):L14. https://doi.org/10.1088/2041-8205/758/1/l14
Rechester AB, Rosenbluth MN (1978) Electron heat transport in a tokamak with destroyed magnetic surfaces. Phys Rev Lett 40:38–41. https://doi.org/10.1103/PhysRevLett.40.38
Reid J, Hood AW, Parnell CE, Browning PK, Cargill PJ (2018) Coronal energy release by MHD avalanches: continuous driving. Astron Astrophys 615:A84. https://doi.org/10.1051/0004-6361/201732399
Richardson LF (1926) Atmospheric diffusion shown on a distance-neighbour graph. Proc Roy Soc Lond A 110(756):709–737. https://doi.org/10.1098/rspa.1926.0043
Rickard GJ, Titov VS (1996) Current accumulation at a three dimensional magnetic null. Astrophys J 472:840–852. https://doi.org/10.1086/178114
Ritchie ML, Wilmot-Smith AL, Hornig G (2016) The dependence of coronal loop heating on the characteristics of slow photospheric motions. Astrophys J 824:19. https://doi.org/10.3847/0004-637X/824/1/19
Rogers BN, Denton RE, Drake JF, Shay MA (2001) Role of dispersive waves in collisionless magnetic reconnection. Phys Rev Lett 87(19):195004. https://doi.org/10.1103/PhysRevLett.87.195004
Rosdahl KJ, Galsgaard K (2010) Test particle acceleration in a numerical MHD experiment of an anemone jet. Astron Astrophys 511:A73. https://doi.org/10.1051/0004-6361/200913541
Rouppe van der Voort LHM, Rutten RJ, Vissers GJM (2016) Reconnection brightenings in the quiet solar photosphere. Astron Astrophys 592:A100. https://doi.org/10.1051/0004-6361/201628889. arXiv:1606.03675 [astro-ph.SR]
Rouppe van der Voort L, De Pontieu B, Scharmer GB, de la Cruz Rodríguez J, Martínez-Sykora J, Nóbrega-Siverio D, Guo LJ, Jafarzadeh S, Pereira TMD, Hansteen VH, Carlsson M, Vissers G (2017) Intermittent reconnection and plasmoids in UV bursts in the low solar atmosphere. Astrophys J Lett 851(1):L6. https://doi.org/10.3847/2041-8213/aa99dd
Roytershteyn V, Daughton W, Karimabadi H, Mozer FS (2012) Influence of the lower-hybrid drift instability on magnetic reconnection in asymmetric configurations. Phys Rev Lett 108(18):185001. https://doi.org/10.1103/PhysRevLett.108.185001
Russell AJB, Yeates AR, Hornig G, Wilmot-Smith AL (2015) Evolution of field line helicity during magnetic reconnection. Phys Plasmas 22:032106. https://doi.org/10.1063/1.4913489
Rust DM, Kumar A (1994) Helical magnetic fields in filaments. Sol Phys 155(1):69–97. https://doi.org/10.1007/BF00670732
Rutherford PH (1973) Nonlinear growth of the tearing mode. Phys Fluids 16:1903–1908. https://doi.org/10.1063/1.1694232

Sakurai T, Levine RH (1981) Generation of coronal electric currents due to convective motions on the photosphere. Astrophys J 248:817–829

Samtaney R, Loureiro NF, Uzdensky DA, Schekochihin AA, Cowley SC (2009) Formation of plasmoid chains in magnetic reconnection. Phys Rev Lett 103:105004. https://doi.org/10.1103/PhysRevLett.103.105004

Sato T (1979) Strong plasma acceleration by slow shocks resulting from magnetic reconnection. J Geophys Res 84:7177–7190. https://doi.org/10.1029/JA084iA12p07177

Savcheva A, Pariat E, van Ballegooijen A, Aulanier G, DeLuca E (2012) Sigmoidal active region on the Sun: comparison of a magnetohydrodynamical simulation and a nonlinear force-free field model. Astrophys J 750(1):15. https://doi.org/10.1088/0004-637X/750/1/15

Savcheva A, Pariat E, McKillop S, McCauley P, Hanson E, Su Y, Werner E, DeLuca EE (2015) The relation between solar eruption topologies and observed flare features. I. Flare ribbons. Astrophys J 810(2):96. https://doi.org/10.1088/0004-637X/810/2/96. arXiv:1506.03452 [astro-ph.SR]

Schindler K, Hesse M, Birn J (1988) General magnetic reconnection, parallel electric fields, and helicity. J Geophys Res 93:5547–5557. https://doi.org/10.1029/JA093iA06p05547

Schindler K, Hesse M, Birn J (1991) Magnetic field-aligned electric potentials in nonideal plasma flows. Astrophys J 380:293–301. https://doi.org/10.1086/170586

Schmieder B, Aulanier G, Démoulin P, van Driel-Gesztelyi L, Roudier T, Nitta N, Cauzzi G (1997) Magnetic reconnection driven by emergence of sheared magnetic field. Astron Astrophys 325:1213–1225

Schmieder B, Démoulin P, Fletcher L, López Fuentes M, Mandrini C, Mason H, Young P, Nitta N (2001) CDS UV brightenings explained by quasi-separatrices and bald patches in an S-shaped active region. In: Brekke P, Fleck B, Gurman JB (ed) Recent Insights into the Physics of the Sun and Heliosphere: highlights from SOHO and Other Space Missions. vol 203. ASP Conf. Ser., San Francisco, p 314

Schnack DD, Killeen J (1979) Nonlinear saturation of the tearing mode in a reversed-field pinch. Nucl Fusion 19:877–887

Scholer M (1989) Undriven magnetic reconnection in an isolated current sheet. J Geophys Res 94:8805–8812. https://doi.org/10.1029/JA094iA07p08805

Schrijver CJ, Title AM (2002) The topology of a mixed-polarity potential field, and inferences for the heating of the quiet solar corona. Sol Phys 207:223–240. https://doi.org/10.1023/A:1016295516408

Schrijver CJ, Title AM, Harvey KL, Sheeley NR, Wang YM, van den Oord GHJ, Shine RA, Tarbell TD, Hurlburt NE (1998) Large-scale coronal heating by the small-scale magnetic field of the Sun. Nature 394:152–154

Schrijver CJ, DeRosa ML, Title AM (2010) Magnetic field topology and the thermal structure of the corona over solar active regions. Astrophys J 719(2):1083–1096. https://doi.org/10.1088/0004-637X/719/2/1083

Scott RB, Pontin DI, Yeates AR, Wyper PF, Higginson AK (2018) Magnetic structures at the boundary of the closed corona: interpretation of S-web arcs. Astrophys J 869(1):60. https://doi.org/10.3847/1538-4357/aaed2b

Scott RB, Pontin DI, Wyper PF (2019) Magnetic structures at the boundary of the closed corona: a semi-automated study of S-web morphology. Astrophys J 882(2):125. https://doi.org/10.3847/1538-4357/ab364a

Scott RB, Pontin DI, Antiochos SK, DeVore CR, Wyper PF (2021) The dynamic formation of pseudostreamers. Astrophys J 913(1):64. https://doi.org/10.3847/1538-4357/abec4f

Seehafer N (1986) On the magnetic field line topology in solar active regions. Sol Phys 105:223–235. https://doi.org/10.1007/BF00172044

Semenov VS, Kubyshkin IV, Heyn MF (1983) Asymptotic solution for field-line reconnection. Compressible case of Petschek's model. J Plasma Phys 30:303–320. https://doi.org/10.1017/S0022377800001203

Shay MA, Drake JF, Denton RE, Biskamp D (1998) Structure of the dissipation region during collisionless magnetic reconnection. J Geophys Res 103(A5):9165–9176. https://doi.org/10.1029/97JA03528

Shay MA, Drake JF, Rogers BN, Denton RE (1999) The scaling of collisionless, magnetic reconnection for large systems. Geophys Res Lett 26:2163–2166. https://doi.org/10.1029/1999GL900481

Shay MA, Drake JF, Swisdak M, Rogers BN (2004) The scaling of embedded collisionless reconnection. Phys Plasmas 11(5):2199–2213. https://doi.org/10.1063/1.1705650

Shay MA, Drake JF, Swisdak M (2007) Two-scale structure of the electron dissipation region during collisionless magnetic reconnection. Phys Rev Lett 99(15):155002. https://doi.org/10.1103/PhysRevLett.99.155002. arXiv:0704.0818 [physics.plasm-ph]

Shepherd LS, Cassak PA (2010) Comparison of secondary islands in collisional reconnection to Hall reconnection. Phys Rev Lett 105:015004. https://doi.org/10.1103/PhysRevLett.105.015004

Shibata K, Tanuma S (2001) Plasmoid-induced-reconnection and fractal reconnection. Earth Planets Space 53:473–482. https://doi.org/10.1186/BF03353258

Shibata K, Nozawa S, Matsumoto R (1992) Magnetic reconnection associated with emerging magnetic flux. Publ Astron Soc Jpn 44:265–272

Simakov AN, Chacón L, Knoll DA (2006) Semi-analytical model for flux-pileup-limited, dynamically reconnecting systems in resistive magnetohydrodynamics. Phys Plasmas 13(8):082103. https://doi.org/10.1063/1.2244531

Smith DF, Priest ER (1972) Current limitation in solar flares. Astrophys J 176:487. https://doi.org/10.1086/151651

Smitha HN, Anusha LS, Solanki SK, Riethmüller TL (2017) Estimation of the magnetic flux emergence rate in the quiet Sun from Sunrise data. Astrophys J Suppl 229:17. https://doi.org/10.3847/1538-4365/229/1/17. arXiv:1611.06432 [astro-ph.SR]

Solanki SK, Barthol P, Danilovic S, Feller A, Gandorfer A, Hirzberger J, Riethmüller TL, Schüssler M, Bonet JA, Martínez Pillet V, del Toro Iniesta JC, Domingo V, Palacios J, Knölker M, Bello González N, Berkefeld T, Franz M, Schmidt W, Title AM (2010) SUNRISE: instrument, mission, data, and first results. Astrophys J Lett 723:L127–L133. https://doi.org/10.1088/2041-8205/723/2/L127

Somov BV, Syrovatsky SI (1976) Hydrodynamic plasma flow in a strong magnetic field. Neutral current sheets in plasmas. Lebedev. Phys. Inst, Moscow, pp 13–72

Sonnerup BUO, Priest ER (1975) Resistive MHD stagnation-point flows at a current sheet. J Plasma Phys 14:283–294. https://doi.org/10.1017/S0022377800009570

Soward AM, Priest ER (1977) Fast magnetic field-line reconnection. Philos Trans R Soc A 284:369–417. https://doi.org/10.1098/rsta.1977.0013

Speiser TW (1965) Particle trajectories in model current sheets. J Geophys Res 70:4219–4226

Stanier A, Daughton W, Chacón L, Karimabadi H, Ng J, Huang YM, Hakim A, Bhattacharjee A (2015) Role of ion kinetic physics in the interaction of magnetic flux ropes. Phys Rev Lett 115(17):175004. https://doi.org/10.1103/PhysRevLett.115.175004

Stanier A, Daughton W, Simakov AN, Chacón L, Le A, Karimabadi H, Ng J, Bhattacharjee A (2017) The role of guide field in magnetic reconnection driven by island coalescence. Phys Plasmas 24(2):022124. https://doi.org/10.1063/1.4976712. arXiv:1611.05933 [physics.plasm-ph]

Stanier A, Daughton W, Le A, Li X, Bird R (2019) Influence of 3D plasmoid dynamics on the transition from collisional to kinetic reconnection. Phys Plasmas 26(7):072121. https://doi.org/10.1063/1.5100737. arXiv:1906.04867 [physics.plasm-ph]

Stein RF (2012) Solar surface magneto-convection. Living Rev Sol Phys 9:4. https://doi.org/10.12942/lrsp-2012-4

Strauss HR (1981) Resistive ballooning modes. Phys Fluids 24:2004–2009. https://doi.org/10.1063/1.863285

Strauss HR (1988) Turbulent reconnection. Astrophys J 326:412. https://doi.org/10.1086/166104

Sturrock PA (1966) Model of the high-energy phase of solar flares. Nature 211(5050):695–697. https://doi.org/10.1038/211695a0

Sturrock PA, Woodbury ET (1967) Force-free magnetic fields and solar filaments. In: Sturrock PA (ed) Plasma astrophysics. Academic Press, London, pp 155–167

Su Y, Liu R, Li S, Cao W, Ahn K, Ji H (2018) High-resolution observations of flares in an arch filament system. Astrophys J 855(2):77. https://doi.org/10.3847/1538-4357/aaac31. arXiv:1803.06085 [astro-ph.SR]

Sun X, Hoeksema JT, Liu Y, Aulanier G, Su Y, Hannah IG, Hock RA (2013) Hot spine loops and the nature of a late-phase solar flare. Astrophys J 778:139. https://doi.org/10.1088/0004-637X/778/2/139

Sweet PA (1958a) The neutral point theory of solar flares. In: Lehnert B (ed) Electromagnetic phenomena in cosmical physics. Cambridge University Press, Cambridge, pp 124–134

Sweet PA (1958b) The production of high energy particles in solar flares. Nuovo Cimento Suppl 8:188–196. https://doi.org/10.1007/BF02962520

Sweet PA (1969) Mechanisms of solar flares. Annu Rev Astron Astrophys 7:149–177. https://doi.org/10.1146/annurev.aa.07.090169.001053

Swisdak M, Liu YH, Drake JF (2008) Development of a turbulent outflow during electron-positron magnetic reconnection. Astrophys J 680(2):999–1008. https://doi.org/10.1086/588088. arXiv:0803.3415 [astro-ph]

Syntelis P, Priest ER (2020) A cancellation nanoflare model for solar chromospheric and coronal heating. III. 3D simulations and atmospheric response. Astrophys J 891(1):52. https://doi.org/10.3847/1538-4357/ab6ffc

Syntelis P, Priest ER, Chitta LP (2019) A cancellation nanoflare model for solar chromospheric and coronal heating. II. 2D theory and simulations. Astrophys J 872(1):32. https://doi.org/10.3847/1538-4357/aafaf8. arXiv:1901.02798 [astro-ph.SR]

Syrovatsky SI (1969) On the mechanism of solar flares. In: de Jager C, Švestka Z (eds) Solar flares and space research. North-Holland, Amsterdam, pp 346–355

Syrovatsky SI (1971) Formation of current sheets in a plasma with a frozen-in strong magnetic field. Sov Phys JETP 33:933–940

Tajima T, Shibata K (1997) Plasma astrophysics. Addison-Wesley, Reading

Takasao S, Asai A, Isobe H, Shibata K (2011) Simultaneous observation of reconnection inflow and outflow associated with the 2010 august 18 solar flare. Astrophys J 745(1):L6. https://doi.org/10.1088/2041-8205/745/1/l6

Takeshige S, Takasao S, Shibata K (2015) A theoretical model of a thinning current sheet in the low-β plasmas. Astrophys J 807(2):159. https://doi.org/10.1088/0004-637X/807/2/159

Tassev S, Savcheva A (2017) QSL squasher: a fast quasi-separatrix layer map calculator. Astrophys J 840(2):89. https://doi.org/10.3847/1538-4357/aa6f06. arXiv:1609.00724 [astro-ph.SR]

Taylor JB (1974) Relaxation of toroidal plasma and generation of reverse magnetic fields. Phys Rev Lett 33:1139–1141. https://doi.org/10.1103/PhysRevLett.33.1139

Thurgood JO, Pontin DI, McLaughlin JA (2017) Three-dimensional oscillatory magnetic reconnection. Astrophys J 844:2. https://doi.org/10.3847/1538-4357/aa79fa

Thurgood JO, Pontin DI, McLaughlin JA (2018a) Implosive collapse about magnetic null points: a quantitative comparison between 2D and 3D nulls. Astrophys J 855(1):50. https://doi.org/10.3847/1538-4357/aab0a0

Thurgood JO, Pontin DI, McLaughlin JA (2018b) Resistively-limited current sheet implosions in planar anti-parallel (1D) and null-point containing (2D) magnetic field geometries. Phys Plasmas 25(7):072105. https://doi.org/10.1063/1.5035489

Thurgood JO, Pontin DI, McLaughlin JA (2019) On the periodicity of linear and nonlinear oscillatory reconnection. Astron Astrophys 621:A106. https://doi.org/10.1051/0004-6361/201834369

Titov VS (1992) On the method of calculating two-dimensional potential magnetic fields with current sheets. Sol Phys 139:401–404. https://doi.org/10.1007/BF00159161

Titov VS (2007a) Generalized squashing factors for covariant description of magnetic connectivity in the solar corona. Astrophys J 660:863–873. https://doi.org/10.1086/512671

Titov VS (2007b) Pinching of coronal magnetic fields. In: Birn J, Priest ER (eds) Reconnection of magnetic fields: MHD and collisionless theory and observations. Cambridge University Press, Cambridge, pp 250–258

Titov VS, Démoulin P (1999) Basic topology of twisted magnetic configurations in solar flares. Astron Astrophys 351:707–720

Titov VS, Priest ER (1993) The collapse of an X-type neutral point to form a reconnecting time-dependent current sheet. Geophys Astrophys Fluid Dyn 72:249–276. https://doi.org/10.1080/03091929308203614

Titov VS, Priest ER, Démoulin P (1993) Conditions for the appearance of bald patches at the solar surface. Astron Astrophys 276:564–570

Titov VS, Hornig G, Démoulin P (2002) Theory of magnetic connectivity in the solar corona. J Geophys Res 107:1164. https://doi.org/10.1029/2001JA000278

Titov VS, Galsgaard K, Neukirch T (2003) Magnetic pinching of hyperbolic flux tubes. I. Basic estimations. Astrophys J 582:1172–1189. https://doi.org/10.1086/344799

Titov VS, Tassi E, Hornig G (2004) Exact solutions for steady reconnective annihilation revisited. Phys Plasmas 11(10):4662–4671. https://doi.org/10.1063/1.1789159

Titov VS, Forbes TG, Priest ER, Mikić Z, Linker JA (2009) Slip-squashing factors as a measure of three-dimensional magnetic reconnection. Astrophys J 693:1029–1044. https://doi.org/10.1088/0004-637X/693/1/1029.0807.2892

Titov VS, Mikić Z, Linker JA, Lionello R, Antiochos SK (2011) Magnetic topology of coronal hole linkages. Astrophys J 731:111. https://doi.org/10.1088/0004-637X/731/2/111
Titov VS, Mikic Z, Török T, Linker JA, Panasenco O (2012) 2010 August 1–2 sympathetic eruptions. I. Magnetic topology of the source-surface background field. Astrophys J 759:70. https://doi.org/10.1088/0004-637X/759/1/70
Török T, Aulanier G, Schmieder B, Reeves KK, Golub L (2009) Fan-spine topology formation through two-step reconnection driven by twisted flux emergence. Astrophys J 704:485–495
Tortosa-Andreu A, Moreno-Insertis F (2009) Magnetic flux emergence into the solar photosphere and chromosphere. Astron Astrophys 507(2):949–967. https://doi.org/10.1051/0004-6361/200912394
Tur TJ (1977) Aspects of current sheet theory. PhD thesis, St Andrews University, St Andrews
Ugai M (1984) Self-consistent development of fast magnetic reconnection with anomalous plasma resistivity. Plasma Phys Contr Fusion 26:1549–1563. https://doi.org/10.1088/0741-3335/26/12B/010
Ugai M (1999) Computer studies on the spontaneous fast reconnection model as a nonlinear instability. Phys Plasmas 6:1522–1531. https://doi.org/10.1063/1.873405
Ugai M (2000) Computer simulations of asymmetric spontaneous fast reconnection. Phys Plasmas 7:867–874. https://doi.org/10.1063/1.873883
Ugai M (2008) Impulsive chromospheric heating of two-ribbon flares by the fast reconnection mechanism. Phys Plasmas 15(3):032902. https://doi.org/10.1063/1.2884715
Ugai M, Kondoh K (2001) Computer studies on the spontaneous fast reconnection evolution in various physical situations. Phys Plasmas 8:1545–1552. https://doi.org/10.1063/1.1360212
Ugai M, Tsuda T (1977) Magnetic field-line reconnection by localised enhancement of resistivity. I: Evolution in a compressible MHD fluid. J Plasma Phys 17:337–356. https://doi.org/10.1017/S0022377800020663
Ugai M, Wang WB (1998) Computer simulations on three-dimensional plasmoid dynamics by the spontaneous fast reconnection model. J Geophys Res 103:4573–4586. https://doi.org/10.1029/97JA01646
Ugai M, Zheng L (2005) Conditions for the fast reconnection mechanism in three dimensions. Phys Plasmas 12(9):092312. https://doi.org/10.1063/1.2047327
Ugai M, Kondoh K, Shimizu T (2004) Computer studies on the three-dimensional spontaneous fast reconnection model as a nonlinear instability. Phys Plasmas 11:1416–1423. https://doi.org/10.1063/1.1677110
Ugarte-Urra I, Warren HP, Winebarger AR (2007) The magnetic topology of coronal mass ejection sources. Astrophys J 662(2):1293–1301. https://doi.org/10.1086/514814. arXiv:astro-ph/0703049 [astro-ph]
Uzdensky DA, Kulsrud RM (2000) Two-dimensional numerical simulation of the resistive reconnection layer. Phys Plasmas 7(10):4018–4030. https://doi.org/10.1063/1.1308081. arXiv:astro-ph/0003305 [astro-ph]
Uzdensky DA, Loureiro NF (2016) Magnetic reconnection onset via disruption of a forming current sheet by the tearing instability. Phys Rev Lett 116(10):105003. https://doi.org/10.1103/PhysRevLett.116.105003
Uzdensky DA, Loureiro NF, Schekochihin AA (2010) Fast magnetic reconnection in the plasmoid-dominated regime. Phys Rev Lett 105:235002. https://doi.org/10.1103/PhysRevLett.105.235002
van Ballegooijen AA (1985) Electric currents in the solar corona and the existence of magnetostatic equilibrium. Astrophys J 298:421–430. https://doi.org/10.1086/163626
van Ballegooijen AA (1988a) Force free fields and coronal heating, part I. The formation of current sheets. Geophys Astrophys Fluid Dyn 41(3–4):181–211
van Ballegooijen AA (1988b) Magnetic fine structure of solar coronal loops. In: Altrock RC (ed) Solar and stellar coronal structure and dynamics: a festschrift in honor of Dr. John W. Evans. Proceedings of the ninth sacramento peak summer symposium, Sunspot, NM, 17–21 August, 1987. Harvard-Smithsonian Center for Astrophysics, Cambridge, MA, pp 115–124
van Ballegooijen AA, Martens PCH (1989) Formation and eruption of solar prominences. Astrophys J 343:971. https://doi.org/10.1086/167766
van Driel-Gesztelyi L, Culhane JL, Baker D, Démoulin P, Mandrini CH, DeRosa ML, Rouillard AP, Opitz A, Stenborg G, Vourlidas A, Brooks DH (2012) Magnetic topology of active regions and coronal holes: implications for coronal outflows and the solar wind. Sol Phys 281(1):237–262. https://doi.org/10.1007/s11207-012-0076-8
Vekstein GE, Priest ER (1992) Magnetohydrodynamic equilibria and cusp formation at an X-type neutral line by footpoint shearing. Astrophys J 384:333–340. https://doi.org/10.1086/170876

Vekstein G, Priest ER (1993) Magnetostatic equilibria and current sheets in a sheared magnetic field with an X-point. Sol Phys 146:119–125. https://doi.org/10.1007/BF00662173
Vekstein GE, Priest ER, Amari T (1991) Formation of current sheets in force-free magnetic fields. Astron Astrophys 243:492–500
Viall NM, Borovsky JE (2020) Nine outstanding questions of solar wind physics. J Geophys Res 125(7):e2018JA026005. https://doi.org/10.1029/2018JA026005
Vissers GJM, de la Cruz Rodríguez J, Libbrecht T, Rouppe van der Voort LHM, Scharmer GB, Carlsson M (2019) Dissecting bombs and bursts: non-LTE inversions of low-atmosphere reconnection in SST and IRIS observations. Astron Astrophys 627:A101. https://doi.org/10.1051/0004-6361/201833560. arXiv:1905.02035 [astro-ph.SR]
Waddell BV, Rosenbluth MN, Monticello DA, White RB (1976) Non-linear growth of the $m = 1$ tearing mode. Nucl Fusion 16:528–532
Wang J, Li W, Denker C, Lee C, Wang H, Goode PR, McAllister A, Martin SF (2000) Mini-filament eruption on the quiet Sun. I. Observations at Hα central line. Astrophys J 530(2):1071–1084. https://doi.org/10.1086/308377
Warnecke J, Peter H (2019) Data-driven model of the solar corona above an active region. Astron Astrophys 624:L12. https://doi.org/10.1051/0004-6361/201935385
Wendel DE, Adrian ML (2013) Current structure and nonideal behavior at magnetic null points in the turbulent magnetosheath. J Geophys Res 118(4):1571–1588. https://doi.org/10.1002/jgra.50234
Wesson J (1997) Tokamaks. Clarendon Press, Oxford
White RB, Monticello DA, Rosenbluth MN, Waddell BV (1977) Saturation of the tearing mode. Phys Fluids 20:800–805. https://doi.org/10.1063/1.861939
Wilmot-Smith AL, Priest ER (2007) Flux tube disconnection: an example of 3D reconnection. Phys Plasmas 14:102903 (1–9). https://doi.org/10.1063/1.2783257
Wilmot-Smith AL, Priest ER, Hornig G (2005) Magnetic diffusion and the motion of magnetic field lines. Geophys Astrophys Fluid Dyn 99:177–197. https://doi.org/10.1080/03091920500044808
Wilmot-Smith AL, Hornig G, Pontin DI (2009a) Magnetic braiding and parallel electric fields. Astrophys J 696:1339–1347. https://doi.org/10.1088/0004-637X/696/2/1339
Wilmot-Smith AL, Hornig G, Pontin DI (2009b) Magnetic braiding and quasi-separatrix layers. Astrophys J 704:1288–1295. https://doi.org/10.1088/0004-637X/704/2/1288
Wilmot-Smith AL, Pontin DI, Hornig G (2010) Dynamics of braided coronal loops. I. Onset of magnetic reconnection. Astron Astrophys 516:A5. https://doi.org/10.1051/0004-6361/201014041
Wilmot-Smith AL, Pontin DI, Yeates AR, Hornig G (2011) Heating of braided coronal loops. Astron Astrophys 536:A67. https://doi.org/10.1051/0004-6361/201117942
Wright AN, Berger MA (1989) The effect of reconnection upon the linkage and interior structure of magnetic flux tubes. J Geophys Res 94:1295. https://doi.org/10.1086/174157
Wyper P, Jain R (2010) Torsional magnetic reconnection at three-dimensional null points: a phenomenological study. Phys Plasmas 17:092902
Wyper PF, DeVore CR (2016) Simulations of solar jets confined by coronal loops. Astrophys J 820(1):77. https://doi.org/10.3847/0004-637X/820/1/77
Wyper PF, Hesse M (2015) Quantifying three-dimensional reconnection in fragmented current layers. Phys Plasmas 22(4):042117. https://doi.org/10.1063/1.4918335
Wyper PF, Pontin DI (2013) Kelvin-Helmholtz instability in a current-vortex sheet at a 3D magnetic null. Phys Plasmas 20(3):032117. https://doi.org/10.1063/1.4798516
Wyper PF, Pontin DI (2014a) Dynamic topology and flux rope evolution during non-linear tearing of 3D null point current sheets. Phys Plasmas 21(10):102102. https://doi.org/10.1063/1.4896060
Wyper PF, Pontin DI (2014b) Non-linear tearing of 3D null point current sheets. Phys Plasmas 21(8):082114. https://doi.org/10.1063/1.4893149
Wyper PF, DeVore CR, Karpen JT, Lynch BJ (2016) Three-dimensional simulations of tearing and intermittency in coronal jets. Astrophys J 827(1):4. https://doi.org/10.3847/0004-637x/827/1/4
Xiao CJ, Wang XG, Pu ZY, Zhao H, Wang JX, Ma ZW, Fu SY, Kivelson MG, Liu ZX, Zong QG, Glassmeier KH, Balogh A, Korth A, Reme H, Escoubet CP (2006) In situ evidence for the structure of the magnetic null in a 3D reconnection event in the Earth's magnetotail. Nature Phys 2(7):478–483. https://doi.org/10.1038/nphys342
Xiao CJ, Wang XG, Pu ZY, Ma ZW, Zhao H, Zhou GP, Wang JX, Kivelson MG, Fu SY, Liu ZX, Zong QG, Dunlop MW, Glassmeier K, Lucek E, Reme H, Dandouras I, Escoubet CP (2007) Satellite observations of separator-line geometry of three-dimensional magnetic reconnection. Nat Phys 3:609–613. https://doi.org/10.1038/nphys650

Yamada M, Ono Y, Hayakawa A, Katsurai M (1990) Magnetic reconnection of plasma toroids with cohelicity and counter-helicity. Phys Rev Lett. https://doi.org/10.1103/PhysRevLett.65.721
Yamada M, Kulsrud R, Ji H (2010) Magnetic reconnection. Rev Mod Phys 82:603–664. https://doi.org/10.1103/RevModPhys.82.603
Yan M, Lee L, Priest ER (1992) Fast magnetic reconnection with small shock angles. J Geophys Res 97:8277–8293. https://doi.org/10.1029/92JA00170
Yan M, Lee LC, Priest ER (1993) Magnetic reconnection with large separatrix angles. J Geophys Res 98:7593–7602. https://doi.org/10.1029/92JA02644
Yang K, Guo Y, Ding MD (2015) On the 2012 October 23 circular ribbon flare: Emission features and magnetic topology. Astrophys J 806:171. https://doi.org/10.1088/0004-637X/806/2/171
Yeates AR, Hornig G (2013) Unique topological characterization of braided magnetic fields. Phys Plasmas 20(1):012102. https://doi.org/10.1063/1.4773903
Yeates AR, Hornig G, Wilmot-Smith AL (2010) Topological constraints on magnetic relaxation. Phys Rev Lett 105(8):085002. https://doi.org/10.1103/PhysRevLett.105.085002
Yeates AR, Russell AJB, Hornig G (2015) Physical role of topological constraints in localized magnetic relaxation. Proc R Soc London Ser A 471:50012. https://doi.org/10.1098/rspa.2015.0012
Yokoyama T, Shibata K (1995) Magnetic reconnection as the origin of X-ray jets and Hα surges on the Sun. Nature 375(6526):42–44. https://doi.org/10.1038/375042a0
Yokoyama T, Shibata K (1996) Numerical simulation of solar coronal X-ray jets based on the magnetic reconnection model. Publ Astron Soc Jpn 48(2):353–376. https://doi.org/10.1093/pasj/48.2.353
Zemanová A, Dudík J, Aulanier G, Thalmann JK, Gömöry P (2019) Observations of a footpoint drift of an erupting flux rope. Astrophys J 883(1):96. https://doi.org/10.3847/1538-4357/ab3926. arXiv:1908.02082 [astro-ph.SR]
Zhang Q, Drake JF, Swisdak M (2019) Particle heating and energy partition in low-β guide field reconnection with kinetic Riemann simulations. Phys Plasmas 26(7):072115. https://doi.org/10.1063/1.5104352. arXiv:1904.12922 [physics.plasm-ph]
Zhao J, Gilchrist SA, Aulanier G, Schmieder B, Pariat E, Li H (2016) Hooked flare ribbons and flux-rope-related QSL footprints. Astrophys J 823(1):62. https://doi.org/10.3847/0004-637X/823/1/62. arXiv:1603.07563 [astro-ph.SR]
Zhao L, Landi E, Lepri ST, Kocher M, Zurbuchen TH, Fisk LA, Raines JM (2017) An anomalous composition in slow solar wind as a signature of reconnection in its source region. Astrophys J Suppl Ser 228(1):4. https://doi.org/10.3847/1538-4365/228/1/4
Zharkova VV, Arzner K, Benz AO, Browning P, Dauphin C, Emslie AG, Fletcher L, Kontar EP, Mann G, Onofri M, Petrosian V, Turkmani R, Vilmer N, Vlahos L (2011) Recent advances in understanding particle acceleration processes in solar flares. Space Sci Rev 159(1–4):357–420. https://doi.org/10.1007/s11214-011-9803-y
Zheng R, Chen Y, Wang B (2016) Slipping magnetic reconnections with multiple flare ribbons during an X-class solar flare. Astrophys J 823(2):136. https://doi.org/10.3847/0004-637X/823/2/136. arXiv:1604.04982 [astro-ph.SR]
Zhou M, El-Alaoui M, Lapenta G, Berchem J, Richard RL, Schriver D, Walker RJ (2018) Suprathermal electron acceleration in a reconnecting magnetotail: large-scale kinetic simulation. J Geophys Res 123:8087–8108. https://doi.org/10.1029/2018JA025502
Zweibel EG (1994) Magnetic fields and star formation. In: Lynden-Bell D (ed) Cosmical magnetism. NATO ASI Series C, vol 422. Kluwer, Dordrecht, p 73. https://doi.org/10.1007/978-94-011-1110-2_8
Zweibel EG, Li HS (1987) The formation of current sheets in the solar atmosphere. Astrophys J 312:423. https://doi.org/10.1086/164887
Zweibel EG, Yamada M (2009) Magnetic reconnection in astrophysical and laboratory plasmas. Annu Rev Astron Astrophys 47(1):291–332. https://doi.org/10.1146/annurev-astro-082708-101726

Publisher's Note Springer Nature remains neutral with regard to jurisdictional claims in published maps and institutional affiliations.

Authors and Affiliations

David I. Pontin[1] · **Eric R. Priest**[2]

✉ David I. Pontin
david.pontin@newcastle.edu.au

Eric R. Priest
eric.r.priest@gmail.com

[1] School of Information and Physics Sciences, University of Newcastle, Callaghan, NSW 2308, Australia

[2] Mathematics Institute, St Andrews University, St Andrews KY16 8QR, UK